

SSC-393

**EVALUATION OF DUCTILE
FRACTURE MODELS**



This document has been approved
for public release and sale; its
distribution is unlimited

SHIP STRUCTURE COMMITTEE

1997

G-M Technical Resources Center



00001791

Member Agencies:

*American Bureau of Shipping
Defence Research Establishment Atlantic
Maritime Administration
Military Sealift Command
Naval Sea Systems Command
Transport Canada
United States Coast Guard*



**Ship
Structure
Committee**

An Interagency Advisory Committee

Address Correspondence to:

Executive Director
Ship Structure Committee
U.S. Coast Guard (G-MMS/SSC)
2100 Second Street, S.W.
Washington, D.C. 20593-0001
Ph:(202) 267-0003
Fax:(202) 267-4816

SSC-393
SR-1349

January 8, 1997

EVALUATION OF DUCTILE FRACTURE MODELS

This report extends our understanding of the behavior of ships which have experienced some yielding in service. Once an initial (even small) crack has occurred in a structural component, the ductility of the remaining structure is relied upon for the overall structure's survivability. In the study large scale tests were conducted of components containing long fatigue cracks to measure the post yield fracture behavior of the structure at several details. These cracks were predominantly located in the base metals of the test components. The results of the tests were used to evaluate the conservatism that is expected in the current models of ductile fracture. The results were compared against the British Standards Institute Document PD6493-91, a stable tearing-analysis using finite element analysis to calculate the J integral, Landes' normalization method, and a limit-load analysis. Because of the high fracture toughness, relative thin structural thickness of the components tested, and the substantial amount of stable crack growth these test pieces were generally not under a J controlled field. Through the results of these comparisons, guidance for use of these methods is given and simplified methods for routine usage with ship structures is provided.

J.C. CARD
Rear Admiral, U.S. Coast Guard
Chairman, Ship Structure Committee

1. Report No. SSC-393		2. Government Accession No. PB 97 - 109979		3. Recipient's Catalog No.	
4. Title and Subtitle Evaluation of Ductile Fracture Models for Ship Structural Details				5. Report Date June 1996	
				6. Performing Organization Code	
7. Author(s) Robert J. Dexter and Michael L. Gentilcore				8. Performing Organization Report No. SSC Project SR1349 ATLSS Report No. 96-09	
9. Performing Organization Name and Address ATLSS Engineering Research Center Lehigh University 117 ATLSS Drive Bethlehem, PA 18015-4729				10. Work Unit No. (TRAIS)	
				11. Contract or Grant No. DTCG23-92-C-E01031	
12. Sponsoring Agency Name and Address Ship Structures Committee c/o U.S. Coast Guard 2100 Second Street, S.W. Washington, D.C. 20593-0001				13. Type of Report and Period Covered Final Report	
				14. Sponsoring Agency Code G-M	
15. Supplementary Notes Sponsored by the Ship Structure Committee and its member agencies					
16. Abstract Ductile fracture is the expected failure mode at service temperatures for relatively thin sections (less than 26 mm thick) of common ship steels and weld metals. This report provides guidelines for calculating the load-displacement curves for ductile fracture of cracked ship structural members. These analyses may be used to determine the maximum crack size that can be tolerated in typical ship structure without significant loss of load capacity or ductility. Experiments were conducted on over 30 large-scale welded structural members containing fatigue cracks. These members consistently reached at least the net-section collapse load and deformed to several times the yield-point displacement. The experiments were analyzed with a variety of ductile-fracture models including the three levels in the British Standards Institute document PD 6493, a stable tearing-analysis using finite-element analysis to calculate the J integral, Landes' normalization method, and a limit-load analysis. These models were studied in order to evaluate their usefulness and degree of conservatism relative to experimental results. Guidelines are provided for applying several ductile fracture models to complex structural details. The models embodied in the British Standards Institute PD6493 adequately predict the peak load but were not intended to predict the descending part of the load-displacement relation, i.e. the ductility, of the cracked members. The ductility can be estimated using a stable tearing analysis to predict crack extension and either limit-load analysis, finite-element analysis, or Landes' normalization method to calculate the load. Simple models to calculate the load-displacement curve are suggested which may be more practical for routine use.					
17. Key Words Ship structure, Fracture, Ductility, Finite element, Ductile tearing, PD 6493, J-integral, Limit load			18. Distribution Statement Distribution unlimited, available from: National Technical Information Service U. S. Department of Commerce Springfield, VA 22151 Ph (703) 487-4650		
19. Security Classif. (of this report) Unclassified		20. Security Classif. (of this page) Unclassified		21. No. of Pages 293	22. Price

NIST

United States Department of Commerce
Technology Administration
National Institute of Standards and Technology
Metric Program, Gaithersburg, MD 20899

METRIC CONVERSION CARD

Approximate Conversions from Metric Measures

Symbol When You Know Multiply by To Find Symbol

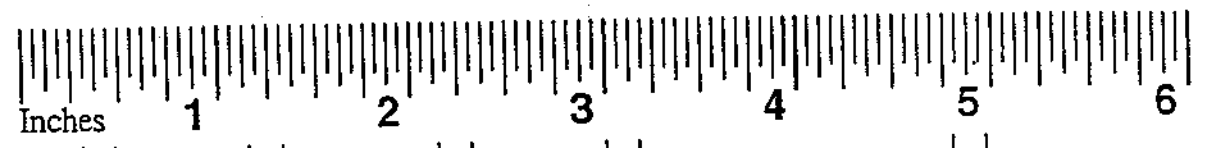
LENGTH			
mm	millimeters	0.04 inches	in
cm	centimeters	0.4 inches	in
m	meters	3.3 feet	ft
m	meters	1.1 yards	yd
km	kilometers	0.6 miles	mi

AREA			
cm ²	square centimeters	0.16 square inches	in ²
m ²	square meters	1.2 square yards	yd ²
km ²	square kilometers	0.4 square miles	mi ²
ha	hectares	2.5 acres	
	(10,000 m ²)		

MASS (weight)			
g	grams	0.035 ounces	oz
kg	kilograms	2.2 pounds	lb
t	metric ton	1.1 short tons	
	(1,000 kg)		

VOLUME			
mL	milliliters	0.03 fluid ounces	fl oz
mL	milliliters	0.06 cubic inches	in ³
L	liters	2.1 pints	pt
L	liters	1.06 quarts	qt
L	liters	0.26 gallons	gal
m ³	cubic meters	35 cubic feet	ft ³
m ³	cubic meters	1.3 cubic yards	yd ³

TEMPERATURE (exact)			
°C	degrees Celsius	multiply by 9/5, add 32	degrees Fahrenheit
°F	degrees Fahrenheit	subtract 32, multiply by 5/9	degrees Celsius



Approximate Conversions to Metric Measures

Symbol	When You Know	Multiply by	To Find	Symbol
LENGTH				
in	inches	2.5	centimeters	cm
ft	feet	30	centimeters	cm
yd	yards	0.9	meters	m
mi	miles	1.6	kilometers	km

AREA			
in ²	square inches	6.5 square centimeters	cm ²
ft ²	square feet	0.09 square meters	m ²
yd ²	square yards	0.8 square meters	m ²
mi ²	square miles	2.6 square kilometers	km ²
	acres	0.4 hectares	ha

MASS (weight)			
oz	ounces	28 grams	g
lb	pounds	0.45 kilograms	kg
	short tons	0.9 metric ton	t
	(2000 lb)		

VOLUME			
tsp	teaspoons	5 milliliters	mL
Tbsp	tablespoons	15 milliliters	mL
in ³	cubic inches	16 milliliters	mL
fl oz	fluid ounces	30 milliliters	mL
c	cups	0.24 liters	L
pt	pints	0.47 liters	L
qt	quarts	0.95 liters	L
gal	gallons	3.8 liters	L
ft ³	cubic feet	0.03 cubic meters	m ³
yd ³	cubic yards	0.76 cubic meters	m ³

TEMPERATURE (exact)			
°F	degrees Fahrenheit	subtract 32, multiply by 5/9	degrees Celsius
°C	degrees Celsius	multiply by 9/5, add 32	degrees Fahrenheit

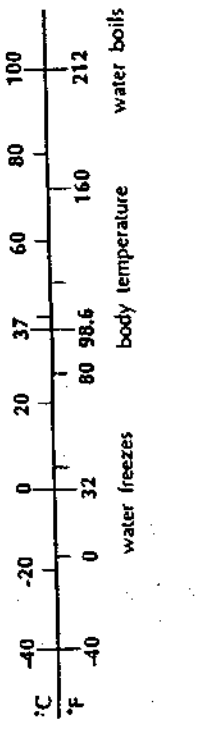


Table of Contents

1.0	Introduction	1
2.0	Background	12
2.1	Identification of critical fatigue-sensitive details	12
2.2	Types of fracture behavior	15
2.3	Fracture mechanics analysis	16
3.0	Fracture Experiments	35
3.1	Specimen fabrication, residual stress, and materials characterization	35
3.2	I-beams with structural details in bending	41
3.3	Box-beams with stiffened shell in bending	45
3.4	Cope-hole and CCT specimens in tension	47
4.0	Analyses of Experiments	98
4.1	PD6493 calculations	100
4.2	Plastic limit-load calculations for propagating cracks	111
4.3	Finite-element analyses to calculate applied J	112
4.4	J estimation schemes	115
4.5	Predicting crack propagation by the J-R curve analysis	121
4.6	Landes' normalization method	125
4.7	Predicting crack propagation by the crack opening angle	129
5.0	Guidelines for Application of Ductile Fracture Models to Ship Structures	180
5.1	Specification of steel and filler metal	180
5.2	Fracture mechanics test methods	183
5.3	Recommended ductile fracture models	185
6.0	Conclusions and Recommendations for Further Research	191
Appendix 1:	Selected J-R Curves for the HSLA-80 and EH-36 Material	
Appendix 2:	Experimental Data from I-Beam Experiments	
Appendix 3:	Experimental Data from Box-Beam Experiments	
Appendix 4:	Experimental Data from Cope-Hole Experiments	
Appendix 5:	Sample Stress Intensity Factor Calculation	
Appendix 6:	Limit-Load Predictions for I-Beam and Box-beam Specimens	

Acknowledgements

This work was supported by the interagency Ship Structure Committee under contract DTCG23-92-C-EO1031. The authors are grateful for the guidance of the Project Technical Committee, especially the Chairman Walter Reuter of Idaho National Engineering Laboratory and the Technical Advisor John Landes of the University of Tennessee. Stanley Rolfe of the University of Kansas served as a consultant to Lehigh University on this project and provided overall guidance on fracture mechanics assessment of ship structure, particularly on the use of CTOD. Harold Reemsnyder of Bethlehem Steel Corporation provided valuable insight and advice, particularly on the application of PD6493. In addition to the authors, many others at Lehigh have contributed to this research, especially Bruce Somers and Dayan Xiao. Professors John Fisher and Richard Roberts provided guidance and advice. Several undergraduate students at Lehigh University contributed to the project, especially Kenneth Gilvary and Kenneth George. The authors are also grateful for the work of the technical staff at the ATLSS Laboratory and Fritz Laboratory, especially David Schnalzer who fabricated many of the specimens and the photography of Richard Sopko. Most of the test specimens were fabricated at Ingalls Shipbuilding.

1.0 INTRODUCTION

There is a need to predict the behavior of ship structures after yielding, particularly the ductility of members and their connections. The ductility is required to develop a reserve capacity that is actually counted on for the safety of ships. Because ship structural details may have fatigue cracks, it is necessary to assess the ductility and residual load capacity of cracked ship structural details. Ductile fracture models are required for this assessment. This report presents an evaluation of various ductile fracture models for this purpose. The process for evaluating the post-yielding behavior of a ship structure is discussed below. Criteria for adequate ductility and the cost impact are discussed. The required qualities of the steel are briefly discussed.

It is particularly important that ships and marine structures have good ductility because of the probability of extreme loading [1.6]. The wave-loading probability density function has a long tail of extreme values. Extreme loading also may occur in ships due to excessive speed for the conditions. Fortunately, most ships and other marine structures can tolerate limited extreme loads larger than the design loads. Extreme loading results in local damage but typically will not result in catastrophic failure [1.3, 1.7].

It has been established that properly proportioned and detailed welded steel structures can consistently exceed their yield strength, achieve the calculated fully-plastic "limit load", and deform in a ductile manner to a total displacement many times larger than the displacement at the yield point [1.1]. Ship structures should be designed to develop this ductility, which allows the development of reserve capacity beyond yielding, as shown in Figure 1.1. However, improper design and/or improper maintenance may prevent the structure from developing the reserve capacity and withstanding the extreme loading. The critical issues in design include poor detailing and/or the use of brittle materials. The critical issues in maintenance include excessive fatigue cracking, corrosion wastage, or other structural damage [1.8].

The reserve capacity is due to strain hardening of the steel and, as shown in Figure 1.1, the increase in bending moment from initial yield of the section until the yielding has spread across the section [1.2]. Most modern shipbuilding steels have relatively low strain-hardening, and therefore the reserve capacity is due primarily to spreading of yielding across the section. The maximum bending moment capacity is called the plastic moment or the limit load [1.2].

The reserve capacity is counted on to achieve the desired margin of safety or reliability level in design specifications. The reserve capacity is explicitly calculated in design specifications for bridges, buildings, and a variety of other steel structures, which are based on the limit load rather than an allowable stress. Such "limit-state" design specifications include the "Load and Resistance Factor Design (LRFD) Specification for Structural Steel Buildings" from the American Institute of Steel Construction (AISC) and the "AASHTO LRFD Bridge Design Specifications" from the American Association of

State Highway and Transportation Officials. The trend in ship design [1.2-1.4] and offshore structure design [1.5] also is moving toward limit-state design.

After a ship is designed for strength in the conventional manner, a further effort can be made to assure structural integrity in the event of an extreme load larger than the design load. Design for structural integrity does not involve specific loads. The philosophy is to maximize the strength and ductility without increasing the basic scantlings required to satisfy rules or strength requirements. The objective is to get the yielding to spread across the cross section and develop the reserve capacity of the structural system without allowing premature failure of an individual component to precipitate total failure of the structure [1.3].

The process of design for structural integrity involves: 1) predicting conceivable failure modes due to extreme loading; then, 2) correctly selecting materials for and detailing the "critical" members and connections involved in each failure mode to achieve maximum ductility. In a typical ship structure, maximum ductility of the hull girder is associated with failure modes of general gross-section yielding in the tension zone and post-yield column or grillage buckling in the compression zone [1.2]. Critical members and connections are those which are required to yield, elongate, or form a plastic hinge before the ultimate strength can be achieved for these conceived failure modes.

The overall hull girder is essentially under "fixed-load" or "load-control" boundary conditions as shown in Figure 1.1, i.e. catastrophic failure will occur instantly if loads exceed the ultimate strength of the overall hull girder. On a local scale, however, most individual members and connections are essentially under "displacement-control" boundary conditions [1.3]. In other words, because of the stiffness of the surrounding structure, the ends of the member have to deform in way that is compatible with nearby members. Under displacement control, a member can continue to provide integrity (e.g. transfer shear and prevent leaking) after it has reached ultimate strength and is in the descending branch of the load-displacement curve. This behavior under displacement control is referred to as load shedding. In order to develop the full ultimate strength of the hull girder without catastrophic fracture of the hull or localized fracture that leads to leaking of tanks, individual critical members in the tension zone must elongate to several times the yield strain locally without fracturing.

In order to quantify this elongation requirement, the "ductility factor" is defined here as the ratio of the total deformation at fracture of a member to the yield deformation. There are various other definitions of ductility factor in the literature. The ductility factor is a fairly general way to express ductility, since this could be the ratio of any measure of deformation, e.g. the ratio of strain to yield strain or the ratio of displacement to yield displacement.

The required level of ductility is usually not explicitly specified in design codes. The AISC LRFD Specification states that for seismic resistance members should have a

ductility factor of from 3 to 5. This level of ductility is probably as good as can be expected for members with welded connections. For example, Wells' criterion for good performance from wide-plate tests in the early 60's was a ductility factor of 4 [1.9]. In a recent paper by Rudi Denys [1.10], a criterion for acceptability of defective welds is proposed to assure pipeline integrity. Denys proposes that wide-plate tests are acceptable if there is greater than 0.8 percent strain over the gage length. For a steel with a yield point of about 350 MPa, this is equivalent to a ductility factor between 4 and 5. Based on these indications of the best expected performance of welded members, a criterion for adequate ductility of ship structures, which have fairly complex geometries, is that a member should achieve a ductility factor of at least 3.0.

Unfortunately, many ships and other structures were not adequately designed for fatigue, and consequently these ships develop many large fatigue cracks, i.e. visually-detectable cracks on the order of 50 mm or more in length on the surface [1.13]. In these cases, if the desired level of reliability of the structure is to be maintained, it is essential that members with typical cracks can still achieve adequate ductility. Therefore, as part of the structural integrity assessment of these ships, a ductile fracture assessment should be conducted to assure that members with cracks can achieve a ductility factor of at least 3.0.

Modern ships fabricated from notch-tough thin plates (less than 26 mm) have only a very small probability that fracture will occur directly from notches or fabrication flaws. Fracture of fabrication flaws usually occurs only in low-toughness materials, i.e. materials that do not have a specified level of low-temperature notch toughness (Charpy energy). Such "brittle" fractures occurred in more than 20 percent of the 4694 merchant ships built during the World War II, causing 145 of these ships to break in two [1.11]. As a result of the understanding of brittle fracture [1.12], improvements were made in steel processing, steel specifications, weld procedures, and structural detailing.

Often, assurance of adequate ductility for structural integrity under extreme loads can be achieved with only a small cost increase relative to a structure that is designed to meet the strength criteria only. The cost may increase due to: 1) details which are more expensive to fabricate; 2) more expensive welding procedures; and, 3) more expensive materials.

Steel and filler metals with very high toughness are available at slightly greater cost and may be warranted in certain applications where very large cracks must be tolerated. Fine-grain-practice ship steels (ASTM A131 grades other than A, B, AH32, and AH36) have very high toughness. The use of very-high-toughness steel and weld metal has become prevalent in Naval surface combatant construction. These steels are used for sheer and bilge strakes, flight decks, protective plating and some equipment foundations. The recent cruiser (CG-47 class) and destroyer (DDG-51 class) designs made extensive use of both ASTM A710 (HSLA) and quenched and tempered (HY) steels. Thermo-Mechanically Controlled Process (TMCP) steel (such as API Spec 2W) made in Europe

and Asia typically has very high toughness. Many other steels used for offshore structures also have very high toughness, especially API Spec 2H and Spec 2Y. The use of these cleaner low-carbon materials may actually lead to savings in welding and NDE. The increased reliability accrued from using these materials may also justify the cost.

In most cases, however, the steels and filler metals which are presently used in shipbuilding are specified with a Charpy test requirement. Charpy test requirements are discussed further in Chapter 5, where the Charpy test requirements for ASTM A131 ship steels are provided in Table 5.1. Pense, in SSC-307 [1.14], showed that these Charpy test requirements should assure that the materials have sufficient toughness over the range of possible service temperatures, especially for plates less than 26 mm thick. Here sufficient toughness means toughness which would allow yielding to occur despite the existence of a large crack. A large crack will likely extend under a strain level of several times the yield strain, but this is acceptable provided that the crack extension is limited and takes place in a stable manner.

In fact, it is not clear that the high-toughness steel will necessarily lead to greater ductility than steel of moderate but adequate toughness. Experiments described in Chapter 3 indicate that, beyond a certain level of toughness, the yield-to-tensile strength ratio (Y/T) of the steel has a greater effect on ductility than increased toughness. Steels with a low Y/T (lower than about 0.8) can spread the plastic deformation away from a notch or crack, develop gross-section yielding, and increase overall elongation. Steels with a high Y/T (over 0.87) tend to concentrate the plastic deformation in a narrow band near a notch or crack. The difference in tensile behavior of steels with low and high Y/T is illustrated in Figure 1.2. Figure 1.2 shows a comparison of the normalized stress-strain curves for typical flat tensile test specimens of HSLA-80 steel (Y/T of 0.88) and an A36 structural steel (Y/T of 0.6). Tensile tests with a hole as a stress concentration show the greater ductility of the steel with the lower Y/T [1.15]. Typical small-specimen Charpy V-notch (CVN) and fracture-toughness tests (J/CTOD) are too small and deeply notched to develop the benefit of gross-section yielding that is promoted by a low Y/T. Therefore, these tests do not show much difference between steels with widely varying Y/T. In fact, the steel that gives better structural ductility may not have better CVN and J/CTOD test results.

In order to estimate the ductility factor for members with fatigue cracks, methods to predict the load-displacement curve for ship structural details are required. In order to estimate the load-displacement curve, it is necessary to predict the initiation of tearing and the stable tearing or propagation of cracks in these details. There are numerous available ductile fracture models that can be used to make such predictions [1.16]. The abundance of approaches and lack of clear guidance makes a ductile fracture assessment seem very perplexing for a non-expert. Fortunately, most of these approaches share an essentially equivalent basis, and can therefore be related to one another. For example, the J integral and the CTOD are directly proportional, therefore the use of one of these fracture criteria is equivalent to the use of the other [1.17,1.18]. The differences between the ductile

fracture models arise in the "rules" for measurement and application of the fracture criteria, i.e. in the methods of application.

This report addresses issues that arise in application of fracture models, including: 1) variability of material properties; 2) changes in apparent toughness values with changes in test specimen size and geometry; 3) differences in toughness and strength of the weld zone; 4) complex residual stresses; 5) high gradients of stress in the vicinity of the crack due to stress concentrations; and, 6) the behavior of cracks in complex structures of welded intersecting plates (e.g. tearing behavior of cracks with multiple ends). This report provides guidelines for how to handle these issues in a ductile fracture analysis to determine the maximum load capacity and ductility of cracked ship structural details. The ductile fracture analysis can be used to determine the maximum crack size that can be tolerated in a typical ship structural member or connection without significant loss of load capacity or ductility (e.g. decreased by 20 percent or more). Together with crack-growth-rate calculations, the maximum or critical crack size can be used to set inspection intervals or to justify deferring the repair of a subcritical crack found in service. As an example of the typical fracture resistance of ship structure, a recent assessment of the critical crack size for a long shell crack propagating in a stiffened tanker bottom concluded that a crack longer than 400 mm would not be unstable [1.19].

The emphasis in this report is on predicting ductile fracture as opposed to either 1) brittle fracture; or, 2) elastoplastic fracture in the transition between brittle and ductile fracture behavior [1.16]. Ductile fracture is emphasized because it is the expected failure mode for relatively thin sections (less than 26 mm thick) of modern ship steels and weld metals at service temperatures. Brittle or elastoplastic fracture may be more of a possibility for marine structures which were fabricated from thick plates or from steel or weld metal without adequate toughness.

There are many aspects of brittle and elastoplastic fracture which are not discussed in this report.. For example, brittle fracture and elastoplastic fracture are very sensitive to the effects of constraint, residual stress, and variations in weld metal strength; whereas these effects are not that significant for ductile fracture [1.20,1.21]. Taking these effects into account can make analysis of brittle and elastoplastic fracture very complex. There are other sources of information on these complex analyses [1.22-1.25]. Fortunately, brittle materials are rarely used today in marine structures. Therefore there is little need for non-experts to become familiar with these complex analyses.

The objectives of this research were to:

1. summarize the current knowledge regarding ductile fracture models applicable to modern ship structures,
2. evaluate the limitations of ductile fracture models with respect to use for typical cracked ship structural details;
3. make recommendations to facilitate the application of such models in the routine evaluation of fatigue cracks in ship structures.

The research is expected to be applicable to commercial and naval ship structural members which are fabricated from plates with sufficient toughness, i.e. relatively thin plates (less than 26 mm thick) of most types of ship steel (e.g. all ASTM A131 grades with the possible exception of grades A, B, AH32, and AH36). Even the grades of steel which are supplied to a less restrictive Charpy requirement, e.g. Grade A, will often have much more than the minimum required toughness due to the generally improved "clean steel" technology and lower carbon contents that have been generally adopted in the steel industry today. Since cracks typically propagate out of the weld and into the base metal, the analyses typically did not specifically account for the weld properties. There may be problems where cracks propagate strictly in the weld or HAZ that may require more complicated analysis procedures. However, provided weld procedures are followed, weld metals will typically have much higher toughness than the base plate and will typically be overmatched in strength, therefore it is usually conservative to treat the welds as if they are homogeneous base metal. Local brittle zone (LBZ) in the HAZ may trigger "pop-in" brittle fractures [1.27-1.30]. However; the alignment of the HAZ is typically such that these cracks propagate into the base metal and therefore the LBZ are not significant in overall ductile fracture behavior.

The approach to this research is described below:

1. A summary of the current state of knowledge was developed by extensive literature review, conference attendance, and personal communication with other researchers. This information is discussed in Chapters 2, 4, and 5.
2. Welded joints that are susceptible to fatigue cracking were identified and classified as discussed in Chapter 2.
3. Small-scale material property tests and large-scale experiments on members with typical ship structural details were conducted to determine the accuracy of these models. Chapter 3 contains the specimen description, procedures, and results of these tests.
4. The experiments were analyzed (pre-test and post-test) with a variety of ductile-fracture models. Peak load was predicted using British Standards Institute document PD 6493 [1.26]. Crack extension as a function of increasing displacement was predicted using: 1) a constant crack-opening angle; and, 2) a J-R curve analysis (using finite-element analysis as well as a variety of estimation schemes to calculate the J integral. The load-displacement curve was computed using either a simple limit-load analysis or a finite-element analysis. Chapter 4 explains the fracture prediction methods and the results of the analyses.
5. The findings from the testing and analysis are synthesized and developed into guidelines for the application of ductile fracture models to ship structural details in Chapter 5. Specification of steel and filler metals using Charpy impact-toughness requirements, a review of linear elastic fracture mechanics analysis, fracture mechanics test methods, and plastic limit-load calculations are then presented.

1.1 References

- 1.1 ASCE-WRC (1971), Plastic Design in Steel, A Guide and Commentary, Second Edition, Joint Committee of the Welding Research Council and the American Society of Civil Engineers, ASCE, New York, 1971
- 1.2 Mansour, A.E., and Thayamballi, A., Ultimate Strength of a Ship's Hull Girder in Plastic and Buckling Modes, Report SSC-299, Ship Structure Committee, Washington, D.C., 1980.
- 1.3 Das, P.K., and Garside, J.F., Structural Redundancy for Continuous and Discrete Systems, Report SSC-354, Ship Structure Committee, Washington, D.C., 1992
- 1.3 Hughes, O.F., Ship Structural Design, John Wiley and Sons, New York, 1983
- 1.4 Hughes, O., Nikolaidis, E., Ayub, B., White, G., and Hess, P., Uncertainty in Strength Models for Marine Structures, Ship Structure Committee, Washington, D.C., 1994.
- 1.5 API RP2A-LRFD, Recommended Practice for Planning, Designing, and Constructing Fixed Offshore Platforms - Load-Resistance Factor Design, American Petroleum Institute, Washington, D.C., 1993.
- 1.6 Jennings, E., Grubbs, K, Zanis, C., and Raymond, L., Inelastic Deformation of Plate Panels, Report SSC-364, Ship Structure Committee, Washington, D.C., 1991.
- 1.7 Ghose, D.J., Nappi, N.S., and Wiernicki, C.J., Residual Strength of Damaged Marine Structures, Report SSC-381, Ship Structure Committee, Washington, D.C., September, 1994.
- 1.8 Bea, R.G., and Hutchison, S.C., Maintenance of Marine Structures; A State of the Art Summary, Report SSC-372, Ship Structure Committee, Washington, D.C., 1993.
- 1.9 Wells, A.A, "Application of Fracture Mechanics at and Beyond General Yielding," *British Welding Journal*, Vol. 10, 1963, pp. 563-570.
- 1.10 Denys, R. M., "Toughness Requirements for Pipeline Integrity", Proceedings of the 14th International Conference on Offshore Mechanics and Arctic Engineering Conference (OMAE), 18-22 June 1995, Copenhagen Denmark, Salama et al, eds., ASME, Vol. III, Materials Engineering, pp 93--100, 1995.

- 1.11 Irving, Bob "Way Back When", *Welding Journal*, pg 22, Sept. 1994.
- 1.12 Irwin, G.R., and Kies, J.A., "Critical Energy Rate Analysis of Fracture Strength", *Welding Journal*, Research Supplement, April 1954.
- 1.13 Liu, D., and Thayamballi, A., "Local Cracking in Ships- Causes, Consequences, and Control", Proceedings: Workshop and Symposium on the Prevention of Fracture in Ship Structure, March 30-31, 1995, Washington, D.C., Marine Board, Committee on Marine Structures, National Research Council, 1996.
- 1.14 Pense, A.W., "Evaluation of Fracture Criteria for Ship Steels and Weldments", Report SSC-307, Ship Structure Committee, Washington, D.C., 1981.
- 1.15 Green, P.S., Sooi, T.K., Ricles, J.M, Sause, R., and Kelly, T., "Inelastic behavior of structural members fabricated from high-performance steel", Structural Stability Research Council Annual Meeting, Bethlehem, PA, June 1994.
- 1.16 Reemsnyder, H. S., "Fatigue and Fracture of Ship Structures", Proceedings: Workshop and Symposium on the Prevention of Fracture in Ship Structure, March 30-31, 1995, Washington, D.C., Marine Board, Committee on Marine Structures, National Research Council, 1996.
- 1.17 Dexter, R.J., Norris, E.B., Schick, W.R., and Watson, P.D., Performance of Underwater Welds, Report SSC-335, Ship Structure Committee, Washington, D.C., 1990.
- 1.18 Dexter, R.J., "Fracture Toughness of Underwater Wet Welds," Fatigue and Fracture Testing of Weldments, ASTM STP 1058, H.I. McHenry, and J.M. Potter, Eds., American Society for Testing and Materials, Philadelphia, Vol. 1058, pp. 256-271, 1990.
- 1.19 Rolfe, S.T., Hays, K.T., and Henn, A.E., "Fracture Mechanics Methodology for Fracture Control in VLCC's", Ship Structures Symposium '93, November 16-17, 1993, Arlington VA, available from SNAME, Jersey City, NJ, 1993.
- 1.20 R.J. Dexter and T.J. Griesbach, "The Causes of Geometry Effects in Ductile Tearing", Fracture Mechanics Verification by Large-Scale Testing, Proceedings of the IAEA/CSNI Specialists Meeting, Oak Ridge Tennessee, 26-29 October, 1992, pp. v.5.1-v.5.38, 1992.

- 1.21 Formby, C.L., and Griffiths, J.R., "The Role of Residual Stresses in the Fracture of Steel," Proceedings of the International Conference "Residual Stresses in Welded Construction and Their Effects," 15-17 November 1977, London, The Welding Institute, Abington Hall, Abington, Cambridge, CB1 6AL, UK, pp. 359, 1977.
- 1.22 Anderson, T.L., Elastic-plastic fracture mechanics - marine structural applications, SSC-345-Part 2, Ship Structure Committee, Washington D.C., 1991.
- 1.23 Dodds, R.H. Jr., Anderson, T.L., and Kirk, M.T., "A Framework to Correlate a/W Ratio Effects on Elastic-Plastic Fracture Toughness (J_{Ic})," International Journal of Fracture, Vol. 48, pp. 1-22, 1991.
- 1.24 Wallin, K., "Statistical Aspects of Constraint with Emphasis to Testing and Analysis of Laboratory Specimens in the Transition Region," Presented at ASTM Symposium on Constraint Effects in Fracture, Indianapolis, May 8-9, 1991.
- 1.25 Kirk, M., and Bakker, A., eds. Constraint Effects in Fracture Theory and Applications: 2nd Volume, ASTM STP 1244, 1995.
- 1.26 BSI, Guidance on the Methods for Assessing the Acceptability of Flaws in Fusion Welded Structures, PD 6493: 1991, Published by the British Standards Institution (BSI), 1991.
- 1.27 Denys R, McHenry H I: 'Local Brittle Zones in Steel Weldments: An Assessment of Test Methods', Proc. of 7th Int. Conference on Offshore Mechanics and Arctic Engineering, Vol.III, ASME, 1988, pp.379-386.
- 1.28 Kocak M, Terlinde G, Schwalbe K-H, Gnirss G: 'Fracture Toughness Testing of Heat Affected Zones of Weldments and the Significance of Pop-ins', EGF Publication 2, Mechanical Engineering Publications, London, pp.77-95, 1987.
- 1.29 Dawes M G: 'Quantifying Pop-in Severity in Fracture Toughness Testing', Fatigue and Fracture of Engineering Materials and Structures, Vol. 14, pp.1007-1014, 1991.
- 1.30 Sumpter J D G: 'Pop-in and Crack Arrest in an HY80 Weld', Fatigue and Fracture of Engineering Materials and Structures, Vol.14, 1991, pp.565-578.

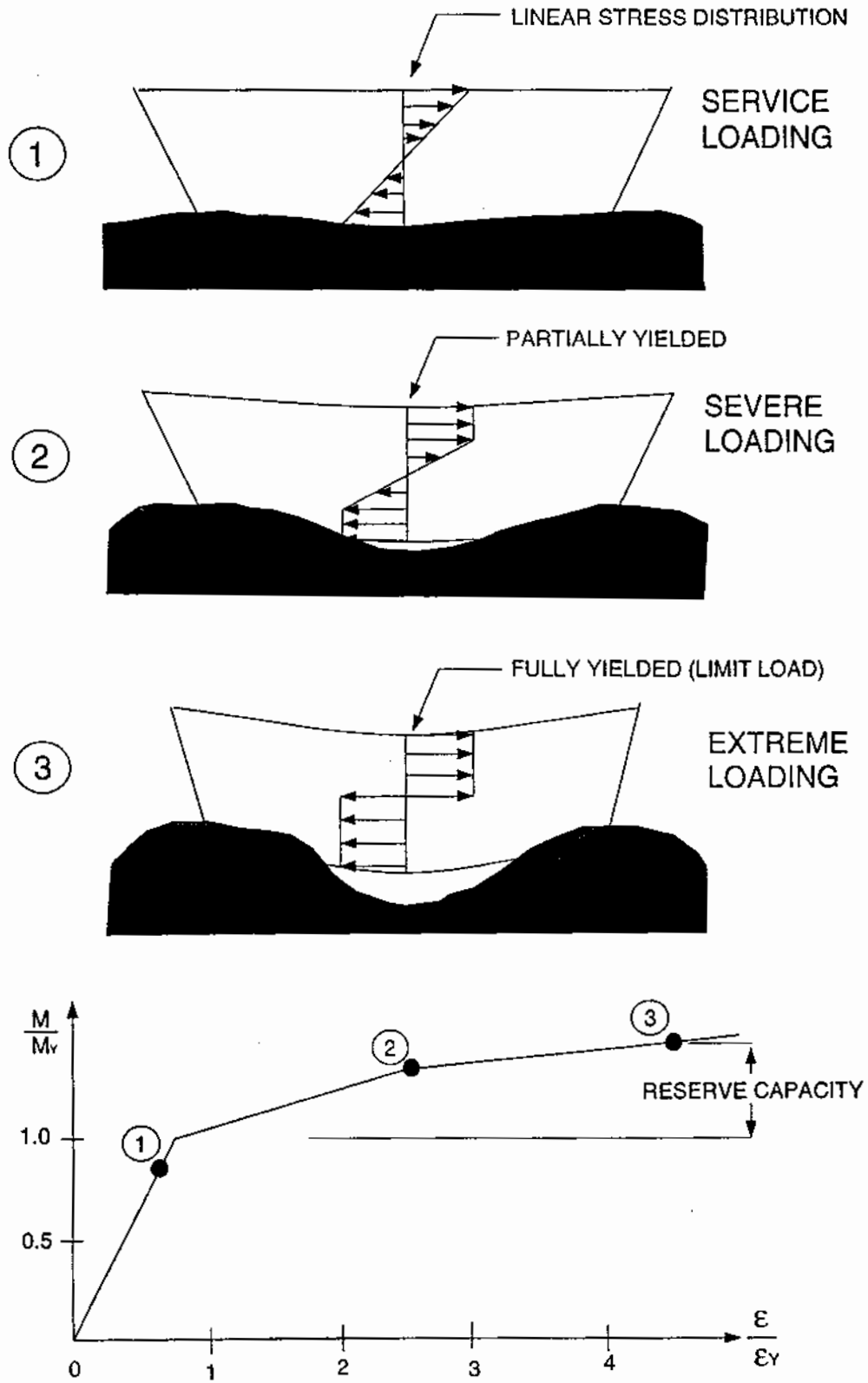


Figure 1.1 Schematic of the development of hull-girder reserve capacity

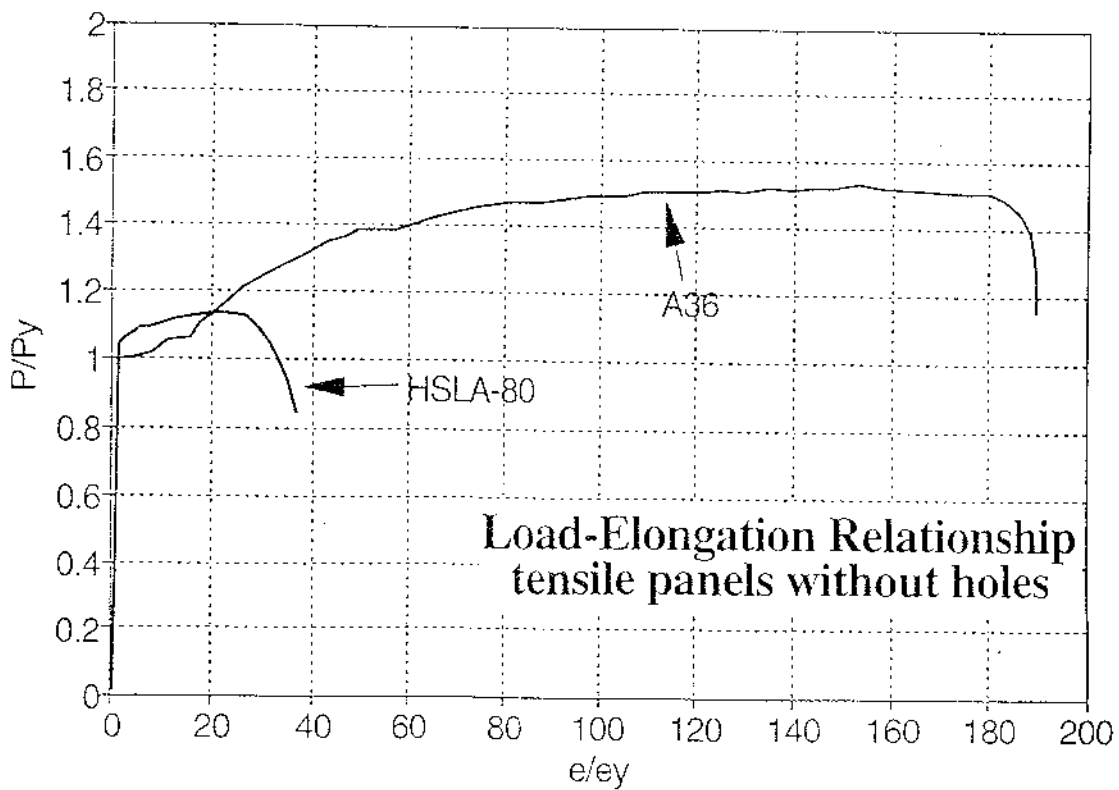
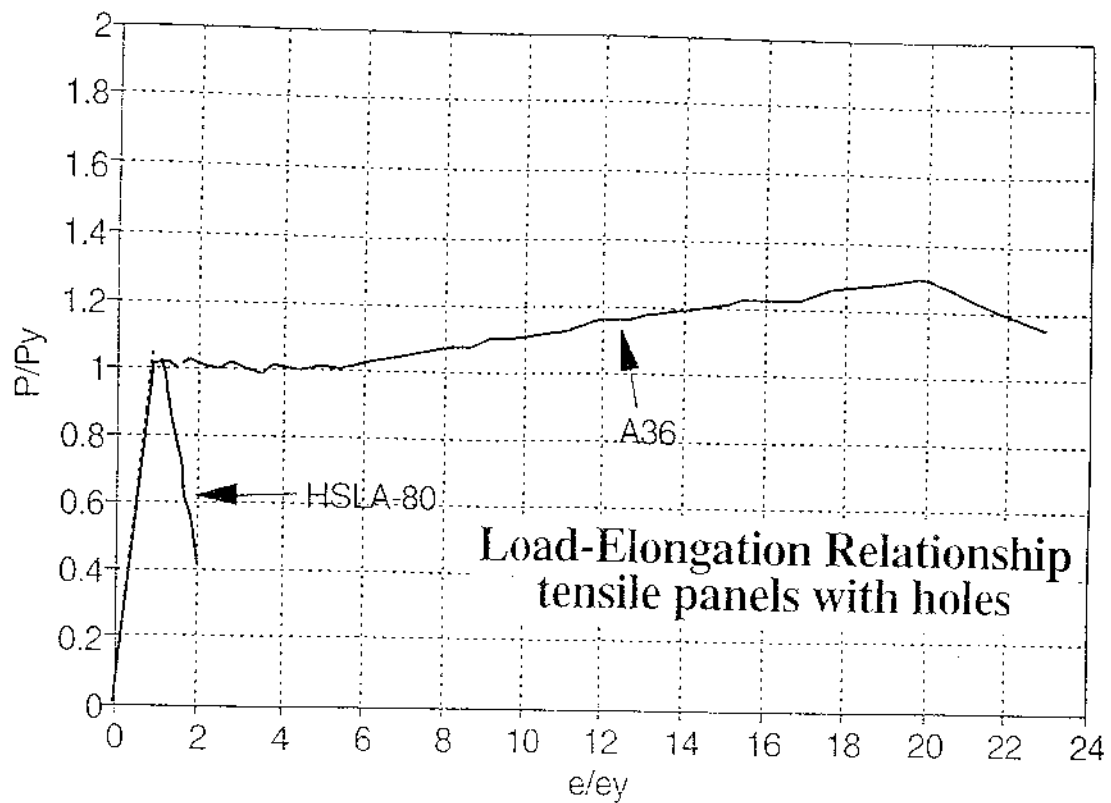


Figure 1.2 Normalized load-displacement curve for tensile test with and without a hole as a stress concentration showing the effect of yield-to-tensile (Y/T) ratio on ductility

2.0 BACKGROUND

In the introduction it was established that for an assessment of the plastic load capacity and ductility of a welded steel ship or other type of marine structure, it is prudent to consider the possibility of fatigue cracks. Fatigue cracks will affect the plastic behavior and could even lead to brittle fracture below the limit load. This Chapter provides a brief summary of the essential background on critical details and fracture analysis that is the basis of the discussion in the remaining Chapters. A few of the more common examples of fatigue-sensitive details in ships are identified and classified in the following section. Various types of fracture behavior ranging from brittle cleavage fracture to fully-plastic ductile fracture are then discussed.

There are many other areas of fracture mechanics that are not discussed, in order to provide a thorough discussion of the ductile fracture problem in a limited number of pages. There are several good books which can be referred to for further information on fracture mechanics from various perspectives [2.1-2.5].

2.1 Identification of critical fatigue-sensitive details

For a ship, all of the members and connections in the hull, the bottom, and the upper deck are critical from a standpoint of structural integrity. Particularly important are areas around the corners of the hull girder, i.e. turn of the bilge and the sheer strake. Longitudinal bulkheads may also be critical for primary strength. Intermediate decks and transverse bulkheads are less sensitive to fracture, since their primary structural role is to transfer shear.

These members and connections are especially critical and of interest in this research if they are prone to fatigue cracking. Surveys of service repair and inspection of ships have indicated an average of 86 cracked structural details per ship [2.6-2.9]. This cracking is usually caused by service fatigue loads [2.10, 2.11]. Because of more stringent detailing practice and design criteria, the Navy does not in general have the significant problem with fatigue that is apparent in many commercial ships [2.12]. However, a recent survey of damage in British Navy combatants found an average of 4.6 fatigue cracks reported per year in destroyers that were 7 years old on average, and 7.6 cracks per year in frigates that were 15 years old on average [2.13]. In general, fatigue cracks are only a serviceability problem, e.g. repair costs and damage from leaking [2.6, 2.13-2.15]. In rare cases, however, the result can be rapid fracture leading to major damage or catastrophic failure [2.9, 2.13, 2.16-2.18].

High-strength steel structures are more likely to have fatigue cracks. The fatigue strength of welded details is essentially independent of the type and strength of the steel [2.4, 2.19-2.23]. If the maximum allowable stress is increased and scantlings decreased to take advantage of the high-strength steel, the fatigue stress ranges increase in magnitude. If the same low-fatigue-strength details are used, they are more likely to exhibit cracking in high-strength steel structures. In commercial tankers and bulk carriers fabricated from high-strength steel, this increase in fatigue cracking has become a serious problem [2.9, 2.18].

Welded details are typically grouped into categories of details with similar fatigue strength. The low-fatigue-strength categories are the details which are most likely to be cracked in service and are

therefore the most likely to require fracture evaluation. The fatigue design provisions in the American Welding Society (AWS) Structural Welding Code D1.1 [2.24] are used to design welded plate and tubular structures. The AWS fatigue design provisions for tubular joints are essentially the same as the fatigue design provisions of the API RP-2A for offshore structures [2.25]. The AWS provisions are applicable to design and service evaluation of ships and other marine structures. The AWS provisions for structures comprised of welded plates and shapes are essentially the same as the AASHTO bridge specifications [2.26] and the AISC specifications for steel buildings [2.27]. Eurocode 3 [2.28] and the British Standard 7608 [2.29] use similar provisions but have different names for S-N curves. For example, the BS Category D S-N curve is essentially the same as the AWS Category C S-N curve. ABS guidelines [2.30], the U.K. Health and Safety Executive [2.31], and other groups in the marine industry use S-N curves from the British Standard 7608.

The S-N curves corresponding to the categories used in the AWS, AISC, and AASHTO codes are shown in Figure 2.1. These categories range from A to E' in order of decreasing fatigue strength. Most common ship details can be idealized as analogous to one of the drawings of details that are given in the codes. The Eurocode 3 and the British Standard 7608 have more detailed illustrations for their categorization than does the AWS, AISC, or AASHTO specifications. A book by Maddox [2.23] discusses categorization of many details in accordance with BS 7608.

The following presents a brief overview of categorization according to the AWS, AISC, and AASHTO codes. Details in categories A, B, and B' do not need to be discussed because they never govern the fatigue life of ships. There are always more severe details. Category C includes transverse stiffeners and full-penetration groove welds (butt joints). However, because there are numerous E and E' and even worse details in ship structure, butt welds between plates (without any other stress concentration) are rarely fatigue cracked and are therefore not deemed to be critical.

Continuous welds are not fatigue critical, however the terminations of these welds are often critical. The termination of longitudinal fillet welds are Category E details. The fillet-weld terminations at the edges of members which are lapped are Category E' or worse.

There have been many fatigue-cracking problems in structures at miscellaneous and seemingly unimportant attachments to the structure for such things as racks and hand rails. Attachments are a "hard spot" on the strength member which create a stress concentration at the weld. Most attachments normal to flanges or plates are at best Category E details. The Category E', slightly worse than Category E, applies if the attachment plates or the flanges exceed 25 mm in thickness. This thickness effect is partly due to the relative size of the welds and the residual stress field.

There are several references which discuss fatigue-susceptible details in tankers. For example, the Tanker Structure Cooperative Forum has published several books which show pictorials of the types of cracks which commonly occur in tankers and suggested repairs [2.34-2.36]. Many groups have modelled fatigue-sensitive ship details using the finite-element method to determine hot-spot stress ranges [2.37, 2.38].

The intersection of longitudinal and transverse members is always a fatigue sensitive location. High stresses can be induced by incompatibility of curvature in the two directions. An example of

such a fatigue-prone intersection is the connection of the longitudinal stiffeners with transverse web frames or bulkheads in tankers and many other types of commercial ships. Figure 2.2 shows cracks which occur around the cutout in the transverse member. These cracks are due to the distortion of the cutout and typically do not continue to grow after reaching 100 mm or so in length. The cracks "arrest" because the distortion-induced stress which drives the crack is diminished as the crack allows the distortion to occur more freely. For this reason, and because the transverse members are primarily carrying shear as opposed to tension, these cracks are not likely to lead to catastrophic failure of the ship, and are therefore not critical.

The distortion-induced cracks in these connections can be reduced by changes in the design of the cutout, adding a lug to stiffen the cutout, or adding a stiffener to the transverse member landing on the longitudinal. Figure 2.3 shows a connection with a stiffener. Although the stiffened connection is less likely to crack for a given loading, if cracking does occur it is likely to grow across the flange of the longitudinal and down the web toward the sideshell as shown in Figure 2.3. If this crack reaches the sideshell it may result in a significant leak or other problems. Therefore this type of crack is critical. Most of the experiments (described in Chapter 3) were designed to simulate this type of crack in a longitudinal at an attachment.

Brackets at the intersections of large girders are also a common location of fatigue cracks. Figure 2.4 shows different types of brackets. The two drawings at the bottom of the figure illustrate the two types of cracks which can occur in any type of bracket. Depending on the relative magnitude of the tensile stress range in each member, the bracket may crack or the longitudinal may crack. The crack in the longitudinal is more critical, for reasons explained above. This crack in the longitudinal is similar to the crack in Figure 2.2, and is also similar to the experimental specimens.

Hatch openings, such as shown in Figure 2.5, are frequently cracked in bulk carriers [2.39]. These cracks are very critical, since they are at the narrowest section of the deck.

Cracks often occur at the ratholes or weld-access holes in the longitudinals in way of the erection butt welds, as shown in Figure 2.6 [2.40]. This was the type of cracking discussed by Rolfe et al [2.41] for TAPS trade tankers. Because the shell is cracking, these are obviously critical cracks. However, as discussed by Rolfe et al, if the stiffener remains intact and can bridge over the crack, it can reduce the driving force significantly and the structure can tolerate a crack more than 400 mm long. Some of the experiments described in Chapter 3 were therefore designed to simulate this type of crack bridged by a stiffener.

2.2 Types of fracture behavior

Consider a notched or cracked test specimen made of ordinary ship steel, or a welded structural steel specimen with the notch located in the weld. When a notched specimen is fractured from axial tension or tension due to bending, the resultant load, deformation, and energy absorbed should undergo a transition from brittle behavior to ductile behavior as the temperature increases. For example, a plot of CVN energy vs. temperature for a Grade 50 structural steel (A588) is shown in Figure 2.7. The transition with increasing temperature from the lower shelf to the upper shelf is a result of changes in the underlying microstructural fracture mode.

There are really at least three distinct types of fracture with distinctly different behavior.

- 1) Brittle fracture is associated with cleavage on a microstructural scale and occurs at the lower end of the temperature ranges, although the brittle behavior can persist up to room temperature for low-toughness materials. This part of the temperature range is called the lower shelf because the minimum toughness is fairly constant up to the transition temperature. Brittle fracture is sometimes called elastic fracture because the plasticity that occurs is negligible.
- 2) Transition-range fracture occurs at temperatures between the lower shelf and the upper shelf and is associated with a mixture of cleavage and fibrous fracture on a microstructural scale. Because of the mixture of micromechanisms, transition-range fracture is characterized by extremely large variability. Fracture in the transition region is sometimes referred to as elastic-plastic fracture because the plasticity is limited in extent but has a significant impact on the toughness.
- 3) Ductile fracture is associated with a process of void initiation, growth, and coalescence on a microstructural scale and occurs at the higher end of the temperature range. This part of the temperature range is referred to as the upper shelf because the toughness levels off and is essentially constant for higher temperatures. Ductile fracture is sometimes called fully-plastic fracture because there is substantial plasticity across most of the remaining cross section ahead of a crack. Ductile fracture is also called fibrous fracture due to the fibrous appearance of the fracture surface, or shear fracture due to the usually slanted shear lips on the fracture surface.

Unfortunately, these terms are often used ambiguously. For example, fracture in the transition region is often called brittle or ductile, depending on the relative toughness. In this study, the testing was performed at room temperature which was in the upper end of the transition region or on the upper shelf region.

2.3 Fracture mechanics analysis

2.3.1 Linear elastic fracture mechanics analysis

Fracture mechanics is based on the mathematical analysis of solids with notches or cracks. Relationships between the material toughness, the crack size, and the stress or displacement are provided by fracture mechanics. Brittle fracture occurs with nominal net-section stresses below or just slightly above the yield point. Therefore, the relatively simple principles of linear-elastic fracture mechanics (LEFM) can be used to conservatively assess whether a welded joint is likely to fail by brittle fracture rather than fail in a ductile manner. The analogous principles of elastic-plastic fracture mechanics (EPFM) were developed to allow for limited plasticity, as discussed in Section 2.3.2. These topics are covered in detail in books on fracture mechanics [2.1-2.5]. Therefore, only the essential principles will be reviewed here.

LEFM gives a relatively straightforward method for predicting fracture, based on a parameter called the stress-intensity factor (K) which characterizes the stresses at notches or cracks [2.42]. The

applied K is determined by the size of the crack (or crack-like notch) and the nominal gross-section stress remote from the crack. Crack-like notches and weld defects are idealized as cracks. In the case of linear elasticity, the stress-intensity factor can be considered as a measure of the magnitude of the crack tip stress and strain fields. Solutions for the applied stress-intensity factor, K , for a variety of geometries can be found in handbooks [2.43-2.47]. Most of the solutions are variations on standard test specimens which have been studied extensively. A few useful solutions and examples of their application to welded joints may be found in Chapter 5.

In general, the applied stress-intensity factor is given as:

$$K = F_c * F_s * F_w * F_g * \sigma \sqrt{\pi a} \quad (2-1)$$

where the F terms are modifiers on the order of 1.0, specifically:

F_c is the factor for the effect of crack shape,

F_s is the factor, equal to 1.12, that is used if a crack originates at a free surface,

F_w is a correction for finite-width which is necessary because the basic solutions were generally derived for infinite or semi-infinite bodies, and

F_g is a factor for the effect of non-uniform stresses, such as bending stress gradient.

The stress, σ , includes residual stress as well as applied stress. Typically, worst-case assumptions are made regarding the residual stress in brittle fracture evaluations [2.47-2.51]. In fact, this simplifies the evaluations significantly because the peak stresses (applied plus residual) are taken as equal to the actual yield strength. This assumption is also made if plastic limit-state design is used. Assuming the stress is at yield strength eliminates the need for detailed analysis to determine the applied stresses.

The stress intensity factor has the unusual units of $\text{MPa}\cdot\text{m}^{1/2}$ or $\text{ksi}\cdot\text{in}^{1/2}$. The material fracture toughness is characterized in terms of the applied K at the onset of fracture in simplified small test specimens, called K "critical" or K_c . The fracture toughness (K_c) is considered a transferable material property, i.e. fracture of structural details is predicted if the value of the applied K in the detail exceeds K_c . Equation 2-1 relates the important factors that influence fracture: " K_c " represents the material, " σ " represents the design, and " a " represents the fabrication and inspection.

In this report, K_c is used as any type of critical K associated with a quasi-static strain rate, derived from any one of a variety of test methods. One measure of K_c is the plane-strain fracture toughness which is given the special subscript "I" for plane-strain mode I, K_{Ic} . K_{Ic} must be measured in specimens which are very thick and approximate plane strain. If the fracture toughness is measured in an impact test, the special designation K_d is used where the subscript "d" is for dynamic. In practice, K_c is often estimated from correlations with the result from a CVN test, because the CVN is much cheaper to perform and requires less material than a fracture-mechanics test, and all test laboratories are equipped for the CVN test. A widely-accepted correlation for the lower shelf and lower transition region between K_d and CVN was proposed by Rolfe and Barsom [2.1]:

$$K_d = 11.5 * \sqrt{\text{CVN}} \quad (2-2)$$

where CVN is given in J and K_d is given in $\text{MPa}\cdot\text{m}^{1/2}$. A different constant is used for English units [2.1]. This correlation is used to construct the lower part of the curve for dynamic fracture toughness

(K_d) as a function of temperature directly from the curve of CVN vs. temperature. There is a temperature shift between the curve for slow and intermediate load rate values of K_c and the impact load rate values of K_d . Ship loading rates are considered intermediate, and intermediate load rate values of K_c for structural steel are conservatively obtained by shifting the K_d curve to a temperature which is about 38 degrees C lower (for ordinary structural steel with yield strength about 350 MPa).

There are size and constraint effects and other complications which make the LEFM fracture toughness K_c less than perfect as a material property. This is especially true when K_c is only estimated based on a correlation to CVN.

2.3.2 Elastic-plastic fracture parameters

Elastic-plastic fracture mechanics (EPFM) is a nonlinear extension of the fracture mechanics concepts discussed above. Theoretically, EPFM is only valid for limited amounts of plasticity, and therefore is intended for the lower transition region where the fracture is not entirely ductile. For lack of an alternative, EPFM is also used for fully-plastic or ductile fracture. The following section provides a brief overview of some background on EPFM models. Additional detail on EPFM can be found in references [2.1, 2.2, 2.5,2.47].

The J-integral is a parameter for EPFM much like K is a parameter for LEFM. The J is often converted to an "equivalent" K by the following relation (for plane stress):

$$K = \sqrt{J * E} \quad (2-3)$$

where E is the modulus of elasticity. K_c values may be obtained using Equation (2-3) where J is obtained from a test such as ASTM E813, "Standard Test Method for J_{Ic} , A Measure of Fracture Toughness". In this case, K is typically given the subscript "J", i.e. K_{Jc} . Test methods are discussed later in Section 5.2.

The crack-tip opening displacement (CTOD) is an alternative EPFM parameter. The CTOD concept and test method were developed at the Welding Institute (TWI) in the United Kingdom. A empirically-based conservative fracture assessment procedure called the "CTOD design curve" was developed around the CTOD test results and was verified through extensive wide-plate tension tests of weldments. This procedure has been extensively used in a wide range of industries, including the pipeline and offshore structures industry. In 1980, the British Standards Institute published a document called PD6493, "Guidance on Some Methods for the Derivation of Acceptance Levels for Defects in Fusion Welded Joints". This document is based on fracture-mechanics fitness-for-purpose concepts, and can be used to assess minor fabrication defects. Originally, the PD6493 procedure was based on fracture toughness measured using the CTOD test and the empirical CTOD design curve. While this approach is still embodied in PD6493, the procedure was generalized in a new version in 1991 to permit any measure of toughness and analysis method [2.47]. The PD6493 document has an easy to follow codified procedure. Further full-scale wide-plate testing and now more than 15 years of experience with this document establishes the reliability of this approach.

The J integral is directly proportional to the CTOD [2.52-2.57]. It can similarly be shown that the rate of increase of J with respect to crack extension (tearing modulus) is proportional to the rate of increase of the CTOD with respect to crack extension or the crack-tip-opening angle (CTOA) [2.53]. The CTOD can be related to J and also to K, and therefore CTOD fracture toughness values are often converted to equivalent K values using:

$$J = 1.6 * \sigma_y * CTOD \quad (2-4)$$

substituting Equation (2-4) into Equation (2-3) gives:

$$K = \sqrt{1.6 * \sigma_y * E * CTOD} \quad (2-5)$$

It should be noted that the CTOD can be theoretically related to K only for linear elastic conditions (brittle materials). Therefore, in the case of brittle materials, it is valid to convert CTOD test results to equivalent K_c values. However, it has also become common to convert CTOD test results to equivalent K_c values even for materials in the transition range or upper shelf. It is also common for the fracture assessment to be carried out in terms of the applied K using LEFM. While the LEFM assessment is valid for brittle materials, it should be noted that this procedure may not be conservative for elastic-plastic fracture. For elastic-plastic fracture, the fracture toughness is derived from small-scale test with net section yielding which can enhance the apparent toughness. It is possible that due to lower net-section stresses and/or greater constraint in the structure, the fracture toughness is not enhanced significantly by yielding and could be brittle. Thus the small-specimen value of the toughness may not always be conservative.

2.3.3 Local approach to ductile fracture

On a local level, the process of ductile fracture, void growth and coalescence, is known to be governed by a critical strain criterion [2.58-2.62]. A critical strain could be used in simplified fracture models. Many investigators have noted approximate relations between the fracture strain (derived from the reduction in area of tensile tests) and fracture criteria such as J and CTOD. For example, Miyata et al [2.62] showed that J_c ought to be a linear function of the fracture strain times the yield stress.

Green and Knott [2.63] expressed the CTOD as the product of the fracture strain, ϵ_f , times a microstructural gage length, l , equal to the participating inclusion spacing (the critical distance for ductile fracture).

$$\mathbf{CTOD} = \epsilon_f * l \quad (2-6)$$

This simple relation is based on the notion that the process zone is approximately triangular with a base equal to the CTOD and a height equal to the critical distance. Ritchie and Thompson [2.64] pointed out that if this relation is multiplied by the flow stress σ_f it expresses a link between the plastic work density in the fracture process zone (which relates these quantities to Sih's strain-energy density (SED) [2.65]) and J_c :

$$\mathbf{J_c} = \sigma_f * \mathbf{CTOD} = \sigma_f * \epsilon_f * l = \mathbf{SED} * l \quad (2-7)$$

Equation (2-7) rationalizes the empirical correlation between J_c and the product of the flow stress and the fracture strain (i.e. an approximation of the strain energy density or the plastic work density).

There are alternative methods of predicting fracture which can be generally referred to as the local approach to fracture [2.65-2.71]. In the local approach, the composite weldment is modelled (usually with finite elements) and toughness criteria are based only on the deformation very local to the crack tip. Notwithstanding the complexity of such an analysis, the local approach has the advantage of not being influenced by the relative strength of the base metal and weld metal and the geometry of the test specimen and structure, as J and CTOD are influenced [2.66-2.69].

One example of a simple local approach is the work of Matic and Jolles [2.67, 2.68, 2.72-2.74] of NRL. The failure criterion used was the attainment of a critical strain-energy density for fracture [2.75-2.76]. For materials with a relatively constant flow stress, the use of strain energy density is approximately equivalent to the use of a critical effective strain [2.58].

The local approach has been applied to crack propagation with limited success. Applications have required extensive computational resources and to date, no one has succeeded in propagating a crack more than about 12 mm using this approach [2.69]. While the local approach is certainly interesting basic research, it is not suitable for predicting the extensive ductile tearing expected in ship structures.

2.4 References

- 2.1. Barsom, J.M., and Rolfe, S.T., Fracture and Fatigue Control in Structures, Second Edition, Prentice-Hall, Englewood Cliffs, New Jersey, 1987.
- 2.2. Anderson, T.L., Fracture Mechanics - Fundamentals and Applications, Second Edition, CRC Press, Boca Raton FL, 1995.
- 2.3 Broek, D. Elementary Fracture Mechanics, Fourth Edition, Martinis Nijhoff Publishers, Dordrecht, Netherlands, 1987.
- 2.4 Fisher, J.W., Fatigue and Fracture in Steel Bridges, John Wiley and Sons, ISBN0-471-80469-X, New York, 1984.
- 2.5 Kanninen, M.F., and Popelar, C.H., Advanced Fracture Mechanics, Oxford University Press, New York, 1985.
- 2.6 Antoniou, A.C., A survey of cracks in tankers under repair, PRADS-International Symposium on Practical Design in Shipbuilding, Tokyo, October 1977.
- 2.7 Jordan, C.R. and Cochran, C.S., In-service performance of structural details, SSC-272, Ship Structure Committee, Washington D.C., 1978.
- 2.8 Jordan, C.R. and Krumpfen, R.P., Jr., Design guide for ship structural details, SSC-331, Ship Structure Committee, Washington D.C., 1985.
- 2.9 Liu, D., and Thayamballi, A., "Local Cracking in Ships- Causes, Consequences, and Control", Proceedings: Workshop and Symposium on the Prevention of Fracture in Ship Structure, March 30-31, 1995, Washington, D.C., Marine Board, Committee on Marine Structures, National Research Council, 1996.
- 2.10 Petershagen, H., Fatigue problems in ship structures, Advances in Marine Structures, Elsevier Applied Science, London, pp. 281-304, 1986.
- 2.11 Vedeler, G., To what extent do brittle fracture and fatigue interest shipbuilders today?, Det Norske Veritas Publication No. 32, 1962.
- 2.12 Malakhoff, A., Packard, W.T., Engle, A.H., and Sielski, R.A., Towards rational surface ship structural design criteria, Advances in Marine Structures - 2, C.S. Smith and R.S. Dow, (eds), Elsevier Applied Science, London, pp. 495-528, 1991.

- 2.13 Clarke, J.D., Fatigue crack initiation and propagation in warship hulls, Advances in Marine Structures - 2, C.S. Smith and R.S. Dow, (eds), Elsevier Applied Science, London, pp. 42- 60, 1991.
- 2.14 Jordan, C.R. and Krumpfen, R.P. Jr., Performance of ship structural details, Welding Journal, pp. 18-28, January, 1984.
- 2.15 Ayyub, B.M., White, G.J., and Purcell, E.S., Estimation of structural service life of ships, Naval Engineers Journal, pp. 156-166, May, 1989.
- 2.16 Lessons from 'Kurdistan', The Motor Ship, January 1982.
- 2.17 Yamamoto, Y., Fukusawa, T., Arai, T., Iida, M., Murakami, T., and Ando, T., Analysis of structural damages of the fore body of a container ship due to slamming, Journal of the Society of Naval Architects of Japan, Vol. 155, 1984.
- 2.18 Alman, P., Cleary, Jr. W.A., Dyer, M.G., and Paulling, J.R., The International Load-Line Convention: Crossroads to the Future, Marine Technology, Vol. 29, No. 4, Oct. 1992, pp. 233-249.
- 2.19 Hollister, S.C., Garcia, J., and Cuykendall, T.R., Fatigue tests of ship welds, SSC-7, Ship Structure Committee, Washington D.C., 1946.
- 2.20 Hollister, S.C., Garcia, J., and Cuykendall, T.R., Final report on fatigue tests of ship welds, SSC-14, Ship Structure Committee, Washington D.C., 1948.
- 2.21 Fisher, J.W., Frank, K.H., Hirt, M.A., and McNamee, B.M., Effect of weldments on the fatigue strength of steel beams, National Cooperative Highway Research Program (NCHRP) Report 102, Highway Research Board, Washington, D.C., 1970.
- 2.22 Fisher, J.W., Albrecht, P.A., Yen, B.T., Klingerman, D.J., and McNamee, B.M., Fatigue strength of steel beams with welded stiffeners and attachments, National Cooperative Highway Research Program (NCHRP) Report 147, Transportation Research Board, Washington, D.C., 1974.
- 2.23 Maddox, S.J., Fatigue Strength of Welded Structures, 2nd Edition, Abington Publishing, Cambridge, UK, 1991.
- 2.24 ANSI/AWS D1.1, "Structural Welding Code - Steel", American Welding Society, Miami, 1992.

- 2.25 RP2A-WSD, Recommended Practice for Planning, Designing, and Constructing Fixed Offshore Platforms - Working Stress Design, 20th Edition, American Petroleum Institute, Washington, D.C., 1993.
- 2.26 "AASHTO LRFD Bridge Design Specifications", First Edition, The American Association of State Highway Transportation Officials, Washington, D.C., 1994.
- 2.27 "Load and Resistance Factor Design Specification for Structural Steel Buildings", Second Edition, American Institute of Steel Construction (AISC), Chicago, .1994.
- 2.28 ENV 1993-1-1, "Eurocode 3: Design of steel structures - Part 1.1: General rules and rules for buildings", European Committee for Standardization (CEN), Brussels, April 1992.
- 2.29 BS 7608, "Code of practice for fatigue design and assessment of steel structures", British Standards Institute, London, 1994.
- 2.30 Guide for Fatigue Assessment of Tankers, American Bureau of Shipbuilding, ABS, New York, NY, June 1992
- 2.31 "Fatigue Design Guidance for Steel Welded Joints in Offshore Structures", UK Health & Safety Executive (formerly the UK Dept of Energy), H.M.S.O., London, 1984.
- 2.32 Fisher, J.W., et. al., "Development of Advanced Double Hull Concepts, Phase I.3a, Structural Failure Modes: Fatigue", Final Report for Cooperative Agreement N00014-91-CA-0001, Vol.3a, TDL 91-01, Lehigh University, Bethlehem, PA, March 1993b.
- 2.33 Kober, G.R., R.J. Dexter, E.J. Kaufmann, B.T. Yen, and J.W. Fisher, "The Effect of Welding Discontinuities on the Variability of Fatigue Life", Fracture Mechanics, Twenty-Fifth Volume, ASTM STP 1220, F. Erdogan and Ronald J. Hartranft, Eds., American Society for Testing and Materials, Philadelphia, pp. 533-545, 1994.
- 2.34 Guidance Manual for the Inspection and Condition Assessment of Tanker Structures, issued by: International Chamber of Shipping and Oil Companies International Marine Forum, on behalf of Tanker Structure Co-operative Forum, published by: Witherby & Co. Ltd., London, England, 1986
- 2.35 Guidelines for the Inspection and Maintenance of Double Hull Tanker Structures, issued by: International Chamber of Shipping and Oil Companies International Marine Forum, on behalf of Tanker Structure Co-operative Forum, published by Witherby & Co. Ltd., London, England, 1995.

- 2.36 Condition Evaluation and Maintenance of Tanker Structures, Tanker Structure Co-operative Forum, published by Witherby & Co. Ltd., London, England, 1992.
- 2.37 Cheung, M.C., "Cost Effective Analysis for Tanker Structural Repairs", Proceedings: Workshop and Symposium on the Prevention of Fracture in Ship Structure, March 30-31, 1995, Washington, D.C., Marine Board, Committee on Marine Structures, National Research Council, 1996.
- 2.38 Xu, T. and Bea, R.G., "Fitness for Purpose Analysis of Cracked Critical Structural Details (CSD) in Tankers", Journal of Marine Structures, May 1995
- 2.39 Isbester, Capt. J., Bulk Carrier Practice, The Nautical Institute, London, 1993.
- 2.40 N.S. Basar, V.W. Jovino, "Guide for Ship Structural Inspections", SSC-332, Ship Structure Committee, August 2, 1990
- 2.41 Rolfe, S.T., Hays, K.T., and Henn, A.E., "Fracture Mechanics Methodology for Fracture Control in VLCC's", Ship Structures Symposium '93, November 16-17, 1993, Arlington VA, available from SNAME, Jersey City, NJ, 1993.
- 2.42 Irwin, G.R., "Analysis of Stresses and Strains Near the End of Crack Traversing a Plate", Transactions, ASME, Journal of Applied Mechanics, Vol. 24, 1957, also reprinted in ASTM volume on classic papers.
- 2.43 Murakami, Y., et al, (eds.), Stress Intensity Factors Handbook (Vol.1 and 2), Pergamon Press, Oxford, U.K., 1987.
- 2.44 Tada, H., The Stress Analysis of Cracks Handbook, Paris Productions, Inc., Saint Louis, 1985.
- 2.45 Rooke, D.P., and Cartwright, D.J., Compendium of Stress Intensity Factors, Her Majesty's Stationery Office, London, 1974.
- 2.46 Rooke, D.P., Compounding Stress Intensity Factors, Research Reports in Materials Science (Series One), The Parthenon Press, Lancashire U.K., 1986.
- 2.47 Reemsnyder, H. S., "Fatigue and Fracture of Ship Structures", Proceedings: Workshop and Symposium on the Prevention of Fracture in Ship Structure, March 30-31, 1995, Washington, D.C., Marine Board, Committee on Marine Structures, National Research Council, 1996.

- 2.48 Formby, C.L., and Griffiths, J.R., "The Role of Residual Stresses in the Fracture of Steel," Proceedings of the International Conference "Residual Stresses in Welded Construction and Their Effects," 15-17 November 1977, London, The Welding Institute, Abington Hall, Abington, Cambridge, CB1 6AL, UK, pp. 359, 1977.
- 2.49 Faulkner, D., "A Review of Effective Plating for Use in the Analysis of Stiffened Plating in Bending and Compression", Journal of Ship Research, Vol. 19, No. 1, pp. 1-17, March 1975.
- 2.50 Pang, A.A.-K., R. Tiberi, L.-W. Lu, J.M. Ricles, and R.J. Dexter, "Measured Imperfections and Their Effects on Strength of Component Plates of a Prototype Double Hull Structure", Journal of Ship Production, Vol. 11, No. 1, pp. 47-52, Feb. 1995.
- 2.51 Nussbaumer, A.C., R.J. Dexter, J.W. Fisher, and E.J. Kaufmann, "Propagation of Very Long Fatigue Cracks in a Cellular Box Beam", Fracture Mechanics, Twenty-Fifth Volume, ASTM STP 1220, F. Erdogan and Ronald J. Hartranft, Eds., American Society for Testing and Materials, Philadelphia, pp.518-532, 1994.
- 2.52 McMeeking, R.M., and Parks, D.M., "On Criteria for J-Dominance of Crack-Tip Fields in Large-Scale Yielding," Elastic-Plastic Fracture, ASTM STP 688, J.D. Landes, J.A. Begley, and G.A. Clarke, Eds., American Society for Testing and Materials, pp. 175-194, 1979.
- 2.53 Shih, C.F., "Relationships Between the J-Integral and the Crack Opening Displacement for Stationary and Extending Cracks," Journal of the Mechanics and Physics of Solids, Vol. 29, No. 4, pp. 305-326, 1981.
- 2.54 De Castro, P.M.S.T. Spurrier, J., and Hancock, P., "Comparison of J Testing Techniques and Correlation J-COD Using Structural Steel Specimens," International Journal of Fracture, Vol. 17., pp. 83-95, 1981.
- 2.55 Wellman, G.W., and Rolfe, S.T., "Engineering Aspects of CTOD Fracture Toughness Testing," Welding Research Council Bulletin No. 299, pp. 1-15, November 1984.
- 2.56 Wellman, G.W., Rolfe, S.T., and Dodds, R.H., "Three-Dimensional Elastic-Plastic Finite Element Analysis of Three-Point Bend Specimens," Welding Research Council Bulletin 299, pp. 15-25, November 1984.

- 2.57 Dexter, R.J., "Fracture Toughness of Underwater Wet Welds," Fatigue and Fracture Testing of Weldments, ASTM STP 1058, H.I. McHenry, and J.M. Potter, Eds., American Society for Testing and Materials, Philadelphia, Vol. 1058, pp. 256-271, 1990.
- 2.58 Dexter, R.J. and Roy, S., "The Conditions at Ductile Fracture in Tensile Tests," Fracture Mechanics, Twenty-Third Symposium, ASTM STP 1189, Ravinder Chona, ed., American Society for Testing and Materials, Philadelphia, pp 115-132, 1993.
- 2.59 Reuter, W.G., Lloyd, W.R., Williamson, R., Smith, J.A., and Epstein, J.S., "Relationship Between Stress or Strain and Constraint for Crack Initiation," Presented at the ASTM 23rd National Symposium on Fracture Mechanics, June 18-20, 1991, College Station Texas, ASTM, 1991.
- 2.60 Irwin, G.R. "Use of Thickness Reduction to Estimate Values of K," Technical Report No. 90-3, Mechanical Engineering Department, University of Maryland, College Park, MD, 1990.
- 2.61 MacKenzie, A.C., Hancock, J.W., and Brown, D.K., "On The Influence of State of Stress on Ductile Failure Initiation in High Strength Steels," Engineering Fracture Mechanics, Vol. 9, pp. 167-188, 1977.
- 2.62 Miyata, T., Otsuka, A., Mitsubayashi, M., Haze, T., and Aihara, S., "Prediction of Fracture Toughness by Local Fracture Criterion," Presented at ASTM 21st National Symposium on Fracture Mechanics, Annapolis MD, June 28-30, 1988.
- 2.63 Green, G., and Knott, J.F., "The Initiation and Propagation of Ductile Fracture in Low Strength Steels," Journal of Engineering Materials and Technology, pp. 37-46, January 1976.
- 2.64 Ritchie, R.O., and Thompson, A.W., "On Macroscopic and Microscopic Analysis for Crack Initiation and Crack Growth Toughness in Ductile Alloys," Metallurgical Transactions A, Vol. 16A, pp. 233-248, February 1985.
- 2.65 d'Escatha, Y., and Devaux, J.C., "Numerical Study of Initiation, Stable Crack Growth, and Maximum Load, with a Ductile Fracture Criterion Based on the Growth of Holes," Elastic-Plastic Fracture, ASTM STP 668, J.D. Landes, J.A. Begley, and G.A. Clarke, Eds., American Society for Testing and Materials, pp. 229-248, 1979.
- 2.66 Sih, G.C., and Madenci, E., "Prediction of Failure in Weldments-Part 1: Smooth Joint," Theoretical and Applied Fracture Mechanics, Vol. 3, pp.23-29, 1985.
- 2.67 Matic, P., and Jolles, M.I., "The Influence of Weld Metal Properties, Weld Geometry and Applied Load on Weld System Performance," Naval Engineers Journal, March 1988.

- 2.68 Matic, P., and Jolles, M.I., "Defects, Constitutive Behavior and Continuum Toughness Considerations for Weld Integrity Analysis," NRL Memo. Rpt. No. 5935, 1987.
- 2.69 Batische, R., Bethmont, M., Devesa, G., and Rousselier, G., "Ductile Fracture of A508 Cl 3 Steel in Relation with Inclusion Content: The Benefit of the Local Approach of Fracture and Continuum Damage Mechanics," Nuclear Engineering and Design, Vol. 105, No. 1, pp. 113,120, December, 1987.
- 2.70 Schmitt, W., Sun, D.-Z., and Kienzler, R., "Application of Micro-Mechanical Models to the Prediction of Ductile Fracture," Localized Damage Computer-Aided Assessment and Control, Vol. 1: Fatigue and Fracture Mechanics, Proceedings, First International Conference on Computer-Aided Assessment and Control of Localized Damage, Portsmouth, UK, June 26-28, 1990.
- 2.71 Sun, D.-Z., Siegele, D., Voss, B., and Schmitt, W., "Application of Local Damage Models to the Numerical Analysis of Ductile Rupture," Fatigue and Fracture of Engineering Materials and Structures, Vol. 12, No. 3, pp. 201-212, 1989.
- 2.72 Matic, P., Kirby, G.C., And Jolles, M.I., "The Relationship of Tensile Specimen Size and Geometry Effects to Unique Constitutive Parameters for Ductile Materials," Naval Research Laboratory Memo report 5936, 1987.
- 2.73 Matic, P., "Numerically Predicting Ductile Material Behavior from Tensile Specimen Response," Theoretical and Applied Fracture Mechanics, Vol. 4, pp. 13-28, 1985.
- 2.74 Matic, P., Kirby, G.C. III, and Jolles, M.I., "The Relation of Tensile Specimen Size and Geometry Effects to Unique Constitutive Parameters for Ductile Materials," Proc. R. Soc. London, Vol. A 417, pp. 309-333, 1988.
- 2.75 Sih, G.C., and Madenci, E., "Fracture Initiation Under Gross Yielding: Strain Energy Density Criterion," Engineering Fracture Mechanics, Vol. 18, No. 3, pp. 667-677, 1983.
- 2.76 Sih, G.C., and Madenci, E., "Crack Growth Resistance Characterized by the Strain Energy Density Function," Engineering Fracture Mechanics, Vol. 18, No. 6, pp. 1159-1171, 1983.

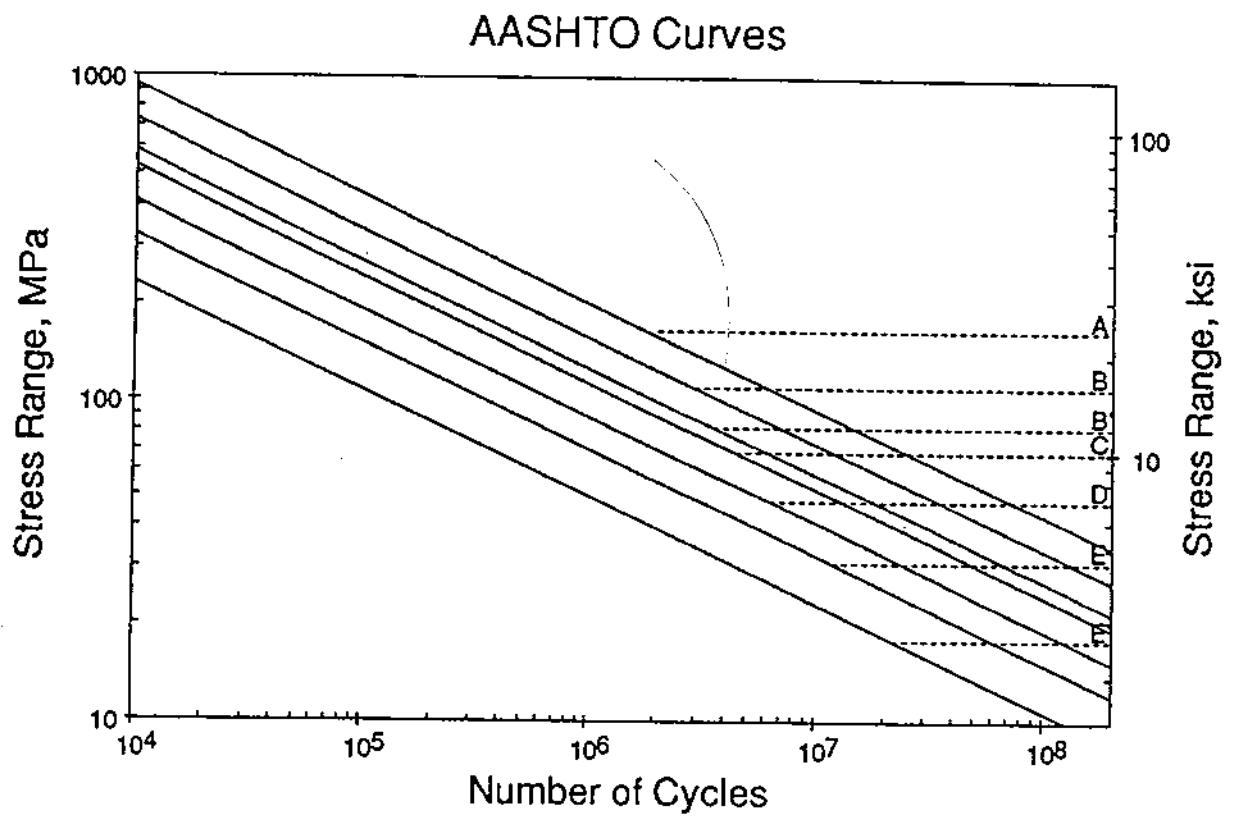


Figure 2.1 Fatigue design S-N curves for Categories A through E' for AWS and AASHTO specifications

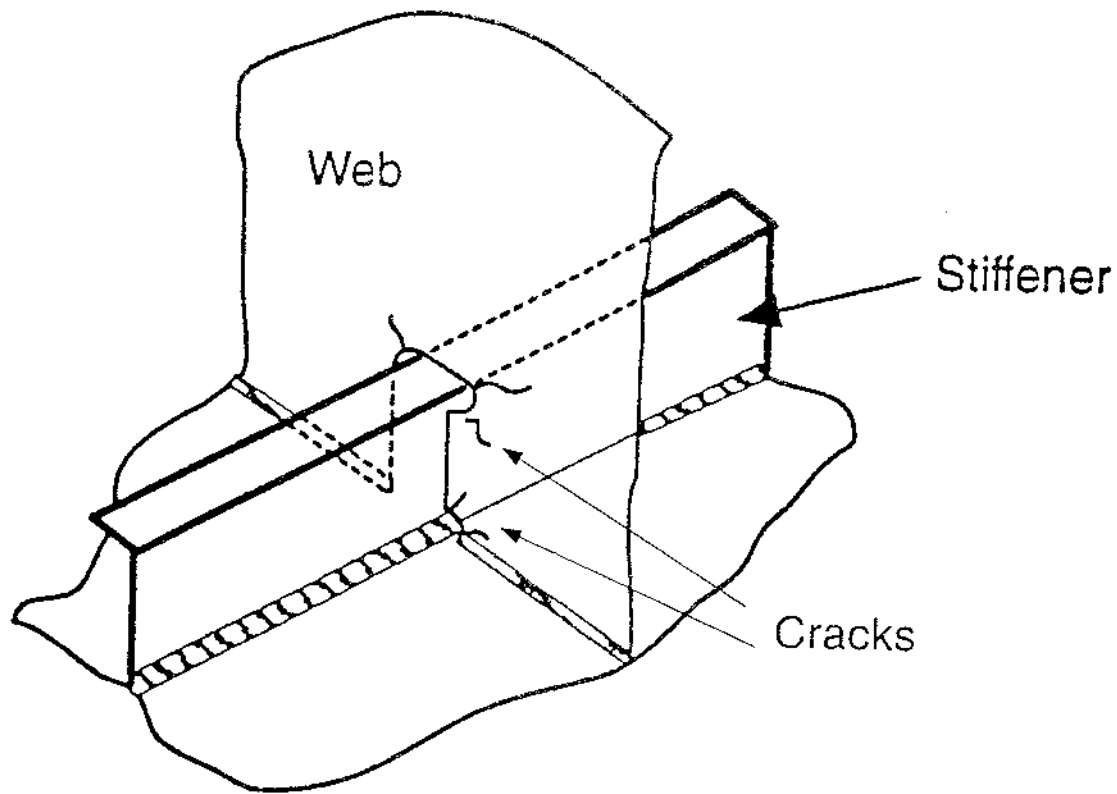


Figure 2.2 Cracking around collar at longitudinal to transverse connection

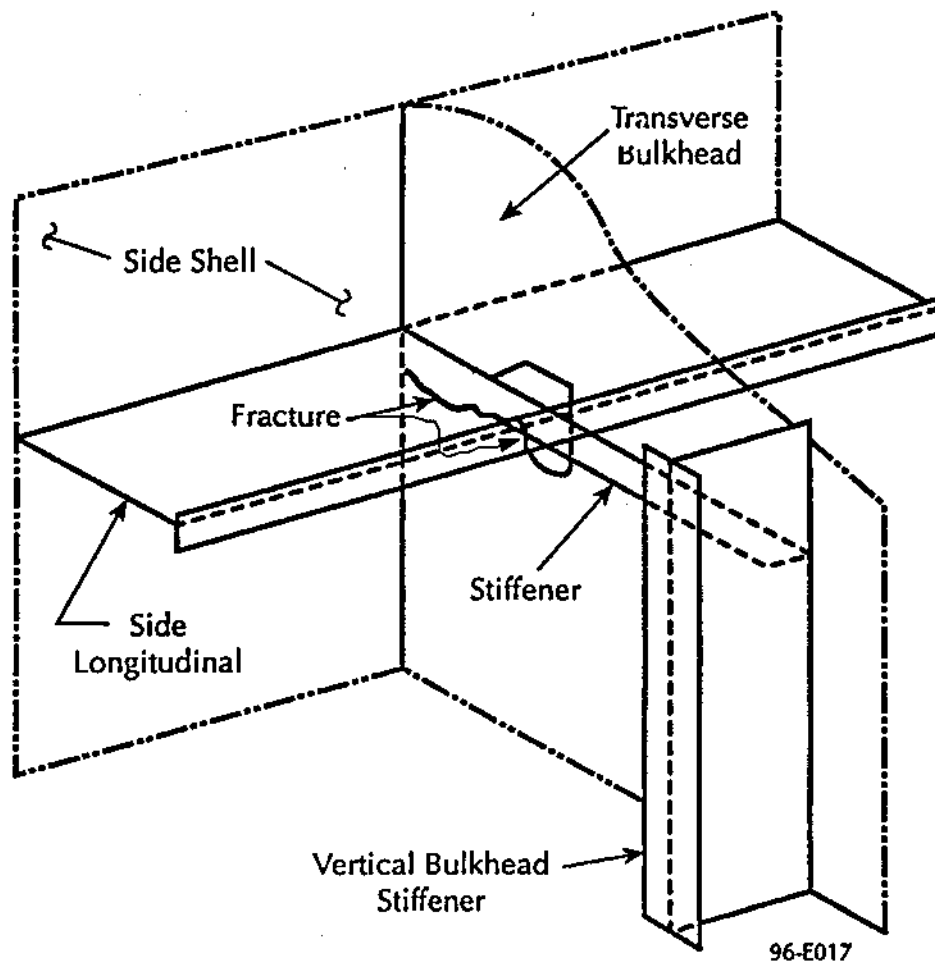


Figure 2.3 Cracking at longitudinal to transverse connection where flat bar stiffener lands on longitudinal

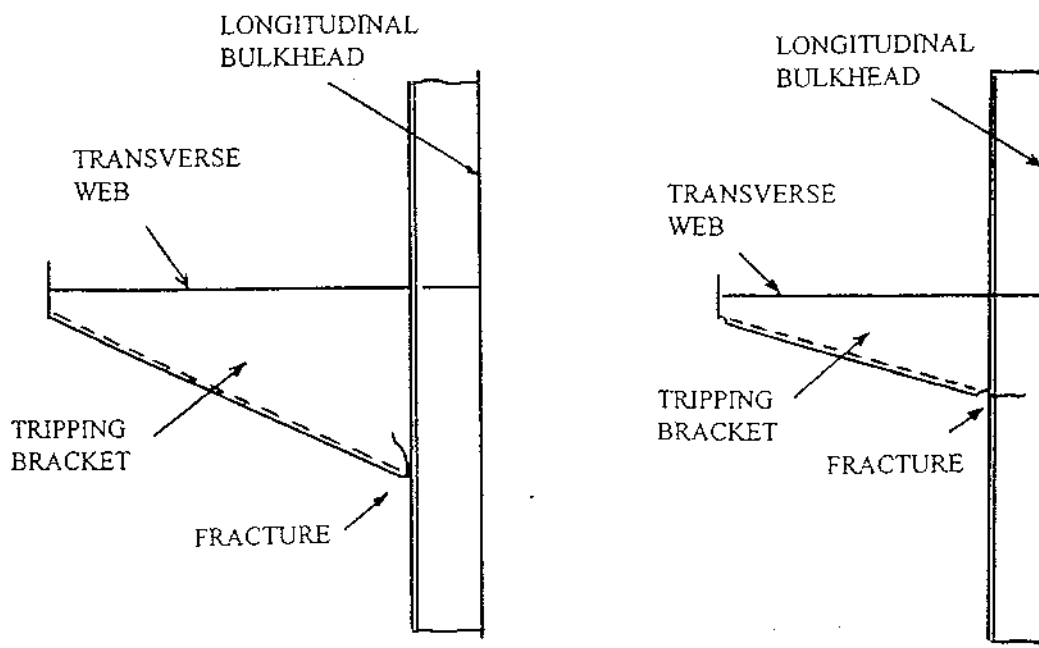
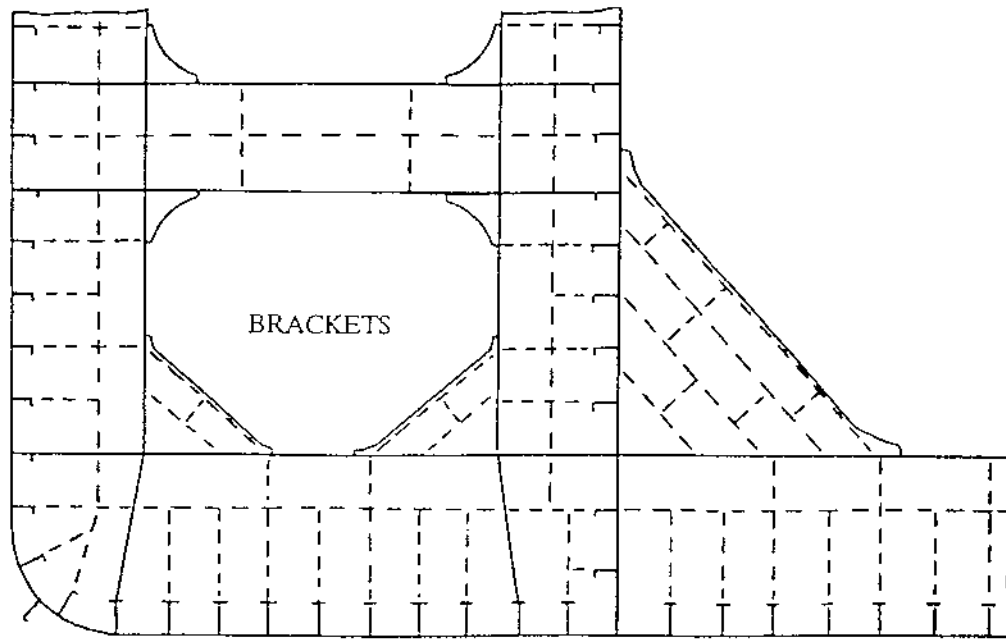


Figure 2.4 Cracking at critical bracket details

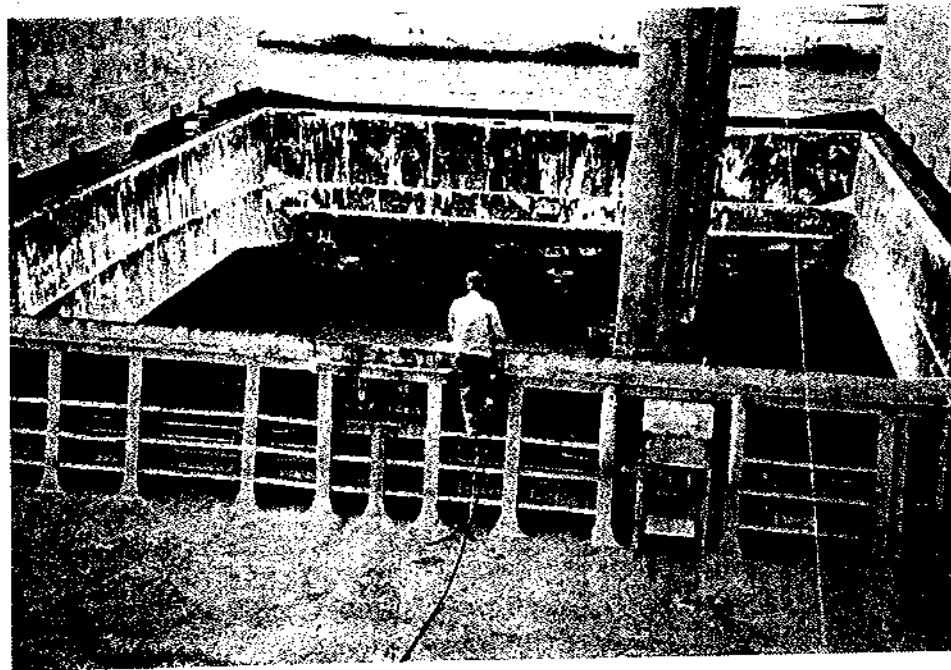


Figure 2.5 Hatch openings are critical in bulk carriers

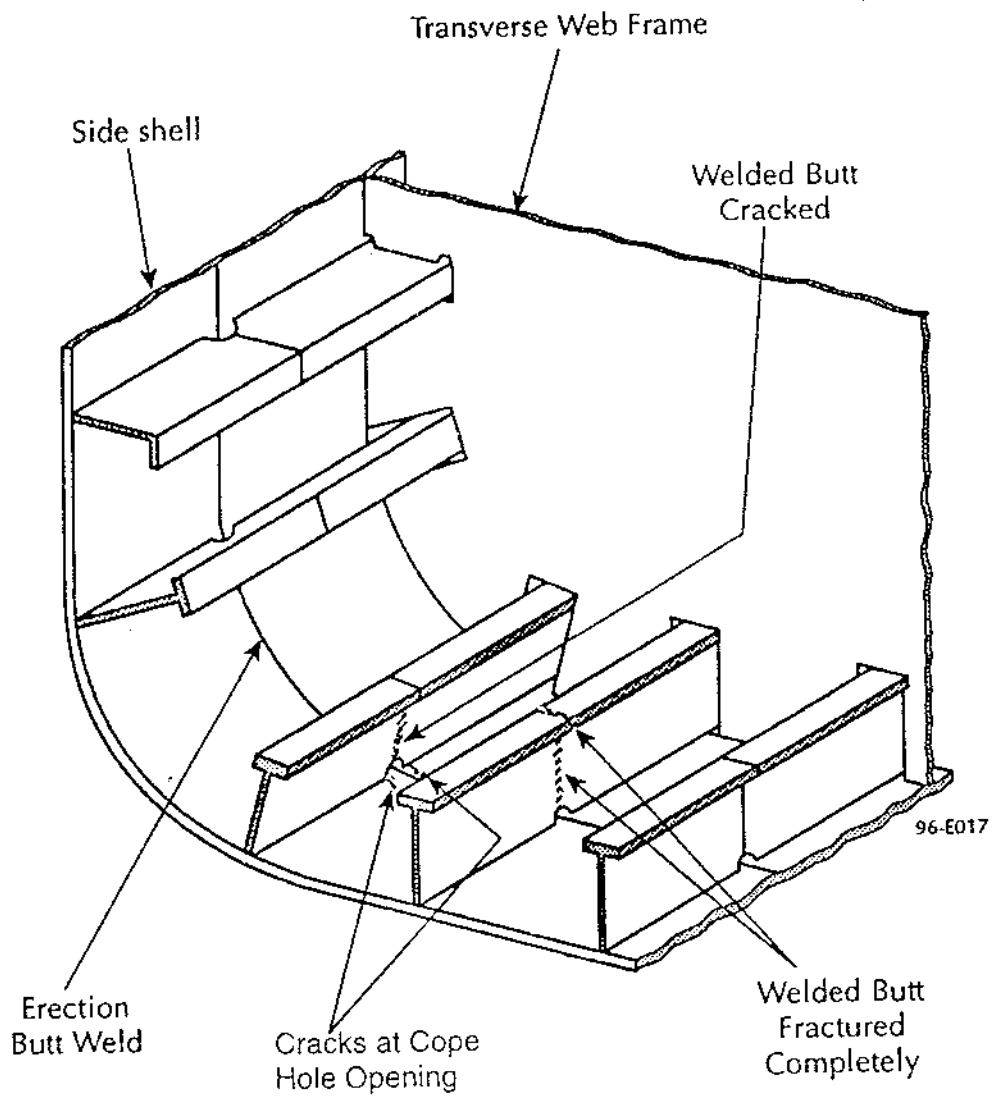


Figure 2.6 Cracking at weld access holes at erection butts where modules are joined.

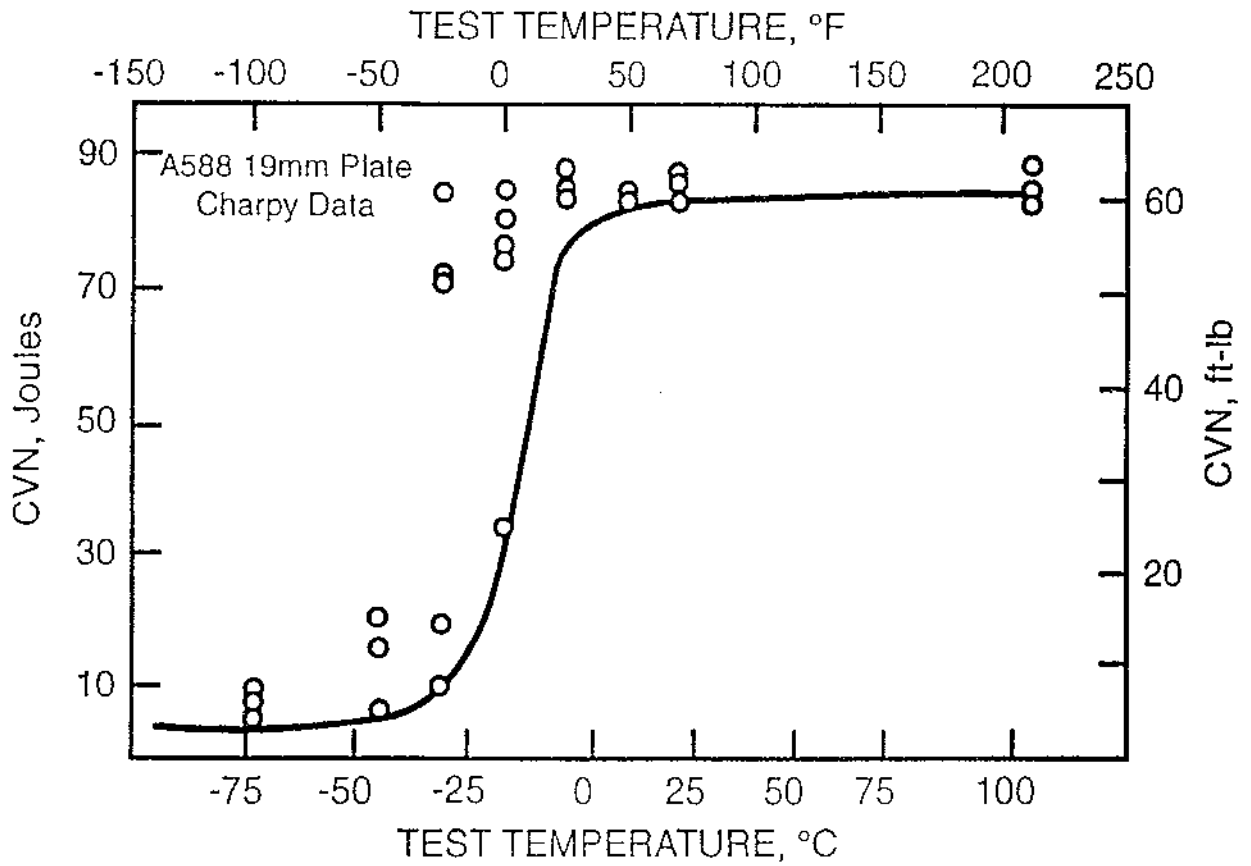


Figure 2.7 Charpy energy transition curve for A588 Grade 50 (350 MPa yield strength) structural steel

CHAPTER 3.0 FRACTURE EXPERIMENTS

Experiments were conducted at room temperature on over 30 full-scale welded structural members containing natural or simulated fatigue cracks. An overall test matrix is shown in Table 3.1. The purpose of the experiments was to evaluate the applicability and accuracy of various ductile fracture models on members with complex structural details. The specimens were fabricated from two different types of high-toughness steels, HSLA-80 and EH-36. Limited tests were also performed on ordinary A36 structural steel.

3.1 Specimen fabrication, residual stress, and materials characterization

I-section and box-section members, shown in Figures 3.1 through 3.3, were fabricated from HSLA-80 steel. The I-section members are intended to study the type of cracks which occur in longitudinal stiffeners or girders at attachments of flatbars or brackets, as shown in Figures 2.3 or 2.4. The I-beam specimens may also be a reasonable model for a cracked hatch opening coaming (such as in Figure 2.5), which resembles a flange while the web of the I beam represents the deck plate. The box beam specimens are intended to simulate the behavior of larger cracks which have penetrated the shell, deck, or bottom and must propagate through intersecting structure such as neighboring stiffeners or bulkheads. The HSLA-80 material is a copper precipitation-hardened steel conforming to MIL-STD-S-24645(SH). The HSLA-80 steel is essentially the same as ASTM Specification A710, Grade A, Class 3. A typical chemical composition for the plates used for the specimens is shown in Table 3.2. The minimum specified yield strength (MSYS) of the steel is 550 MPa. The HSLA-80 steel has extremely good low-temperature toughness properties. MIL-STD-S-24645(SH) requires a minimum specified Charpy-V-Notch test energy (CVN) of 80 J at a temperature of -84°C.

All the HSLA-80 I beam and box beam specimens were fabricated at Ingalls Shipbuilding using materials and fabrication techniques typical of modern surface combatants in accord with MIL-STD-1689 (unless otherwise noted). The weld joint designs are in accord with MIL-STD-22D. The longitudinal fillet welds were made with the submerged arc welding (SAW) process with the MIL 100-S welding wire. The other welding, attachment fillets and groove welds, was done using a semiautomatic carbon-dioxide shielded flux-cored arc weld (FCAW-S) using the MIL 100-TC weld wire. Several undermatched welds were included in the I-beam test specimens with intentionally introduced excessive porosity. Undermatched groove welds were produced using the GMAW process with MIL 70S-3 weld wire. The welds were visually inspected and a randomly selected 10% of the beams were inspected with a magnetic particle test (MT). Groove welds were ultrasonically tested (except the undermatched welds). Tack welding and repair welding were made with both the FCAW process and the shielded-metal arc welding (SMAW) process using E10018 electrodes.

Fatigue cracks typically begin at the toe of a weld, but typically the large cracks either propagate out of the weld as fatigue cracks, or soon after peak load the cracks propagate out of the weld as tearing cracks. Therefore, the welds are not believed to play that significant a role in the ductile fracture behavior of ship structural details. For small surface cracks in low-toughness welds, the weld properties may become very significant. For example, several undermatched welds were included in the I-beam test specimens with intentionally introduced excessive porosity. These welds had very low toughness due to the procedure that was used to introduce the porosity and exhibited brittle fractures. This was not the intended result of these experiments since the scope of this research is limited to ductile fracture. Therefore, the material characterization and detailed analyses of these undermatched groove welds were not performed.

Residual stresses were measured in the HSLA-80 specimens using sectioning and hole-drilling methods. In general, the residual stresses reached about 480 MPa at flame cut edges and about 340 MPa near the welds. Figure 3.4 shows a typical distribution of longitudinal residual stresses in both the I-section and box section. These magnitudes and distributions of residual stress are fairly consistent with previous experience which indicates that the residual stresses approach the yield strength. There was significant scatter among the measured residual stresses as is typical. In general terms, the various measurement methods gave consistent and compatible results.

Cope-hole specimens with stiffeners bridging the crack are shown in Figure 3.5. The stiffened specimens are called "cope-hole" specimens because of the weld access hole. These specimens are intended to represent the type of cracks which are common on tanker bottoms at the weld access holes in way of the master butts, such as shown in Figure 2.5. These specimens represent a different loading mode, tension rather than bending as in the I beams and box beams. Because much higher axial tensile loads are required to achieve the same stress levels as in the bending specimens, these tensile test specimens are necessarily much smaller than the bending specimens.

As shown in the test matrix in Table 3.1, CCT specimens of the same dimensions without the weld or stiffeners were also tested. There are solutions for J in these simpler CCT specimens which are a benchmark for comparison to the cope hole specimens. These CCT and cope-hole specimens were fabricated from the HSLA-80 steel and a high-toughness ASTM A131 Grade EH-36 ship steel. EH-36 is a fine-grain-practice, normalized, C-Mn steel. The typical chemical composition of the EH-36 plates used for the specimens is also shown in Table 3.2. Compared to the HSLA-80, the EH-36 steel has more Carbon and Manganese, but less Nickel, Chromium, and Copper. The EH-36 steel is specified in ASTM Specification A131. The minimum specified yield strength of the steel is 360 MPa, and there is a minimum specified CVN of 34 J at -40°C.

The EH-36 steel specimens were fabricated at the ATLSS Center at Lehigh University by certified welders with shipyard experience. Weld joint designs are in accord with MIL-STD-22D. The welds were made with the FCAW-S process.

3.1.1 Tensile properties

A typical stress-strain curve from the HSLA-80 material is shown in Figure 3.6. A summary of tensile test results for various plate thicknesses of HSLA-80 steel obtained using 6 mm diameter specimens is shown in Table 3.3. The average 0.2 percent offset yield strength from these tests was 607 MPa. The average ultimate tensile strength was 690 MPa. The flow stress, or average of the yield and ultimate strength, is used in fracture mechanics and is taken as 650 MPa for the HSLA-80 steel. As shown in the Table, there was significant scatter in yield strength values even for tensile specimens from the same plate thickness and rolling orientation. The yield strength values ranged from 569 to 635 MPa and the overall coefficient of variation for the yield strength was 3.6 percent. This level of variability gives a 95 percent confidence limit of plus or minus 7 percent, which is important because it determines the best possible accuracy of a failure-mode assessment, i.e. even the most simple failure mode, gross-section yielding, cannot be predicted with accuracy better than plus or minus 7 percent. In other words, a ductile fracture model would be considered sufficiently accurate if it were able to predict failure loads with comparable accuracy, i.e. within plus or minus 7 percent.

As shown in Figure 3.6, the HSLA-80 steel does not exhibit significant strain hardening and has an average yield-to-tensile strength ratio (Y/T) of 0.88. The high Y/T ratio is typical of very low-carbon steels. The Ramberg-Osgood equation:

$$\frac{\varepsilon}{\varepsilon_0} = \frac{\sigma}{\sigma_0} + \alpha \frac{\sigma^n}{\sigma_0^n} \quad (3-1)$$

was fit to the HSLA-80 true-stress true-strain tensile test data in the range after yield up to ultimate strength. This equation was fit because the parameters are used in several analytical fracture mechanics models. Here ε_0 is the yield strain which is 0.29 percent and σ_0 is the yield stress or 607 MPa. The best fit was obtained with α equal to 3.14 and the exponent "n" equal to 10.7.

A simple power-law hardening model is also widely used in analytical solutions:

$$\sigma = \beta \varepsilon^m \quad (3-2)$$

The hardening exponent "m" for the typical power-law hardening equation would be the inverse of "n" for the Ramberg-Osgood equation or 0.094, while β is 940 MPa. The Ramberg-Osgood and power law models are used to represent the material as a nonlinear elastic solid (deformation theory of plasticity) in analytical solutions. Modern finite-element codes use incremental plasticity and usually represent the effective stress-strain curve as a piecewise linear function.

A typical stress-strain curve from the EH-36 material is also shown in Figure 3.6. The average 0.2 percent offset yield strength from these tests was 406 MPa, the ultimate strength was 538 MPa, and the flow stress was 470 MPa. There was much less scatter in yield strength values compared to the HSLA-80 material. Note in Figure 3.6 that the EH-36 specimens exhibited a yield plateau followed by significant strain hardening, giving an average yield-to-tensile strength ratio (Y/T) of 0.76. The low Y/T compared to HSLA-80 steel may be attributed to the lower carbon content relative to the EH-36 steel. Lower Y/T (below 0.8) was typical of most structural steels in the past. However, modern steel has lower carbon content for improved weldability. In many cases, the modern steel also has higher alloy content, with alloying elements added for higher strength. Because much of the modern steel is made in an electric furnace from scrap, it is now common to have alloy elements that are not even specified for the steel which are present because they happened to be present in the scrap. These characteristics of modern steel tend to increase the Y/T ratio.

Note that the strain at ultimate strength, called uniform strain, for the EH-36 steel is greater than the uniform strain for the HSLA-80 steel. In fact, the ductility of the C-Mn EH-36 steel is about the same as the ordinary hot-rolled structural steel (A36) which was compared to HSLA-80 steel in the Introduction and shown in Figure 1.2. Therefore, the EH-36 steel may be expected to show much greater ductility than the HSLA-80 in the presence of a stress concentration or notch, as the A36 steel showed in Figure 1.2.

Consider [3.1] showed that the uniform strain would be equal to the power-law hardening exponent, or 9.4 percent for the HSLA-80 steel. This estimate of the uniform strain follows from the power law hardening model if the rate of change of stress with respect to strain is set equal to zero (at ultimate strength). This estimate of the uniform strain is consistent with the data in Figure 3.6. As the A36 and EH36 steel have much higher power-law hardening exponents than the HSLA-80 steel, this explains the greater apparent ductility in the tensile tests.

Since the stress-strain curve is very different from the HSLA-80 steel, this EH-36 steel provides a good contrast in yield behavior so that ductile fracture models can be evaluated over a broad range of conditions. In fact as discussed below, the HSLA-80 has much higher upper-shelf fracture toughness (as measured by J or CTOD) than the EH-36 steel. Therefore, the experiments will reveal whether the strain hardening or fracture toughness is more important in determining the overall load capacity and ductility of cracked structural members which fail due to tearing or upper-shelf ductile fracture. The A36 steel was not characterized.

3.1.2 Fracture-toughness properties

Fracture-toughness tests were performed in accordance with ASTM E1152-87 "Standard Test Method to Determine J-R Curves". By also following the provisions of ASTM E1290-93 "Standard Test Method for Crack-Tip Opening Displacement (CTOD) Fracture Toughness Measurement", CTOD may be obtained from the test data. A CTOD-R curve can be constructed from the test data, along with CTOD at maximum load (the traditional definition of CTOD for ductile fracture) and the CTOD corresponding to J_c . Compact specimens were made from 9 mm, 13 mm, and 25 mm thick plates of the HSLA-80 steel and 9 mm plates of the EH-36 steel in both the L-T (crack oriented transverse to the rolling direction) and T-L orientation.

Figure 3.7 shows a typical J-R curve from a 50 mm CT specimen (9 mm thick) of both the HSLA-80 and EH-36 steel plates. Note that after some crack propagation, the slope of the J-R curves, called the tearing modulus, is approximately constant and approximately equal for the two types of steel. There was considerable scatter among the fracture-toughness test results. In addition to this scatter, the value of J_{Ic} could vary depending on the method used to fit the J data. The J values determined from our tests were interpreted using a "linear" fit to the J data. An average J_{Ic} value of 630 kJ/m^2 was determined as a reasonable lower bound, which corresponds to a K value, given the symbol K_{Jc} because it is derived from a J test, of $360 \text{ MPa}\cdot\text{m}^{1/2}$.

Table 3.4 summarizes the data from the compact tension tests. The J values determined in these tests exceed the "validity" limits in the ASTM E1152 specification. This is not surprising since valid J values could not be obtained for plates of this thickness in any steel with reasonable toughness. Such "invalid" data have been used in the past, provided both the test specimen and the application are the same thickness. This is a reasonable approach where through-thickness cracks are concerned. However, for surface cracks, the constraint conditions are much different than for through-thickness cracks and the invalid J values may be questionable. The J-R curves and CTOD-R curves from several of these tests are included in Appendix 1.

In general, the J_c data for the HSLA-80 material fall in a scatterband ranging from about 600 to 1000 kJ/m^2 . There is considerable variability in these results, the coefficient of variation is 17 percent. Therefore, 95 percent confidence limit would range from plus to minus 34 percent. As in the case of the tensile test variability, this variability in fracture toughness puts into perspective the required accuracy of ductile fracture models.

There does not appear to be any discernable effect of orientation, width, or thickness among these results. The box sections and I beams were fabricated from different production heats, therefore the heat-to-heat variation does not seem to be significant either. It was anticipated that the sidegrooving would significantly decrease the apparent J_c values by suppressing the occurrence of shear lips and crack tunneling. However the sidegrooving appeared to have no significant effect either.

Since the CCT and cope-hole specimens to be tested were all of the same heat, plate thickness, and rolling direction, four compact tension tests were sufficient to characterize the toughness of the EH-36 material. The results of these four tests are shown in Table 3.4. An average J_c value of 331 kJ/m^2 was determined from the four tests, which corresponds to a K_{Jc} of $260 \text{ MPa}\cdot\text{m}^{1/2}$. Although

this material is also ductile at service temperature, it has a lower upper-shelf fracture toughness than the HSLA-80.

Note that ASTM E1152 states that the maximum crack extension is ten percent of the remaining ligament, or 5 mm in the case of the largest 100 mm compact specimens. Large redundant structures fabricated from relatively thin ductile plates may tolerate hundreds of millimeters of crack extension without serious damage or unstable rapid fracture. Data at such large crack extensions are required for the J-R analyses to be applied to the full-scale specimens as discussed in Section 4.2. Appendix 1 also contains extended J-R curves for several specimens where the J data from 100 mm compact specimens are plotted for up to 15 mm crack extension. This amount of crack extension is far beyond the limits where ASTM E1152 was intended to be used. However, it is not nearly enough crack extension for the analyses of the full-scale specimens.

Although there is great variation in the J-R curves at small crack extension, after crack extensions of about 4 mm the J-R curves seem to have a slope which is generally consistent. Equation (2-4) shows that J is proportional to CTOD. The rate of change of J with respect to crack extension, called the tearing modulus, is proportional to the rate of change of CTOD with crack extension, which is called the crack-opening angle (COA). At low crack extension, where ASTM E1152 indicates the tearing modulus should be measured, the average tearing modulus was 520 MPa for HSLA-80 steel, and 394 MPa for the EH-36 steel. The tearing modulus for larger crack extension is about 200 MPa for both types of steel. The fact that the tearing modulus is approximately constant implies that the COA should be approximately constant.

The flow stresses for the HSLA-80 and EH-36 steels are 650 and 470 MPa, respectively. Using Equation (2-4) to calculate CTOD, the COA corresponding to a tearing modulus of 200 MPa is 19 percent radian for the HSLA-80 steel and 26 percent radian for the EH-36 steel. It is shown below that in the full-scale experiments, notwithstanding a great deal of scatter, the COA was approximately constant after some crack propagation. The COA was the same in various experiments and the COA for the two materials was about the same, equal to about 25 percent radian.

As discussed later, several brittle fractures also occurred in tests where the weld was undermatched and intentionally made with defects. This weld metal apparently had a very low toughness as well, which is probably related to the impurities (grease) used to create the severe porosity. Unfortunately, the compact specimens which were fabricated from these welds did not give reliable results. Based on the observed load at failure of the full scale test, it is estimated that the K value for these welds was about $120 \text{ MPa}\cdot\text{m}^{1/2}$. Also, the A36 structural steel was not characterized.

3.2 I-beams with structural details in bending

As shown in the overall test matrix in Table 3.1, four-point bending tests were performed on 13 I-beam specimens. All specimens were constructed of HSLA-80 steel plates with a web thickness of 9.5 mm and a tension flange thickness of 12.5 mm. The I-beam specimens were shown in Figure 3.1. The flanges of the specimens with attachment details were of equal thickness while the groove welded specimens featured a 25 mm compression flange to ensure crack initiation in the tension flange during precracking. The specimens were stored outdoors after fatigue cracking and prior to fracture testing. Thus the cracks were weathered and contained corrosion deposits. Precrack geometries for each specimen are shown in the crack geometry plots in Appendix 2.

The I-beams were tested in the four-point bending fixture illustrated in Figure 3.8. The fixture was loaded using a Satec 2.7 MN capacity hydraulic testing machine. The overall span length was 2946 mm and the span between load points was 1219 mm. Braces to prevent lateral-torsional buckling were placed at approximately 600 mm intervals along the entire length of the specimen. Roller supports were used at all loading points including the point where load was applied to the spreader beam. The entire setup was fixtured to a floor beam in order to transfer load through the machine load cell. A photograph of the test setup is shown in Figure 3.9a. LVDTs were used to measure deflection at all load points relative to the upper (fixed) machine head. Strain gages were placed at cross sections approximately 150 mm from the crack location to check specimen alignment in the load fixture and verify bending stresses. Clip gages with extended ranges (25 mm and 125 mm) were used to measure deflections at the crack tip and the crack mouth. The crack tip displacements were made between studs welded 2.5 mm above and below the initial fatigue crack tip. This measurement of CTOD on a 5 mm gage length at the original crack tip ($CTOD_5$) has been shown through research at GKSS in Germany to give a value very close to the CTOD measured in the traditional way on standard specimens [3.2]. The $CTOD_5$ has become the basis of a fracture assessment method developed at GKSS [3.2]. Strain gage and clip gage instrumentation is shown in the photograph in Figure 3.9b.

The I-beam specimens were loaded in displacement control with a head travel speed of 0.8 mm/min. Load, deflection, and strain data were collected via a data acquisition system while crack length measurements were obtained visually at approximately 5 mm increments. The tests were completed when the crack extended to the compression flange as shown in Figure 3.10.

Strain data from one of the tests (I-beam specimen A18) are shown in Figure 3.11. Nominal strains in the flanges were very consistent, reaching the yield strain (about 0.29 percent) as the deflection reached the "yield deflection", which is the calculated deflection of the uncracked beam for the bending moment which would just start yielding of the flanges. The magnitude of the strains in each flange were averaged to get the nominal bending strain as shown in Figure 3.12. The flanges reached a peak strain of about 0.45 percent at a deflection equal to 1.5 times the yield deflection, indicating the flanges were yielding as the crack began to grow. The residual plastic strain at the end of the test was just less than 0.2 percent, which is about equal to the difference between the peak strain and the yield strain.

An experimental load-displacement curve for I-beam specimen A18 is shown in Figure 3.13. Load-displacement curves for all the I-beam specimens are shown in Appendix 2. In these figures, load is plotted as the applied bending moment normalized by the fully-plastic moment of the beam based on the remaining cross-sectional area with the initial crack size, and assuming an elastic-perfectly plastic material. Calculation of fully-plastic limit loads is discussed in detail in Section 4.2. Deflection is plotted as the average relative displacement of the specimen load points, d , normalized by the deflection associated with the yield moment of the uncracked section, d_y .

Figure 3.14 shows a crack geometry and extension diagram for specimen A18. Similar crack geometry diagrams for all the I-beam specimens are shown in Appendix 2. In these diagrams, the crack shape is shown at several discrete values of d/d_y corresponding to the load-displacement curves. Crack geometry diagrams are not shown for the groove-welded specimens because the initial geometry was very simple, i.e. the flanges were completely cracked and the cracks were essentially through-thickness edge cracks extending across part of the depth of the web. There was no appreciable ductile crack extension. Brittle fractures occurred in those tests.

Table 3.5 summarizes the significant results from the I-beam tests. The data in Table 3.5 are arranged in order of increasing crack size, except for specimens G27 and G26. These latter two experiments are listed towards the end of the table because they experienced a brittle fracture in the low toughness weld metal. Note that for a given type of specimen, the depth of the plastic neutral axis decreases as the cracked area increases. The net plastic modulus, Z_{net} , the peak load, and moment all decrease with increasing crack area, as expected. The load-point displacement at peak load does not show a trend with increasing crack size, although it is clearly lower for the last three specimens, i.e. the two brittle specimens and the very deeply cracked groove weld specimen. Aside from these and the first specimen, L16, with a very small internal crack, the peak load occurs consistently at about 1.4 times the yield displacement.

Additional data are shown in Table 3.6 at several points on the load displacement curve besides peak load, for specimens for which these data were available. Several specimens failed too rapidly to collect these data, and several specimens were intentionally interrupted before tearing significantly. Data are shown for a point where the crack extension was about one web thickness or 10 mm, which except for one case occurs just after the peak load. Data on the descending branch of the load-displacement curve at 50 percent of the peak load and 25 percent of the peak load are also shown. The crack mouth opening displacement, CMOD, is defined as the deflection at the outer fibre of the beam as measured by a clip gage connected to stud welded mounts on each side of the crack face. The crack tip opening displacement, CTOD₅, is defined as the deflection measured between two points on each side of the crack tip. The distance between these points is 5 mm.

Note that, except for G4 and G27, the displacements at 50 percent and 25 percent of the load are fairly consistent, e.g. d/d_y equals about 2.5 and 3.6 respectively for most specimens. Note that the CMOD and CTOD₅ are also fairly consistent, i.e. 18 and 28 mm at 50 and 25 percent of peak load, respectively. Also note that the relative increase in CMOD and CTOD over this interval, about 55 percent, is about the same as the relative increase in the d/d_y . It is hypothesized that all of the displacements are increasing in proportion to one another.

In Appendix 2, the results of all of the tests (except G26 and G27) are presented in terms of the applied moment normalized by the collapse moment, i.e. the fully-plastic moment on the net section, $M/M_{p,net}$, as a function of the average load-point displacement normalized by the displacement at yield on the gross section, d/d_y . Note that this ratio is typically close to or exceeding 1.0, i.e. the experimental results correspond closely with the maximum load that would be predicted using the fully plastic moment of the net section area of the cracked specimen. As indicated by the data in Table 3.6, most of these curves plot on top of one another. For example, Figure 3.15 shows the superposed load displacement curves for specimens A42, A39, A48 and A18. All of these specimens exhibit nearly identical normalized load-displacement curves, within the limits of experimental error. This is very surprising, since the crack area ranges from 16 to 26 percent of the gross area of these specimens, i.e. the crack area ranged from 1160 to 1890 mm². Similarly, the Z_{net} to Z_{gross} ratio ranges from 75 to 57 percent. Within these bounds at least, the crack size and relative propagation do not have a significant influence on the load-displacement curve, other than fixing the peak magnitude (the effect of $M_{p,net}$).

This observation is similar to the observations made by Landes with respect to his normalization method, i.e. that the fracture toughness has a relatively small influence on the load-displacement curves for relatively tough materials [3.3]. Obviously, there was a significant effect of toughness on the curves for G26 and G27, because these had a very brittle weld. However, it appears that there is a level of toughness such that the normalized load-displacement behavior is unaffected by the crack size. This would be all the fracture toughness that is useable, any further increase in fracture toughness would not increase the load-displacement ductility. Therefore, this level of toughness could be used for rational specification of steel properties.

Table 3.6 also shows the crack extension at the various points along the load deformation curve. Note that the crack extension increases relatively in proportion to the displacements as well. At 50 and 25 percent of the peak load, in particular, the crack appears to be growing in at a relatively constant angle. The ratio of the CMOD to the crack extension is shown in the last column. (The crack opening angle is actually the same as the ratio itself, for these small angles.) For the attachment specimens, the crack opening angle is fairly consistent at about 24 percent (about 14 degrees). Where the CTOD was measured on a gage length of 5 mm at the point of the original fatigue crack tip, the crack opening angle is also shown in terms of this displacement in parentheses. For small crack extension, the result is not very consistent. However, for large crack extension, the result is about the same as the result when the CMOD was used.

3.3 Box-beams with stiffened shell in bending

As shown in the overall test matrix in Table 3.1, four-point bending tests were performed on 4 box-beam specimens. The box-beam specimen was illustrated in Figures 3.2 and 3.3. Figure 3.3 shows the details incorporated into the specimen and Figure 3.2 shows overall specimen dimensions. All of these box specimens were constructed of HSLA-80 material. The specimens were tested in four point bending with a 7620 mm long span and a 1524 mm short span. Load was applied using a Baldwin 22 MN hydraulic testing machine. The test setup is shown in Figure 3.16a. The box-beams were instrumented and tested according to the procedures used for the I-beams as discussed above. Strain gages were placed at cross sections approximately 450 mm from the crack location to verify bending stresses. Clip gages were used to measure deflections at the crack mouth and, where possible, the CTOD₅ at the original crack tip. Clip gage and strain gage instrumentation are shown in Figure 3.16b. Precrack geometries for each box specimen are shown in Figure 3.17. No lateral torsional support was necessary given the inherent stability of the box beam cross section. The specimen was loaded in displacement control with a head travel speed of 1.0 mm/min. Load, deflection, and strain data were collected via a data acquisition system while crack length measurements were obtained visually at approximately 5 mm increments. The test was completed when the crack extended past the second (middle) flange as shown in Figure 3.18. Note the intense plastic deformation of the second flange after the crack has penetrated through this flange.

A typical experimental load-deflection curve from a box-beam test is shown in Figure 3.19 for box-beam specimen 3. Experimental load-deflection curves for all 4 box-beam specimens are shown in Appendix 3. As before, the results of all of the tests are presented in terms of the $M/M_{p,net}$ vs. d/d_y , i.e. the applied moment normalized by the collapse moment (the fully-plastic moment on the net section) vs. the average load-point displacement normalized by the displacement at yield on the gross section. Note that the $M/M_{p,net}$ ratio is typically close to or exceeding 1.0, i.e. the experimental results correspond closely with the maximum load that would be predicted using the fully plastic moment of the net section area of the cracked specimen. Table 3.7 shows crack extension data as a function of applied displacement. A few of the cracks tended to deviate out of the initial plane and sometimes multiple cracks developed on nearby plane. In Table 3.7, these cracks were idealized as a crack equal to the projection of all cracks on a single plane.

Table 3.8 summarizes the significant results from the box-beam tests. Note that for a given specimen, the depth of the plastic neutral axis decreases as the cracked area increases. The net plastic modulus, the peak load, and moment all decrease with increasing crack area, as expected. Aside from specimen 8, the peak load occurs consistently at about 1.6 times the yield displacement, which is about the same as the I-beam tests. Specimen 8 was unique because one of the web cracks was already up to the middle flange. Consequently there was very little crack extension until after the crack broke through the middle flange. Thus, the characteristic decrease in load after d/d_y of 1.6 does not occur for specimen 8. Specimen 10 is also somewhat different than specimens 3 and 9. Specimen 10 had the smallest crack which had not yet penetrated the webs. Because the load was higher, the compression flange on specimen 10 began to buckle locally and only about 10 mm of crack extension occurred. The buckling is shown in Figure 3.20.

Additional data are shown in Table 3.9 at several points on the load displacement curve besides peak load, for specimens for which these data were available. Specimen 10 was interrupted by the

buckling before tearing significantly. Data are shown for a point where the crack extension was about one web thickness or 10 mm, which for specimens 3 and 9 occurs just before the peak load. Data on the descending branch of the load-displacement curve at the point where the bottom flange was completely fractured, at the point where the cracks had grown up to the middle flange, and at the point where the cracks had broken through the middle flange, which generally resulted in a sudden and significant load drop.

Note that specimens 3 and 9 are very consistent in the displacements at which these events occur, despite having quite different initial crack sizes. Therefore, the load displacement curve for these two specimens are nearly the same. Figure 3.21 shows the superposed load-displacement curves for all four specimens. Again, as in the case of the I-beam specimens, the results are fairly consistent when normalized. However, there is a noticeable difference in the normalized load-displacement curves for specimens 10 (which had the small flange crack and failed by buckling rather than crack extension) and specimen 8 (the very deep crack).

Table 3.9 shows that the relative increase in CMOD is about the same as the relative increase in the d/d_y . As in the case of the I beams, all of the displacements are increasing in proportion to one another. Table 3.9 also shows the crack extension at the various points along the load deformation curve. Note that the crack extension increases relatively in proportion to the displacements as well. As the crack propagates across the flange, i.e. up to point C, the crack opening angle is about 12 to 18 percent. As the crack grows up the webs, the crack opening angle increases to between 17 and 22 percent.

3.4 Cope-hole and CCT specimens in tension

As shown in the overall test matrix of Table 3.1, tension experiments were performed on 12 cope-hole specimens and 7 similar center-cracked tension (CCT) specimens without welds and stiffeners. Six of the cope-hole specimens and one of the CCT specimens were made from each of the 9 mm thick HSLA-80 and EH36 plates. As part of a limited quick look at some other materials, several CCT tests were also performed on a 13 mm thick HSLA-80 plate and a two thicknesses of ordinary ASTM A36 structural steel.

There is a 6 mm (0.25 in.) distance from the edge of the cope hole to the toe of the fillet weld which was wrapped around (boxed) and terminated on the opposite side of the stiffener. The stiffener was placed so that the initial notch is right at the termination of the fillet welds at the edge of the cope hole. This is the typical location for these cracks at cope hole details in service, e.g. on the bottoms of single-hull tankers as shown in Figure 2.6.

Three of the specimens were tested with a stiffener on one side which was the originally-planned design. This arrangement is shown in Figure 3.5a. The rotation in these tests about the horizontal centerline was greater than anticipated and confounded the displacement measurements. Also, the objective of these tests was to have pure tension. Therefore, the remaining 9 cope-hole specimens were modified with a stiffener on both sides. This configuration is shown in Figure 3.22b. Note that this configuration remains in uniaxial tension regardless of the crack extension. A summary of the details of the 12 cope-hole specimens and the 7 CCT specimens is shown in Table 3.10.

The cope-hole specimens were loaded using a clevis-pin arrangement and the CCT specimens were loaded using wedge grips. Otherwise the CCT specimens were instrumented identically to the cope-hole specimens and were tested according to the same procedures. Displacement for both the cope-hole and CCT specimens was measured over a 460 mm gage length using an LVDT. All specimens were loaded in displacement control at a rate of 0.5 mm/min. The test setup is shown in Figure 3.22a. Clip gages were used to measure displacements at the crack tip and crack mouth. Strain gages were used to verify strains with those predicted by the finite element models described in Section 4.3. The instrumentation is shown in Figure 3.22b. Crack extension measurements were obtained visually at approximately 5 mm increments.

Table 3.10 shows the results from the tests in terms of the maximum load and displacement over a 460 mm gage length. (The displacement data for the first three tests with one stiffener were not useable due to the rotation as explained above.) The first pair of tests, with EH-36 steel, were intended to compare the behavior of precracked specimens to specimens cut with a jeweler's saw. As shown in the table, the difference in the results is minimal. There was no significant difference between the entire load-deformation curves of the two specimens. The lack of significance of the precracking was expected due to the ductility of this EH36 steel and the HSLA-80. Even in the case of precracking, there is considerable blunting of the crack tip before tearing which makes the results indiscernible from the results of sawcut specimens. Therefore, the remaining cope-hole tests were performed using the fine jewelers sawcut (with a width of 0.2 mm) in lieu of precracking.

For these specimens loaded in tension, the collapse load, P_F , is based on the flow stress times the net section area. The flow stress is the average between yield and ultimate engineering stress, which is 650 MPa for the HSLA-80 steel and 470 MPa for the EH-36 steel. For the bending specimens, the yield strength rather than the flow stress was used to compute the collapse loads. The difference is because the bending collapse load is idealized for the fully-yielded cross-section, which is never actually achieved. Not counting the strain hardening in the bending collapse load compensates for this idealization. In the tension specimens, there is no idealization to compensate for, therefore the strain hardening can be included in the calculated collapse load.

The net section is the section comprised of the remaining ligament of the cracked shell plate and the smallest net section at the top of the semicircular cope hole opening, even though the cross section at the top of the cope hole is not exactly coplanar with the crack plane. As shown in Table 3.12, the experimental result in terms of the percentage of the nominal net-section collapse load is lower for the HSLA-80 than for the EH-36 specimens. This reflects the strain hardening of the EH-36 material, which allows the load to slightly exceed that computed based on the flow stress.

Experimental load-displacement curves for the CCT specimens are shown in Figure 3.23. Two of the specimens in Figure 3.23 for the 9 mm thick HSLA-80 and EH-36 steel plates are examined in greater detail in Figures 3.24 through 3.27. In Figure 3.24, the load-displacement curves for these two specimens are normalized by the collapse load and yield deflection. As is typical of all of these CCT specimens, both specimens were able to reach their collapse load before stable tearing initiated (the descending branch of the load-deflection curve). Figure 3.25 shows the experimental crack length as a function of displacement for both of these CCT specimens.

As shown in the Figures 3.23 and 3.24, the EH-36 material was able to develop a long plateau after yielding and extend to over 1.5 times the maximum displacement of the HSLA-80 material. The effect of Y/T ratio of the steel on ductility was discussed in Section 1. The relatively high strain hardening of the EH-36 steel enables the load carried by the net section to eventually exceed the yield load for the gross section, leading to extensive plasticity and large overall elongation. Figure 3.25 shows that this displacement occurs prior to significant crack extension. This desirable behavior can only occur if the Y/T ratio of the steel is less than the ratio of net-to-gross area, since if the net area reaches the tensile strength the specimen will fracture before reaching the yield stress on the gross area. As shown in Table 3.10, the net-to-gross-area ratio for these specimens was 83 percent which is between the Y/T of the EH-36 steel (0.76) and the HSLA-80 steel (0.88). Therefore, only the EH-36 steel exhibits gross-section yielding.

The EH-36 material was able to extend significantly further than the HSLA-80 material before tearing initiated. This result is interesting because the HSLA-80 steel has almost twice the toughness (J_c) as the EH-36 steel, as described in section 3.1.2. Once tearing initiated, however, both materials behaved with the same normalized load, normalized deflection, and crack length relationship.

Further evidence of this simple principle relating the Y/T and the ratio of net-to-gross area is that the HSLA-80 steel, which appears non-ductile in Figure 3.24, can also be made exhibit a ductile plateau if the ratio of net-to-gross area is small enough. For example, refer to the result in Figure 3.23 for the 13 mm thick HSLA-80 plate with the total crack length ($2a$) of only 13 mm, giving a

ratio of net-to-gross area of 92 percent, slightly above the material Y/T of 0.88. The same thickness HSLA-80 plate with the 76 mm crack exhibits only limited ductility, as did the 9 mm thick plate with the 25 mm crack discussed above.

The same effect occurs with an ordinary ASTM A36 structural steel. The two curves in Figure 3.23 with the smallest loads are tests on a 6 mm thick A36 steel CCT specimen (152 mm wide) with crack lengths ($2a$) of 13 mm and 76 mm. The Y/T of this material is between the net-to-gross area ratios of 50 and 92 percent, and therefore the specimen with the 13 mm crack exhibits a ductile plateau. This A36 steel does not have any particular Charpy specification and would therefore be expected to be representative of the lower bound toughness for typical structural steel. Yet, despite the minimal toughness, this steel can still exhibit a ductile plateau for large net-to-gross area ratios. In a ship with a large cross section, a small fatigue crack less than a meter in length would represent a very small percentage of the total cross section. So this type of ductile behavior would be expected in a ship if the Y/T ratio were reasonably low.

The net-to-gross-area ratio for these specimens was greater than for any of the other experiments on cope-hole specimens, I-beam specimens, or box-beam specimens. Therefore, none of these other experiments developed GSY.

Figure 3.26 shows the experimental crack opening displacement.(COD) data as a function of displacement on the 460 mm gage length for the 9 mm thick HSLA-80 and EH-36 CCT specimens. It can be seen that both curves are linear and of the same slope. For the HSLA-80 steel, it appears that essentially all of the displacement, except the elastic part of the displacement, is concentrated in the crack plane. For the EH-36 steel, after the first 14 mm of displacement that occurs in the gross section, the remaining displacement that occurs after significant crack extension is concentrated primarily in the crack plane. After some crack extension, the net-to-gross area ratio decreases to a level below the Y/T of the steel, ending the GSY.

Figure 3.27 shows the crack length plotted in terms of the COD. The curves for each material in this figure are practically identical. Note that the slope of these lines is equivalent to the crack opening angle (COA) in radian. As shown in the figure, the COA is approximately 24 percent radian, which is in agreement with the COA in the I-beam and box-beam specimens in the latter stages of crack propagation, and is also approximately in agreement with the tearing modulus as explained in Section 3.1.2 above.

Since there is a constant shift in the crack length vs displacement data but not in the crack length vs COD data, it is evident that the extra ductility of the EH-36 specimen resulted from overall elongation of the specimen away from the reduced cross section. The strain-hardening of the EH-36 material tends to spread the plastic strain over a greater area while the low strain hardening of the HSLA-80 material tends to localize strain at the reduced cross section.

Also note in Figure 3.23 that the slopes of the descending branches of the load deflection curves are essentially the same. The load as a function of crack length for the entire descending branch of these curves was equal to the limit load, i.e., the load was equal to the flow stress times the remaining cross sectional area of the specimen. Since the crack extension rate is approximately the same in both specimens as shown in Figure 3.25, the area is changing at the same rate and thus the load is changing at the same rate.

Typical experimental load-displacement curves for a HSLA-80 and an EH-36 cope-hole specimen are shown in Figure 3.28 and 3.29. Load-displacement data for all cope-hole specimens are shown in Appendix 4. In Figure 3.29, after about 13 mm of displacement, the crack had propagated through the plate and all that remained of the specimen was the stiffeners. At this point the load developed a plateau at about 450 kN. This plateau corresponds approximately to the ultimate strength times the remaining area of the stiffeners. This demonstrates the advantage of redundancy of a stiffener which bridges over a crack.

The load-displacement curves for the replicate HSLA-80 specimens 4, 5, and 6 are superposed in Figure 3.30. For this steel there is much greater variability in the load displacement curves among replicate specimens. The level of agreement between the replicate tests exhibited in Figure 3.30 can serve as a benchmark for the level of agreement between experiment and analysis. In other words, this level of variability is as good as can be expected from any predictive analysis. The difference can be seen in the variation of the peak loads which are shown in Table 3.10. The load displacement curves decrease at about the same rate in the descending branch of the curve, however. In fact, the descending branch does not seem to be strongly dependent on the initial crack size.

Note that the HSLA-80 tests do not develop the same elongation as the EH36 tests and do not exhibit the plateau. For the EH-36 specimens, the crack was able to extend the entire width of the baseplate without breaking the stiffeners. This is shown in Figure 3.31a. The stiffeners on the HSLA-80 specimens broke before the crack extended completely to the ends of the baseplate as shown in Figure 3.31b. Table 3.10 also shows a reduced displacement at peak load (the onset of strain localization) and reduced final displacement for the HSLA-80 steel specimens. Apparently the ductility of the HSLA-80 stiffeners was much less than the ductility of the stiffeners made from EH36 steel.

Another way of looking at this is that the ductility of the plate with 50 mm and 76 mm crack lengths is greater than the ductility that can be expected from typical (uncracked) details such as a cope hole. However, the ductility of both the stiffeners and the cracked shell was much greater for the EH-36 steel. So the HSLA-80 steel would be expected to exhibit poorer overall ductility even for an uncracked ship structure.

It appears the ductility is more significantly affected by the yield-to-tensile-strength ratio (Y/T) than the fracture toughness. Strain hardening acts to spread the extent of the plastic zones which increases the length over which plastic strain occurs and increases overall elongation. The lack of strain hardening in the HSLA-80 facilitates localization of the strain and necking of the stiffener at lower values of overall elongation.

Table 3.11 shows some results at several stages during the tests. As was the case for the bending experiment, all the displacement quantities appear to increase proportionally. For example, Figure 3.32 shows the CTOD₅ and the overall displacement increase in proportion after about 1 mm of displacement (the elastic part). In fact, the plastic part of displacement is about equal to the CTOD₅, which means that all the displacement is coming from the crack plane. Figure 3.32 shows that this relationship is constant for all specimens, materials, and crack lengths. This can be contrasted to the behavior shown in Figure 3.26 for the CCT specimen where the two materials with the same initial crack sizes exhibit a constant shift in the COD vs deflection curves. The reason for this difference was explained above in terms of the ratio of net to gross area. As shown in Table 3.10, the net-to-gross-area ratio for the EH-36 CCT specimen is greater than the Y/T ratio of the EH-36 material, while the net-to-gross-area ratio for the cope-hole specimens is less than the Y/T ratio of the EH-36 material.

Table 3.11 also shows an estimate of the crack-opening angle (COA), which was found by taking the rate of change of the CTOD₅ and crack length. This COA is similar for both materials and is comparable to the COA determined in this manner from the bending tests (shown in the Tables 3.6 and 3.9). The COA can also be inferred from a plot of the displacement vs. crack length. Figures 3.33 and 3.34 show such plots for the 50 mm and 76 mm initial crack sizes (2a). The COA which was estimated from the slope of these curves is 23 percent radian from both initial crack sizes. This COA is approximately the same as in all of the other specimens (see Figure 3.25 and Tables 3.6 and 3.9 for example) and is consistent with the measured tearing modulus as explained in Section 3.1.2. The slope of these curves does not seem to be consistently affected by the material or the crack size.

3.5 References

- 3.1 Considere, A., "L'Emploi du Fer et de L'Acier dans les Constructions", Ann. Ponts et Chaussees, Vol. 9, Series 6, pg. 574-775, 1885.
- 3.2 Schwalbe, K.-H., and Cornec, A., "The Engineering Treatment Model (ETM) and its Practical Application", Fatigue and Fracture of Eng. Materials and Structures", Vol. 14, pp.405-412, 1991.
- 3.3 Lee, K. and Landes, J.D., "Development J-R Curves Without Displacement Measured Using Normalization," Fracture Mechanics: Twenty-Third Symposium, ASTM STP 1189, Ravinder Chona, Eds., American Society for Testing and Materials, Philadelphia, 1993, pp. 133-167.

Table 3.1
Overall Matrix of Ductile Fracture Tests of Full-Scale Members

Spec. Type	Loading	Detail Type	Number of Tests	Material
I beam	4 pt. bending	long. weld	2	HSLA-80
I beam	4 pt. bending	butt weld	3	HSLA-80
I beam	4 pt. bending	attachment	8	HSLA-80
Box beam	4 pt. bending	stiffened shell	4	HSLA-80
Cope hole	tension	access hole at butt weld	6	HSLA-80
Cope hole	tension	access hole at butt weld	6	EH-36
CCT	tension	shell	3	HSLA-80
CCT	tension	shell	1	EH-36
CCT	tension	shell	3	ASTM A36

Table 3.2
 Typical Chemical Composition of the Plates Used to Fabricate
 the HSLA-80 and EH-36 Specimens

HSLA-80

Element	% by Weight
Carbon	0.040
Manganese	0.570
Phosphorous	0.013
Sulfur	0.002
Silicon	0.255
Nickel	0.850
Chromium	0.710
Molybdenum	0.180
Copper	1.120
Niobium	0.045
Aluminum	0.047
Tin	-
Vanadium	0.005
Titanium	0.005
Columbium	-
Antimony	-
Nitrogen	-

EH-36

Element	% by Weight
Carbon	0.120
Manganese	1.460
Phosphorous	0.017
Sulfur	0.004
Silicon	0.328
Nickel	0.010
Chromium	0.110
Molybdenum	0.054
Copper	0.014
Niobium	-
Aluminum	0.031
Tin	-
Vanadium	0.004
Titanium	-
Columbium	0.029
Antimony	-
Nitrogen	0.005

Table 3.3
Summary of Tensile Test Results for the HSLA-80 and EH-36 Materials

HSLA-80	Yield	Ultimate
12.7mm plate transverse direction	588	700
	625	694
	569	693
average	594	696
12.7mm plate longitudinal direction	625	707
	644	707
average	635	707
12.7mm plate average, both directions	610	700
9.5mm plate transverse direction	613	691
	613	691
	613	678
average	613	687
9.5mm plate longitudinal direction	575	650
average	575	650
9.5mm plate average, both directions	604	678
overall average both plate sizes	607	690

EH-36	Yield	Ultimate
9.5mm plate longitudinal direction	406	537
	407	539
	404	538
average	406	538

WELD METAL	Yield	Ultimate
70S-3 13mm plate	521	596
	521	598
average	521	596
100S-1 overmatch 10mm plate	638	697
	654	732
average	646	713
100S-1 overmatch 13mm plate	694	745
	711	756
	738	776
	758	827
average	725	774
overall average both plate sizes	654	715

Notes:

All HSLA-80 and weld metal test results were obtained using 6mm diameter specimens

All EH-36 test results were obtained using 35mm X 9mm flat strap specimens

Table 3.4
Results of ASTM E1152 J-R Curve Tests on
Compact Tension Specimens from HSLA-80 and EH-36 Steel Plates

HSLA-80

Spec. Number	Thickness (mm) SG if Sidegroove	Width mm, Orientation	Jc kJ/m ²	Tearing Modulus (MPa)	CTOD i (mm)	CTOD max (mm)
W3	9 SG	51 LT	902	352	0.72	1.1
F6	13	51 LT	675	726	0.53	0.81
B4	13	51 LT	1020	482	1.0	1.3
W1	13	51 LT	750	NA	0.57	0.80
B3	13 SG	51 LT	667	516	0.99	1.4
B2	13	51 TL	750	427	0.61	0.90
F3	25	51 LT	663	503	0.65	1.0
F2	25	51 LT	596	573	0.53	0.82
F1	25	51 TL	676	516	0.55	0.85
F8	25 SG	102 LT	713	529	0.5	0.70
		Average =	740	520	0.67	0.97
		COV (%)=	17		28	24
		value used	630		0.57	0.87

EH-36

Spec. Number	Thickness (mm) SG if Sidegroove	Width mm, Orientation	Jc kJ/m ²	Tearing Modulus (MPa)	CTOD i (mm)	CTOD max (mm)
EH1	9	51 LT	241	348	0.42	0.76
EH2	9	51 LT	215	391	0.63	0.89
EH3	9	51 LT	421	407	0.51	0.71
EH4	9	51 LT	447	428	0.49	0.75
		Average =	331	394	0.51	0.78
		COV (%)=	36	9	17	10
		value used	331	394	0.51	0.78

Notes:

W =material from the webs, W3 from an I beam and W1 from a box section,
 F = material from the flanges of the I beams,
 B = material from the flanges of the box sections.

Table 3.5
Summary of Cracked I-Beam Four-Point-Bending Tests

Spec. Number	Crack a , c (mm)	Crack Location a , c	Crack % gross area	Peak Load (kN)	Load-Pt. Displ.* (mm)	d peak ----- d yield (%)	Peak Moment (kN-m)	M _{p,net} (kN-m)
L16	71, 0	B , B	9	1727	23.4	239	746	649
A1	13, 74	H , B	13	1183	20.8	175	511	496
A42	12, 110	H , B	16	1158	18.8	158	500	462
A34	28, 100	H , B	20	1035	23.3	196	447	425
A39	23, 128	H , B	22	961	19.7	166	415	403
L9	52, 127	B , B	22	919	13.7	140	397	388
A20	32, 110	H , B	22	875	16.5	139	378	399
A48	28, 134	H , B	25	862	16.4	138	372	360
A18	51, 122	H , B	26	875	20.1	169	378	349
A33	31, 143	H , B	27	776	14.6	123	335	334
G27	43, 110	W , W	18	644	7.1	73	278	240
G26	98, 109	W , W	24	576	8.4	86	249	456
G4	193, 152	H , H	40	274	9.5	97	118	114

Notes:

* corresponds to peak load.

The letter appended to the specimen number indicates the type of specimen, L = longitudinal welds only, A = attachment detail, and G = groove weld detail.

All specimens have a moment arm of 864 mm

The nominal yield displacement is 11.9 for A specimens and 9.8 mm for L and G specimens.

The nominal yield moment is 532 kN-m for A specimens and 592 kN-m for L and G specimens.

The nominal area is 7260 mm² for A specimens and 9190 mm² for L and G specimens.

The nominal section modulus is 877,000 mm³ for A specimens and 975,000 mm³ for L and G specimens (to the tension flange).

Table 3.6
Additional Results of Cracked I Beam Four-Point Bending Tests

Spec. Number	Load Stage % of Max.	d / dy	CMOD (mm)	CTOD 5 (mm)	delta a (mm)	tan ⁻¹ CMOD/da (% radian) or (CTOD)
A42	100	1.6			4	
	81	2.2			10	
A34	100	2.0	5.2		5	
	97	2.1	6.5		10	
	50	2.8	17		67	25
	25	3.6	28		112	25
A39	100	1.7	4.4		3	
	99	1.7	5.1		10	
	50	2.7	18		75	24
	25	3.4	28		105	26
L9	100	1.4	4.7		10	
	50	2.4	17		110	15
	25	3.6	29		180	16
A20	76	0.8	1.6	0.9	10	(9)
	100	1.4	4.2	3.6	15	(24)
	50	2.5	18	17	90	20 (19)
	25	3.2	28	26	170	16 (15)
A48	100	1.4	11	4.2	6	(59)
	97	1.6	13	6.1	10	(54)
	50	2.5	20	18	70	28 (25)
	25	3.3	34	28	110	30 (25)
A18	100	1.7	4		2	
	90	1.9	6		15	
	50	2.8	18		80	22
	25	3.5	29		170	17
G27	100	0.7	1.5	1.5		
	25	1.1	8.5	8.5		
G4	100	1.0	6.4	2.1	1	
	50	1.6	13	6.1	40	31 (15)
	25	2.6	22		97	23 (11)

Table 3.7
Crack Sizes Recorded During Box-Beam Tests

All measurements are shown in mm.
c1,c2,a1, and a2 correspond to figure below.

BOX 3					
d/dy	M/Mp.net	c1	c2	a1	a2
1.020	0.753	283	381	45	110
1.432	0.949	284	381	52	113
1.522	0.958	287	381	59	117
1.659	0.959	290	381	71	126
1.812	0.896	293	381	91	138
1.882	0.900	376	381	110	144
1.976	0.899	381	381	116	148
2.223	0.898	381	381	148	165
2.408	0.889	381	381	162	168
2.502	0.883	381	381	168	173
2.627	0.879	381	381	173	178
2.659	0.877	381	381	178	178

BOX 8					
d/dy	M/Mp.net	c1	c2	a1	a2
0.958	0.882	381	361	178	103
1.201	0.953	381	361	178	121
1.217	0.957	381	366	178	121
1.295	0.973	381	381	178	129
1.386	0.988	381	381	178	132
1.560	1.009	381	381	178	143
1.761	1.027	381	381	178	152
1.824	1.033	381	381	178	160
1.936	1.035	381	381	178	160

BOX 9					
d/dy	M/Mp.net	c1	c2	a1	a2
0.617	0.494	331	276	95	31
0.739	0.624	331	276	95	31
0.791	0.678	331	276	95	31
0.896	0.785	331	276	95	31
1.103	0.948	331	276	95	31
1.131	0.962	331	276	95	31
1.191	0.987	331	276	95	31
1.364	1.008	381	281	105	36
1.500	1.033	381	286	115	41
1.715	1.029	381	291	130	63
1.832	0.994	381	294	145	76
1.948	0.943	381	298	160	81
2.079	0.900	381	301	168	136
2.113	0.897	381	381	168	136
2.300	0.889	381	381	172	168
2.689	0.856	381	381	178	178

BOX 10					
d/dy	M/Mp.net	c1	c2	a1	a2
1.579	0.989	197	175	0	0
1.812	0.962	207	185	0	0

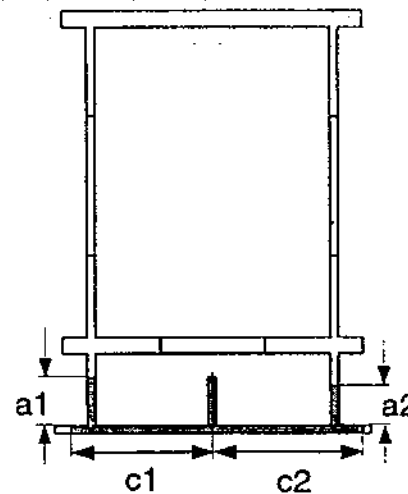


Table 3.8
Summary of Cracked Box-Beam Four-Point-Bending Tests

Box Number	Crack a1 , a2 (mm)	Crack c1 , c2 (mm)	Crack % gross area	Peak Load (kN)	d peak	Peak	M peak
					----- d yield (%)	Peak Moment (kN-m)	----- Mp,net (%)
3	45, 110	283, 381	23	4323	160	6588	96
8	178, 103	381, 326	27	4057	224	6183	104
9	95, 31	331, 276	21	4876	156	7431	104
10	0, 0	197, 175	11	6237	158	9505	99

Notes:

All specimens have a moment arm of 3048 mm

The nominal yield displacement is 38.3 mm using the shear span cross-section

The nominal cross-sectional area at the mid section of the box is 43961 mm²

The nominal section modulus at the mid section of the box is 16,053,000 mm³ (to the tension flange).

The nominal plastic section modulus at the mid section of the box is 17,347,381 mm³

The nominal depth of the plastic neutral axis at the mid section of the box is 260 mm (from the tension flange).

Plastic moment and modulus values take into account the reduction of cross-section due to splice plate holes.

Table 3.9
Additional Results of Cracked Box Beam Four-Point Bending Tests

Box Number	Load Stage *	d / dy	CMOD (mm)	Crack Depth (mm)	\tan^{-1} CMOD/ Crack Depth (% radian)
	A	1.6	12.1	106	11
	B	1.5	10.4	101	10
	C	2.0	21.8	145	15
	D	2.7	38.0	191	20
	E	3.0	48.7	311	16
	A	2.2	33.4	191	17
	B	1.2	10.8	163	7
	C	1.3	12.7	167	8
	D	2.2	33.4	191	17
	E	2.8	51.7	241	21
	A	1.6	14.5	96	15
	B	1.4	10.4	84	12
	C	2.1	29.7	165	18
	D	2.6	42.5	191	22
	E	2.8	49.5	231	21
19	A	1.6	7.2	---	---
	B	1.8	8.3	---	---
	C	---	---	---	---
	D	---	---	---	---
	E	---	---	---	---

Notes:

Crack depth is defined as the distance from the bottom of the tension flange to the top of the web cracks (average).

Load Stages:

A: peak load

B: 10mm of crack depth growth

C: bottom flange completely exhausted

D: bottom webs completely exhausted

E: crack snaps through middle flange

Table 3.10
Summary of Cracked Cope-Hole Specimen Tension Test Data

Specimen	2a mm	Anet mm ²	Anet/Agross	Peak Load kN	P/Pf,max	d/dy,peak	d/dy final
*EH-36 #1	50	1391	0.605	600	1.06	---	---
*EH-36 #2	50	1391	0.605	606	1.07	---	---
EH-36 #3	50	1815	0.789	913	1.04	---	---
EH-36 #4	76	1573	0.684	816	1.08	5.56	18.22
EH-36 #5	76	1573	0.684	802	1.06	4.78	17.86
EH-36 #6	76	1573	0.684	809	1.07	5.36	14.44
*HSLA-80 #1	50	1391	0.605	776	0.92	4.08	15.94
HSLA-80 #2	50	1391	0.605	---	---	---	---
HSLA-80 #3	50	1815	0.789	---	---	---	---
HSLA-80 #4	76	1573	0.684	1188	1.01	2.78	7.15
HSLA-80 #5	76	1573	0.684	1022	1.00	2.74	7.26
HSLA-80 #6	76	1573	0.684	1127	1.10	2.25	7.43
EHCCT	25	1210	0.833	1095	1.07	3.69	7.66
HSLACCT	25	1210	0.833	612	1.05	14.29	26.19
				830	1.06	2.84	15.15

dy=0.91 mm for EH-36 specimens.

dy=1.34 mm for HSLA-80 specimens.

Note: EH-36 #1 featured a fatigue precrack, all other specimens featured sawcut precracks

* indicates specimens with a one-sided stiffener

Table 3.11
Summary of Clip Gauge and Crack Length Data from the Cope-Hole Specimens

	stage	da (mm)	2a (mm)	d/dy	cod (mm)	cod5 (mm)	coa (rad)
EH-36 #3	1	3	56	5.6	3.8	4.2	-
	2	8	66	7.6	5.6	6.2	-
	3	18	86	10.5	7.9	9.0	0.28
	4	50	150	15.4	11.6	13.8	0.15
EH-36 #4	1	1	78	4.8	3.9	4.1	-
	2	11	98	7.0	5.9	6.3	-
	3	18	112	8.8	7.8	8.2	0.28
	4	33	142	14.4	13.0	13.3	0.34
EH-36 #5	1	3	82	5.4	3.7	3.8	-
	2	10	96	8.6	6.1	6.9	-
	3	22	120	10.3	8.2	8.6	0.15
	4	33	142	14.4	11.5	12.5	0.36
EH-36 #6	1	1	78	4.1	2.5	3.2	-
	2	9	94	7.6	4.8	6.4	-
	3	23	122	11.0	7.7	9.7	0.24
	4	33	142	15.5	12.4	14.0	0.43
HSLA-80 #3	1	0	50	2.8	3.4	3.1	-
	2	10	70	5.6	7.2	7.3	-
	3	18	86	7.2	9.1	9.5	0.28
	4	18	86	7.2	9.1	9.5	-
HSLA-80 #4	1	0	0	2.8	2.4	3.0	-
	2	7	90	6.1	6.2	8.0	-
	3	-	-	-	-	-	-
	4	-	-	-	-	-	-
HSLA-80 #5	1	1	78	2.3	2.1	2.4	-
	2	9	94	4.4	4.7	5.6	-
	3	17	110	5.6	6.4	7.4	0.23
	4	25	126	7.4	9.1	10.1	0.34
HSLA-80 #6	1	3	82	3.7	3.2	3.9	-
	2	10	96	5.8	6.1	7.0	-
	3	19	114	7.7	8.6	9.5	0.28
	4	19	114	7.7	8.6	9.5	-

stage 1 corresponds to peak load
stage 2 corresponds to da = 9 mm (approx.)
stage 3 corresponds to da = 18 mm (approx.)
stage 4 corresponds to end of stable crack extension

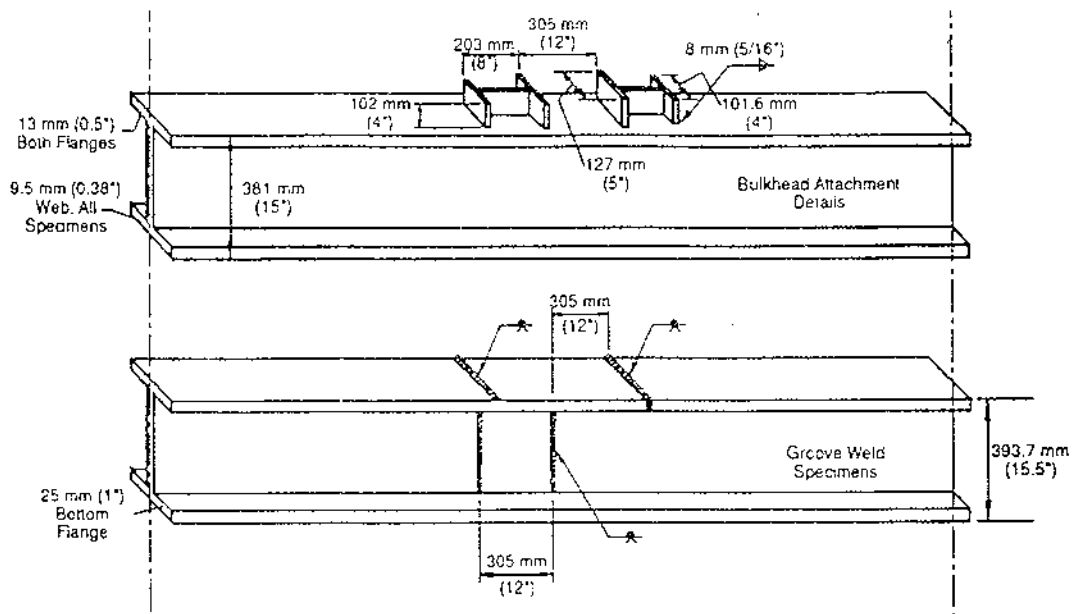


Figure 3.1 I-beam specimens featuring bulkhead attachment details (top) and transverse groove welds (bottom).

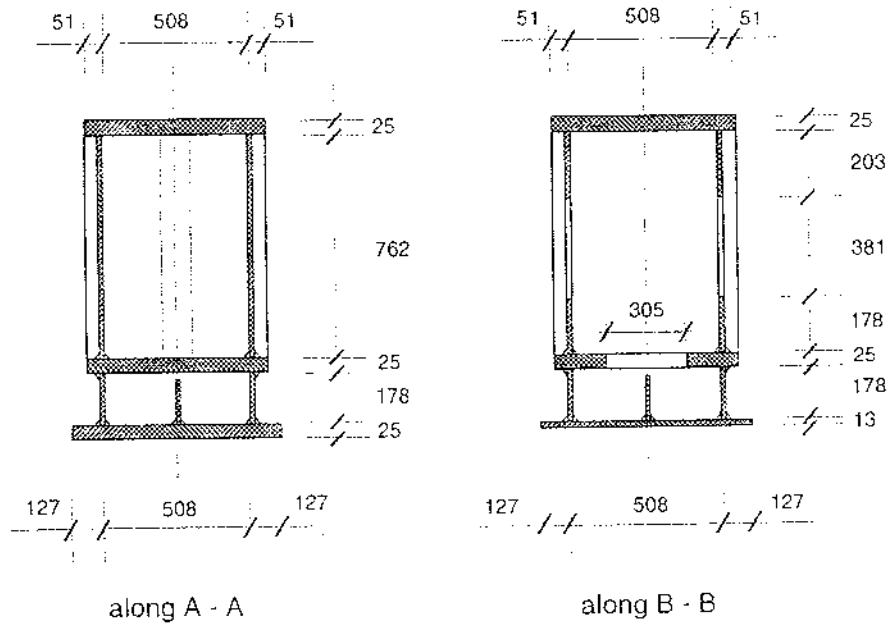
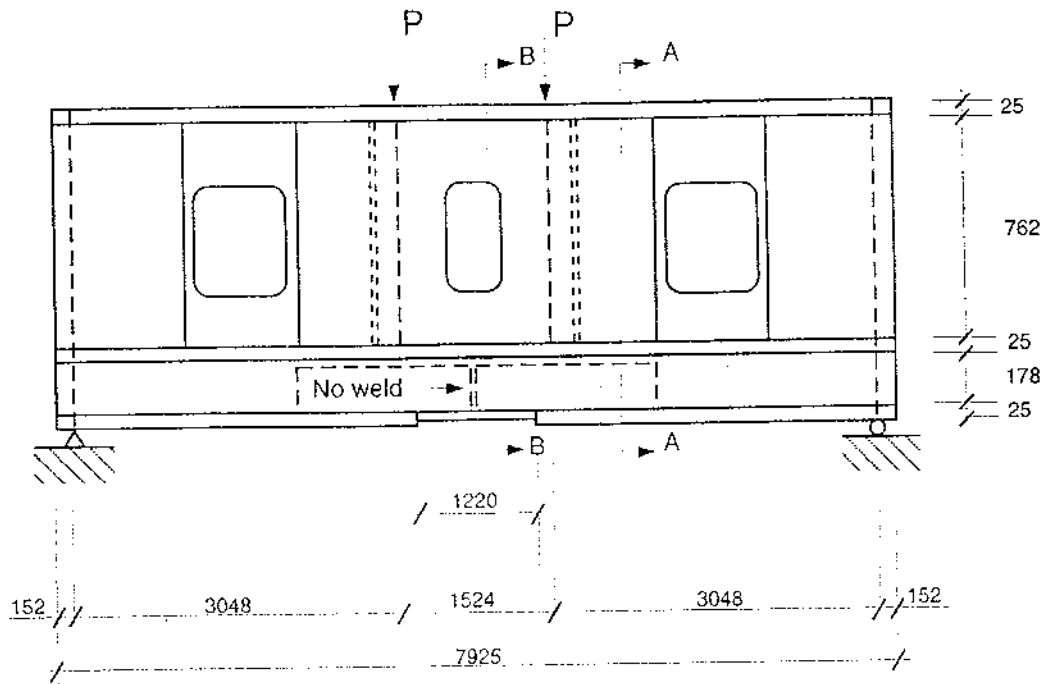


Figure 3.2 Box-beam elevation with principal dimensions in mm

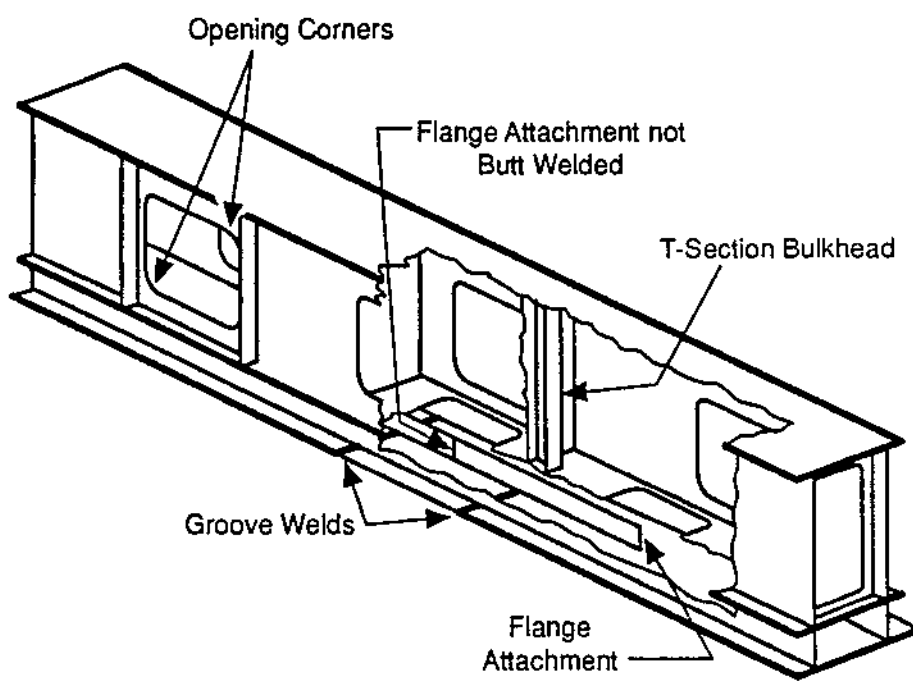


Figure 3.3 Cutaway diagram of the box-beam specimen showing internal details

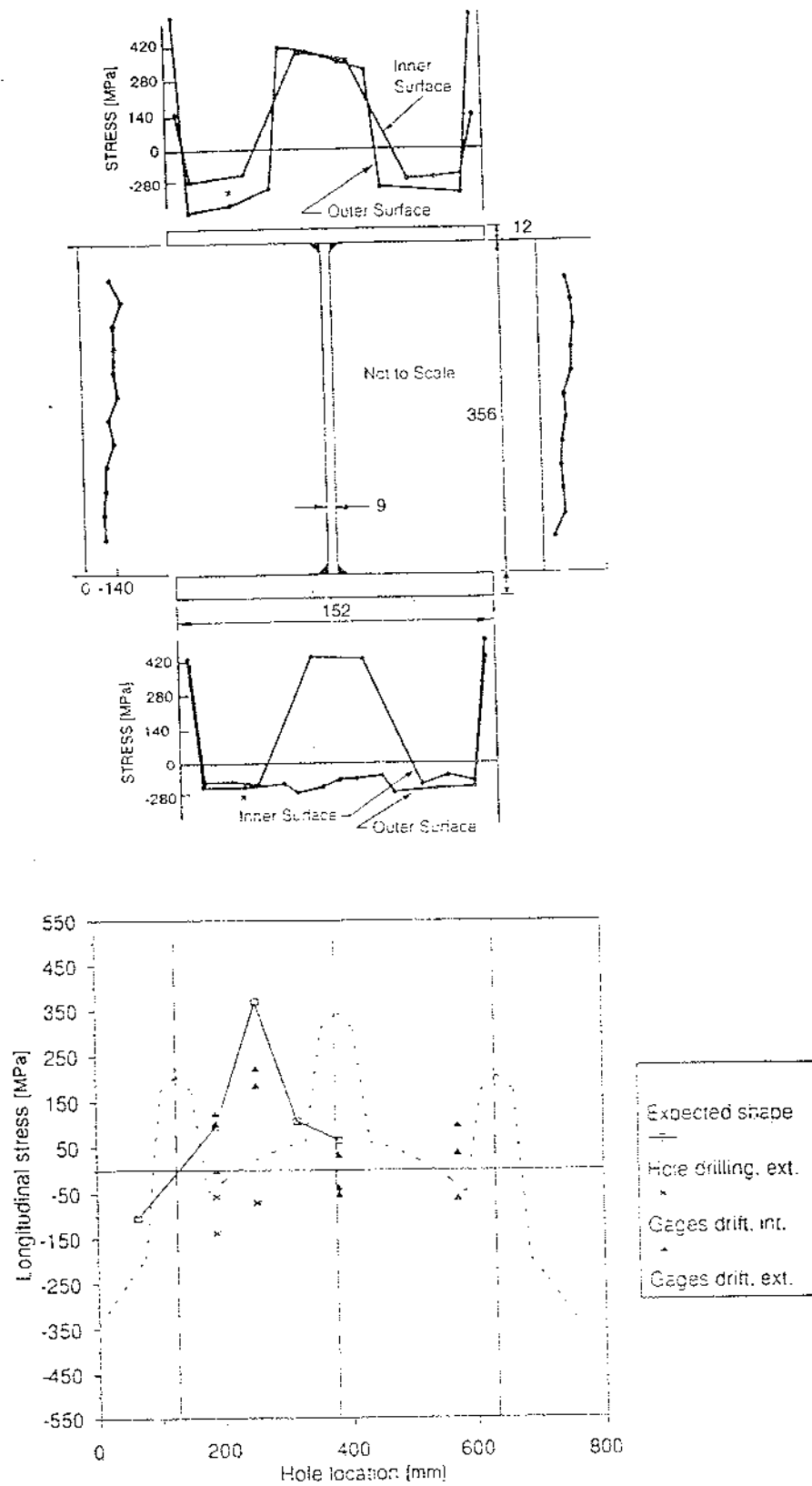
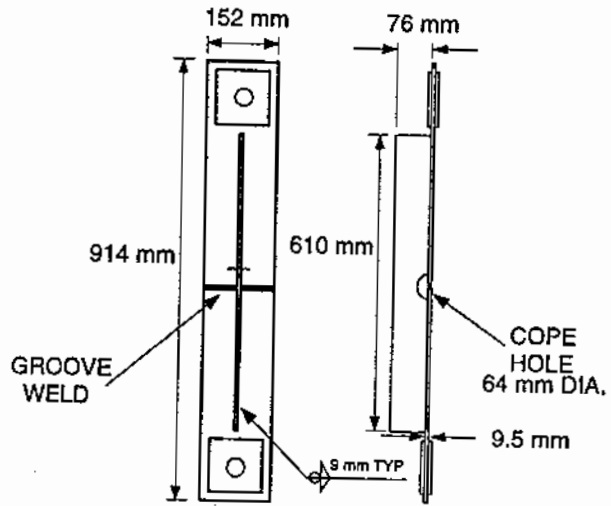
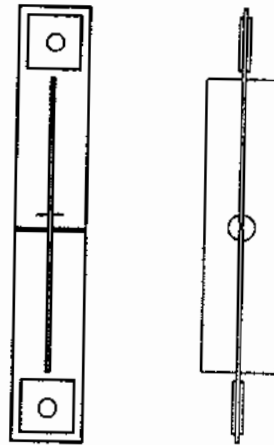


Figure 3.4 Typical distribution of longitudinal residual stresses in the I section (above) and box section (below) obtained using the hole drilling method



(a)



(b)

Figure 3.5 Cope-hole specimens with stiffeners bridging the crack. Specimens with one-sided stiffeners (a) and two-sided stiffeners (b) are shown

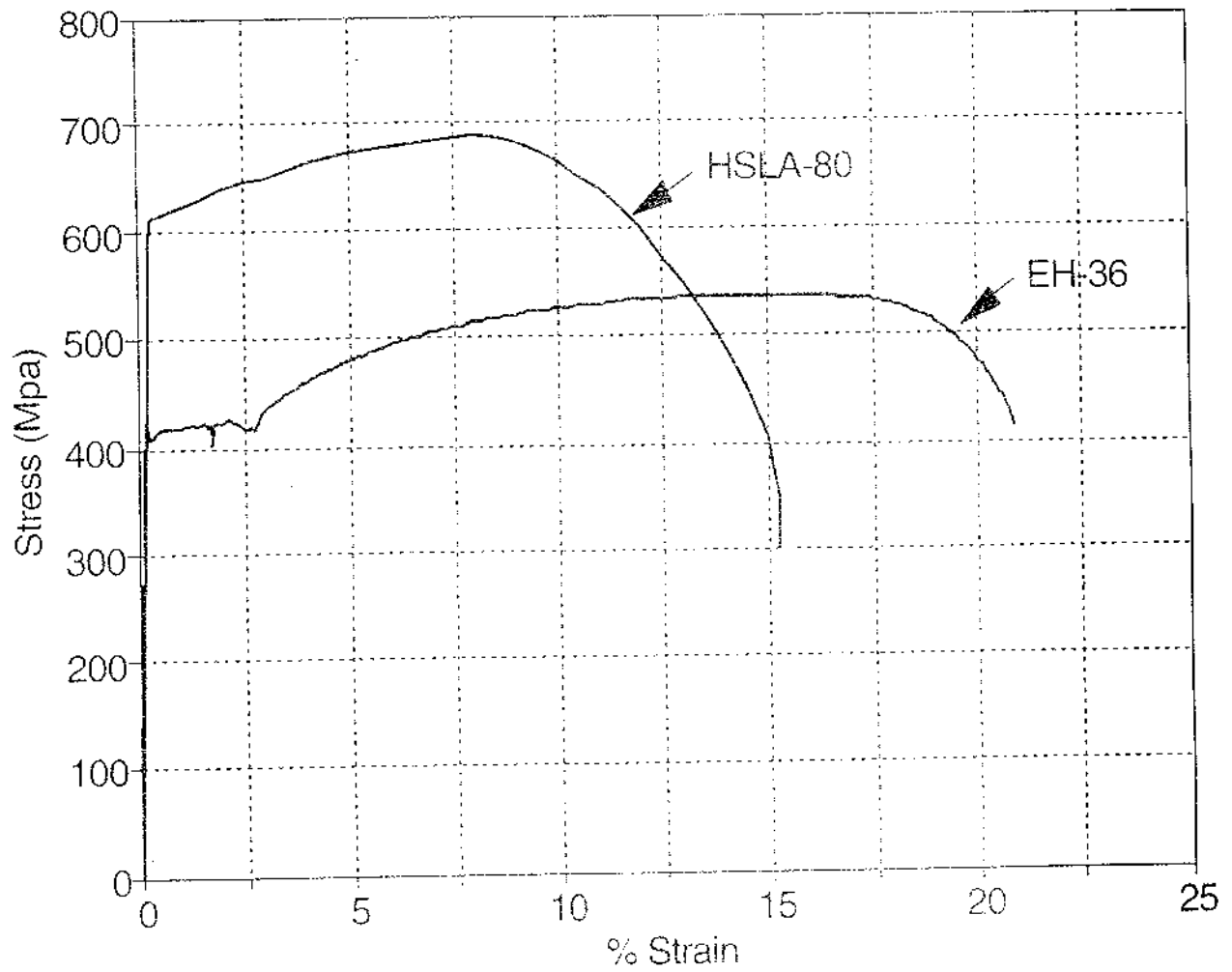


Figure 3.6 Typical engineering stress-strain curves from the HSLA-80 and EH-36 materials

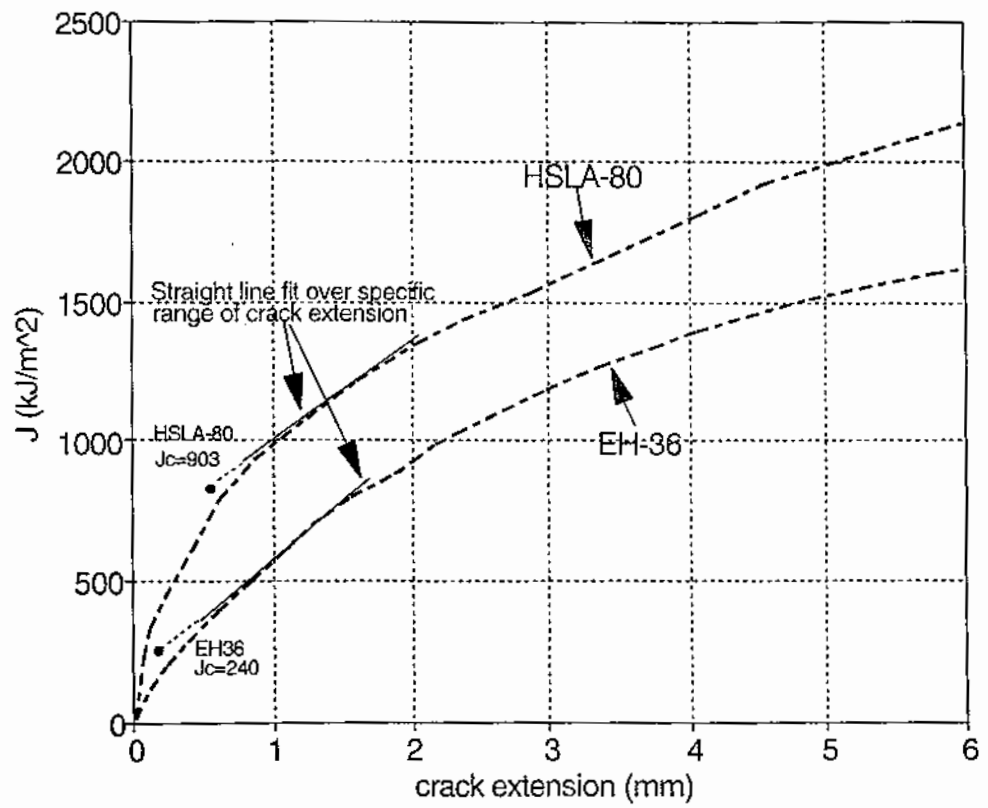


Figure 3.7 Typical J-R curves from 50 mm C(T) specimens (9 mm thick) for the HSLA-80 and EH-36 materials

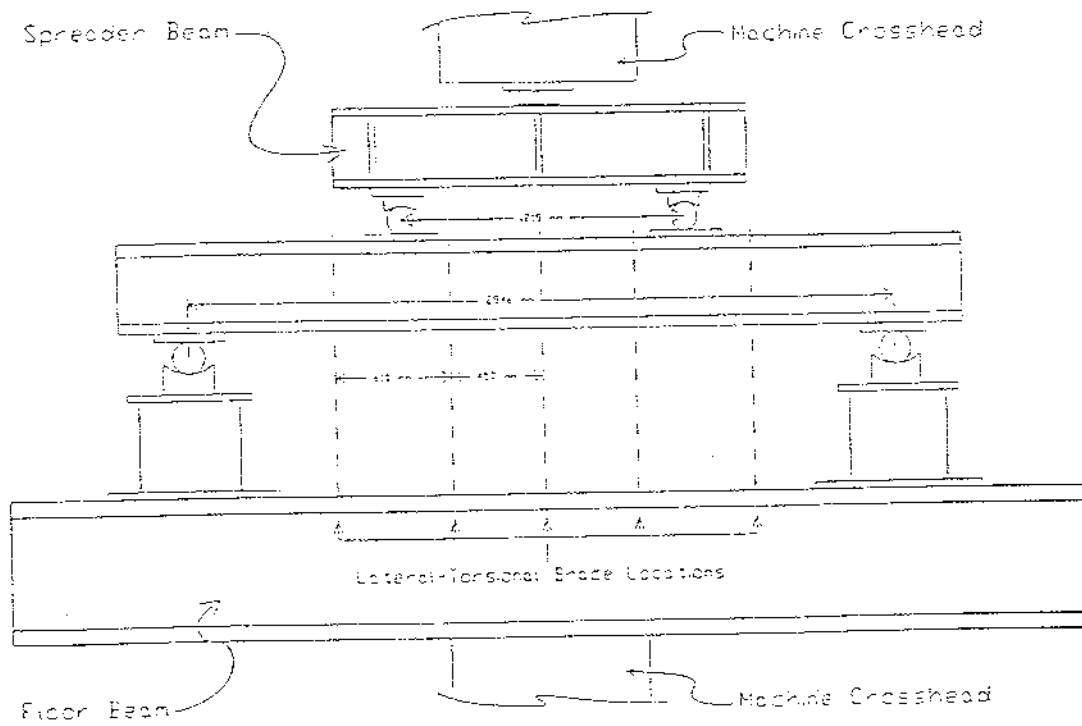
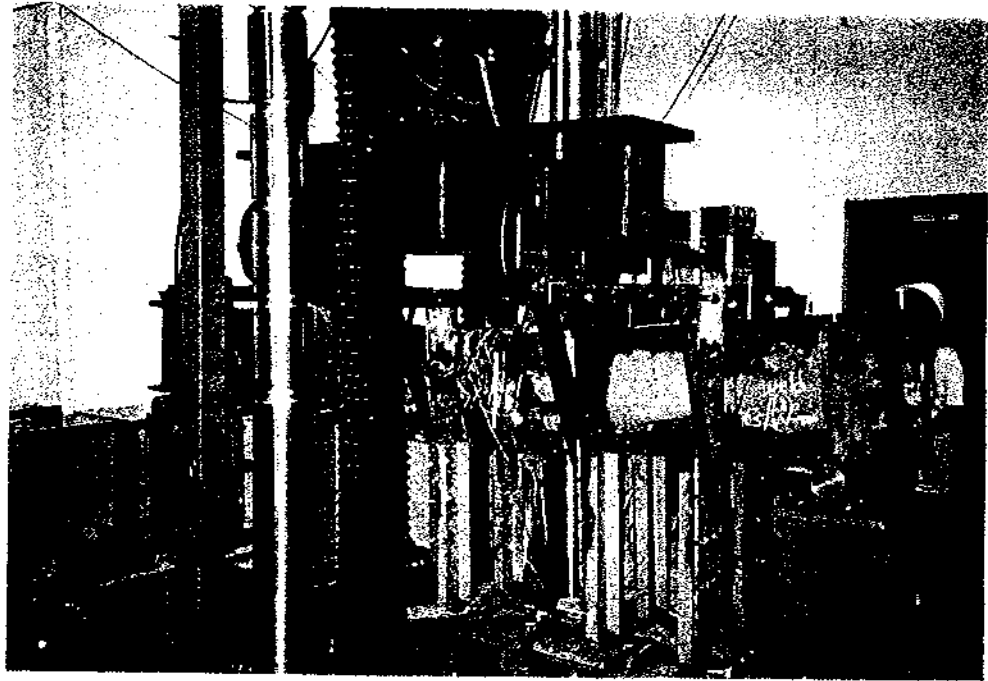
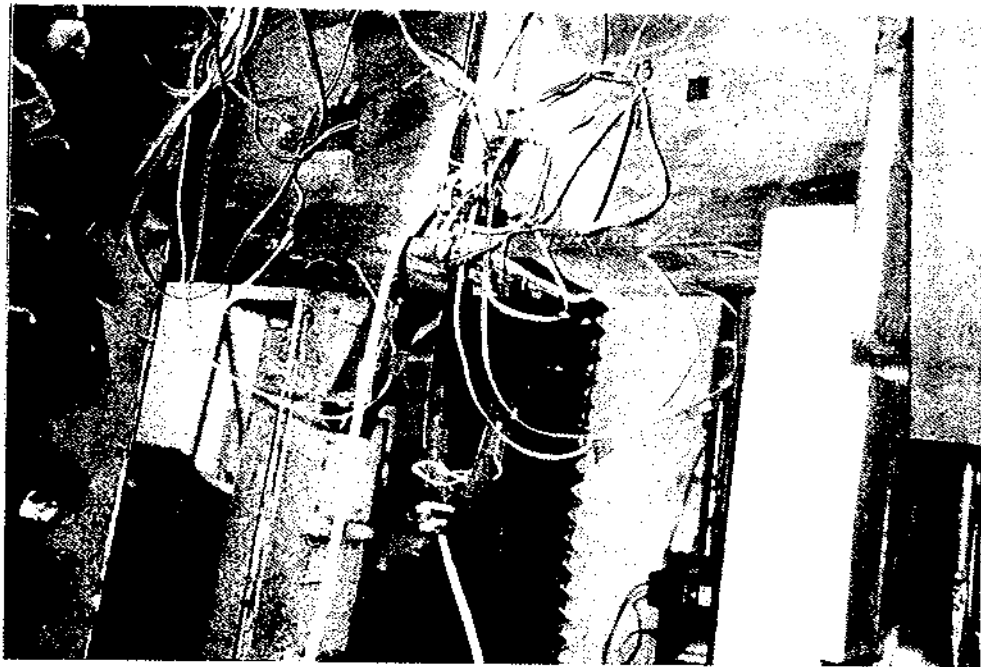


Figure 3.8 Four-point bending fixture used to test I-beam specimens. The fixture was loaded using a 2700 kN capacity hydraulic testing machine



(a)



(b)

Figure 3.9

Photographs of I-beam tests showing overall test setup (a) with strain gage and clip gage instrumentation (b)

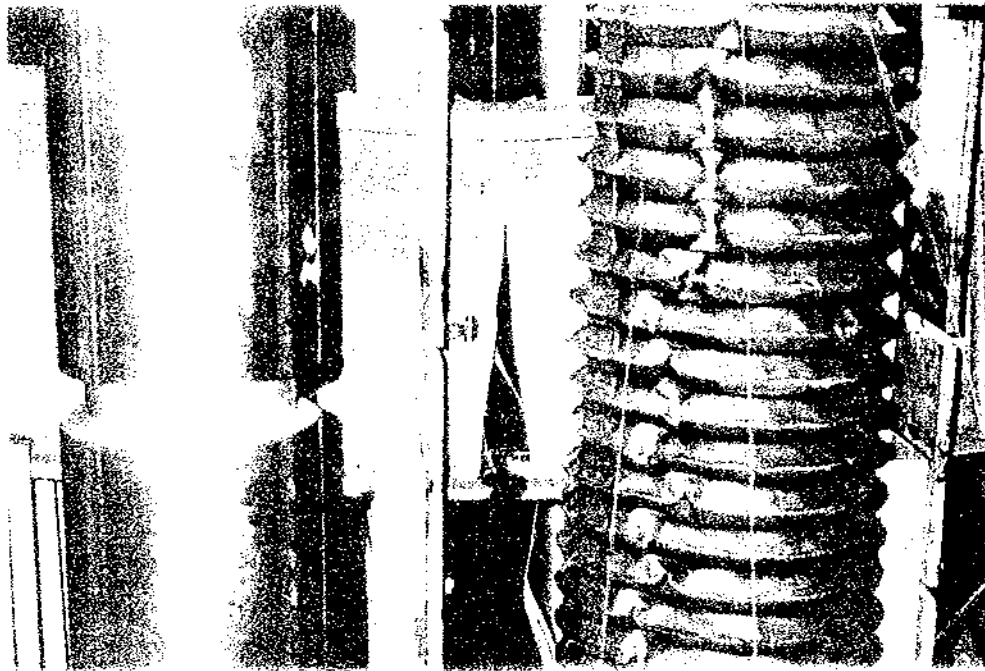


Figure 3.10

Typical I-beam specimen at the end of the test with the crack extended almost to the compression flange

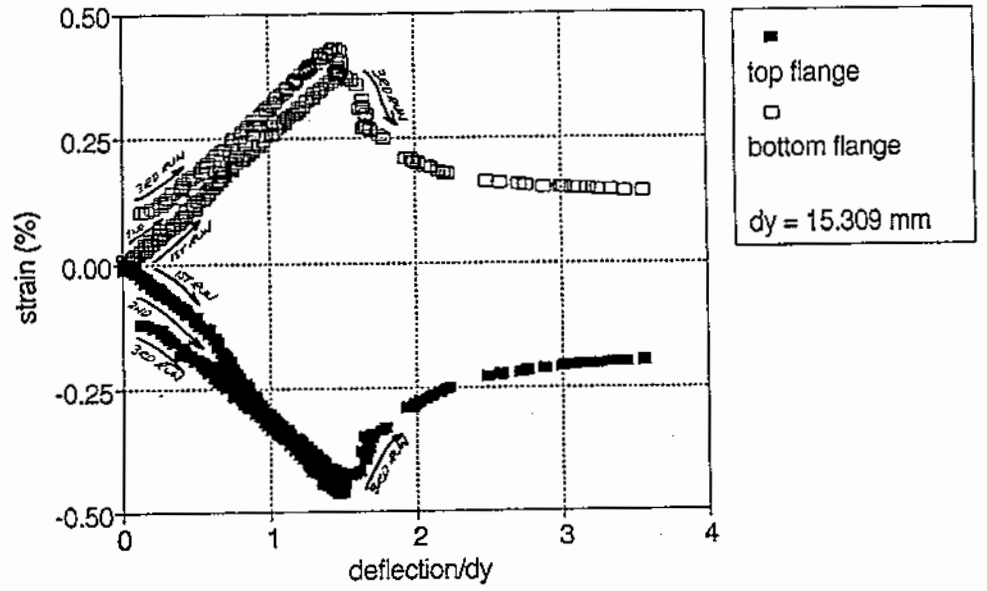


Figure 3.11

Top (compression) and bottom (tension) flange strain vs. centerline deflection normalized by yield deflection. Strain values were obtained by the average of two strain gages located on the top and bottom flanges at midspan.

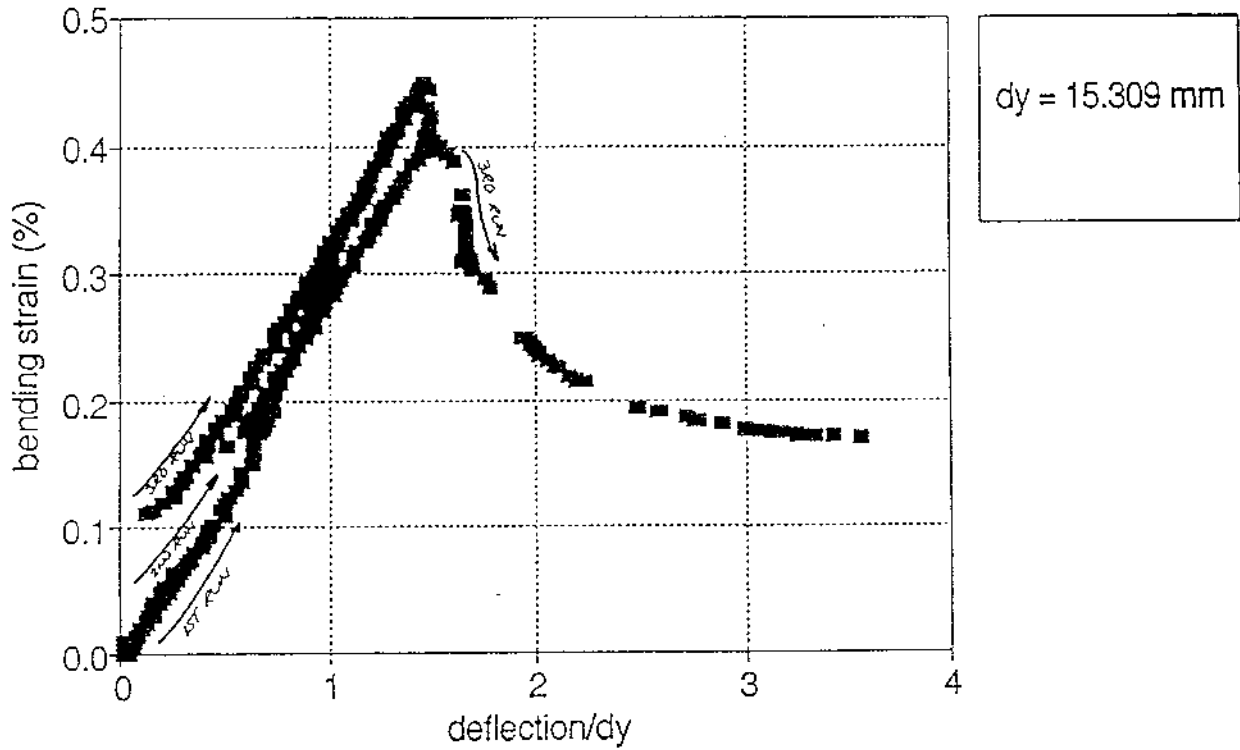


Figure 3.12 Average bending strain vs deflection normalized by yield deflection. Values were obtained by averaging the strain magnitude from the gages on the top and bottom flanges

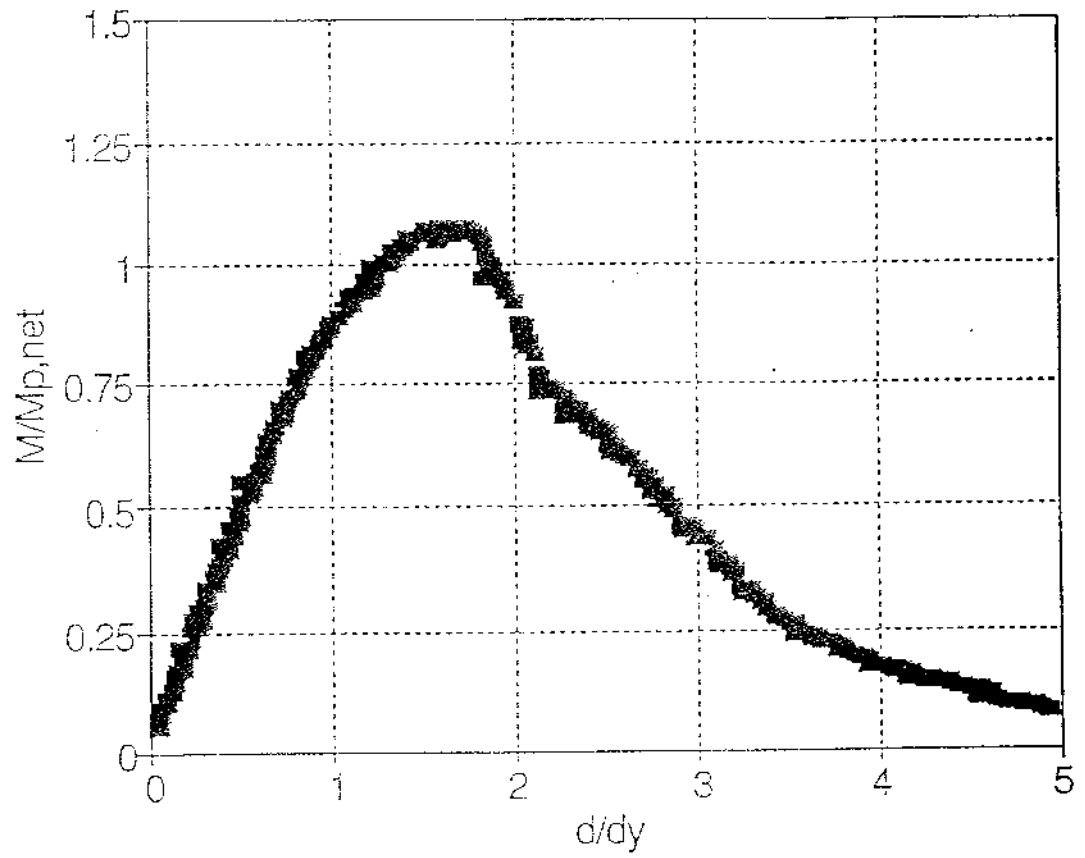


Figure 3.13 Load-deflection curve for I-beam specimen A18. Applied moment is normalized by $M_{p,net} = 349$ kN.m. Deflection is normalized by $d_y = 11.9$ mm.

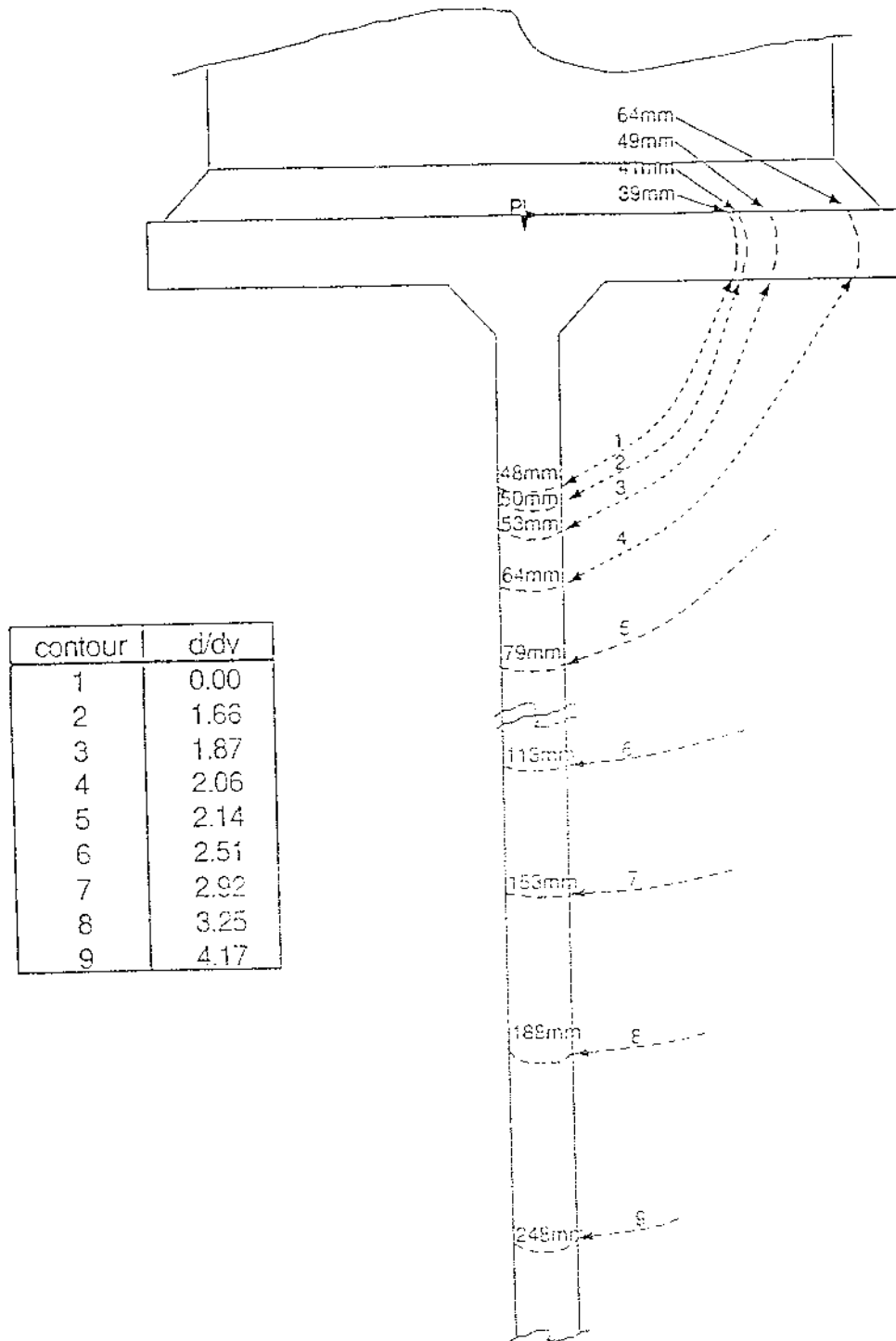


Figure 3.14 Crack size measurements recorded during test of I-beam specimen A18. Crack lengths are measured from point P. Values of d/d_y associated with each crack position (contour) are shown in the table.

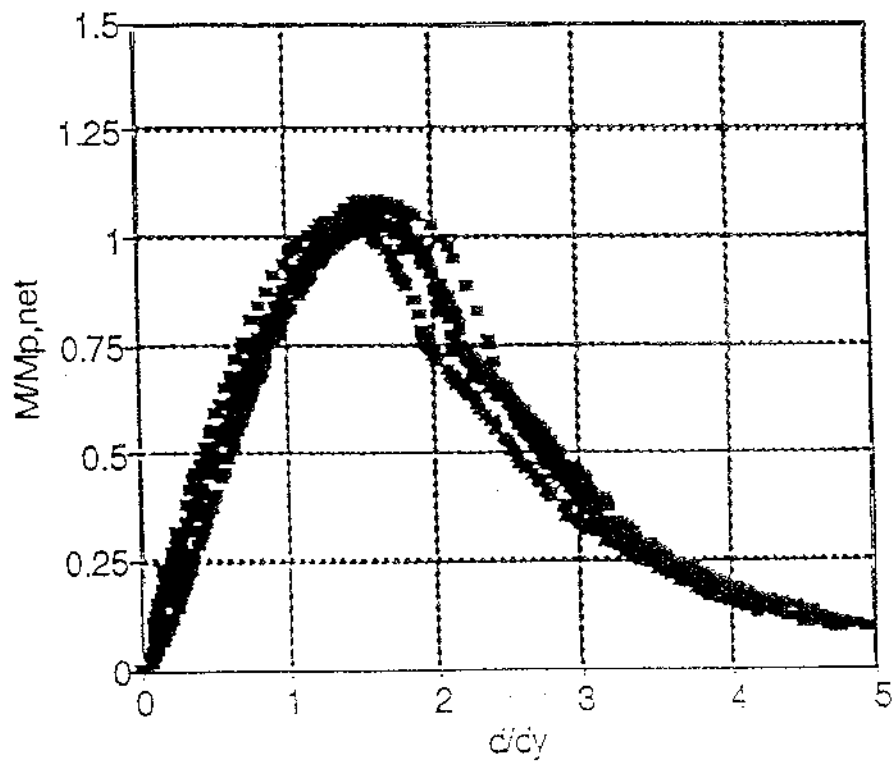
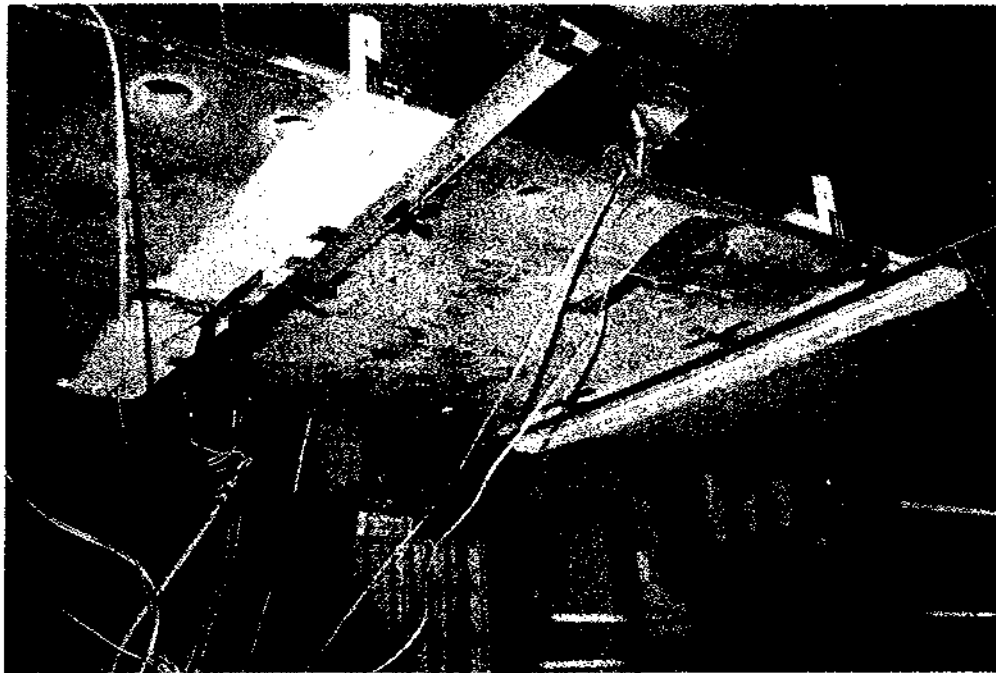


Figure 3.15 Combined normalized load-displacement curves for specimens A42, A39, A48, and A18 with a wide range of initial crack sizes



(a)



(b)

Figure 3.16 Photographs of box-beam tests showing overall test setup (a) with strain gage and clip gage instrumentation (b)

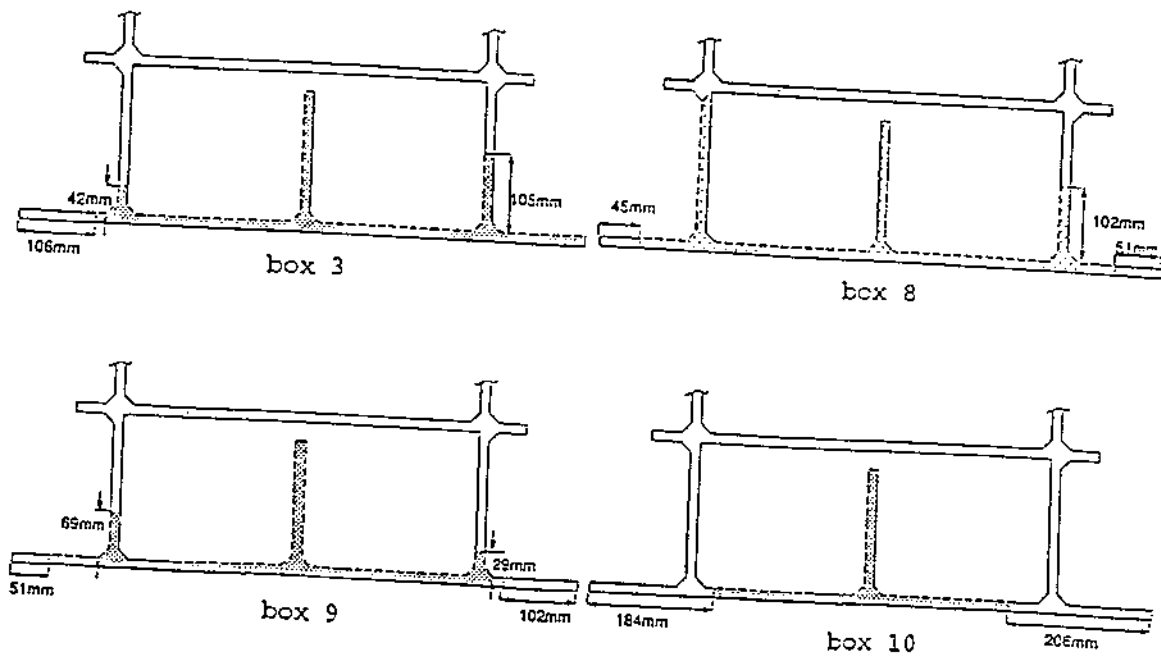


Figure 3.17 Precrack geometries for the box-beam specimens

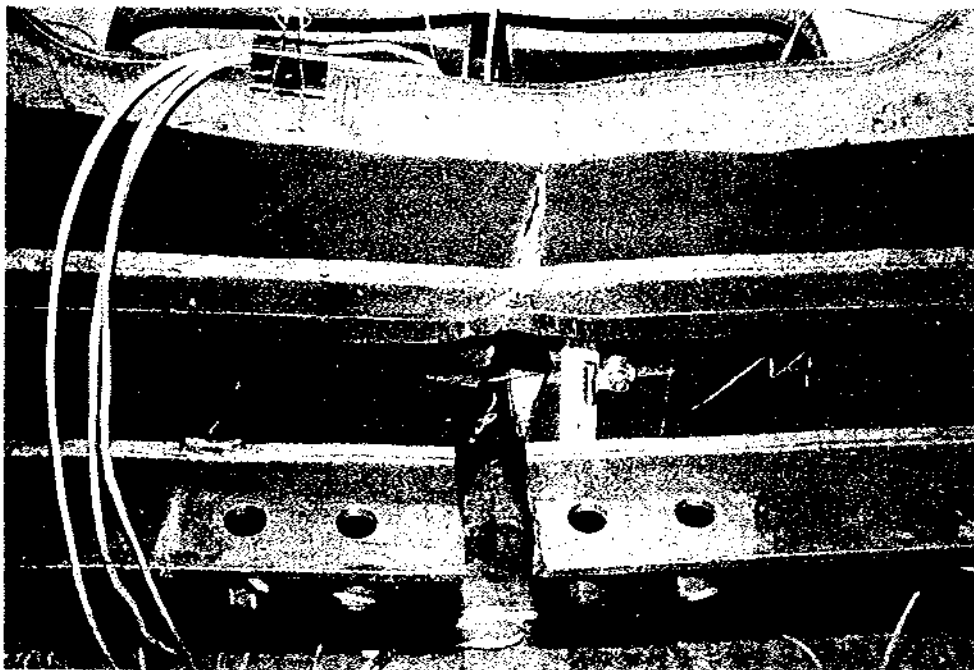


Figure 3.18 Typical box-beam specimen at the end of the test after the crack burst through the middle flange

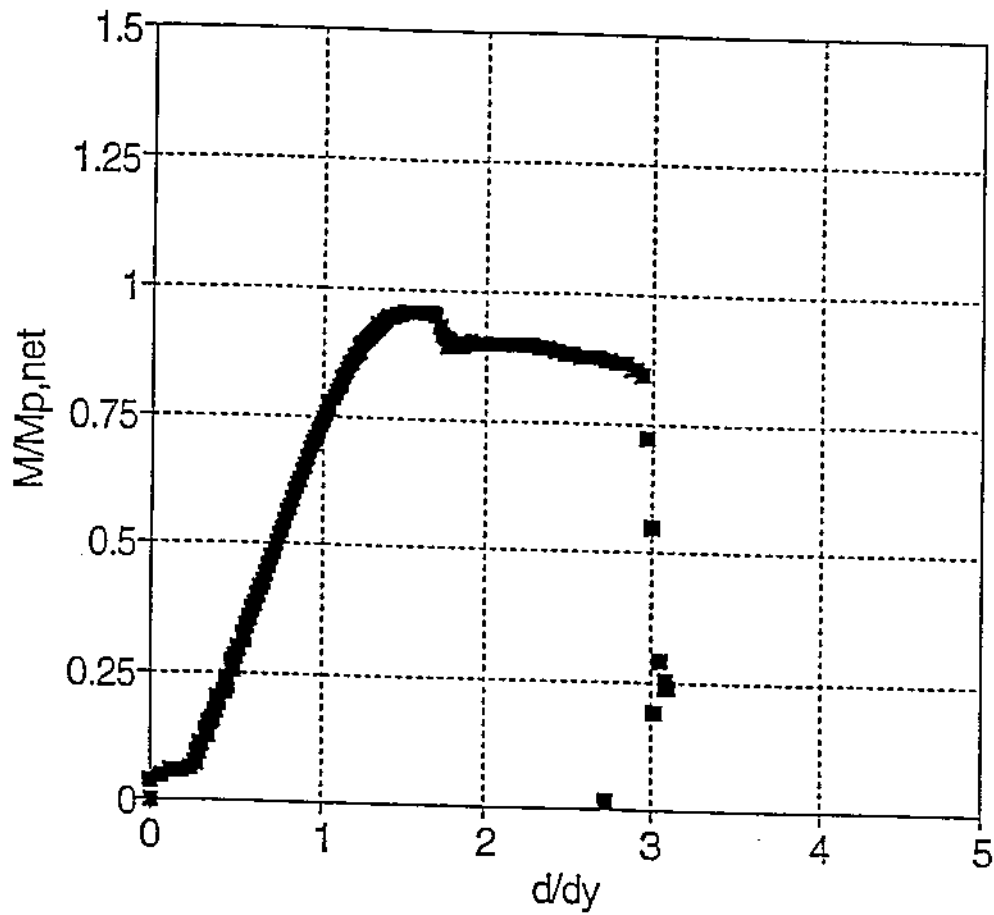
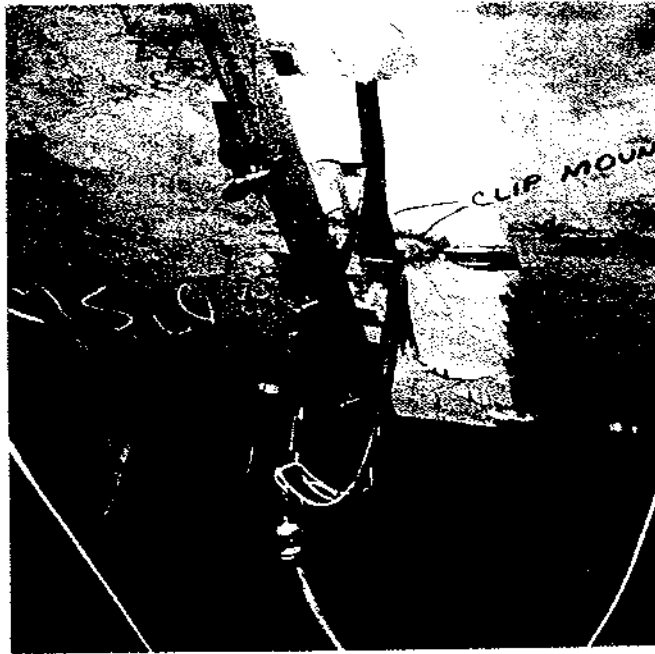


Figure 3.19 Load-deflection curve for box-beam specimen 3. Applied moment is normalized by $M_{p,net} = 6857$ kN.m. Deflection is normalized by $d_y = 38.3$ mm.



(a)



(b)

Figure 3.20 Photograph of box-beam specimen 10 showing local buckling of the compression flange (a) and the crack opening at maximum load (b)

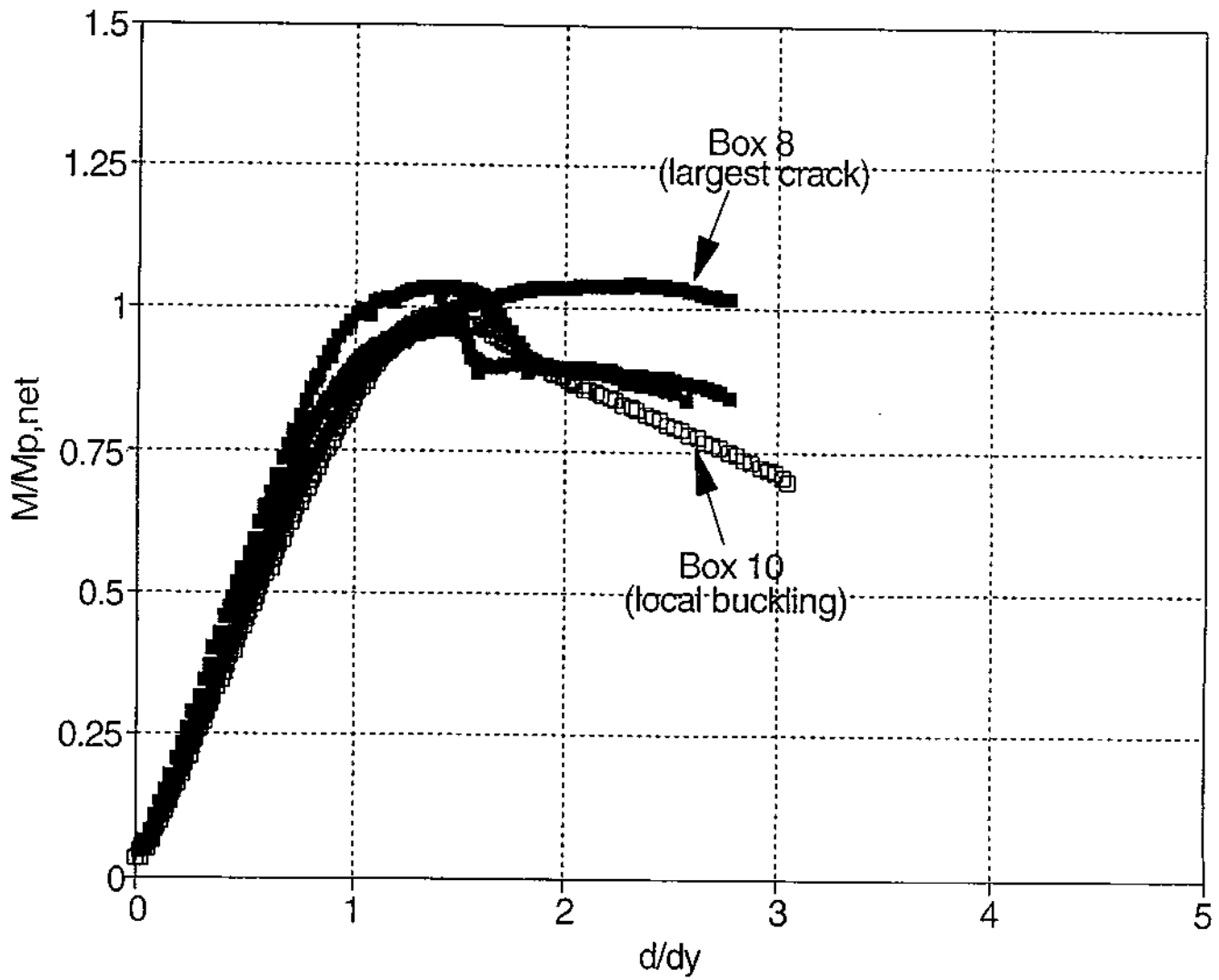
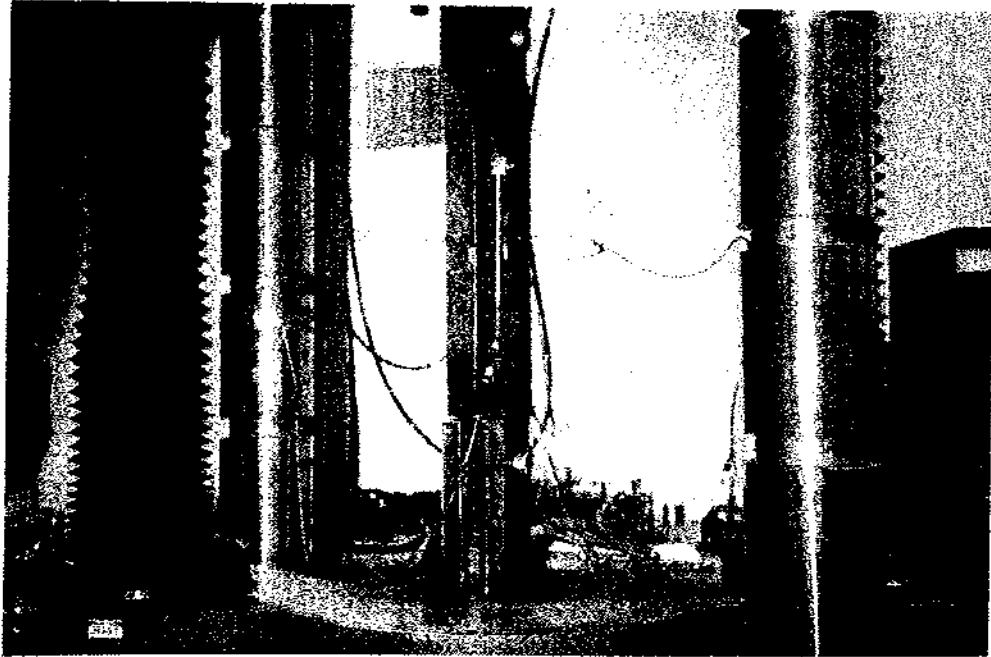
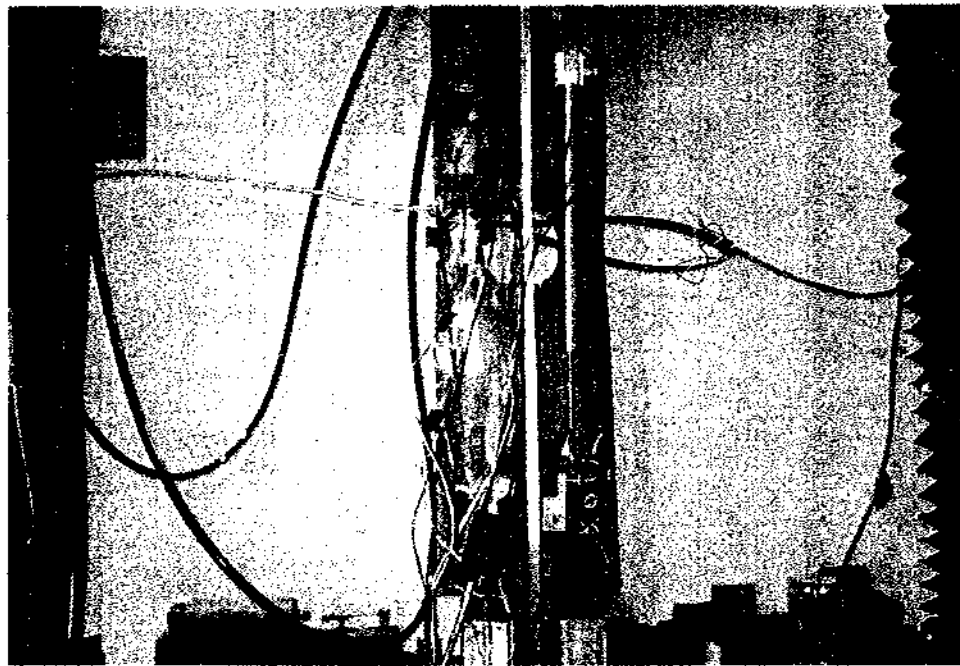


Figure 3.21 Combined normalized load-displacement curves for all 4 box beam specimens. Box-beam 10 experienced local buckling in the compression flange and is shown as empty squares



(a)



(b)

Figure 3.22 Photographs of tension tests on stiffened center cracked panels (cope-hole specimens) showing overall test setup (a) and strain gage, clip gage, and LVDT positions (b)

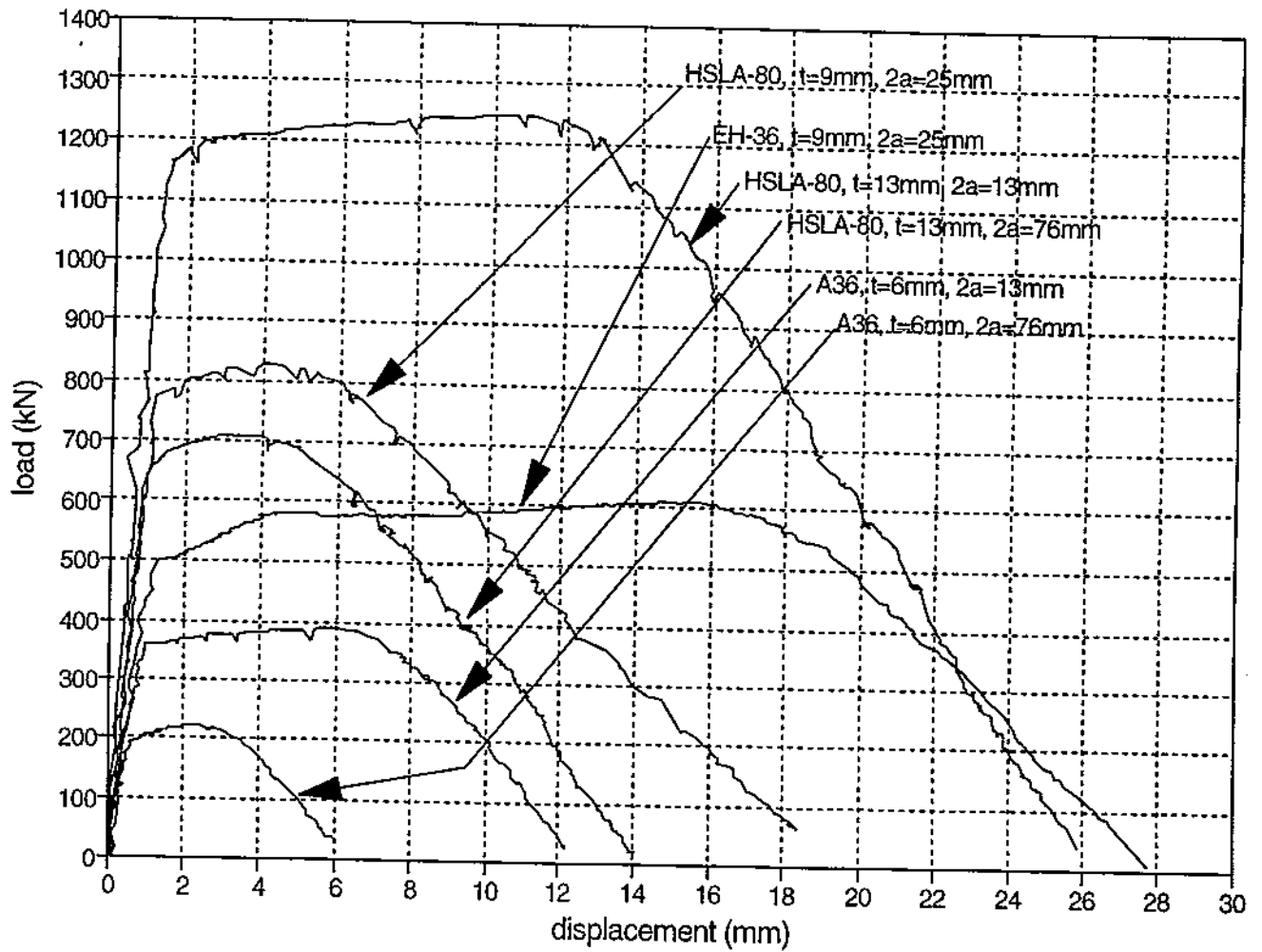
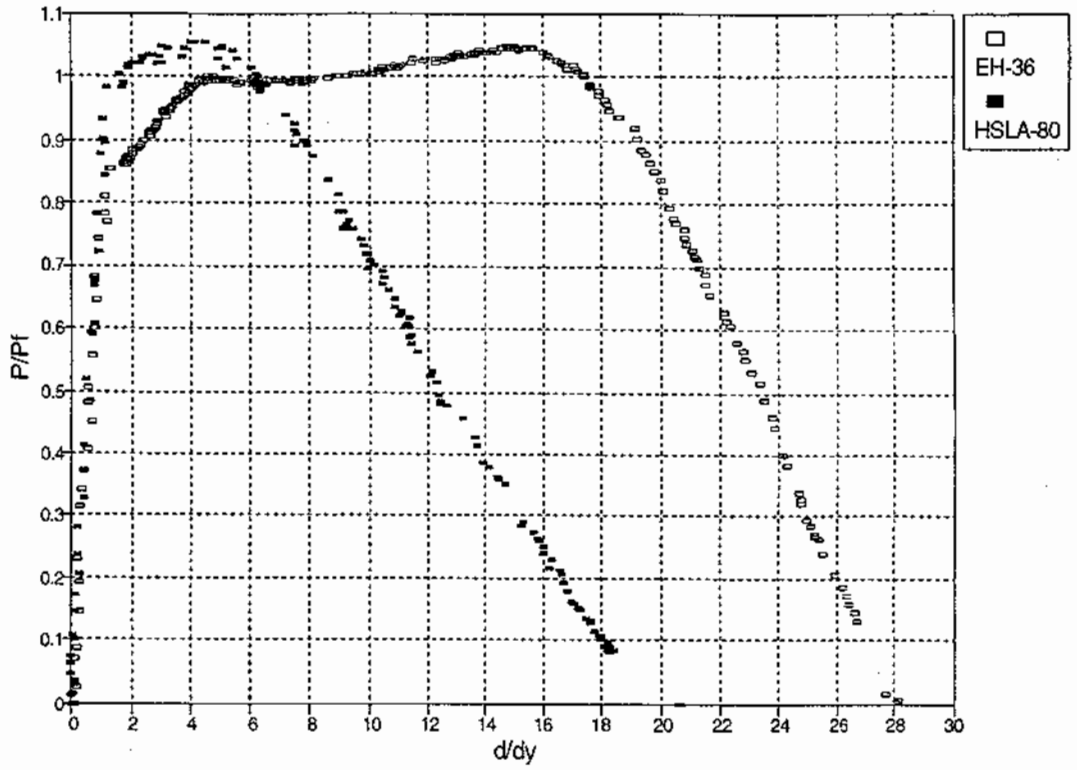
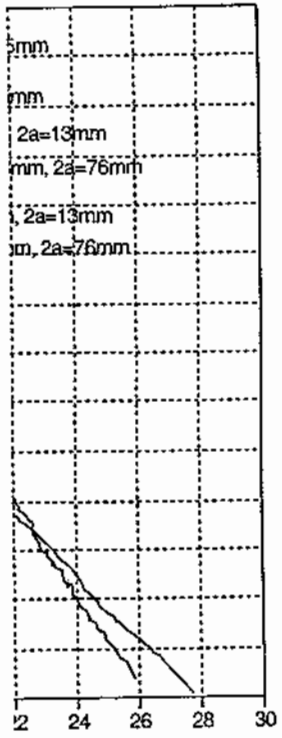


Figure 3.23

Experimental load-deflection curves for the CCT specimens. Displacement was measured over a 460 mm gage length. The 9 mm thick HSLA-80 and EH-36 specimens were used for comparison with the cope hole specimens.



specimens. Displacement
mm thick HSLA-80 and
mm cope hole specimens.

Figure 3.24

Experimental load-deflection curves for the HSLA-80 and EH-36
CCT specimens normalized by their collapse loads and yield
deflections

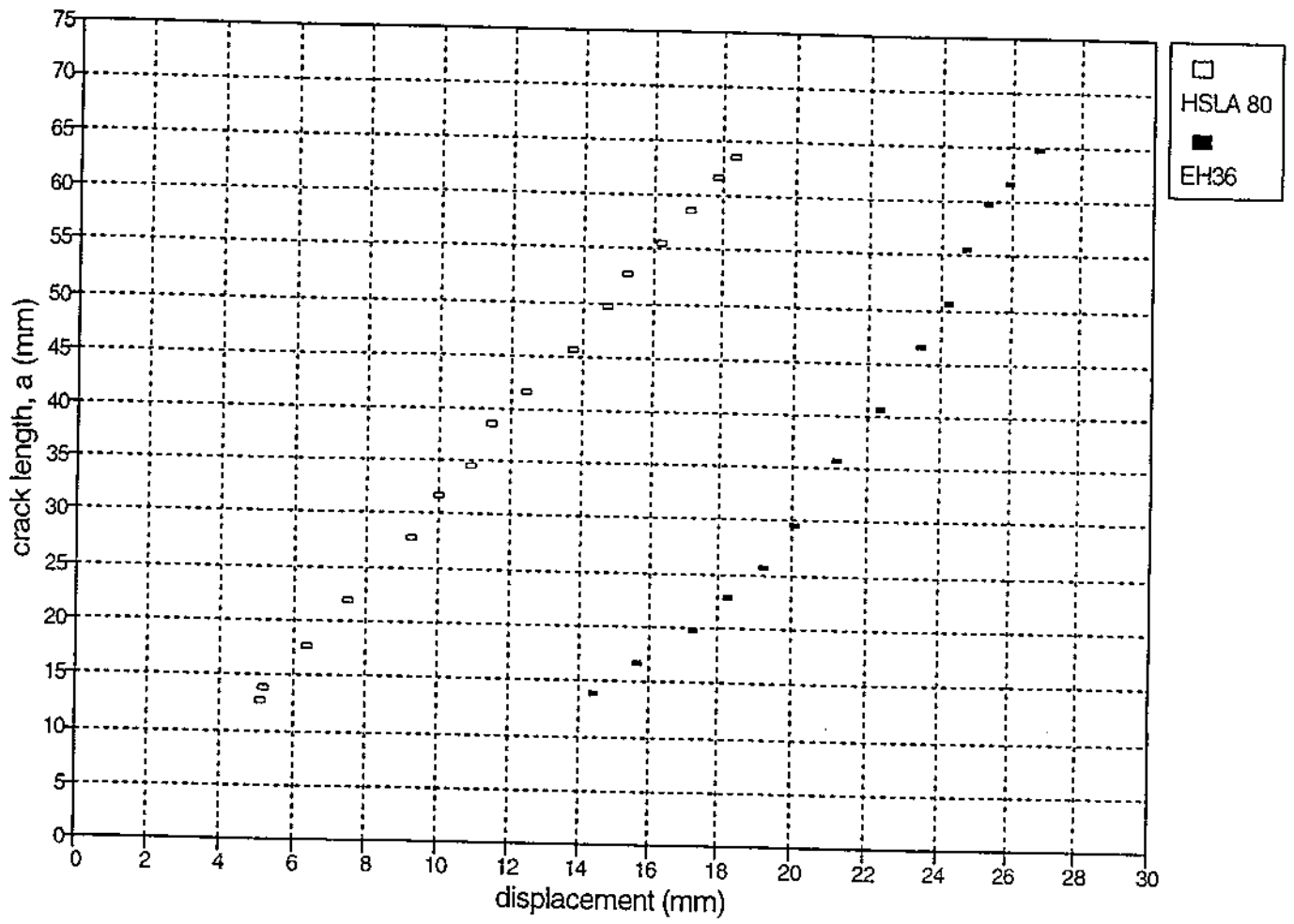


Figure 3.25 Experimental crack length-displacement data for the HSLA-80 and EH-36 CCT specimens

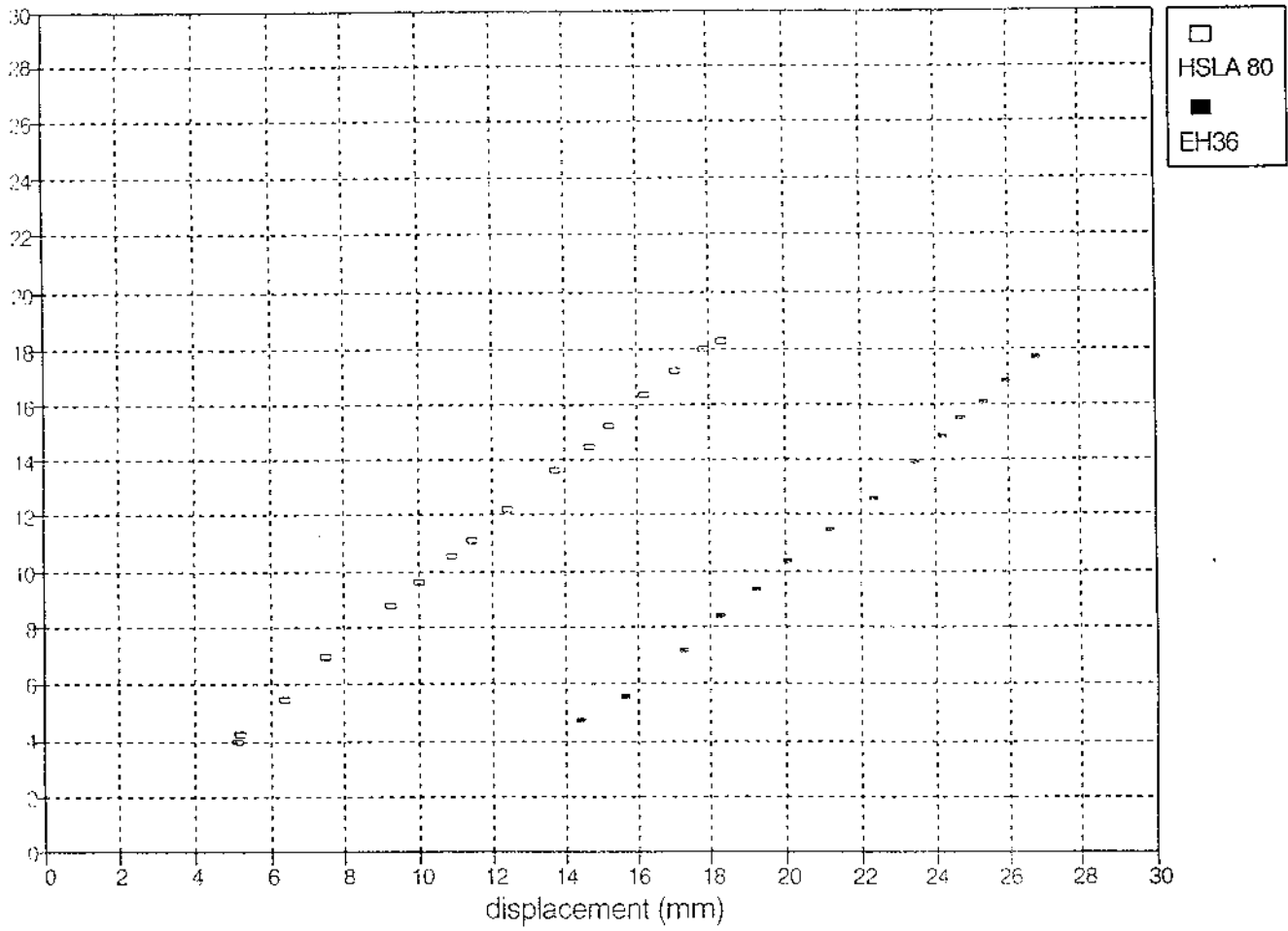


Figure 3.26 Experimental COD-displacement data for the HSLA-80 and EH-36 CCT specimens

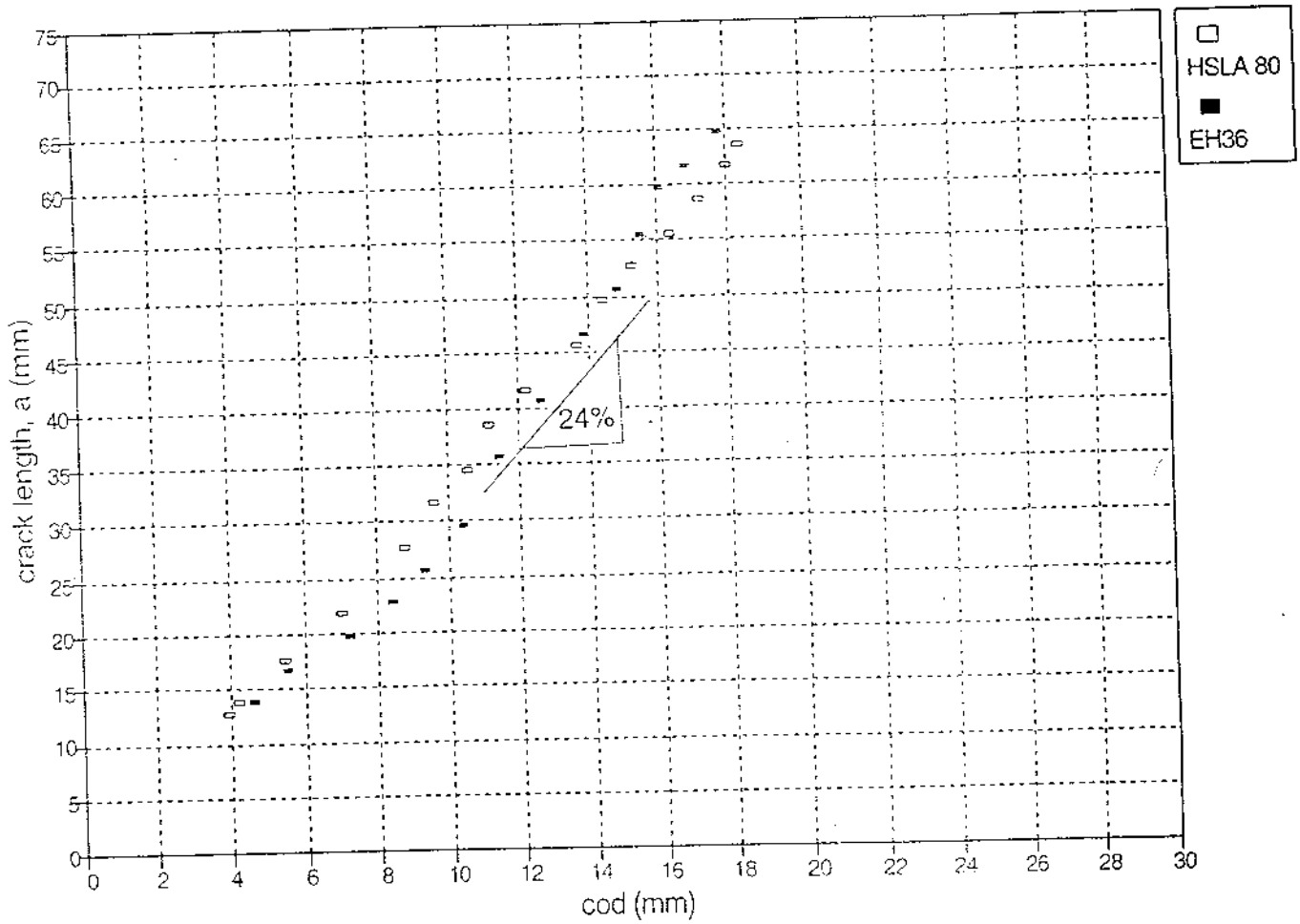


Figure 3.27 Experimental crack length data as a function of COD for the HSLA-80 and EH-36 CCT specimens. The linear slope of the data represents a crack opening angle (COA) of 24% radian

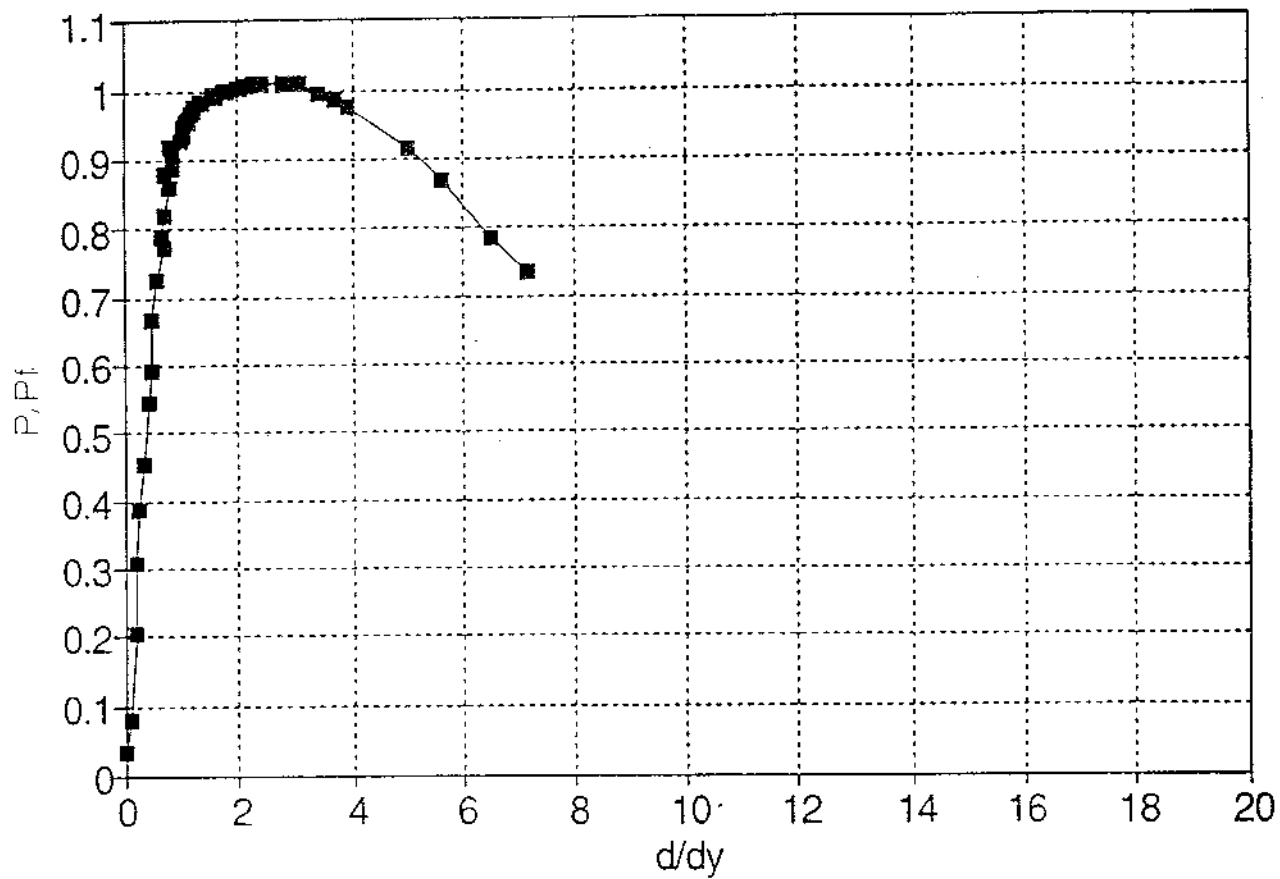


Figure 3.28 Load-deflection curve for cope-hole specimen HSLA-80 #3. Applied load is normalized by $P_f = 1176$ kN. Deflection is normalized by $d_y = 1.34$ mm

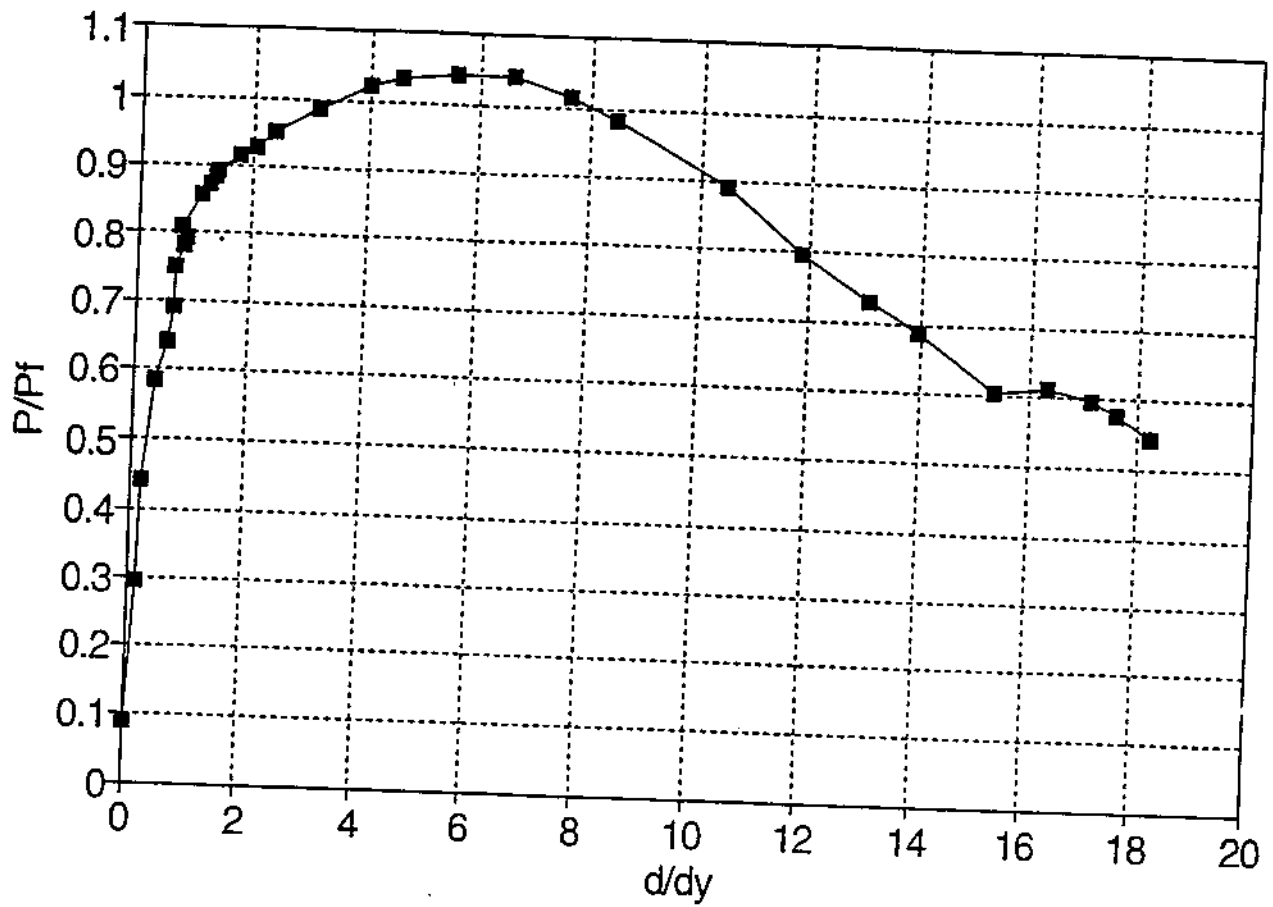


Figure 3.29

Load-deflection curve for cope-hole specimen EH-36 #3. Applied load is normalized by $P_r = 878$ kN. Deflection is normalized by $d_y = 0.91$ mm

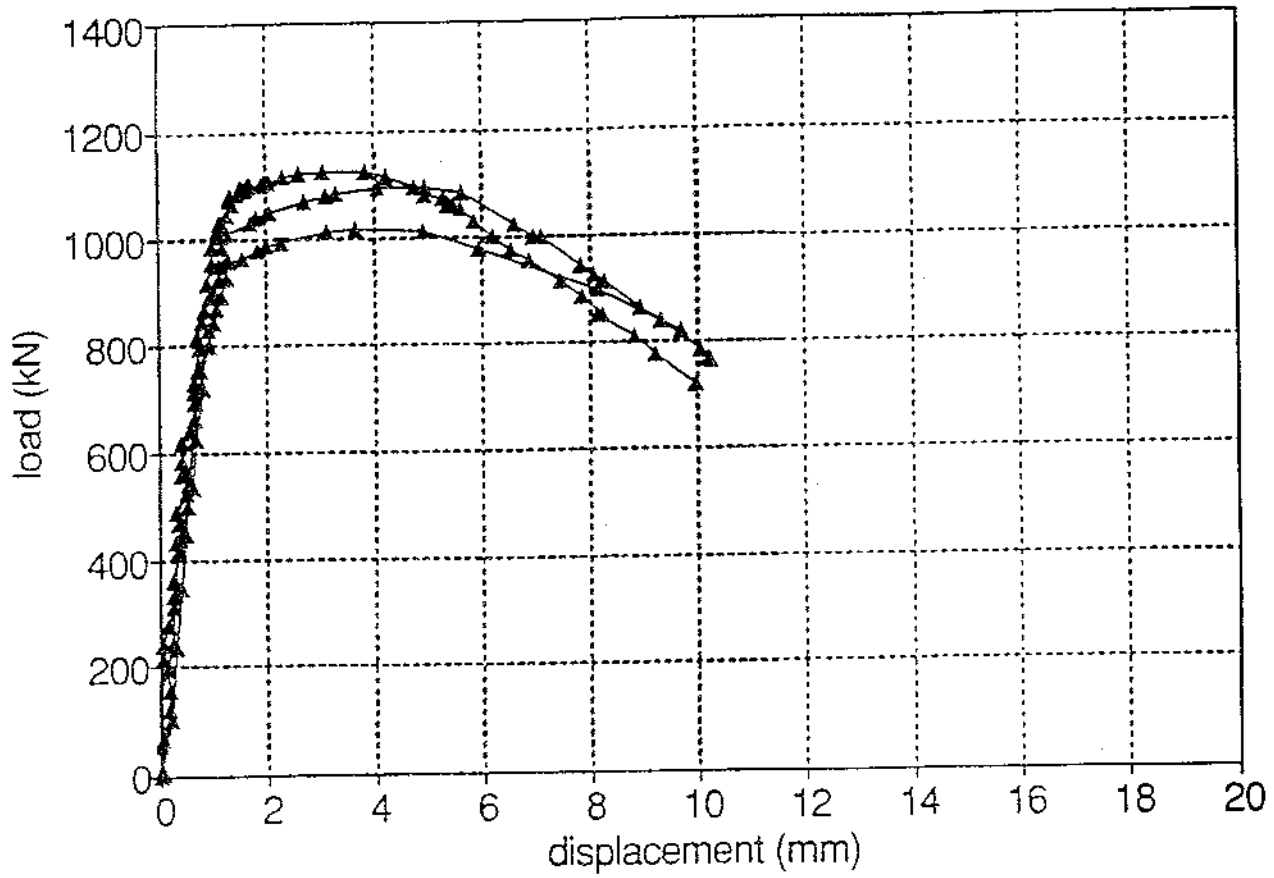
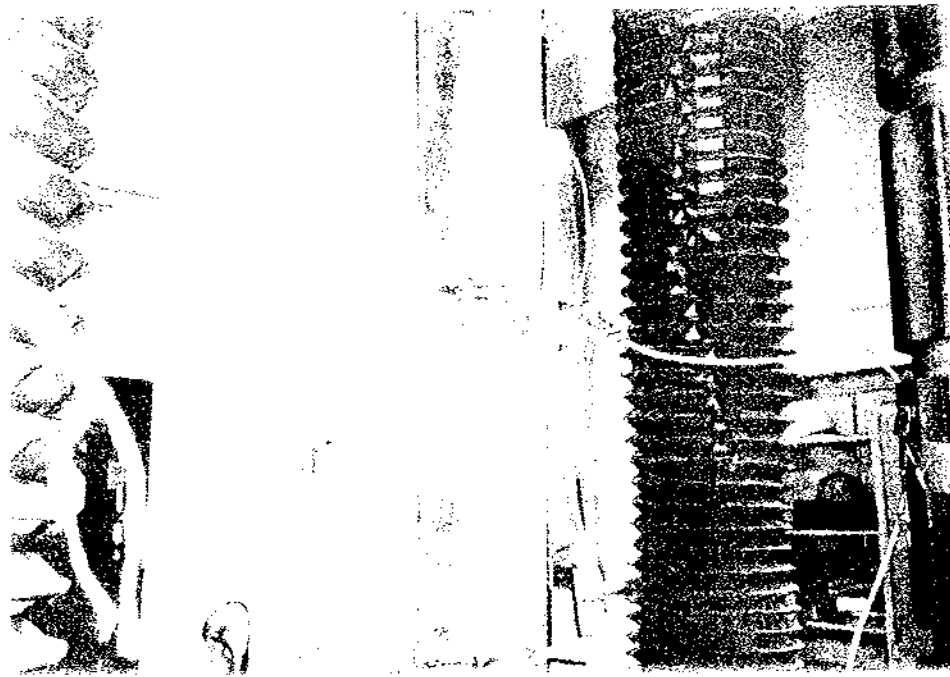


Figure 3.30

Combined load-deflection curves from HSLA-80 cope-hole specimens #4, #5, and #6 showing variability among replicate specimens



(a)



(b)

Figure 3.31

Photographs of EH-36 (a) and HSLA-80 (b) cope-hole specimens after testing. Note that the crack in the EH-36 specimen was able to extend the entire width of the baseplate without fracturing the stiffeners. The stiffeners on the HSLA-80 specimen fractured before the crack could extend the entire width of the baseplate.

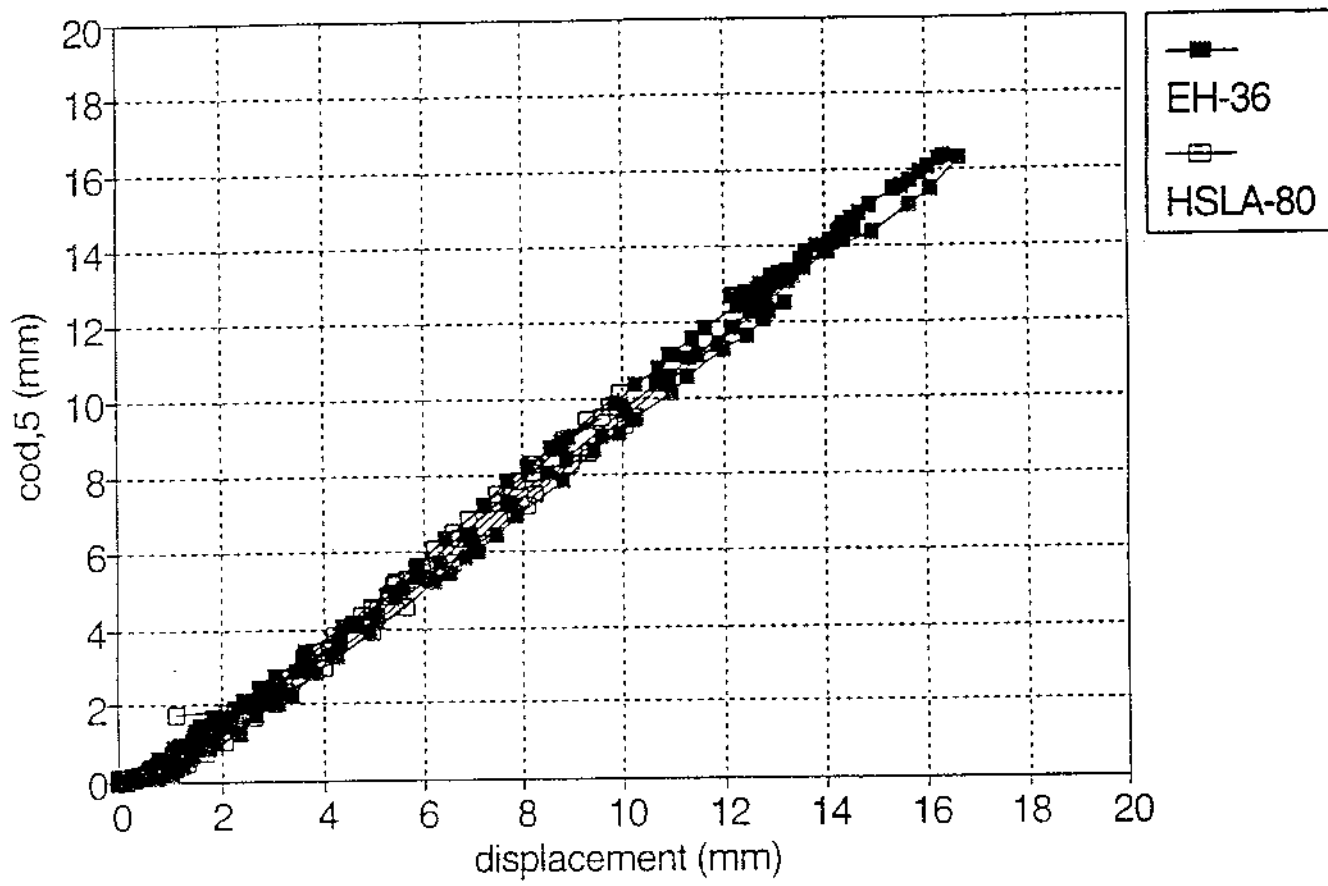


Figure 3.32 CTOD₅ plotted vs. displacement for all cope-hole specimens with symmetrical stiffeners showing that essentially all the displacement is coming from the crack plane for both materials and crack lengths

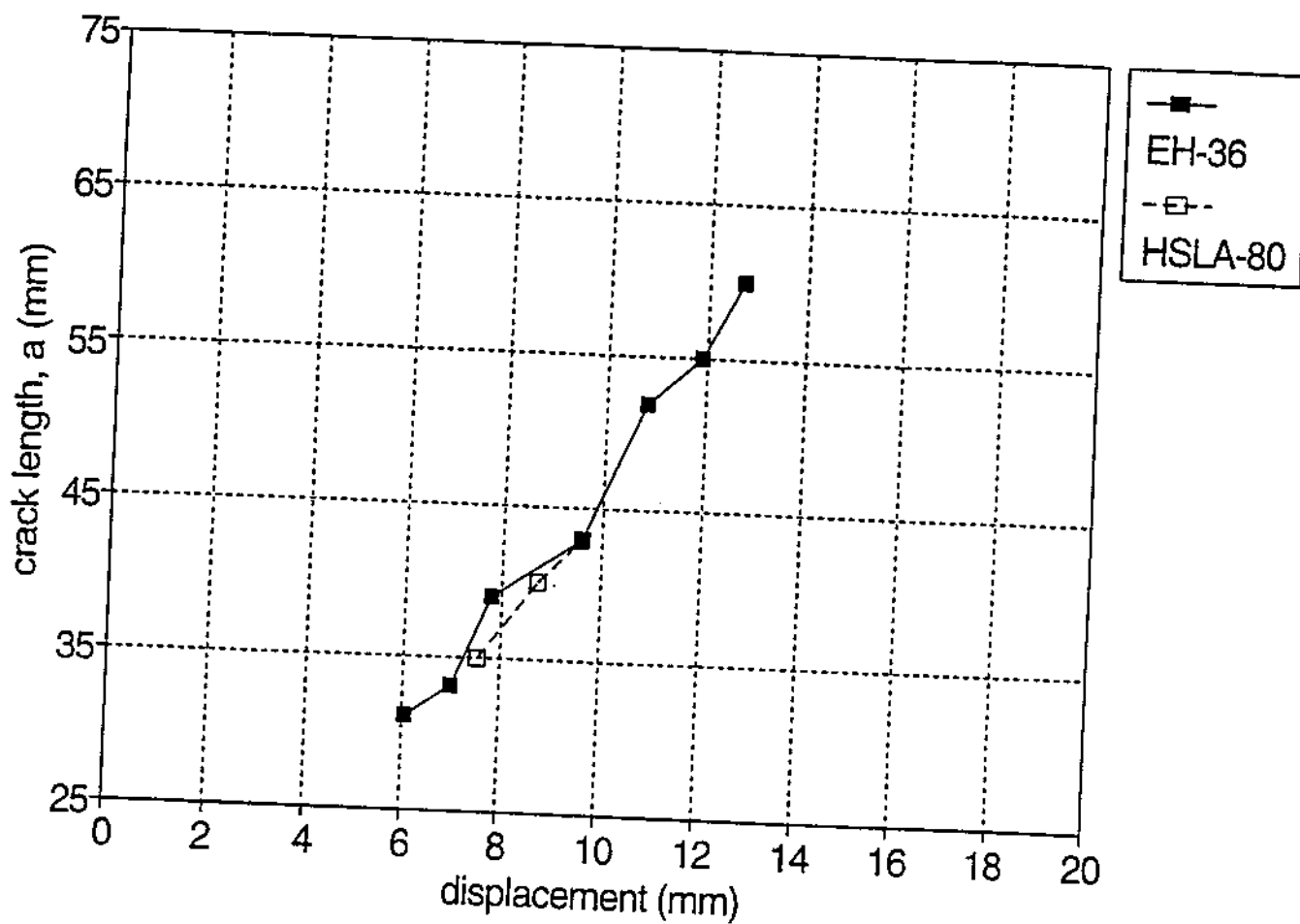


Figure 3.33 Crack length vs. displacement relationship for EH-36 and HSLA-80 cope-hole specimens with initial crack sizes of 50 mm

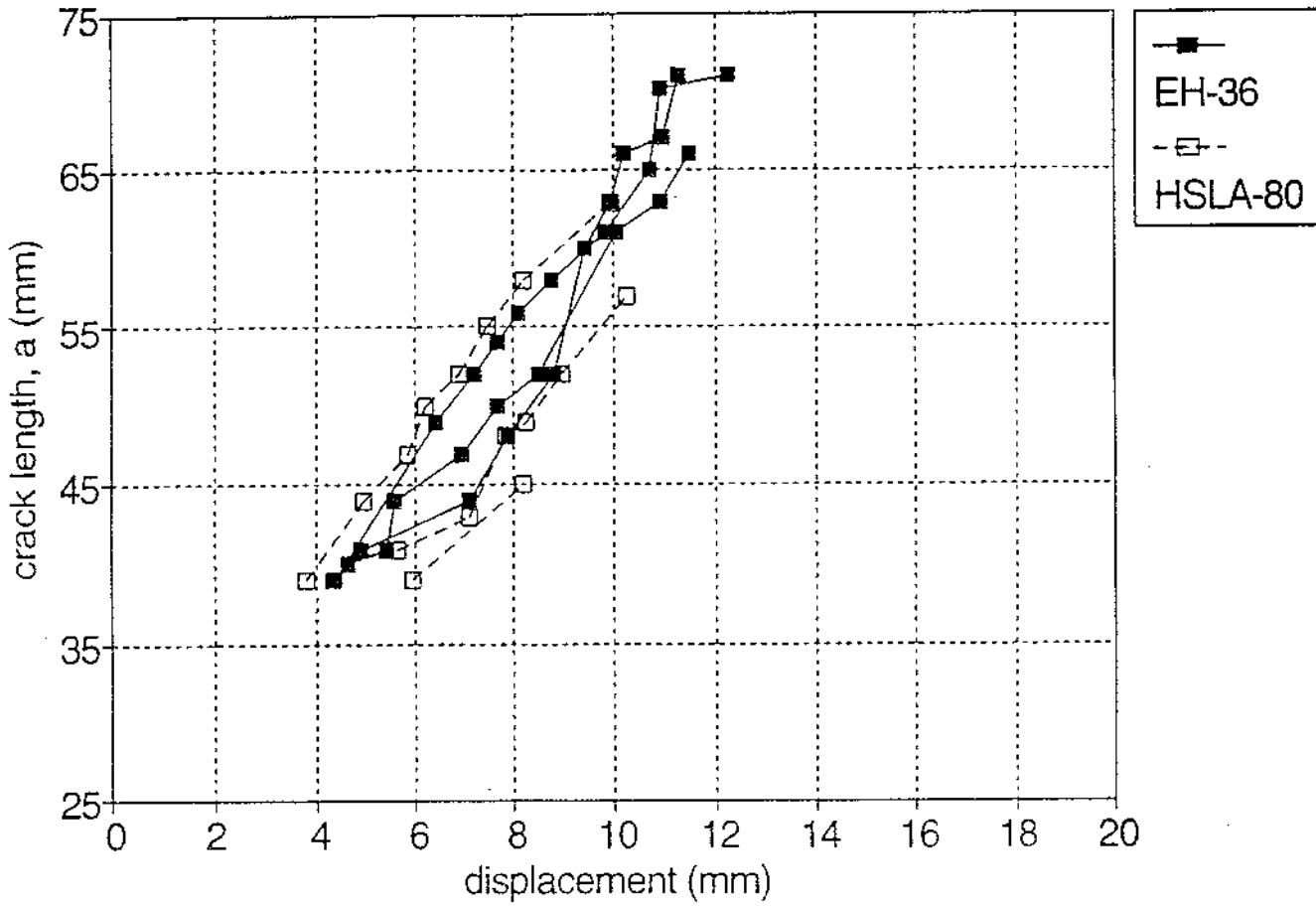


Figure 3.34 Crack length vs. displacement relationship for EH-36 and HSLA-80 cope-hole specimens with initial crack sizes of 76 mm

4.0 ANALYSES OF EXPERIMENTS

A variety of ductile-fracture models were evaluated for their ease of use, range of applicability, and accuracy. Among the ductile fracture models evaluated were the various levels of analysis of British Standards Institution published document PD 6493:1991: "Guidance on the Methods for Assessing the Acceptability of Flaws in Fusion Welded Structures". PD 6493 allows the fracture toughness to be defined as K_{Ic} , CTOD, or J_c . Thus any test method or ductile-fracture parameter can be used in conjunction with PD 6493. This document incorporates what was previously referred to as the "CTOD design curve" and the "CEGB R6 method" [4.1]. The CEGB R6 method continues as a document specifically suited to assessment of pressure vessels [4.2], but the general aspects of the R6 method have been incorporated into PD 6493. The unique aspects of the R6 method and the ASME Boiler and Pressure Vessel Code, methods which are suited specifically for pressure vessels, are not applicable to ductile fracture in relatively thin plates (i.e. less than 51 mm thick) and will therefore not be reviewed here.

The accuracy of the ductile-fracture models was evaluated by attempting to predict the results of the experiments described in the previous section. In addition to the basic ductile-fracture models, there are significant issues that are separable from and germane to all fracture models, e.g. how to deal with residual stress, stress concentrations, etc. As discussed in this section, several assumptions must be made with regarding these issues in order to get accurate predictions. The original predictions of the first few tests, based on strict interpretation of PD 6493, were conservative by up to 60 percent. Results that are not very accurate, but are at least conservative, may be the best that can be expected if predictions are made about structures which are significantly different than the knowledge base behind the assessment procedures. This level of accuracy would have been obtained on all the experiments if all the predictions had been made before any of the experiments. This is a good example of why such extrapolations from the knowledge base should never be made without some full-scale testing for validation.

It turns out that most of the error was attributable to the assumptions regarding germane issues such as residual stress. It is concluded that these assumptions have a much larger effect on the accuracy of the predictions than the choice of ductile fracture model. The assumptions and procedures were fine tuned after two or three experiments. The revised assumptions are justifiable and may even have been immediately apparent to a more experienced analyst. When these same assumptions were consistently applied to subsequent experiments, good pre-test predictions were obtained. It is concluded that these assumptions are sufficiently well validated that they can now be applied generally to ship structure that is similar to the structural elements that were tested. Guidelines are summarized in Section 5 that are based on these revised assumptions and procedures, along with recommended ductile fracture model.

Therefore, the "pre-test" predictions reported in this section were influenced by the fine-tuning that took place in the first few experiments. The accuracy of these predictions is much better than the accuracy that could be expected had no experiments been done. Also, the actual crack size (determined after fracturing) is not always consistent with the originally-postulated crack size (determined by dye-penetrant testing). Therefore, some inaccuracy in the pre-test predictions was due to error in the estimated crack size. Therefore, "postdictions" (after the tests, using actual crack sizes) are more useful for evaluating the relative accuracy of ductile fracture models.

The PD 6493 procedures are well thought out, widely applicable, and sufficiently accurate given the set of assumptions which was developed for application to ship structural members. However, the PD 6493 procedures will give an estimate of the failure load or stress, and are not intended for predicting the descending branch of the load displacement curve and the associated ductility. In those cases where the load-displacement curve must be predicted, additional techniques can be used.

Predicting the load-displacement curve can be broken down into two separable tasks. First, the crack-extension history must be predicted (as a function of applied displacement) and then the load at each displacement level can be computed based on the crack size at that displacement level. In order to predict crack extension, J-R curve analyses were performed as well as simple kinematic models such as a constant crack-opening angle. As discussed in the previous section, after some initial crack propagation, the measured crack-opening angle in the large-scale experiments was relatively constant for both types of steel and for each type of test specimen.

Note that a constant crack-opening angle is the same as a constant tearing modulus or slope of the J-R curve [4.3]. An assumption must eventually be made regarding the J-R curve at large crack extension beyond the capacity of the small compact specimens. For example, in the predictions described below, it was assumed that the J-R curve had a constant tearing modulus for large crack extension based on a line fit to an extended J-R curve plotted out to 15 mm of crack extension.

For the J-R curve approach, the applied J in the experiments was calculated using finite-element analysis as well as several estimation schemes, including the "EPRI-GE Handbook" [4.4-4.7], the GKSS "Engineering Treatment Model" [4.8,4.9], and other reference stress approaches [4.10].

Given a crack extension history, predicting the load turns out to be relatively straightforward. For these high-toughness steels, the load is always the limit load for the cracked section, which can be calculated using simple hand calculations. Finite-element analyses and Landes' normalization method [4.11-4.12] were also evaluated as ways to calculate the load history given the crack extension history.

4.1 PD 6493 calculations

The wide acceptance of fracture mechanics assessment has been facilitated by the British Standards Institution published document PD 6493: "Guidance on the Methods for Assessing the Acceptability of Flaws in Fusion Welded Structures". PD 6493 was first published in 1980 and incorporated the CTOD design curve as the fracture model which included both brittle and ductile fracture modes. The equation for the CTOD design curve, for $\varepsilon_f / \varepsilon_y > 0.5$, is:

$$\frac{CTOD}{2\pi \varepsilon_y a} = \frac{\varepsilon_f}{\varepsilon_y} - 0.25 \quad (4-1)$$

where: ε_f is the failure strain corresponding to ductile fracture;
 ε_y is the yield strain;
CTOD is the fracture toughness;
and, a is a through thickness crack length or an equivalent crack length.

The definition of "failure strain" in the original PD6493 corresponded to the nominal overall-gage-length strain at rupture in wide-plate tests conducted under displacement control. In this context, the initiation of ductile crack extension may occur prior to failure. PD 6493 was relatively easy to use and provided extensive guidance on how to idealize irregularly-shaped flaws in terms of an equivalent crack length and how to treat residual stress, misalignment and other stress concentrations, as well as other problems associated with welded joints.

In 1991, PD 6493 was substantially revised, including the CEGB R6 methods and generalizing the crack driving force to include K and J as well as CTOD [4.1]. Although these changes made the PD 6493 more inclusive and hence more widely applicable, it also made the document significantly more difficult to understand and apply. However, the previous simplified procedures using the CTOD design curve are still included, and it is possible to still use PD 6493 in the same way as the 1980 version. The reliability of the assessment procedures in PD 6493 has been established by an extensive series of large-scale wide-plate tests and more than 15 years of experience and further development.

Another major revision of PD 6493 is due out in 1996 and Garwood and Phaal have described the proposed changes [4.13]. A major emphasis of the revisions (which is certainly welcomed) has been to increase the readability and usability, e.g. by providing flow diagrams for the fracture assessment procedures. Additional appendices have been added to give particular industrial applications (one is for offshore structures), more guidance on residual stress, and more solutions for stress-intensity factor and limit loads. After trying to apply PD 6493 to ship structures, it is clear that a special appendix for application to ships also would be a good idea. The guidelines presented herein can serve as a preliminary basis for such an appendix.

The fracture model in PD 6493 is in the form of failure assessment diagrams (FAD). These diagrams consist of a failure assessment curve (FAC) that represents the ultimate state of a cracked

member and one or more failure assessment points (FAP) that represent the current state of the cracked member. There are three levels of assessment. The first level uses a simplified stress distribution and a failure curve based on the CTOD design curve. This level is intended to be a "screening" level and is very conservative. The second level uses a more accurate stress distribution and a failure curve based on a strip-yield model (Dugdale model) assuming an elastic-perfectly plastic material. A level 1 and a level 2 FAD are shown in Figure 4.1. The level 3 FAD will be discussed later.

The failure assessment diagrams used in PD 6493 are constructed with the collapse ratio, S_r , on the abscissa and the stress intensity ratio, K_r , on the ordinate axis. S_r is defined as the ratio of the load or bending moment on the net-section of a cracked member to the load or bending moment on that net-section at plastic collapse. For tension loading, this ratio is the same as the ratio of the nominal net-section stress to the flow stress. For bending, however, because the load increase is partly due to spreading of yielding across the section (as shown in Figure 1.1) as well as increases in the stress, the collapse ratio cannot be related to a stress ratio.

K_r for the FAC is the ratio of the elastic component of crack driving force to the total crack driving force (sum of elastic and plastic components). The crack driving force ratio is expressed in terms of K (Equation 2-1). If J or CTOD is to be used, they are related to K as in Equations 2-3 and 2-5, i.e. K_r is the square root of the ratio of the elastic part of J or CTOD to the total J or CTOD. Because only the elastic component of the crack driving force is required, the analysis of the cracked structure can be based on linear elastic analysis and the stress intensity factor, K . This is a tremendous simplification relative to calculating the applied J or CTOD in a complex component. K can usually be calculated from a handbook solution, whereas calculating an applied J or CTOD typically requires detailed finite-element analysis. The decrease in the tolerable K_r for S_r increasing beyond 0.4 in the FAC represents the compensation for using the elastic K analysis when in fact the driving force would be much higher as large-scale yielding takes place under a fixed load.

The two vectors labelled "flange crack" and "web crack" in Figure 4.1 represent a locus of FAPs for two ends of crack in an I beam specimen. K_r for the FAP is the ratio of the elastic component of crack driving force to the fracture toughness. PD 6493 allows the fracture toughness to be defined as K_{Ic} , CTOD, or J_c , but just as in the case of the FAC, if K units are not used, the K_r coordinate is the square root of J_{el}/J_c or $CTOD_{el}/CTOD_c$. PD 6493 even provides a correlation of K_{Ic} to CVN, albeit as different one than Equation 2-2. For a known crack tip location and stress at that location, K_r and S_r are calculated and the resulting point is plotted on the failure assessment diagram. A FAP which lies within the FAC is safe, while a FAP outside the FAC may possibly fail.

In the context of the FAD, failure has a different definition than in the 1980 version of PD 6493. For low values of S_r , the FAD implies failure due to initiation of crack extension. For low values of K_r , the FAD implies failure due to the attainment of the limit load, which is not related to the initiation of crack extension, and may occur prior to or after crack initiation. For conditions of high K_r and S_r , the definition of failure is a mixture of these two extreme cases. Note that failure due to attainment of the limit load implies load-control boundary conditions. In the event of displacement-control conditions, such as most highly redundant structures such as ship structures, the attainment of limit load is a very conservative definition of failure since there is considerable residual load capacity and much greater displacement capacity.

A locus of FAPs such as shown in Figure 4.1 is constructed for a given weld flaw or crack by incrementing the applied load. The predicted failure load for a particular end of the crack is the load where the FAP vector associated with that crack end crosses the FAC. In the case of failure by ductile tearing, "failure" implies the onset of tearing or plastic collapse. If there is a fixed load as in a very compliant structure, this will result in catastrophic failure. However, if there is a fixed displacement (i.e. loading is under displacement control), as in the experiments and in most stiff redundant structures, then there is considerable additional ductile tearing before the structural member is actually broken. In the case of a two-ended crack, the lower of the two predicted loads would be the predicted failure load, in this case at a moment of about 88 percent of $M_{p,net}$.

There is no inherent factor of safety if the level 2 FAC is used for this prediction, although conservative values of the fracture toughness and yield strength may introduce some safety. Appendix A of PD 6493:1991 suggests that the fracture toughness used in an assessment be the lowest of at least three tests or the mean minus one standard deviation of a larger sample.

It is the tensile properties, more than the fracture toughness, which determines the maximum load capacity for ductile fracture. As shown in Section 3.1.1, the tensile properties of HSLA-80 vary as much as ± 7 percent. TMCP steels also exhibit higher variability. Yet the number of tensile tests required to estimate the yield stress is not discussed in PD 6493:1991. This is an unfortunate oversight, because it is not clear if mean values should be used or lower bound values as in the case of the fracture toughness. In some cases, when test data are not available, the minimum specified yield strength (MSYS) could be used, but the ramifications of this on safety factors are not discussed.

Partial safety factors are suggested in Appendix A of PD 6493:1991 for the stress, flaw size, and fracture toughness (which is the lowest of at least three tests). Two partial safety factors are given for each in accordance with the consequences of failure. If the failure would have moderate consequences, safety factors of about 1.0 are used. For severe consequences of failure, safety factors up to 1.6 on stress, 1.4 on flaw size, and 1.4 on fracture toughness. Lower safety factors are allowed if there is a known lower variability in these quantities.

The level 1 FAD consists of a limit on K_r equal to 0.707, which is equivalent to a factor of safety of 1.4 on K which is equivalent to a factor of safety of 2.0 on crack length. The level 1 FAD also has a limit of 0.8 on the collapse ratio, which represents a lower factor of safety (1.25) for the more desirable collapse failure mode. These built-in safety factors are somewhere between the safety factors for moderate and severe consequences for level 2 and 3. The safety factors based on consequences in level 2 and 3 seem more reasonable for ship structure where there is often a big difference in the criticality of various members. The safety factors are about the same as used in strength design and should be reasonably consistent with the reliability anticipated for strength design. For the purposes of comparison with the experiments in this report, we will use lower bound estimates of the yield strength and fracture toughness with no additional safety factors which would obscure the accuracy.

PD 6493 was developed to treat flaws in plates, primarily small surface cracks or buried internal flaws. Therefore, the definition of collapse has been the local collapse of the remaining ligament

between the edge of the flaw and the edge of the plate. Note that this definition of collapse is not the same as the limit-load of the structure, because the part of the plate experiencing local collapse can shed load to nearby parts of the plate which have yet to fully yield, increasing substantially the load-carrying capacity of the structure. PD 6493 recommends the use of the flow stress to compute the limit load in tension or bending.

The application of PD6493 to through cracks in tension, as in the cope hole and CCT experiments, is relatively straightforward. To define S_r for the cope-hole specimens, the applied tensile load was normalized by the limit load of the net section (including the stiffener) calculated using the flow stress as recommended in PD 6493. Using a stress greater than the yield stress for tension on the net section is consistent with structural engineering procedures for limit-state strength design of tension members.

However, the application to the through cracks in the complex structural members was less clear. First of all, there are several possible definitions of collapse to consider:

- 1) local collapse in the ligament adjacent to the flaw (the definition of collapse intended by PD 6493);
- 2) net-section collapse in which the structural member containing the flaw collapses as illustrated in Figure 4.2; and,
- 3) gross-section collapse in which the entire structure fails due to excessive plastic straining and is not necessarily influenced by the flaw, as was illustrated in Figure 1.1.

Several of the specimens tested had shallow surface cracks at the toe of the attachment welds which had not completely penetrated the flange. This situation is similar to the surface cracks in plates which is the primary emphasis in PD 6493. Figure 4.3 shows a case of a long surface crack with a depth equal to about 60 percent of the thickness of the flange plate. The flange could be treated as a cracked plate essentially in tension, since the bending stress gradient was not significant through the thickness of the flange plate. In this case, shown in Figure 4.3a, local collapse by the first definition would consider the stress in the remaining 40 percent of the thickness (the ligament). This gave a result which was far too conservative, predicting failure at a bending moment which was 30 percent or less of the ultimate bending moment of the cracked beam.

Alternatively, the crack can be considered in the context of the overall structural member. In this case, shown in Figure 4.3b, the "plate thickness B" is taken as the overall depth of the beam, and the stress is considered as bending stress rather than tension stress in the flange alone. This treatment of the crack uses the second definition of collapse, i.e. collapse of the structural member, which is what was being measured in the experiments. Choosing B equal to the full depth of the member had other ramifications as well, for example it reduced the finite-width correction on the stress-intensity factor which was significant when the thickness was taken as the thickness of the flange plate. In general, taking the thickness equal to the overall depth of the member led to much improved predictions of the ultimate bending moment.

Although collapse of the structure, i.e. the third definition of collapse, is what is really significant with respect to the structure, it is probably prudent to assess flaws on their effect on the structural member alone (i.e. the second definition). If necessary, a global structural analysis can be used to determine what effect loss of this structural member may have on the overall structure.

Therefore, for ductile fracture of complex structural members, the second definition of collapse, as illustrated in Figure 4.2, is most appropriate. However, this is not the same definition of collapse inherent in PD 6493:1991. Garwood and Phaal indicate that there will be expanded discussion of various collapse modes and their implications in the 1996 revised PD 6493.

In the context of the first definition of collapse, local ligament collapse, PD 6493 recommends that bending limit loads be computed using the flow stress. While this might be conservative for local ligament collapse, it is not conservative with respect to collapse of a structural member. For example, in structural engineering the limit-state for bending strength is the plastic moment which is the product of the plastic section modulus and the yield stress. It will be shown that better agreement with the bending experiments was obtained using the yield stress rather than the flow stress in the denominator of S_r . Therefore, it is slightly unconservative to use the flow stress for plastic collapse of a structural member, while it would be very conservative to use the local ligament collapse, even based on the flow stress. In the analyses reported below, to define S_r for the I-beam and box-beam specimens, the applied bending moment was normalized by the fully-plastic bending moment (based on the net cross-section of the cracked section of the beam) using the yield stress. This definition of S_r is recommended for ship structural members loaded primarily in bending, whereas the flow stress may be used for ship structural members loaded primarily in tension. Most ship structural members are loaded primarily in tension due to the large depth of the hull girder relative to the depth of the member and the associated small stress and strain gradients across the member.

Structural engineers use the yield stress to compute the limit load in bending because the slightly unconservative assumption of rectangular stress blocks is made (see Figure 4.2). This assumption is unconservative because there is an elastic region close to the neutral axis until infinitely large rotations are applied. Therefore, ignoring the beneficial effect of the hardening compensates for the error in assuming rectangular stress blocks. No such error must be compensated for in tension, so it is more appropriate to use the flow stress. In the case of the EH-36, using the yield stress as opposed to the flow stress would decrease the predicted load by 14 percent as will be discussed below. The difference would be even less for the HSLA-80 steel. This added conservatism compensates partly for the more liberal definition of collapse being used to assess these experiments.

Example calculations of the stress intensity factors for the I-beam, box-beam, and cope-hole specimens are shown in Appendix 5. To determine K_r for the through-thickness cracks in cope-hole specimens, the stress intensity factor at the crack tip was determined using a handbook solution for a stiffened sheet [4.14]. This solution is similar to the solution for a center-cracked tension panel except it provides for the closure force of the stiffener bridging the crack.

Analytical stress-intensity factor solutions for the complex crack geometries encountered in the bending specimens do not currently appear in the literature. To determine K_r for the I-beam and box-beam specimens, the stress intensity factor at each crack tip in the specimen was approximated by treating the beam section as a monolithic block and using an equivalent semi-elliptical or quarter-elliptical surface crack solution. This idealization is illustrated in Figure 4.4. The idealized model for a multi-ended crack can be summarized as follows:

- 1) The cross section is idealized as a solid rectangular bar of dimensions equal to the outermost extremities of the cross section.

2) The crack is idealized as an elliptical surface crack in the idealized monolithic bar. The edges of the surface crack coincide with the ends of the multi-ended crack. The surface crack is subjected to the same nominal bending stress with the same neutral axis.

3) The stress-intensity factors at various ends of the multi-ended crack are approximately equal to the stress-intensity factors for the corresponding point on the hypothetical surface crack.

There is a free surface at the plate surfaces at the ends of these cracks whereas the idealized surface crack does not account for the presense of these free surfaces. Nevertheless, finite-element analyses have shown that these surface crack idealizations for the three-ended crack are typically accurate to within five percent [4.15]. This good agreement despite the free surfaces (among other simplifications) could be because the free surfaces are not unrestrained, e.g. as is the mouth of an edge crack when contrasted to a center crack of the same half length. Actually, in the multi-ended cracks, the crack is restrained by the ligaments at the other crack tips, therefore the free surfaces are not that significant.

Figure 4.5 shows the idealization of a two-ended crack as a quarter-elliptical crack, commonly referred to as a corner crack. This is the geometry of the crack in the specimen for which the loci of FAPs were shown in Figure 4.1. Crack position 1 is the flange crack. These cracks occurred at the toe of a welded attachment, and the stress concentration factor (SCF) associated with that attachment, 1.6, has been applied to the stress to determine K_r for this flange crack. This SCF was measured with strain gages at the toe of the weld. Crack position 2, the web crack, is more distant from the toe of the weld, i.e. more than several times the weld leg length away. Therefore, crack position 2 is far enough away from the toe of the attachment weld that the SCF does not influence the stress. In the context of structural member collapse, the SCF is not applied in calculating the S_r since at collapse all stresses are more or less uniform.

PD6493 recommends that residual stress be added to the applied stress to obtain the total stress to determine K_r . S_r is calculated from the bending moment divided by the net-section plastic moment. Residual stress and other secondary stresses such as thermal stress do not influence the plastic moment since secondary stresses are caused by small differences in the elastic strains, which are overwhelmed by the large plastic strains at collapse. Formby and Griffiths [4.16] showed that residual stress had little effect in the case of ductile fracture. Therefore, PD6493 recommends that residual stresses not be included in S_r .

For non-ductile fracture at nominal stresses below the yield stress, residual stresses are expected to have a significant influence and must be taken into account as recommended by PD6493. However, in the case of ductile fracture, S_r typically exceeds 0.8 (e.g. both the web and flange crack shown in the FAD in Figure 4.1). In this case, the nominal stresses also are nearly at or above the yield stress. Figure 3.11 showed high plastic strains in a typical ductile fracture experiment, for example. It is concluded from the following analyses that, for ductile fracture only, it is too conservative to add the residual stress to obtain a total stress exceeding the yield stress for the evaluation of K_r .

Neglect of residual stress in both the K_r and S_r terms would be more consistent with the findings of Formby and Griffiths [4.16] that residual stress had little effect in the case of ductile fracture. The neglect of residual stress in K_r for the special case of S_r greater than 0.8 can be rationalized on the same basis as the rationale to neglect residual stress in S_r . At high plastic strains, the residual

stresses are overwhelmed as in the case of plastic collapse. Therefore, it is recommended that for the special case of ductile fracture, the effect of residual stress should be ignored.

For example, there should be large tensile residual stresses at the top of the flange for crack position 1 (flange crack) in Figure 4.5. However, when the residual stress is included in the analysis, the vector representing the flange crack in the FAD in Figure 4.1 was offset by an increment on the K_r axis. The resulting predicted maximum load was conservative by as much as 60 percent.

The addition of residual stress, and this result, would be appropriate if brittle fracture were the anticipated failure mode. Brittle fracture depends more on a single critical initiation site, whereas ductile fracture depends more on the average properties across the crack front. The neglect of residual stress can also be rationalized because the magnitude of residual stress decreases with depth through the thickness of the plate. Also, the large crack tends to alleviate the residual stresses by reducing the constraint on the weld.

The level 3 assessment in PD 6493 has several options. The level 3 material-specific FAC uses the true stress-strain curve of the subject material. A comparison of the material specific level 3 FACs for both the HSLA-80 and EH-36 steel and the level 2 FAC is shown in Figure 4.6. Level 3 uses a collapse parameter, L_r , which is like S_r except it is based on the yield stress rather than the flow stress. Actually, as explained above, the level 2 analyses for bending experiments were also carried out using L_r rather than S_r , which was a modification of PD 6493 as explained above.

Considering that the yield strength of each material varies as much as ± 7 percent and the fracture toughness varies by as much as ± 34 percent, it seems that the differences between level 3 and level 2 are not that significant. This is illustrated by comparing the two material-specific FACs for HSLA-80 which are shown in Figure 4.6. These two HSLA-80 FACs are based on two different tensile-test results. Thus the variation in the level 3 FACs due to variation in tensile properties of a specific steel is as large as the difference between the two materials. This finding would justify the use of a single FAC for all ship steel. The level 3 analysis is really intended primarily for high-strain hardening steels such as stainless steels, where there would be a dramatic difference between level 2 and level 3. The second option in level 3 is a general FAC representing typical level 3 material-specific FAC's for a variety of steels including an elastic-perfectly plastic material. Level 3 assessment also allows crack extension for ductile tearing, which will be discussed further. A detailed discussion on the background theory for each level can be found in PD 6493.

The fracture toughness value used to compute K_r was $360 \text{ MPa}\cdot\text{m}^{1/2}$ for the HSLA-80 steel and $260 \text{ MPa}\cdot\text{m}^{1/2}$ for the EH-36 steel. These values were computed from the average J-integral values taken from several 50 mm C(T) specimens of the same thickness as the specimens as discussed in Section 3.1. With the exception of the groove weld specimens, the cracks had grown out of the weld metal and into the base metal. This is the usual situation for large fatigue cracks, which makes characterization of the fracture properties of the welds less important. The full-scale groove weld specimen tests resulted in brittle fracture at relatively low stress levels. This weld metal was made with relatively low toughness intentionally, as explained in Section 3.1. Several compact specimens were made with the notch in the weld and J tests were attempted, but these tests did not give reliable results. Based on the results of the full-scale tests, a value of $180 \text{ MPa}\cdot\text{m}^{1/2}$ was estimated for this

weld metal. Because these full-scale tests did not exhibit ductile fracture, they are outside the scope of this project. The poor performance of these intentionally poor welds is not representative of the performance normally expected for welds. Unfortunately, tests with more typical high-toughness weld metal were not performed.

Pre-test predicted values of maximum load using level 1 and 2 of PD 6493 for most of the I-beam tests are shown in Table 4.1. The post-test predictions, based on the actual crack length, also are given in Table 4.1. The pre-test and post-test predicted maximum load values are conservative compared to experimental results. The pre-test prediction for Specimen A1 is the only unconservative exception. The original pretest prediction for Specimen A1 was unconservative because the originally-estimated crack size was half of the actual crack size. The error in the crack size estimation was random and not systematic. For example, with the exception of this specimen and Specimen A48, the remaining originally-estimated crack sizes were within 10 percent of the actual crack sizes.

Fortunately, the predictions are not very sensitive to the error in crack size. For example, Table 4.1 shows that this 50 percent error in the crack size for Specimen A1 resulted in only a 20 percent change in the predicted failure load (using the level 2 results). This is consistent with Equation (2-1), which shows that the stress intensity factor is proportional to only the square root of the crack size, diluting the impact of variation of crack size. It is concluded from comparing the pre-test and post-test analyses that at least for relatively small cracks up to 37 mm long, the estimate of the crack size will occasionally be off by ± 50 percent. Therefore, there will occasionally be error in any ductile fracture model of at least ± 20 percent due to error in the estimated crack size.

To eliminate this occasional error, and focus on the relative accuracy of the various ductile fracture models, the remaining discussion will pertain to post-test analyses, which, perhaps improperly, are still called predictions. The post-test predictions were done consistently, i.e. after the first few tests there was no fine-tuning of these results on an individual specimen basis to get better agreement with the experiments. Therefore, these post-test predictions are still a critical test for the ductile fracture models.

Referring to Table 4.1, the post-test predicted failure loads using the level 2 FAC are all conservative and, except for the specimens with groove welds, within 19 percent of the experimental data. The groove welds were made with intentionally poor weld metal which was not adequately characterized, and therefore there is even greater difference between analysis and experiment. Level 3 analyses are slightly better accuracy, only up to 13 percent variation between analysis and experiment for specimens other than the groove welds. However, many of the predictions using level 3 were on the unconservative side. This disadvantage, together with 1) the fact that variation in the level 3 due to natural variation in tensile properties; and, 2) the fact that there is a natural 20 percent error due to variation of the crack size; leads to the conclusion that, for typical ship steels, the level 3 does not offer any advantages over level 2 assessment that are commensurate with the increased level of effort in the analysis.

Predicted values of maximum load for each of the box-beam specimens are shown in Table 4.2. One problem that arose with the analysis of the box sections was how to deal with cracks which deviate out of plane and with multiple cracks in different but nearby planes. These odd cracks were

idealized as a single crack in a single vertical plane which had the dimensions of the projection of all nearby cracks on that plane. As shown in the table, the predicted maximum load values were also conservative (within 39% of the experimental results). The level of conservatism is larger than was the case for the I-beam specimens. Therefore, as the structural complexity and redundancy increases, the conservatism of the PD 6493 procedures increases. The procedures would be expected to be even more conservative when applied to the ship hull girder.

Predicted values of maximum load for the cope-hole specimens are shown in Table 4.3. As shown in the table, the predicted values of maximum load are conservative compared to experimental results for both the HSLA-80 and EH-36 materials. For the level 2 analysis, the error (i.e. maximum difference between a predicted maximum load and the experimentally measured maximum load) is no larger than 10 percent, which is considered excellent. In fact, by examining the variation among replicate specimens such as specimens 4, 5, and 6 for each material, it can be seen that the natural variation in these experiments is as large as 10 percent. The error gets slightly worse for the level 3 analysis. The improved accuracy in these analyses of the cope-hole specimens relative to the analyses of the I beams and especially the box beams would be expected, considering the relative simplicity of the cope-hole specimens.

Figures 4.7 and 4.8 show the level 3 FAD for each material and show the assessment points for both crack sizes. The Level 3 analyses are supposed to reflect the effect of the strain hardening better than the level 2 analyses, since the failure analysis diagram (FAD) is calculated directly from the stress strain curve. However, as was discussed above, Figure 4.6 shows there is not much significant difference between the level 3 FADs for these steels and the level 2 FAD (plotted in terms of L_r). Although the experimental results show a greater percentage of limit load for the EH-36 steel, the Level 3 analysis predicts a lower percentage of limit load for the EH-36 specimens.

For materials which exhibit ductile tearing such as these steels, the PD6493 currently allows a tearing stability analysis to be made which allows for a slightly greater predicted maximum load than the conventional analysis based on initiation. The tearing stability analysis requires very complex calculations which are explained in Section 4.5 below. Figure 4.9 shows a typical result from I-beam specimen A18. Because the assessment point is on the collapse part of the FAD for all these materials and crack sizes, the point where the tearing curve is tangent to the FAD is not significantly greater than the assessment point based on initiation. The locus of points representing the tearing curve will always have the same general shape, i.e. decreasing K_r with slightly increasing S_r . Because of the shape of the tearing curve relative to the collapse part of the FAD, the instability analysis is only useful if the fracture load is determined by K_r , i.e. if fracture is predicted to occur at applied stresses much less than the yield stress.

Finally, PD 6493 still allows the CTOD design curve, i.e. Equation (4-1), to be used in its original form, without a collapse cutoff on S_r , for cases of displacement control loading. Equation (4-1) can be rearranged for the purposes of predicting the failure strain:

Substituting the material properties CTOD and ϵ_y for HSLA-80 (0.97 mm, 0.29 percent) and for

$$\frac{\epsilon_f}{\epsilon_y} = \frac{CTOD}{2\pi \epsilon_y a} + 0.25 \quad (4-2)$$

EH-36 (0.78 mm, 0.20 percent), Equation (4-2) reduces to the following. For HSLA-80 steel:

$$\frac{\varepsilon_f}{\varepsilon_y} = \frac{53mm}{a} + 0.25 \quad (4-3)$$

For EH-36 steel:

$$\frac{\varepsilon_f}{\varepsilon_y} = \frac{63mm}{a} + 0.25 \quad (4-4)$$

For the cope-hole specimens with "2a" equal to 76 mm for example, the CTOD design curve would give $\varepsilon_f / \varepsilon_y > 1.6$ for the HSLA-80 and $\varepsilon_f / \varepsilon_y > 1.9$ for the EH-36. This seems like an improvement on the FADs with the cutoff on S_r for collapse. However, for the box beam specimens, the large cracks had an "a" ranging from 45 to 100 mm, which would give $\varepsilon_f / \varepsilon_y$ ranging from 1.4 to 0.8, when in fact the peak load occurred at about $\varepsilon_f / \varepsilon_y > 1.6$ regardless of crack length.

Also, as in the case of the FAD calculations, residual stresses are supposed to be included. In the case of the CTOD design curve, the ϵ_f will include a strain equivalent to the residual stress, which would approach ϵ_y for the cope hole specimens and the flange crack of the I beam specimens. This would leave only a fraction of the yield strain available for the applied primary stresses. Therefore, the CTOD design curve does not appear to be very accurate, although it is conservative. For bending, the collapse load does not occur until several times the yield strain anyway, so the CTOD design curve is not necessarily more liberal.

The following conclusions can be drawn from the analyses using PD6493.

1. The level 2 procedures contained in PD 6493 can be used to make conservative and relatively accurate predictions of the maximum load prior to onset of stable crack extension for cracked structural members. While it does predict maximum load, PD 6493 cannot predict ductility beyond the limit load which may also be needed for an evaluation of structural integrity in the presence of large fatigue cracks.
2. Level 3 analysis does not add sufficient accuracy to justify the increase in complexity relative to a Level 2 analysis and therefore the Level 3 analysis is not warranted for structural steels such as HSLA-80 and EH-36.
3. Tearing instability analysis using PD6493 level 3 is not useful when applied to structures undergoing fully-plastic collapse.
4. The CTOD design curve without a cutoff for S_r can give more liberal results that allow for several times yield strain under displacement control, however it is not very accurate.

4.2 Plastic limit-load calculations for propagating cracks

The I-beam and box beam experiments were analyzed using a basic limit load analysis. Limit load solutions for the C(T) specimen geometry were investigated by Hu and Albrecht [4.17], who noted that the ductile specimens were at their limit load as the crack propagated. In this study, it was found that crack extension occurred under fully plastic conditions as predicted by a modified Green's solution.

Limit load solutions for common geometries of test specimens, plates and pipes are discussed in a review by Miller [4.18]. The limit load for tension specimens such as the CCT and cope-hole specimens is equal to the flow stress times the net area. The analysis of the I-beam and box-beam specimens featured considerably more complex geometries and crack extension paths. The cracks in the I-beams and box-beams were located in the constant moment region of the loading span. The limit load is based on rectangular stress blocks such as shown in Figure 4.2 on the cracked net section area. The rectangular stress block implies elastic-perfectly plastic behavior.

For each step of crack advancement (as measured during the experiment) the centroid of the remaining area was determined and a limit load was calculated. The limit load was also calculated using crack lengths increased and decreased by 5 mm from the experimentally measured values to investigate the sensitivity to crack length measurement error (if any) on the calculations. An example of this calculation is shown in Figure 4.10 for I-beam specimen A18 and box-beam specimen 3. At values of d/d_y for which there are experimental crack length measurements, there are three calculated limit load values. The upper and lower points correspond to the reduced and enlarged crack length measurements, respectively. As shown in the figure, the predicted values of load agrees exceptionally well with both types of experiments. This calculation worked well for all the I-beam and box-beam specimens for which it was applied. Calculation for several of the I-beam and box-beam specimens are shown in Appendix 6.

The limit load approach provides a simple and accurate method of predicting the specimen's remaining load capacity with respect to crack extension. These calculations were simple enough to be performed with a spreadsheet, and are the type of calculation that can be practically implemented with regard to common structural members. Of course, in order to predict the load-deformation curve without prior knowledge of crack extension, it is necessary to predict the crack extension history correctly. This is the topic of section 4.5.

4.3 Finite-element analysis to calculate applied J

Finite-element analyses (FEA) were performed to determine the applied J as a function of displacement for the I-beam and cope-hole specimens using ABAQUS finite-element software. The results of these analyses were used to predict crack propagation by J-R curve analysis as will be discussed in section 4.5. The finite-element models and procedures used to obtain results are presented here.

Eight-noded quadrilateral shell elements with 5 degrees of freedom and reduced integration were used to model the test specimens. For example, the model used to simulate the cope hole experiments is shown in Figure 4.11. The model for the CCT specimens is the same except there is no stiffener. The shell elements with one fewer degrees of freedom are not good for shells that intersect perpendicularly. Reduced integration gives improved results relative to full integration which tends to be too stiff in elastoplastic problems. The planar dimensions of the elements ranged from 12 to 25 mm square. Shell elements are not intended for such small width-to-thickness ratios as small as 1.3, and would not be expected to give realistic through-thickness gradients. Notwithstanding these shortcomings, these shell elements should give reasonable overall plastic behavior. The analysis would be prohibitively time-consuming and expensive with solid elements.

The elastoplastic material model consisted of a Von Mises yield criterion with isotropic hardening. The stress-strain properties were input as a piecewise linear effective-stress-strain curve that closely represented a typical engineering stress-strain curve from a tensile test for each steel.

Cracks were simulated by restraining only one corner node of a shell element at the "crack tip", while the next element ahead of the crack tip is attached to either a plane of symmetry or another element. No special crack-tip elements were used, these special elements are only used for small-scale yielding analyses and the strength of the singularity of the crack-tip fields must be known. In reality, crack-tip fields are affected by large strain near the crack tip. Therefore, even if the special crack tip elements are valid for elastoplastic small-strain analysis, the results right at the crack tip would not be any closer to the real "large-deformation" crack tip fields than the results from regular quadratic elements.

Although this simplified crack representation does not accurately represent crack-tip stress and strain fields, it does provide the necessary resolution to perform reasonable J-integral estimates. Three contour paths were used around the crack tip to calculate J. In some cases, one or more of these paths was corrupted by not being far enough away from the crack tip or by intersecting the specimen boundaries. In most cases, two or all of the contours gave consistent results, and one of these was chosen as the result from the analysis.

The most simple geometry modelled was the CCT specimen. Twelve elements were used across the width of the baseplate. Models with stationary cracks of 25 mm (the initial crack size), 50 mm, 76 mm 101 mm and 127 mm were loaded under displacement control. The J solution was checked in the elastic range by converting to an equivalent K value by Equation 2-3 and comparing to the handbook solution for K. At a nominal gross-section stress level of 77 MPa, the J from FEA was 4.3 kJ/m^2 which corresponds to an equivalent K of $30 \text{ MPa}\cdot\text{m}^{1/2}$, while the handbook solution was $32 \text{ MPa}\cdot\text{m}^{1/2}$, which is only eight percent greater than the K from FEA and is considered good

agreement. Plots of force vs. displacement and J vs. displacement were generated for each crack size.

Figure 4.12 shows J vs. displacement for 76 mm (a/W of 0.5) for the HSLA-80 and EH-36 steels. Note that for both the EH-36 and HSLA-80 steel in the 9 mm thickness plates, J has exceeded the "validity" limits in the ASTM E1152 test specification. This is not surprising since valid J values could not be obtained for plates of this thickness in any high-toughness steel. Since J exceeds the validity limits, it is no longer associated directly with the crack tip stress and strain fields and therefore would not necessarily be expected to be a good fracture parameter. Nevertheless, such "invalid" J data have been used in the past, provided both the test specimen and the application are the same thickness. Note that the applied J is greater at a given displacement for the HSLA-80 steel which is expected because of the greater flow stress.

In the case of the CCT specimen, McCabe and Ernst [4.19] published a J solution which can be calculated (independent of the contour integral) from the load, and displacement, and crack length data. The calculated J using the McCabe and Ernst solution is also shown in Figure 4.12, including the elastic and plastic parts as well as their sum. The relatively good agreement between the contour integral and the McCabe and Ernst solution, at least up to about 7 mm of displacement, verified the accuracy of using shell elements with a relatively coarse mesh near the crack tip. At values of J exceeding 4 MJ/m^2 , the error in the FEA results is as large as 25 percent.

The CCT solution of McCabe and Ernst also was used to calculate J for the cope hole specimens. The width and remaining ligament of the cope-hole specimens was adjusted to include the net section of the stiffener as well as the actual width of a ligament of the 152 mm wide plate. In other words, the stiffener was treated as if it were coplanar with the main plate and contributed additional plate width on the sides of the specimen. Figure 4.13 shows the J computed from ABAQUS compared to this solution. The agreement is even better than it was for the CCT specimens. Therefore, the applied J vs. displacement for shell cracks bridged by a stiffener or girder can be calculated from an idealized CCT model incorporating all of the section as if it were coplanar.

The analyses for the cope-hole specimens were carried out in the same manner. Models with stationary cracks of 50 mm and 76 mm (the initial crack sizes), as well as 101 and 127 mm, were loaded under displacement control. Plots of J integral vs. displacement for the first three crack sizes in the cope-hole specimens, as well as the CCT specimen with the 76 mm crack, are shown in Figure 4.14 for the two materials. As the remaining ligament gets smaller, a larger proportion of the ligament has elevated stresses due to proximity to the crack tip. The computed J is slightly higher for the larger cracks because the average net section stresses are higher. However, the difference between these curves for different crack lengths is small compared to the scatter among measured J-R curves from replicate specimens and compared to the discrepancy between J computed from FEA and J from the solution of McCabe and Ernst.

Figure 4.15 shows plots of J integral calculated using the McCabe and Ernst solution for the CCT and cope-hole specimens. While there is slightly greater variation among different crack lengths, the magnitudes of the J curves rank in the same order as the J curves from FEA.

Figures 4.16 and 4.17 show two models for the I-beam specimens. The model shown in Figure 4.16 is a fully detailed model of I-beam attachment specimen such as specimen A18. The elements were 25 mm square throughout this model except in the refined region near the crack where 12 mm square elements were used. The model features shells which represent the attachment details and cause a stress concentration near the crack. The refined mesh region around the crack location extends deep into the web enabling longer web cracks to be modeled. The beam was laterally supported in the experiment which restrained some displacement which occurs due to the eccentric location of the crack. This support was modelled in the finite-element analysis by constraining the edges of the flanges at the load points from lateral deflection.

The model shown in Figure 4.17 is a simplified model of a I-beam attachment specimen such as specimen A18. In contrast to the simplified model described above, the crack is located in the center of the span, allowing for half-symmetry to be used, although the crack was actually located about 150 mm from the center of the span. Attachment details were not included and lateral-torsional support was not included. The purpose of these analyses was to assess the impact of these simplifications and hence the necessity of these complexities. Figure 4.18 shows the computed J vs. displacement for the flange crack from the two models. This agreement is considered very good, and it can be concluded that: 1) the mesh was adequately refined; and, 2) the simplifications in the model had little effect. Therefore, it can be recommended that if FEA of cracked geometries is performed that the crack may be located on the centerline of a member for convenience and it is not necessary to include the stress concentration of any attachments.

The analyses of the I-beam specimens were conducted using the detailed model in Figure 4.16. Models with stationary cracks (corresponding to the crack configuration measured at various stages of the tearing failure) were loaded under displacement control. Plots of J integral vs. displacement for the first four crack configurations for specimen A18 are shown in Figure 4.19. Note that, as in the case of the cope-hole specimens, there is not very much difference among the various crack configurations when J is plotted as a function of displacement.

4.4 J estimation schemes

Various J estimation schemes have been proposed in the literature. The EPRI/GE power-law method is widely used for the analysis of pressure vessels and piping [4.4-4.7]. This same type of power law reference stress method is used in the GKSS Engineering Treatment Model (ETM) [4.8,4.9]. Discussions with researchers at TWI and with Prof. Schwalbe of GKSS confirm that reference stress methods were developed and intended primarily for high-strain-hardening steels such as stainless steel, and these methods are not sufficiently accurate for low-strain-hardening steels (most structural steels as well as EH-36 and HSLA-80) under fully-plastic conditions.

The objective of these schemes has been to calculate the plastic part of J, or J^p , based on the solution for J^p at the limit load, P_0 . The assumption is made that the plastic part of J increases in proportion to the material stress-strain curve, specifically the ratio of the load to P_0 (after exceeding P_0) raised to the hardening exponent from a power law like the Ramberg Osgood law. The J and displacement (V) estimation schemes have the form:

$$J = J^{el} + \alpha \varepsilon_0 \sigma_0 \quad (4-5)$$

$$V = V^{el} + \alpha \varepsilon_0 \quad (4-6)$$

For HSLA-80, ε_0 is the yield strain which is 0.29 percent and σ_0 is the yield stress or 607 MPa. The α was equal to 3.14 and the hardening exponent, n, was 10.7, as discussed in Section 3.1.1. The functions $h_1(a/W,n)$ and $h_2(a/W,n)$ are tabulated in the EPRI Handbook [4.7] and reports [4.4-4.6] as well as several books [4.20,4.21] for a variety of test specimens and flawed cylinders. For a hardening exponent of 10, similar to the HSLA-80 material, and a CCT specimen with an a/W ratio of 0.5, h_1 is 1.43 and h_2 is 0.87.

It is not clear if P_0 and σ_0 should be based on the yield stress or the flow stress. For tension specimens such as the cope-hole specimens, it probably doesn't matter as long as they are defined consistently. However, there is a related problem in these type of estimation schemes that has not been discussed in the literature. The assumption is made that the plastic part of J increases in proportion to the strain in the uniaxial stress-strain curve. The strain is assumed to increase in proportion to the ratio P/P_0 , which for tension specimens is proportional to σ/σ_0 . However, for bending, the P/P_0 ratio is the M/M_0 ratio which increases because of the spreading of plasticity across the section (the effect shown in Figure 1.1) as well as because of strain hardening. In fact, for low strain hardening steels such as HSLA-80, the bending effect dominates the smaller strain hardening effect. Because of this inconsistency, these types of estimation schemes inherently will perform differently when applied to bending members than when applied to tension members.

To avoid possible confounding with this bending effect, the estimation schemes are evaluated on the basis of their ability to estimate the FEA results for CCT specimens, specifically load and applied J vs. displacement results for stationary cracks. Figure 4.20 shows the load vs. displacement data from the finite-element analysis (FEA) of the stationary crack in the HSLA-80 CCT specimen made from 9 mm thick plate, i.e. the analysis which was used to generate the J from the contour integral (Figure 4.14a) and from the Ernst and McCabe [4.14] solution (Figure 4.15a). P_0 was taken as the flow stress times the net area. Equation (4-6) was evaluated in a spreadsheet by incrementing P/P_0 from 1.0 to 1.4. Figure 4.20 shows the predicted displacement (V) from Equation (4-6) as a

function of P for the HSLA-80 CCT specimen, compared to the FEA result. The shape of the curve is similar to the FEA curve, but the estimation scheme significantly overestimates the displacements at corresponding P levels. Unless the corresponding points are compared as in Figure 4.20, this error is not readily apparent due to the flat slope of the curves at high P levels, i.e. the error in the displacement is obscured.

Equation (4-5) was evaluated in a similar manner. The estimated J is plotted in Figure 4.21 (labelled EPRI) as a function of the FEA displacements corresponding to the P/P_0 . The FEA displacements are used rather than the displacements from Equation (4-6) to avoid any error due to Equation (4-6) in the comparisons of the J vs. displacements plots. Figure 4.21 shows that the EPRI/GE estimation scheme is conservative but significantly overestimates J at large displacements. The EPRI/GE estimation scheme is being used here for to estimate J values which exceed the validity limits of ASTM E1152, i.e. for J values that are no longer associated directly with the crack tip stress and strain fields. In other words, the estimation schemes were never intended to be used at these invalid J levels. However, in order to be useful for the prediction of ductile tearing in ship structural details, it is necessary to use these invalid J values.

At very large displacements the solution changes curvature. This is an artifact of the high-order power law which was fit to the stress-strain data over the range P/P_0 up to 1.2, but is being used here at higher P/P_0 levels (up to 1.4). In other words, the power law is being used outside the range over which it was fit to the stress-strain data and it has spurious characteristics outside this range. The reason the P/P_0 in the CCT and cope-hole specimens exceeds the P/P_0 of the tensile data is that the cracked specimens develop some constraint which raises the average stress on the net section. The uniaxial tensile specimens do not develop any constraint until after necking. The problem of using these power laws at higher P/P_0 levels than supported by the tensile data was probably not encountered in the EPRI work. The typical applications were fracture problems in pressure vessels and piping of moderate toughness with a low Y/T , which involved only moderate plastic strain levels, as opposed to these fully-plastic collapse-dominated experiments on relatively-thin high-toughness steel with relatively-high Y/T .

The main problem with applying the power-law estimation scheme to these experiments is that the load was typically at or only slightly above the limit load for all stages of crack propagation, as explained in Section 4.2 above. The ratio of P/P_0 is only slightly greater than 1.0 and the actual value is extremely sensitive to the value of yield stress or flow stress used to compute the limit load P_0 , the hardening exponent n which depends on the curve fitting process, and the limit load solution. For large strain-hardening (low Y/T) steels such as stainless steels which were the materials of primary interest in the EPRI/GE work, these issues are insignificant in comparison to the large increases in load due to strain hardening. Another problem, which is shared by J calculated by FEA, is that the J calculated by the estimation scheme will be much greater than that which is considered valid for these high-toughness steels in thin plates. Therefore, these levels of J are beyond the limits for "J dominance" for which the schemes were derived.

Ainsworth [4.10] formulated a similar estimation scheme which is based on the strain rather than the load and therefore is more appropriate for materials for which the stress-strain curve is not well represented by a power law. An equation for this "reference stress" method is:

$$J = J^{el} + \sigma_{ref} \quad (4-7)$$

where the reference stress, σ_{ref} , is equal to $\sigma_0 (P/P_0)$ and ϵ_{ref} is the strain corresponding to σ_{ref} in the uniaxial stress-strain curve. For the power law, Equation (4-7) will give results equivalent to Equation (4-5). However, Equation (4-7) is more general and can be used with different constitutive models. The results are higher and therefore less accurate than the EPRI estimation scheme. However, this scheme (as any other estimation scheme or FEA) was not intended to be used for these invalid J values.

A further simplification is to use the h_1 function for elastic material, rather than have a function of "n". For elastic material and an a/W ratio of 0.5, h_1 is 2.21, which is 54 percent greater than the h_1 for "n" of 10. The following simple equation is obtained:

$$J = K^2 \frac{\epsilon_{ref}}{\sigma_{ref}} \quad (4-8)$$

The results from Equation (4-8) are labelled "Ainsworth" in Figure 4.21. The resulting J values are greater and hence less accurate than Equations (4-5 and 4-7), but are at least considerably easier to calculate. Another issue with these reference stress methods (Equation (4-7) and (4-8)) is that for higher σ_{ref}/σ_0 levels (i.e. higher P/P₀ levels), the end of the stress-strain data is reached and it is no longer possible to determine ϵ_{ref} . This limit is the reason that the Ainsworth calculations only extend to a displacement up to 2.8 mm. This problem is analogous to the problem with the power law at higher P/P₀ levels, which also should not be used outside the range of the P/P₀ for the stress-strain data.

The GKSS Engineering Treatment Model (ETM) is completely empirical. The ETM is based on the observation from experiment that:

$$\frac{J}{J_0} = \frac{CTOD}{CTOD_0} = \frac{\varepsilon}{\varepsilon_0} = \left(\frac{P}{P_0}\right)^n \quad (4-9)$$

Similar observations were made about the experiments in Section 3, specifically that all the displacements increased approximately linearly. Figure 4.21 shows this ETM estimation is conservative but also significantly overestimates J. However, this method has the least pretense of theoretical basis and implied accuracy.

At 2.8 mm of displacement, about the point of maximum strain of the stress-strain curve, all of these J estimation schemes overestimate J by about a factor of 3. When used in a J-R curve analysis, this error will cause a much greater error in crack extension. Obviously these estimation schemes are unsuitable for ductile fracture of relatively-thin high-toughness steel plates with low strain-hardening.

As shown in Figures 4.12-4.14, 4.17 and 4.18, the finite-element based J analyses predict that J as a function of displacement increases linearly after some displacement. This linearity suggests that a "calibrated" empirical J estimation scheme may be possible with a very simple form. For example, it could be possible to estimate J from a bilinear function of displacement. Since the first part is the "elastic-dominated" part and the resulting J is trivial in comparison to the large J^p in the second part, the model could be J equal to zero up to a displacement corresponding to the intercept of a linear fit to the second part. Such linear fits to the J solution of McCabe and Ernst for various cope-hole and CCT configurations are shown in Figure 4.22. The proportionality constant for this model would ideally depend on material and crack size. However, in view of the relatively small variation in J with respect to crack size variation, at least over the range of 2a from 25 to 150 mm, a simplified J model could be proposed that is a function of material only.

J could be based on the total plastic work done on the specimen, which is determined from the overall load vs. displacement data. Figure 4.23 shows J along with the total work and the plastic part of the work as a function of displacement for the cope-hole specimens of both materials with a 76 mm crack size. Figure 4.23 shows that the J is approximately equal to the plastic work per unit area of the net section. Figure 4.24 shows the plastic work per unit area of the net section as a function of displacement for all crack sizes for each material, which can be compared to the solution for J in Figure 4.15.

The J integral is proportional to the work per unit area in a way which does not depend on material, as shown in Figure 4.25. The slope of this line, which is referred to as η (eta), is estimated from the graph to be about 0.8. Eta is discussed further in Section 4.6. This is reasonably close to the known eta factor for center-cracked tension specimens, which is nearly 1.0. Since the J changes with crack length but the work done does not, it is clear that the eta factor is a function of crack length. However, if the change in J due to crack length is small relative to uncertainty in the J-R curve and uncertainty in the FEA computations, it may be sufficient to estimate J as a function of displacement in a way which does not depend on crack length.

J is approximately equal to the total plastic work for a tension member. The plastic work per unit area can be estimated by the average net-section stress times the plastic part of the displacement. In these tensile tests, the displacement occurred almost entirely on the crack plane. Figure 4.26 shows the average net section stress, which was computed from FEA results by dividing the total load by the net remaining ligament area, normalized by the yield stress. This average net-section stress is analogous to σ_{ref} . Figure 4.26 shows the effect of constraint which increases the average net-section stress with increasing crack length. This is the primary reason for the relatively small effect of crack size on the applied J vs. displacement function.

Figure 4.26 shows that for the HSLA-80 steel, the average net-section stress was relatively constant at about 1.3 times the yield stress throughout the displacement, i.e. the σ_{ref}/σ_0 value was about 1.3. Note that this is higher than the inverse of the Y/T ratio, i.e. the tensile strength of the steel is only 1.13 times higher than the yield strength, or about 1.2 times higher in terms of true stress. The constraint discussed above is the reason the relatively greater σ_{ref}/σ_0 levels in the fracture tests than in the tensile tests.

For the EH-36 steel, the average net-section stress increases from 1.25 to 1.75 times the yield stress as the displacement increased. An average value of 1.3 could be used to approximate the average net section stress for both of these materials and for all displacements. Since the Y/T of these steels are at the ends of the distribution for modern ship steel, the average value of about 1.3 times yield should be widely applicable.

This average net-section stress suggests a possible simple model for estimating J:

- 1) use J^p of zero up to the "limit-load" displacement, d_0 ;
- 2) J^p increases as 1.3 times the yield stress times the change in displacement, i.e, for $d > d_0$:

$$J = J^{el} + 1.3 \sigma_0 (d - d_0) \quad (4-10)$$

Figure 4.22 showed the result of this approximation with the actual slopes from regression analysis of the data from the solution of McCabe and Ernst. Also, this approximate equation for J is also shown in comparison to the FEA calculations for the flange crack in the I-beam specimen in Figure 4.19a.

In order to plot the approximate J as a function of displacement over yield displacement in the bending tests, it is necessary to estimate an effective longitudinal displacement on the crack plane. For the bending tests, displacements were measured at various locations, but it was noted that all displacements increased approximately in proportion to one another. The beams formed a plastic hinge on the crack plane and all displacements resulted primarily from rotation, Θ , of this hinge. At peak load, Θ_0 is equal to 3.2 percent radian. Taking the depth of the beam as 190 mm and assuming a linear displacement gradient, the "effective average" displacement at the outer fibers is about 6 mm.

This simple J estimation scheme is adequate in view of the uncertainties in the problem, especially the variation in measured J - R curves. It is certainly far more accurate than the published J estimation schemes. It is also robust in that it can be used on tension or bending specimens. It is presently calibrated to give accurate results on average. The coefficient of 1.3 could be increased to make sure the estimation scheme is always conservative. Obviously, it is not very accurate and unconservative at low J values. (The published estimation schemes may be more appropriate for low J values). However, the effect of this shortcoming will not be apparent in problems where large amounts of crack extension are to be modelled and J eventually becomes quite large.

4.5 Predicting crack propagation by the J - R curve analysis.

The accuracy of the process of calculating the applied J driving force vs. displacement function for a particular cracked configuration, as described above, can be separated from the accuracy of a stable crack propagation (tearing) analysis using the experimentally measured J - R curve. Both of these can be separated from the process of calculating the load-displacement curve given the crack extension-displacement history. As shown in Section 2.3, calculating the load-displacement relation can be very simple.

Stationary-crack I-beam and cope-hole finite-element models with several crack configurations were loaded under displacement control. The crack configurations for the bending tests corresponded to successive measured crack configurations such as shown in Figure 3.14. Crack extension in the cope-hole model was more straightforward and was simply modeled in symmetric 12.7 mm increments for each material.

The analysis begins with the model for the initial crack configuration. At each increment of displacement, the value of J at each crack tip was evaluated to see if it exceeded J_{Ic} . The displacement was increased further until the value of J at one of the crack tips was sufficient to cause an increment of crack extension according to the J - R curve. The increment of crack extension at each crack tip was relatively coarse, corresponding to the difference between successive measured crack configurations such as those shown in Figure 3.14.

From this displacement on, the load and J were evaluated from the model with the second crack configuration. The displacement of this model was increased until the J level at one of the cracks was sufficient to cause the next increment of crack extension associated with that crack tip. This usually occurred at all of the crack tips almost simultaneously, as would be expected based on the experiments. Thereafter the model with the third crack configuration was used, and so on. In this manner, the crack-extension-displacement curve and the load-displacement curve are pieced together.

Previous finite-element simulations of crack propagation, using nodal-release schemes, have shown that the J level resulting from a certain crack length and displacement is not significantly influenced by the path that was taken to arrive at that crack size and displacement, i.e. starting with a stationary crack and increasing displacement (as was done here) as opposed to starting with a smaller crack and extending the crack while simultaneously increasing the displacement to arrive at the same crack size and displacement.

Since conventional compact tension tests are carried out with relatively small amounts of crack advance relative to specimen thickness, extended J-R curves were generated to determine critical values of J over a larger range of crack advancement for the HSLA-80 and EH-36 materials as described in section 3.1. Although there is great variation in the J-R curves at small crack extension, after crack extensions of about 4 mm the J-R curves seem to have a slope or tearing modulus which is generally consistent.

An example of an extended J-R curve for each material is shown in Figure 4.27. The tearing modulus for larger crack extension is about 200 MPa for both types of steel. An extrapolated J-R curve with this constant slope was used beyond the crack extension limits of the extended J-R curves. As discussed in Section 3.1, this constant tearing modulus is essentially the same as using a constant crack-opening angle (COA) between 19 and 26 percent radian.

It is understood that these calculations are being carried out well beyond the limits of J-controlled crack growth in the fully plastic regime. However, there is no other option for the analysis of ductile tearing in ship structural details. It is anticipated that the effect of this violation of these limits will tend to be conservative. The purpose of this investigation is to determine the error involved in such an analysis, if any, with respect to the experiments described in Section 3.

The applied J-displacement curves for the cope-hole specimens, using J from the contour integral in the FEA, were shown in Figure 4.14. Together with the J-R curves in Figure 4.27, the applied J curves were used to determine crack extension vs. displacement curves. Figure 4.28 shows the predicted crack extension history as a function of displacement for both the HSLA and EH-36 cope-hole specimens compared to typical experimental results.

The predicted crack extension using the J-R curve is at the lower end of the experimental data or slightly below the experimental data. Underestimating the crack extension is unconservative, and should lead to overestimating the load-displacement curve. However, in view of the complexity of these analyses and the natural variation among replicate test results, the agreement with the cope-hole experiments is considered good. If the J solution from McCabe and Ernst (shown in Figure

4.15) were used, higher applied J values would have been obtained for each displacement, which would have increased the rate of crack extension and led to slightly better agreement.

Figure 4.29 shows the stationary crack load-displacement curves from the HSLA-80 steel cope hole models. These FEA results increase monotonically and are labelled according to the crack length, 2a. The predicted load-displacement curve also is shown on this graph. The predicted curve is pieced together by connecting points along the FEA load-displacement curves for the stationary crack lengths. The displacement at which the predicted curve jumps to the next stationary-crack curve is determined from the crack extension vs. displacement data from the J-R curve analysis in Figure 4.28. The predicted curve can be compared to the experimental load-displacement curve, which is also shown on Figure 4.29. Points corresponding to the attainment of a particular crack length are indicated along the experimental curve. The corresponding points for the predicted curve are where the predicted curve intersects the stationary crack load-displacement curves.

The finite-element analysis overestimated the load by a constant amount throughout the crack propagation. However, this should not be considered a shortcoming of the J-R curve approach, but rather of the finite-element analysis to determine load. To a certain extent, this overestimate of the load will increase the calculated J. However, the J from the contour integral is typically smaller than the J from the McCabe and Ernst solution, therefore this error in load actually improves J in this case. Although there is a slight offset due to this error in load, the FEA/J-R curve analysis correctly predicts the shape of the descending branch of the load-displacement curve.

A better estimate of the load could be obtained by using the simple limit-load solution, which, ironically, is more accurate. The results of these calculations are also shown in Figures 4.30. The FEA results and the limit-load results both use the same crack extension history, which was calculated using the J from FEA. It is seen that the resulting load-displacement curve using limit load is in better agreement with the experiments than the result using the FEA for load. It is concluded that the best approach would be to use the FEA to predict the crack extension history, and then use the simple limit load approach to determine the load-displacement curve.

Similar data are shown in Figures 4.31 and 4.32 for the EH-36 steel cope-hole specimens. The limit-load analysis underestimates the load for most of the crack propagation. Toward the end of the experiment, the FEA is significantly unconservative while the limit-load analysis gives good agreement with the experiment.

The applied J-displacement curves for a typical I-beam specimen were shown in Figure 4.19. The J-R curve in Figure 4.27a was used to determine crack extension. Figure 4.33 shows the measured crack extension in the web as a function of displacement for a number of specimens including specimen A-18, compared to the predicted crack extension for specimen A18. Note that these specimens had different initial crack configurations and are therefore not exactly replicate specimens. The predicted crack extension using the J-R curve agrees with the experiments at smaller crack extension. However, at larger crack extension, the predicted crack extension is less than the experimental data indicate. The rate of increase of the crack length is clearly less than the experiments indicate. The inaccuracy is excessive and unconservative, and should adversely affect the ability to predict the load displacement curve. The inaccuracy is probably due to underestimating the applied J at larger displacements. The inaccuracy may be due to the complexity

of the I-beam cracks and the FEA model relative to the cope hole cracks and FEA model, or it may be due to the effect of bending as opposed to tension. For example, it is known that tension specimens give higher J-R-curves than bending specimens [4.20]. The bending specimen J-R curves often tends to decrease in slope at large crack extension. Therefore, the crack extension will be greater for a given level of J than in a tension specimen. These analyses are using J-R curves that are extrapolated beyond the range of crack extension in the J-R curve tests. Therefore the tearing modulus at large crack extensions is not known.

Figure 4.34 shows the stationary crack load-displacement curves predicted using FEA for the HSLA-80 steel I-beam specimen A18. These FEA results are labelled contour 1 through contour 9, where "contour" refers to a particular crack configuration that was observed in the experiment as the crack grew. The particular crack contours for this specimen A18 were shown in Figure 3.14. These results were generated using the fully detailed FEA model shown in Figure 4.16.

The predicted load-displacement curve also is shown on this graph. The predicted curve is pieced together by connecting points along the FEA load-displacement curves for the stationary-crack contours. The displacement at which the predicted curve jumps to the next stationary-crack curve is determined from the predicted crack extension vs. displacement data in Figure 4.33. The predicted curve can be compared to the experimental load-displacement curve, which is also shown on Figure 4.34. Points corresponding to the particular crack contours are indicated along the experimental curve.

The FEA/J-R curve analysis adequately predicts the beginning part of the descending branch of the load-displacement curve, up to a deflection of d/d_y of 2. For example, propagation into crack configuration (contour) 4 is predicted in at d/d_y of 1.75, while the experimentally observed value for this contour is d/d_y of 2.06. However, at displacements exceeding d/d_y of 2, the experimental curve begins to decrease much more rapidly. For example, the predicted $d/d_y = 3.5$ for contour 6 is much greater than the $d/d_y = 2.5$ at which that contour was experimentally observed. Also, the load is overpredicted by a factor of 2 at d/d_y of 3 and by a factor of 6 at d/d_y of 5.

Figure 4.35 shows the simple limit-load solution, based on the FEA predicted crack extension history shown in Figure 4.33. The resulting load-displacement curve is in better agreement with the experiments than the result using the FEA for load, but the descending branch is still significantly overestimated.

Based on the analysis of the CCT specimens for which there is a solution for J, the J obtained from finite-element analysis was deemed to be much better than the J estimated from the reference stress methods. Based on analysis of the cope-hole specimens and I-beam specimens, the tearing stability analysis method using a J-R curve is conservative (in the early stages of the analysis) when J is measured on compact specimens and applied to structures with larger uncracked ligaments ahead of the crack. However, larger crack extension levels are essential for modelling ductile fracture in the redundant ship structure fabricated from high-toughness steel. For tensile specimens, it appears that the constant tearing modulus of about 200 MPa gives reasonable results. Unfortunately, at larger crack extension levels, the small-specimen J-R curve becomes increasingly unconservative for full-scale bending specimens.

This trend is contrary to the trends which have been observed on small compact specimens with variations in planar size, for small amounts of crack extension. The resistance to crack extension, i.e. the J-R curve, tends to increase in magnitude of J and slope as the size of the uncracked ligament increases [4.20]. (This is in contrast to the size effects in cleavage and transition-range fracture, where larger specimens have lower apparent toughness.) Thus for fully-plastic ductile fracture the J-R curve measured on smaller compact specimens underestimates the greater apparent J-R curve on similarly-proportioned but larger specimens. However, Figures 4.33 and 4.35 show that the small-specimen J-R curve overestimates the resistance to crack extension of the large-scale I beam specimens.

4.6 Landes' normalization method

The Landes normalization method [4.11,4.12] was evaluated by analyzing the cope-hole specimens, the CCT specimens, and compact tension (CT) specimens that were used for the J-R curve measurements. The normalization method is based on the principle of load separation. Using this principle, load is represented as a multiplicative function of geometry and displacement according to:

$$P = G(a / W) H(v_{pl} / W) \quad (4-11)$$

where P is load, a is crack length, v_{pl} is plastic displacement, and W is the specimen width. The $G(a/W)$ function is a geometrical function independent of material properties, and the $H(v_{pl}/W)$ function is a material property function independent of specimen geometry. This method of normalization has been experimentally verified by Sharobeam and Landes [4.11].

There is some analogy between the Landes normalization method and the limit-load analysis procedure described in Section 4.2. In the limit-load analysis, the $G(a/W)$ function is taken into account in the mathematical model for the limit load and how it changes with crack length. In the limit-load analysis, the $H(v_{pl}/W)$ function is essentially the flow stress. Thus, the advantage of the Landes normalization method is that the $H(v_{pl}/W)$ function can include the effects of discontinuous yielding and strain hardening which vary with plastic displacement, whereas the limit-load analysis assumes a rigid-perfectly-plastic material.

Several standard test specimen geometries have known $G(a/W)$ functions. In this case, the load-displacement record can be divided by the $G(a/W)$ function to generate the geometrically independent material property function, $H(v_{pl}/W)$. The $H(v_{pl}/W)$ function can then be coupled with a $G(a/W)$ function for a new specimen geometry (of the same material) and a load-displacement curve can be generated.

The $G(a/W)$ function for the cope-hole geometry was unknown. This would be the case for typical critical ship structural details as well). In these non-standard geometry cases, it is necessary to generate the $G(a/W)$ function using finite element methods. The typical $G(a/W)$ has the form [4.12]:

$$G(2a / W) = B W \left(\frac{2b}{W} \right)^{\eta_{pl}} \quad (4-12)$$

where B is the specimen thickness and W is the specimen width. The a/W ratio is a measure of the relative portion of the gross section that is cracked. The exponent, η_{pl} , commonly referred to as the eta factor, is the ratio of J to plastic work per remaining ligament area, as described in Section 4.4. For tension specimens, eta is about 1 and for bending and CT specimens, eta is about 2. The reason for this difference is that the load for a tensile specimen is proportional to the remaining ligament, b, while the load for a bending specimen is proportional to the ligament squared.

On typical flat test specimens, W is the width of the panel. However, in the case of intersecting structure, it is important to include the whole gross section in an effective W, as if the various parts of the intersecting structure were disconnected and laid side by side. Such intersecting structure is common in critical ship structural details, as discussed in Section 2.1. For cases where part of the critical detail cross section includes continuous plating such as the side shell, some assumptions must be made about the effective W. For the cope-hole specimens, the effective width W included the minimum width of the stiffeners added to the width of the main test panel. Note that the minimum width occurs at the top of the cope-hole (weld-access hole), even though this point is not in the same plane as the crack. The remaining ligament, b, is defined in terms of this effective W, i.e. (W -a).

The $G(a/W)$ function can be defined by conducting a series of stationary blunt notch tests with a series of notch lengths. Alternatively, the $G(a/W)$ function for a non-standard geometry can be defined from FEA simulations of the stationary-crack load displacement curves. Reference [4.11] outlines the procedure for determining the $G(a/W)$ function in detail.

Figures 4.29 and 4.31 showed stationary-crack load-displacement curves generated using the finite element model of the cope hole specimen for the HSLA-80 and EH-36 materials. In Figure 4.36 these curves are shown as a function of plastic displacement. Note that each curve is nearly proportional to the others.

The principle of load separation was applied by dividing all the curves from Figure 4.36 by the curve associated with the largest crack (smallest $2b_i/W$ ratio). The result is the separation parameters S_{ij} , where "i" relates to the crack size for this load curve and "j" relates to the load curve which was used as the divisor. The separation parameters S_{ij} for the load curves in Figure 4.36 are shown in Figures 4.37. As expected, the values were essentially constant over the entire range of plastic displacement. The relative position of these S_{ij} curves can be thought of as the effect of crack extension or the $G(a/W)$ function. They are like scale factors for a master load curve, which is the $H(v_{pl}/W)$ function.

The average constant values of the S_{ij} values were plotted as a function of the remaining net-section ligament-to-width ratio, $2b_i/W$, as shown in Figure 4.38. η is the exponent of a power law of S_{ij} as a function of $2b_i/W$. As shown in Figure 4.38, the S_{ij} are nearly linearly related to $2b_i/W$, as expected for a tensile specimen, for which η is about 1.0. The average η factor was found to be 0.84 for both materials, with each of the load curves serving in turn as the divisor.

While the $G(a/W)$ function is a property of the geometry of the cracked member, the $H(v_{pl}/W)$ function is a property of the material only which is transferable from one geometry to another. To determine the $H(v_{pl}/W)$ function for the HSLA-80 and EH-36 materials, the load-deflection records from the CCT and CT tests were divided by (normalized by) the appropriate $G(a/W)$ function (see Reference 4.11). Typical load-displacement curves from the J tests on CT specimens are shown in Figure 4.39.

The resulting $H(v_{pl}/W)$ functions are shown in Figure 4.40. Also shown in this figure are the $H(v_{pl}/W)$ functions determined by normalizing the experimental load-deflection curves from the cope-hole specimens by the $G(a/W)$ function determined above. As shown in the figure, the $H(v_{pl}/W)$ function for a given material is essentially independent of the specimen geometry from which the $G(a/W)$ function was determined. The good agreement between the various estimates of the $H(v_{pl}/W)$ function is an indication of the validity and accuracy of the Landes normalization method. The variation between these estimates of the $H(v_{pl}/W)$ function is no larger than the typical variation among replicate tests, such as shown in Figure 3.30.

Finally, the $H(v_{pl}/W)$ functions were coupled with the $G(a/W)$ function and the Landes normalization method was used in a predictive mode to generate load-displacement curves for the cope-hole geometry (with 76.2 mm initial crack size) for both the HSLA-80 and EH-36 specimens. The Landes normalization method requires some way to predict crack extension, typically the J-R curve approach has been used [4.11,4.12].

The J-R curve approach to predicting crack extension was discussed in Section 4.5 above. This method requires finite-element analysis or J estimation to determine J and is subject to all the vagaries described in Section 4.5, especially how to extrapolate the J-R curve to large crack extensions. The error in the J-R curve approach, which includes considerable variation in measured J-R curves from replicate specimens, will affect the apparent accuracy of the Landes normalization method, as it has affected the accuracy of the finite-element and limit-load predictions shown in Figures 4.30, 4.32, and 4.35.

However, as noted by Landes [4.11, 4.12], ductile fracture is not as sensitive to the crack size (only inasmuch as the net section is reduced) and error in the J-R curve approach as would be a brittle fracture or an elastoplastic fracture in the lower transition region. In other words the stress-strain properties are more important than the toughness in determining the load-displacement curve. This observation is certainly consistent with the results of the full-scale ductile fracture tests discussed in Section 3. The load displacement curves from radically different experiments all plot on the same master load-displacement curve (normalized by net section limit load and an associated characteristic displacement), regardless of crack size or toughness level.

The resulting predicted load displacement curves are shown in Figure 4.41. By comparing this agreement with the experiment to the results of FEA and limit-load analysis in Figures 4.30 and 4.32, it is noted that the load at a given displacement is better predicted using the Landes normalization method as compared to FEA. However, the accuracy of the limit-load analysis is almost as good as the accuracy of the Landes normalization method, while the Landes method is considerably more difficult to calculate and requires FEA for unique geometries. All of these methods, Landes' method, limit-load analysis, and FEA to determine load, depend upon J-R curve analysis to predict crack extension. Hence the ability to predict crack extension as a function of displacement, which is not very accurate as shown in Figures 4.28 and 4.33, is the critical issue in predicting load deformation behavior.

4.7 Predicting crack propagation by the crack opening angle

As is the case throughout this report, the following discussion applies only to extensive ductile tearing of ships and other large redundant structures fabricated from structural steel plates with a low-temperature Charpy requirement. Given the crack extension history, it was shown in Section 4.2 that the load-displacement curve can be accurately calculated using simple limit-load analysis. Therefore, as stated above, predicting the crack extension as a function of displacement is the critical issue in predicting load-deformation behavior. It was shown in the previous sections that calculating the J integral or CTOD and using a J-R curve approach for extended crack propagation in complex ship structural details requires finite-element analysis and is very difficult and time consuming. In the end this approach is not even very accurate.

As shown in Section 3, the I-beams, box-beams, and cope-hole specimens of both materials exhibited the same constant rate of crack-opening displacement with respect to crack extension. This rate is called the crack-opening angle (COA), and in all of these experiments it was about 24 percent radian (13 degrees), e.g. see Figure 3.27. Many other researchers have shown similar results in tearing of thin steel and aluminum plates, e.g. references [4.22-4.26]. Based on this constant COA concept, a simple kinematic model was developed based on the experimental observations.

The model is based on d_0 , the minimum observed displacement at peak load, just prior to significant crack extension (i.e. more than one or two millimeters) and the descending branch of the load-displacement curve. In the bending tests, d_0 always occurred at 1.5 times the "yield displacement", i.e. the displacement at which the yield stress is reached on the outer fibers of the gross section. (This displacement was chosen for the normalization because it can be easily calculated from strength of materials equations. It is about two-thirds of the displacement at peak load, d_0 .)

For the tensile specimens (CCT and cope-hole specimens) it was noted that d_0 was 4 mm for the HSLA-80 steel and 6 mm for the EH-36 steel. Note that the toughness of the HSLA-80 steel is almost twice as great as the EH-36, so d_0 , which is an indication of the ductility, apparently has more to do with the Y/T ratio of the steel than the toughness. For cracked sections with a net-section to gross-section area ratio greater than the Y/T ratio, it is possible to achieve gross-section yielding and then much higher d_0 , as shown in Figure 3.23 for the EH-36 steel. The development of gross-section yielding is very desirable and the possibility for gross-section yielding must be analyzed for each cracked cross-section. However, the following model conservatively assumes net section collapse.

For the tensile tests (CCT and cope-hole tests), the displacement, d , on the overall gage length is essentially the same as the $CTOD_5$ as shown in Figure 3.32. Therefore the displacement is concentrated on the crack plane. This displacement is equal to:

$$d = d_0 + COA (\Delta a) \quad (4-13)$$

where Δa is the crack extension and the other terms were defined above.

For the bending tests, the displacements were measured at various locations, but it was noted that all displacements increased approximately in proportion to one another. The beams formed a plastic hinge on the crack plane and all displacements resulted primarily from rotation, Θ , of this hinge. At the point where the yield stress is reached on the outer fibers of the gross section, Θ_0 is equal to 3.2 percent radian. Taking the depth of the beam as 190 mm and assuming a linear displacement gradient, the "effective average" displacement at the outer fibers, d_y , is about 6 mm. The displacement at peak load, d_0 , is equal to 1.5 d_y or about 9 mm.

Figure 4.43 shows the results of the predicted load-displacement curves using the COA (Equation 4-13) and the simple limit-load analysis for the I beam specimen A-18. The COA was 24 percent and the d_0 was 9 mm for the HSLA-80. Figure 4.43 is normalized by the plastic moment on the net section and d_y , and therefore is representative of a wide range of bending experiments, including the box sections. This model gives reasonable agreement with the experimental data for the bending experiments as well as tension experiments. Note that the load-displacement curve can be calculated relatively easily with a spreadsheet using this COA/limit-load method..

Figure 4.43 shows that the load-deflection curve for the box beam follows the same normalized load-deflection curve for the I beams except after peak load, where the load curve for the box plateaus while the load continues to drop for the I beam. This difference is clearly where the large crack in the box beam encounters the second flange. The crack does not easily penetrate the second flange because the web is intercostal (not continuous) through the flange. Thus, the second flange is an effective but temporary crack arrestor. After sufficient deformation, the crack bursts through the second flange in a catastrophic manner and the load drops to a fraction of the peak load which is similar to the fraction associated with the I beam at that level of deformation. It would be interesting to do more experiments to characterize the amount of deformation it would take to penetrate various types of crack arresters.

4.8 References

- 4.1 Reemsnyder, H.S., "Fatigue and Fracture of Ship Structures", Proceedings: Workshop and Symposium on the Prevention of Fracture in Ship Structure, March 30-31, 1995, Washington, D.C., Marine Board, Committee on Marine Structures, National Research Council, 1996.
- 4.2 Ainsworth, R.A., and Budden, P.J., "Recent Developments in the R6 Failure Assessment Diagram Approach to Fracture Analysis", Proceedings of the 2nd Griffiths Conference on Micromechanisms of Fracture and Their Structural Significance, 13-15 September 1995, Sheffield U.K., pp. 173-186, 1995.
- 4.3 Shih, C.F., "Relationships Between the J-Integral and the Crack Opening Displacement for Stationary and Extending Cracks", Journal of the Mechanics and Physics of Solids, Vol. 29, No. 4, pp. 305-326, 1981.
- 4.4 Kumar, V., German, M.D., and Shih, C.F., "An Engineering Approach for Elastic-Plastic Fracture Analysis", EPRI Report NP-1931, Electric Power Research Institute, Palo Alto, CA, 1981.
- 4.5 Kumar, V., German, M.D., Wilkening, W.W., Andrews, W.R., deLorenzi, H.G., and Mowbray, D.F., "Advances in Elastic-Plastic Fracture Analysis", EPRI Report NP-3607, Electric Power Research Institute, Palo Alto, CA, 1984.
- 4.6 Kumar, V., and German, M.D., "Elastic-Plastic Fracture Analysis of Through-Wall and Surface Cracks in Cylinders", EPRI Report NP-5596, Electric Power Research Institute, Palo Alto, CA, 1988.
- 4.7 Zahoor, A., Ductile Fracture Handbook, Volume I: Circumferential Throughwall Cracks", EPRI Report NP-6301-D, Electric Power Research Institute, Palo Alto, CA, 1989.
- 4.8 Schwalbe, K.-H., "A Simple Engineering Treatment of Center-Cracked Tension Panels in the Regime of Non-linear Fracture Mechanics Under Plane Stress Conditions", GKSS 84/E/38, GKSS Research Center, Geesthacht, 1984.
- 4.9 Schwalbe, K.-H., and Cornec, A., "The Engineering Treatment Model (ETM) and its Practical Application", Fatigue and Fracture of Eng. Materials and Structures", Vol. 14, pp.405-412, 1991.
- 4.10 Ainsworth, R.A., "The Assessment of Defects in Structures of Strain Hardening Materials", Engineering Fracture Mechanics, Vol. 19, P. 633, 1984.

- 4.11 Sharobeam, M. H. and Landes, J. D., "The Separation Criterion and Methodology in Ductile Fracture Mechanics," *International Journal of Fracture*, Vol 47, 1991, pp. 81-104
- 4.12 Lee, K. and Landes, J.D., "Development J-R Curves Without Displacement Measured Using Normalization," *Fracture Mechanics: Twenty-Third Symposium*, ASTM STP 1189, Ravinder Chona, Eds., American Society for Testing and Materials, Philadelphia, 1993, pp. 133-167.
- 4.13 Garwood, S.J., and Phaal, R., "Developments and Revisions to BS PD6493: 1991 Assessment Procedures", *Proceedings of the 2nd Griffiths Conference on Micromechanisms of Fracture and Their Structural Significance*, 13-15 September 1995, Sheffield U.K., pp. 187-202, 1995.
- 4.14 Poe, C.C., Jr., "Fatigue Crack Propagation in Stiffened Panels", *Damage Tolerance in Aircraft Structures*, ASTM STP 486, American Society for Testing and Materials, Philadelphia, pp.79-97, 1971.
- 4.15 Chen, X.G., Albrecht, P., Wright W., "Stress Intensity Factors for Three-tip Cracks in Bridge Structures", Part 1, FHWA Interim Report, May 1992.
- 4.16 Formby, C.L., and Griffiths, J.R., "The Role of Residual Stresses in the Fracture of Steel," *Proceedings of the International Conference "Residual Stresses in Welded Construction and Their Effects"*, 15-17 November 1977, London, The Welding Institute, Abington Hall, Abington, Cambridge, CB1 6AL, UK, pp. 359, 1977.
- 4.17 Hu, J.M., Albrecht, P., "Limit Load Solution and Loading Behavior of C(T) Fracture Specimen", *International Journal of Fracture*, Vol. 52, pp 19-45, 1991..
- 4.18 Miller, A.G., "Review of Limit Loads of Structures Containing Defects," *International Journal of Pressure Vessels and Piping*, Vol. 32, pp. 107-327, 1988.
- 4.19 McCabe, D.E., and Ernst, H.A., "A Perspective on R-Curves and Instability Theory", *Fracture Mechanics, Fourteenth Symposium - Volume I: Theory and Analysis*, ASTM STP 791, J.C. Lewis and G. Sines, Eds., American Society for Testing and Materials, pp.I-561-I-584., 1983.
- 4.20 Anderson, T.L., *Fracture Mechanics - Fundamentals and Applications*, Second Edition, CRC Press, Boca Raton FL, 1995.

- 4.21 Kanninen, M.F., and Popelar, C.H., Advanced Fracture Mechanics, Oxford University Press, New York, 1985.
- 4.22 Dexter, R.J., "Investigation of Criteria for Ductile Fracture Under Fully-Plastic Conditions", Dissertation, The University of Texas at Austin, December 1992.
- 4.23 Willoughby, A.A., Pratt, P.L., and Turner, C.E., "The Meaning of Elastic-Plastic Fracture Criteria During Slow Crack Growth," International Journal of Fracture, Vol. 17, No. 5, pp. 449-466, October 1981.
- 4.24 Ogasawara, M., "The Crack Tip Opening Angle (CTOA) of the Plane Stress Moving Crack," Engineering Fracture Mechanics, Vol. 18, No. 4., pp. 839-849, 1983.
- 4.25 Demofonti, G., and Rizzi, L., "Experimental Evaluation of CTOA in Controlling Unstable Ductile Fracture Propagation," European Symposium on Elastic-Plastic Fracture Mechanics: Elements of Defect Assessment, Freiburg, Germany, October 9-12, 1989.
- 4.26 Altieri, G.U., Amodio, D., Demofonti, G., and Santucci, G., "F.E. Simulation of Elasto-Plastic Crack Propagation in a Three Point Bending Specimen," 23rd National Symposium on Fracture Mechanics, June 18-20, 1991.

Table 4.1
Summary of Failure Load Predictions for the I-beam Specimens Using PD 6493

(a)
Post Test Predictions Based on Actual Crack Size

SPECIMEN NUMBER	PD6493 PREDICTION			EXPERIMENTAL RESULT		LEVEL 2 ERROR (%)	LEVEL 3 ERROR (%)
	LEVEL 1 MMy	LEVEL 2 MMy	LEVEL 3 MMy	MMy	M/Mfp,net		
L16	0.88	1.07	1.13	1.26	1.15	-15	-10
A1	0.75	0.91	0.96	0.96	1.03	-5	0
A42	0.69	0.86	0.93	0.94	1.08	-9	-1
A34	0.64	0.75	0.81	0.84	1.05	-11	-4
A39	0.61	0.75	0.80	0.78	1.03	-4	3
L9	0.52	0.65	0.68	0.67	1.02	-3	1
A20	0.60	0.72	0.77	0.71	0.95	1	8
A48	0.54	0.66	0.70	0.70	1.03	-5	0
A18	0.49	0.57	0.62	0.71	1.08	-19	-13
A33	0.50	0.62	0.66	0.63	1.00	-1	5
G27	0.29	0.42	0.41	0.47	0.61	-10	-13
G26	0.17	0.28	0.27	0.42	0.68	-34	-36
G4	0.15	0.16	0.12	0.20	1.04	-18	-40

* Nominal Yield Moment, My=592 kN-m for specimens 9, 16, 4, 26, and 27.
My=532 kN-m for all other specimens.

(b)
Comparison of Pre-test and Post-test Analyses

SPECIMEN NUMBER	PRE-TEST PREDICTION				POST-TEST ANALYSIS				PERCENT ERROR			
	a	c	LEVEL 1 MMy	LEVEL 2 MMy	a	c	LEVEL 1 MMy	LEVEL 2 MMy	a	c	LEVEL 1 MMy	LEVEL 2 MMy
L16	71	0	0.85	1.06	71	0	0.85	1.07	0.0	--	3.1	1.3
A1	6	37	0.90	1.11	13	74	0.75	0.91	53.8	50.0	-20.7	-21.5
A42	13	110	0.65	0.80	12	110	0.69	0.86	-8.3	0.0	6.4	6.9
A34	30	94	0.65	0.76	28	100	0.64	0.75	-7.1	6.0	-1.7	-1.2
A39	22	127	0.57	0.71	23	128	0.61	0.75	4.3	0.8	5.9	5.3
L9	52	127	0.52	0.65	52	127	0.52	0.65	0.0	0.0	0.8	-0.2
A20	32	110	0.60	0.71	32	110	0.60	0.72	0.0	0.0	0.0	1.4
A48	36	135	0.51	0.63	28	134	0.51	0.66	-28.6	-0.7	5.8	5.0
A18	51	122	0.52	0.59	64	115	0.49	0.57	20.3	-6.1	-5.4	-3.1
A33	29	138	0.52	0.64	31	143	0.50	0.62	6.5	3.5	-3.5	-3.0
G27	42	127	0.55	0.68	43	110	0.29	0.42	2.3	-15.5	-87.9	-60.5
G26	92	107	0.52	0.61	98	109	0.17	0.28	6.1	1.8	-202.0	-120.5
G4	190	152	0.16	0.13	193	152	0.15	0.16	1.6	0.0	-3.9	20.6

Notes:

- A = Attachment Specimen
- G = Groove Weld Specimen
- L = Longitudinal Weld Specimen

Table 4.2
 Summary of Failure Load Predictions for the box-beam Specimens Using PD 6493

BOX NUMBER	PD6493 PREDICTION		EXPERIMENTAL RESULT	LEVEL 1 ERROR (%)	LEVEL 2 ERROR (%)
	LEVEL 1 M/Mp.net	LEVEL 2 M/Mp.net			
3	0.62	0.82	0.96	-35	-15
8	0.48	0.74	1.04	-54	-29
9	0.80	0.98	1.04	-23	-6
10	0.47	0.60	0.98	-52	-39

Table 4.3
 Summary of Failure Load Predictions for the Cope-hole Specimens Using PD 6493

SPECIMEN	EXPERIMENT	PD6493 PREDICTION			PREDICTION ERROR		
		Level 1	Level 2	Level 3	Level 1	Level 2	Level 3
EH-36 #3	1.04	0.80	0.99	0.99	-23%	-5%	-5%
EH-36 #4	1.08	0.80	0.99	0.91	-26%	-8%	-16%
EH-36 #5	1.06	0.80	0.99	0.91	-25%	-7%	-14%
EH-36 #6	1.07	0.80	0.99	0.91	-25%	-7%	-15%
HSLA-80 #3	1.01	0.80	0.99	1.00	-21%	-2%	-1%
HSLA-80 #4	1.00	0.80	0.99	1.00	-20%	-1%	0%
HSLA-80 #5	1.10	0.80	0.99	1.00	-27%	-10%	-9%
HSLA-80 #6	1.07	0.80	0.99	1.00	-25%	-7%	-7%

Results are shown in terms of P/P_f .

$P_f = 876$ kN for EH-36 specimens with $2a = 50$ mm.

$P_f = 759$ kN for EH-36 specimens with $2a = 76$ mm.

$P_f = 1176$ kN for HSLA-80 specimens with $2a = 50$ mm.

$P_f = 1019$ kN for HSLA-80 specimens with $2a = 76$ mm.

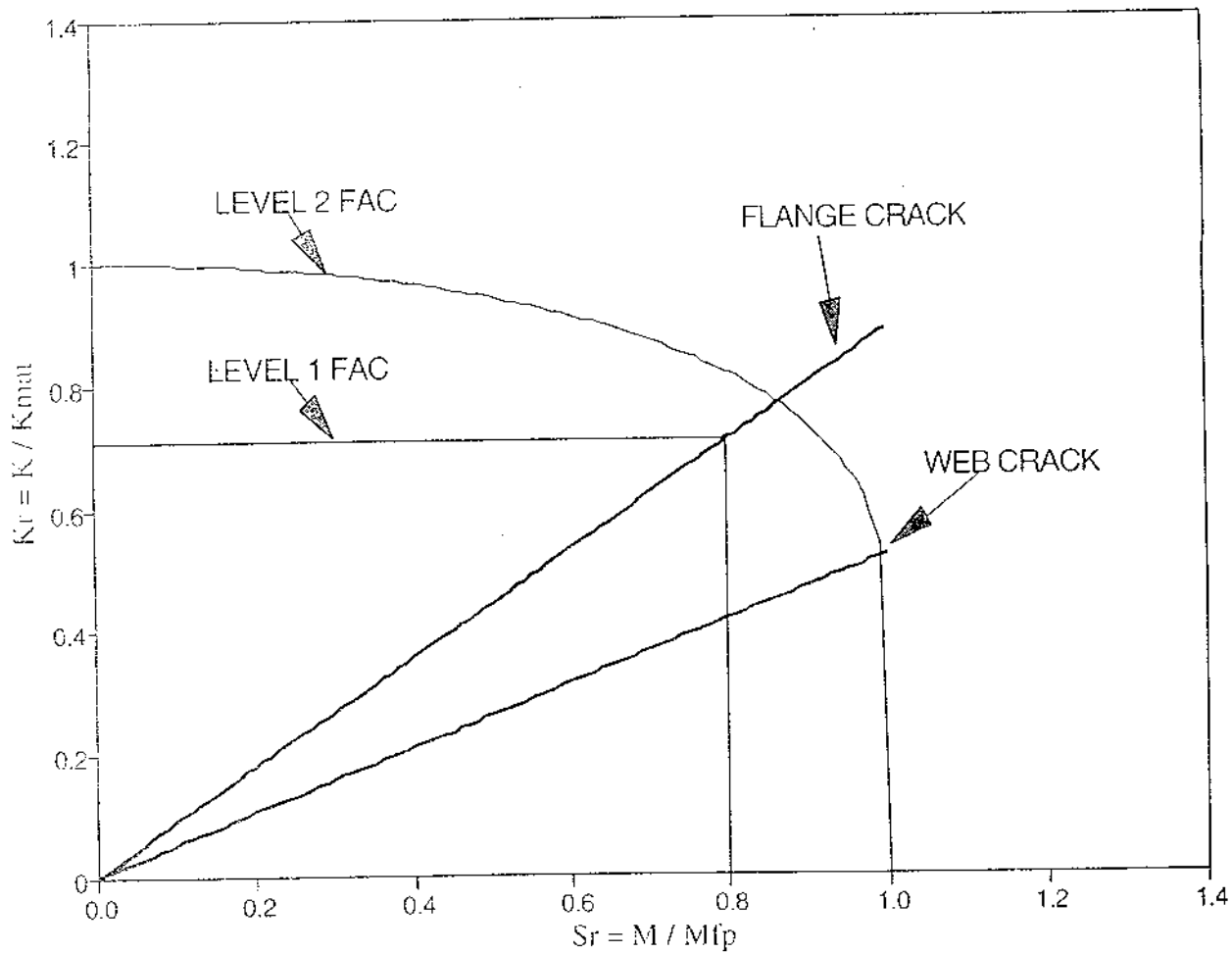


Figure 4.1 Graphical representation of a PD 6493 calculation for an I-beam specimen using the level 1 and level 2 failure assessment diagram

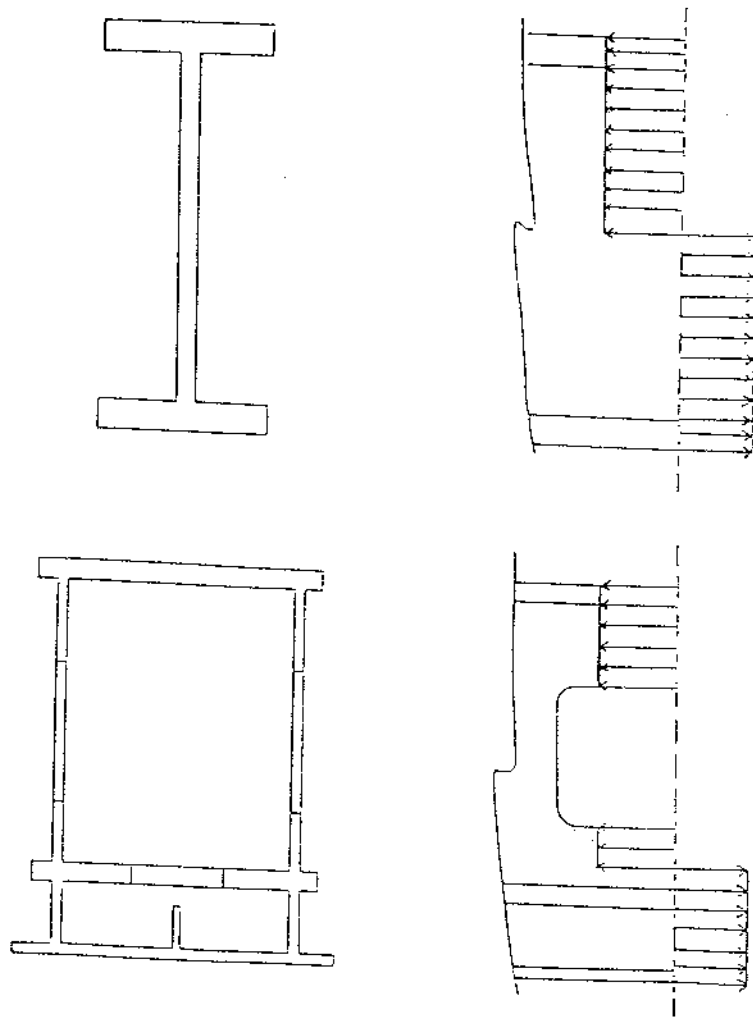


Figure 4.2

Net section collapse occurs when the structural member develops fully-plastic stress distributions. These idealized rectangular stress blocks with the magnitude of the stress equal to the yield stress were used to calculate the limit loads for the I-beam and box beam specimens

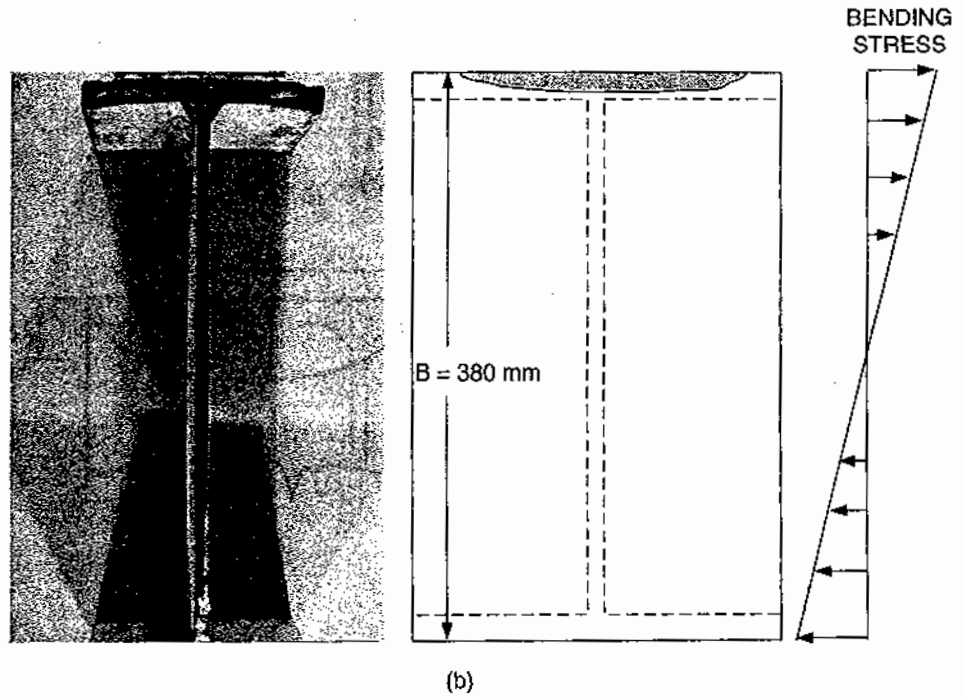
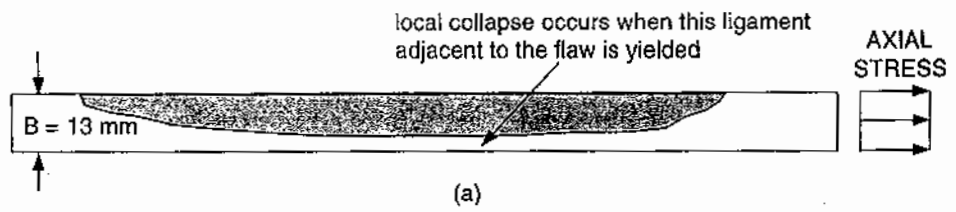


Figure 4.3 Two ways of idealizing a part-through surface crack in the beam flange with respect to thickness B :
 (a) as the flange plate under essentially axial stress; and,
 (b) as a small crack in an idealized monolithic block where B is equal to the depth of the beam.

er develops fully-
 ilar stress blocks
 ess were used to
 n specimens

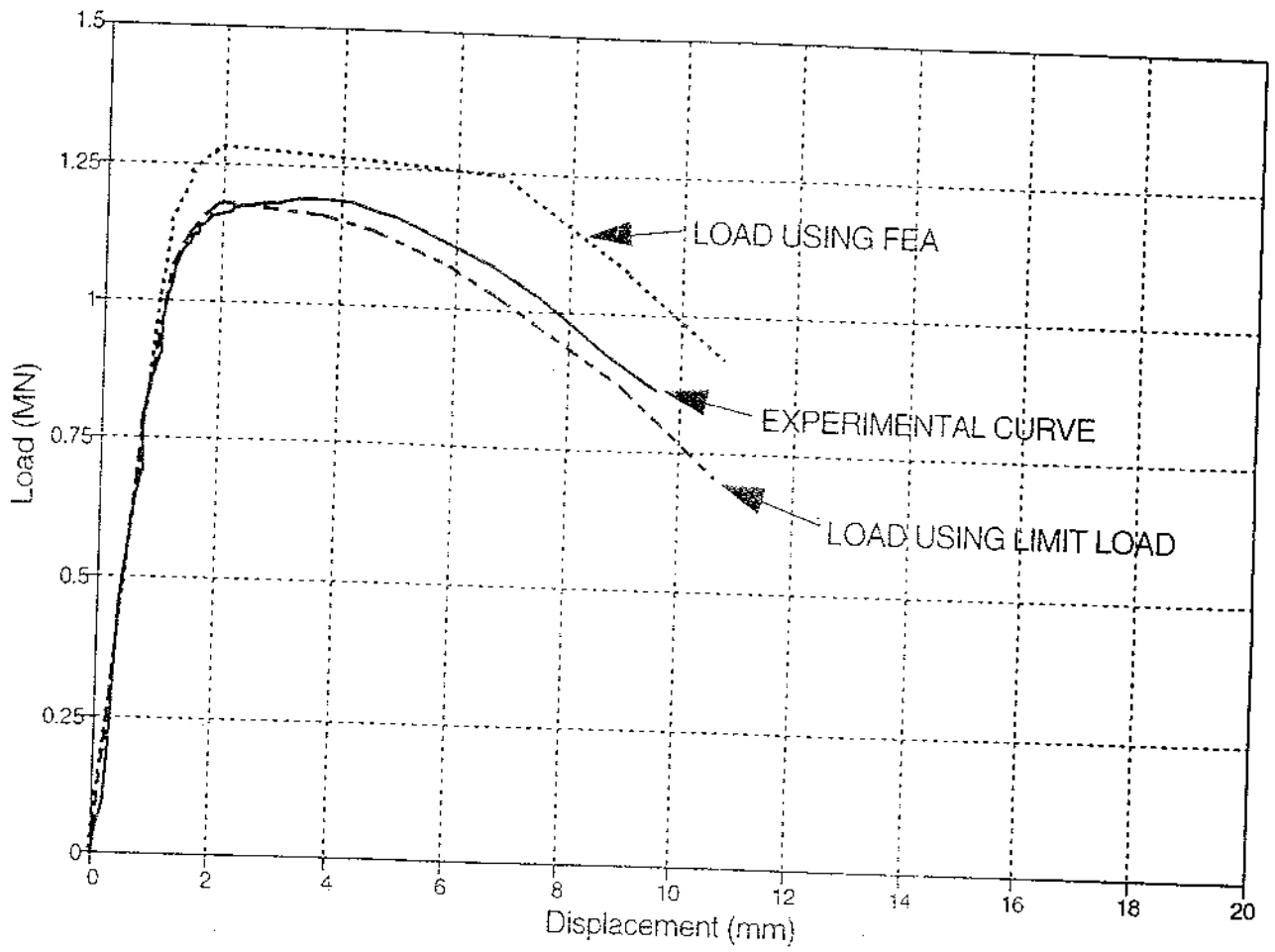


Figure 4.30

Load-displacement curve generated from the crack-extension history from the J-R curve analysis using the finite-element model to compute J only and using a limit-load solution to calculate load for the HSLA-80 cope-hole specimen. Also shown are the experimental result and the finite-element prediction from Figure 4.29

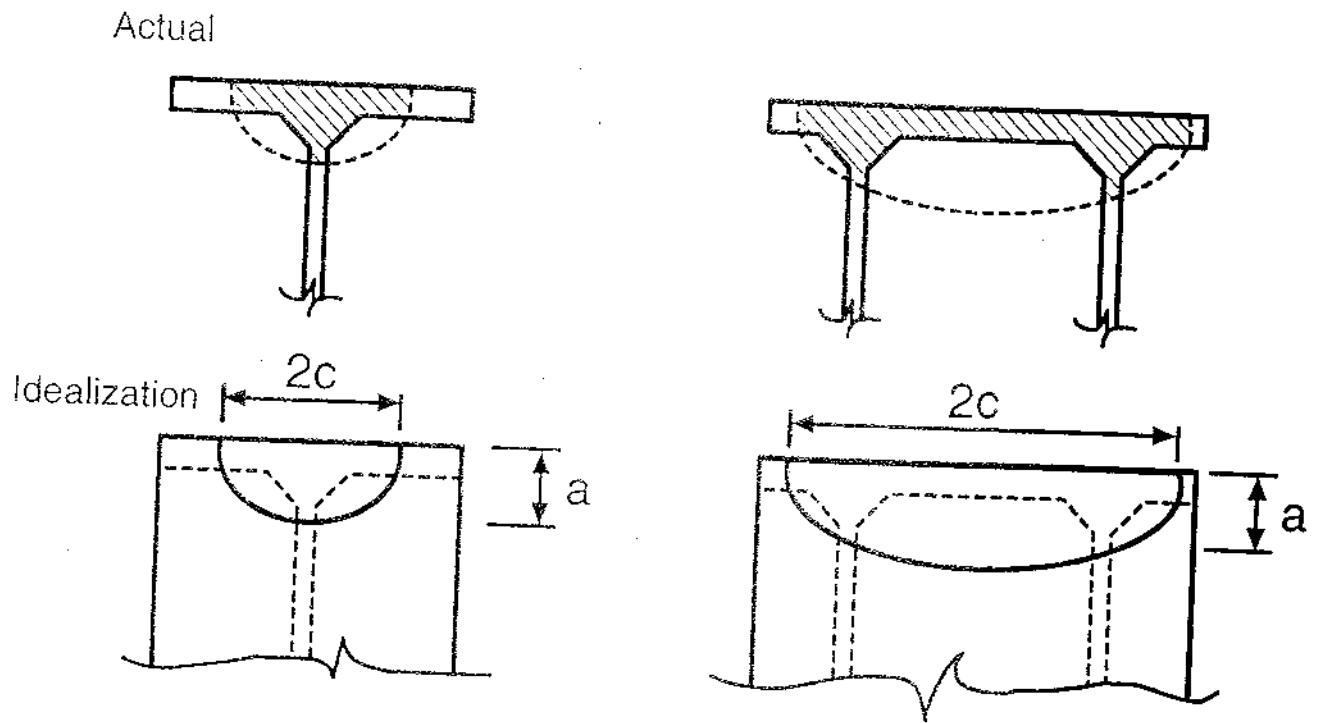


Figure 4.4 Idealization of multi-ended cracks in intersecting structure as a monolithic block using semi-elliptical crack surface crack idealization

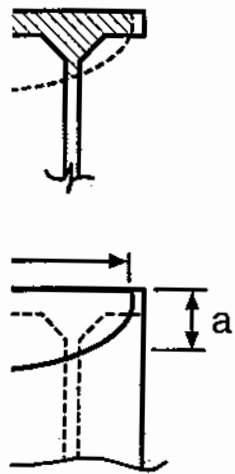


Fig. 4.5 Idealization of a two-ended crack as a quarter-elliptical or corner crack

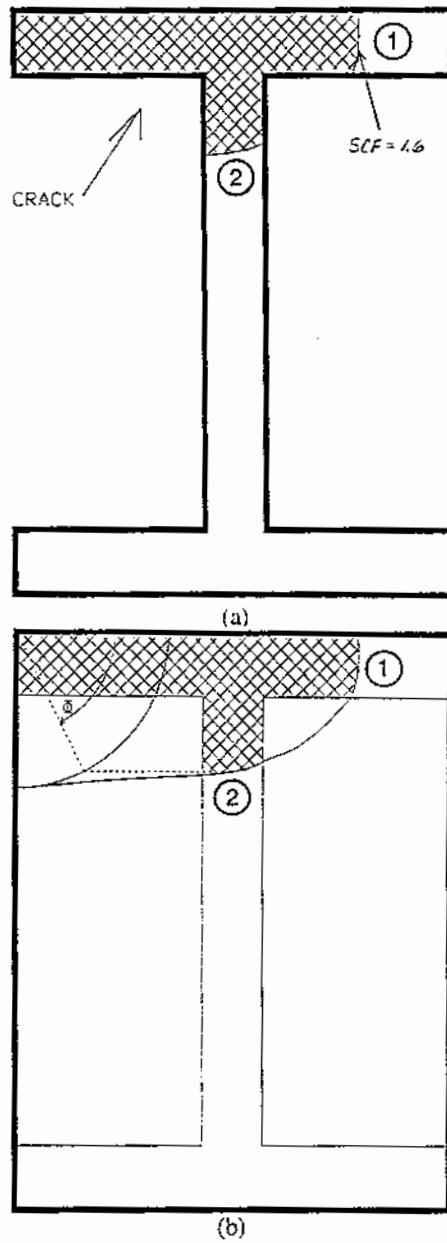


Figure 4.5 Idealization of a two-ended crack as a quarter-elliptical or corner crack (a) showing crack positions and application of the stress concentration factor (SCF); and, (b) the protocol for the angle Φ used in the surface crack equation.

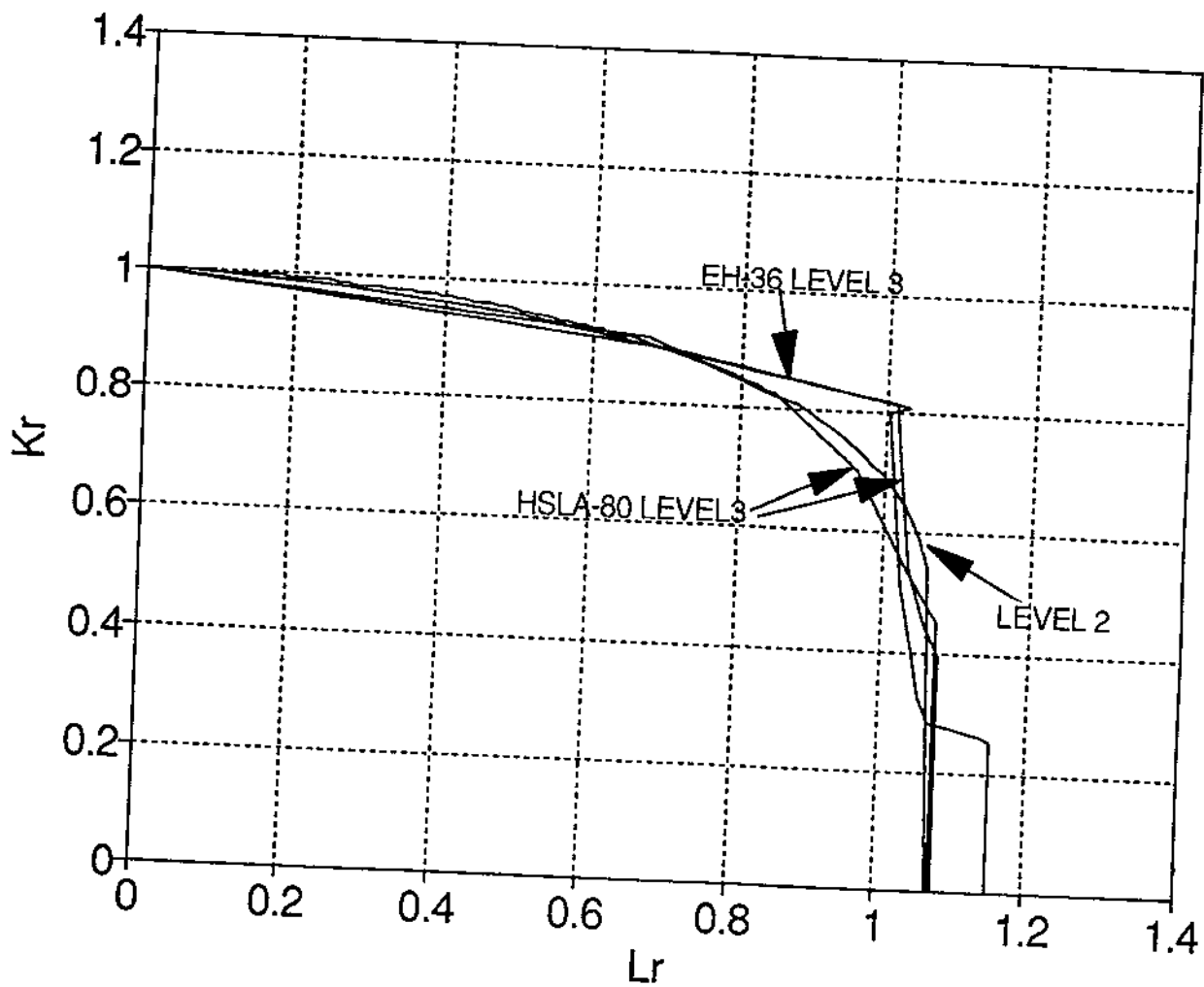


Figure 4.6 Comparison of level 2 and level 3 failure assessment curves for the HSLA-80 and EH-36 materials. HSLA-80 curves generated from two tensile test records are shown to demonstrate the sensitivity of the level 3 curve to variation in tensile properties

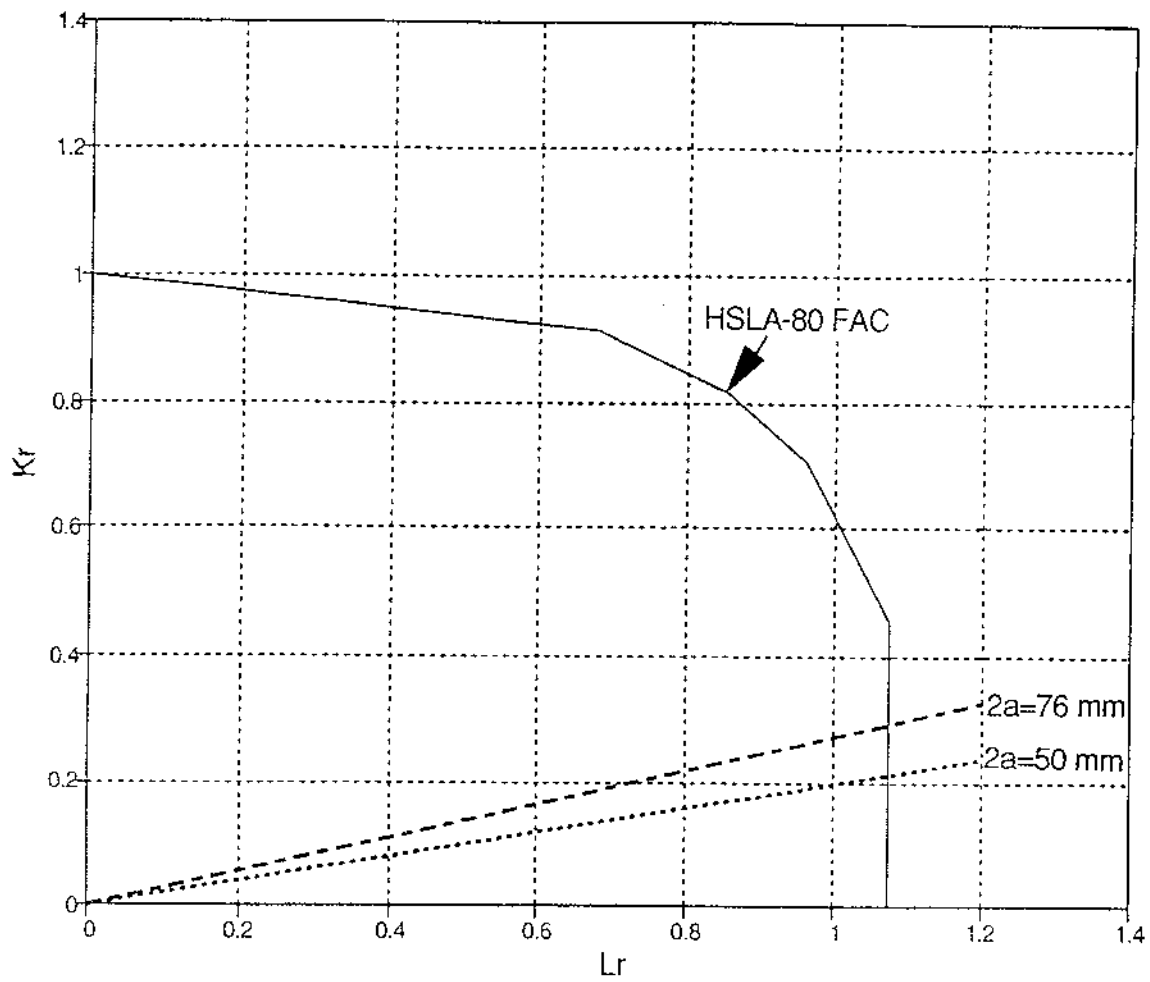


Figure 4.7 Level 3 failure assessment diagram for the HSLA-80 cope-hole specimens

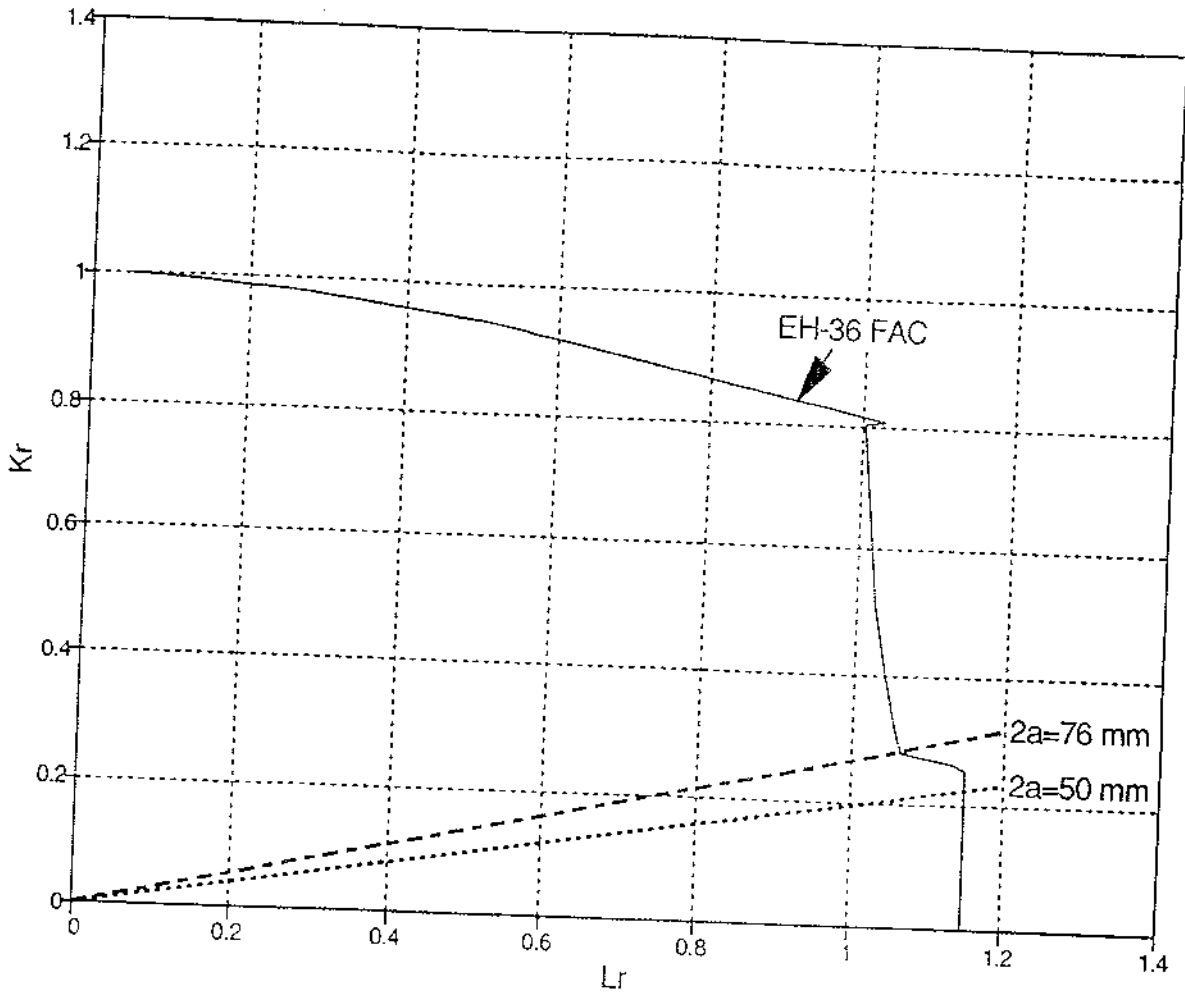


Figure 4.8 Level 3 failure assessment diagram for the EH-36 cope-hole specimens

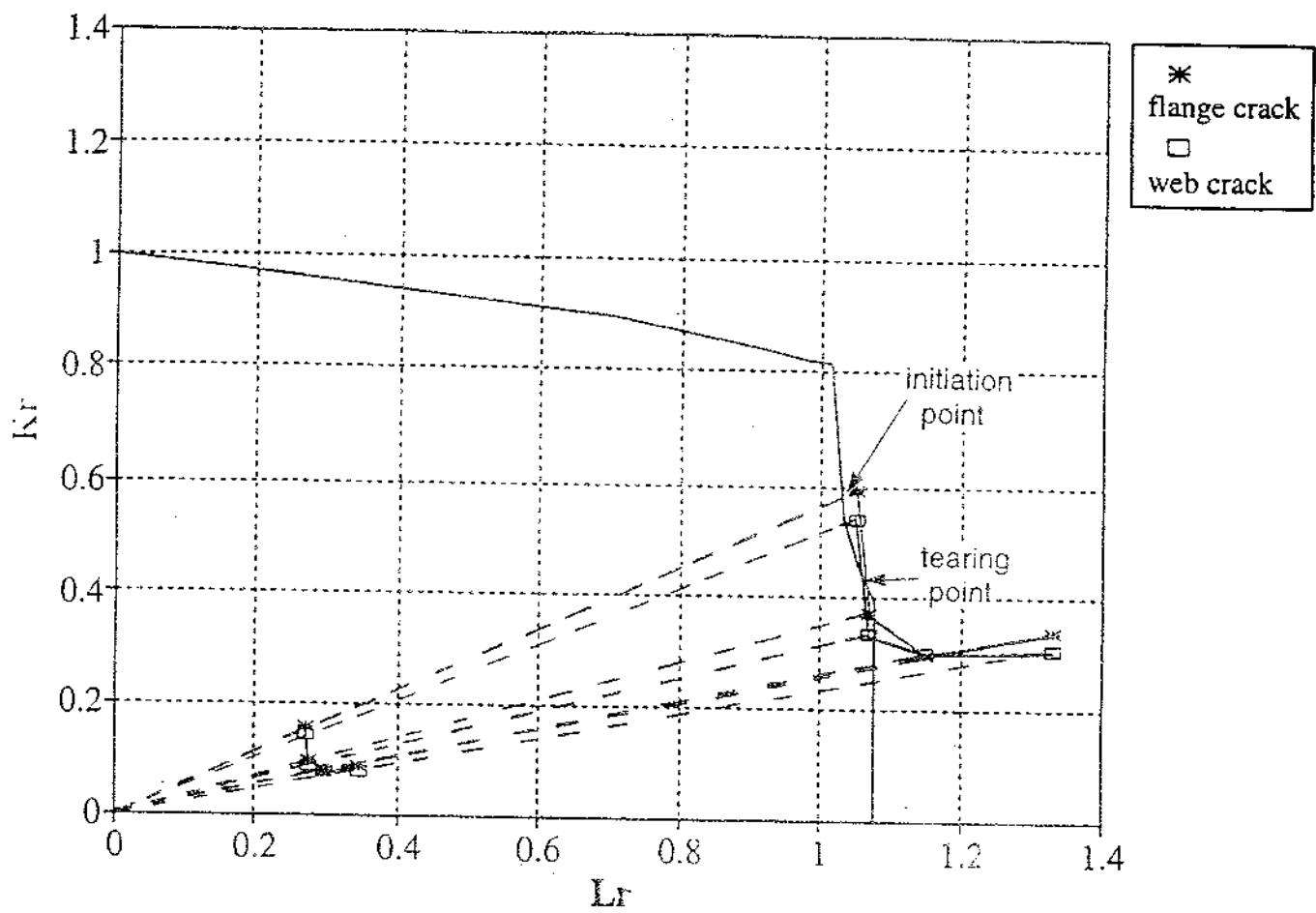


Figure 4.9 Tearing stability analysis for I-beam specimen A18

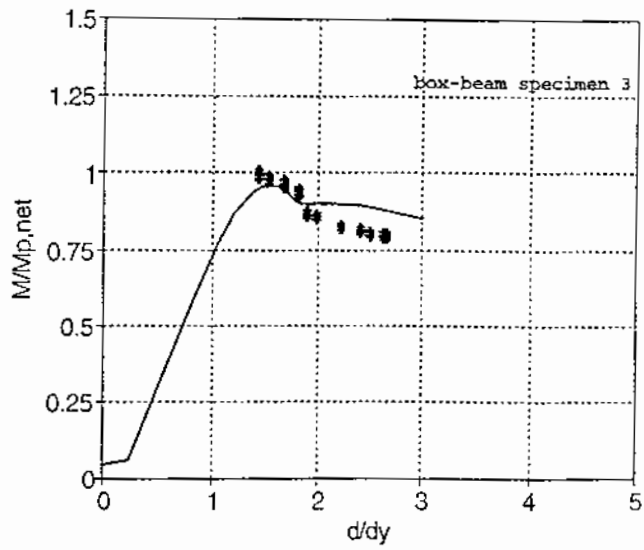
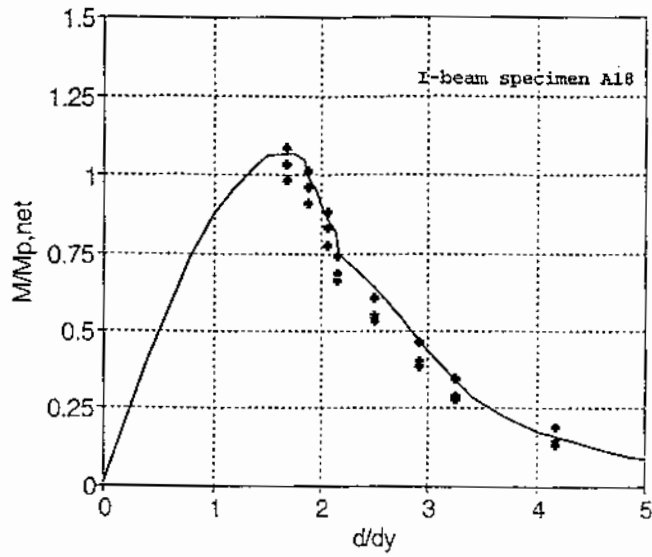


Figure 4.10 Limit-load predictions for I-beam specimen A18 (top) and box-beam specimen 3 (bottom) compared to experimental results (solid lines). Limit load calculations are shown as plus symbols

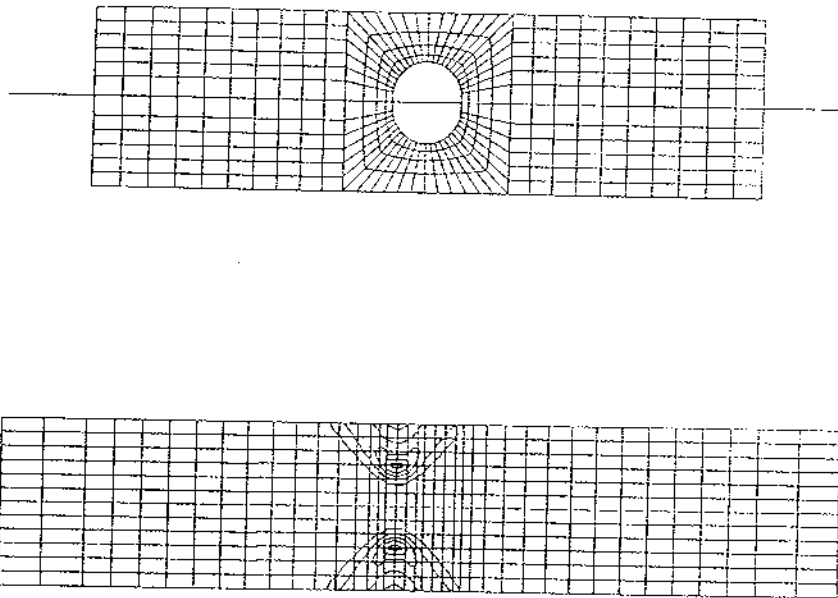


Figure 4.11 Finite-element model of the cope-hole specimen

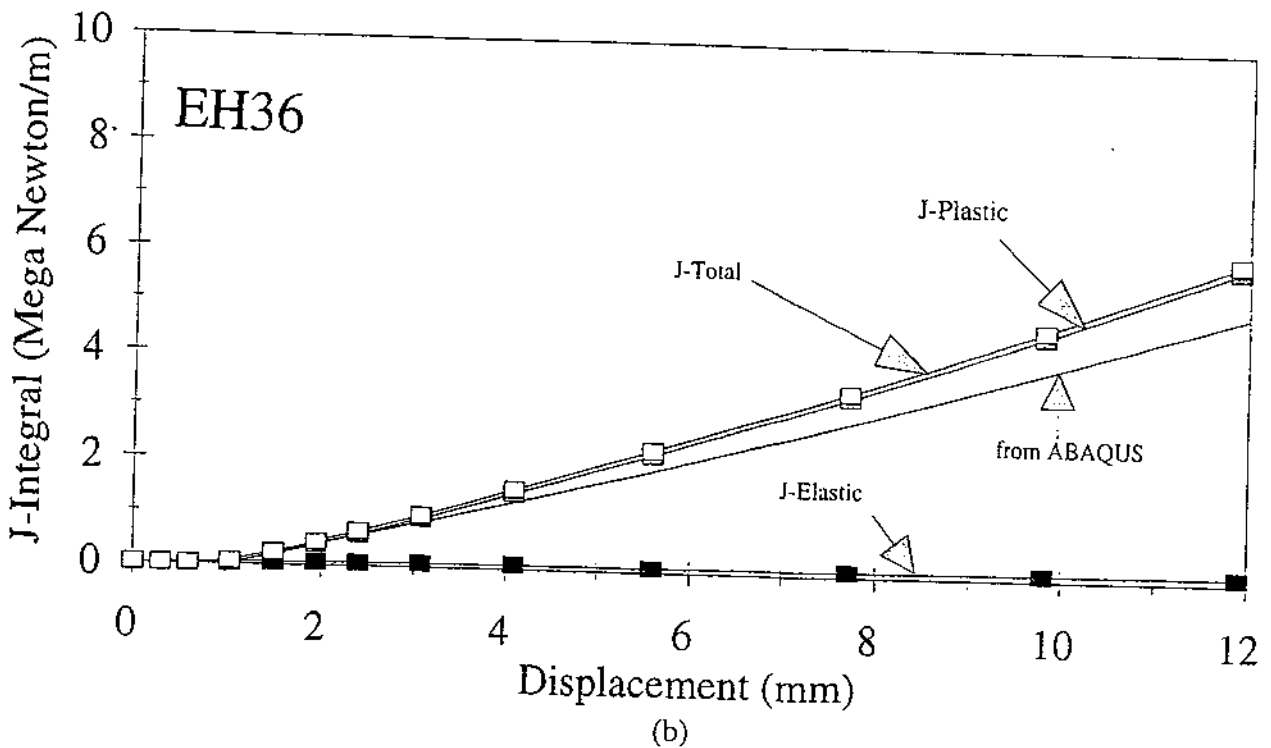
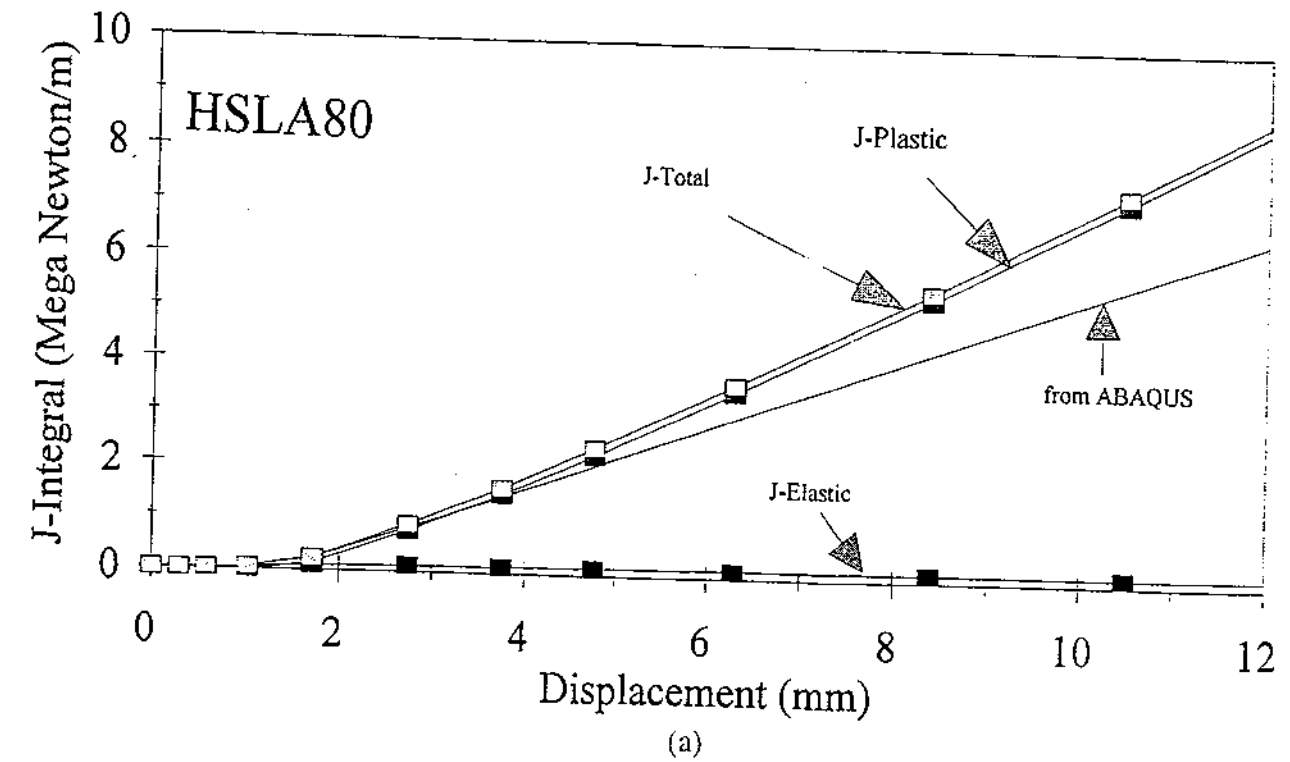
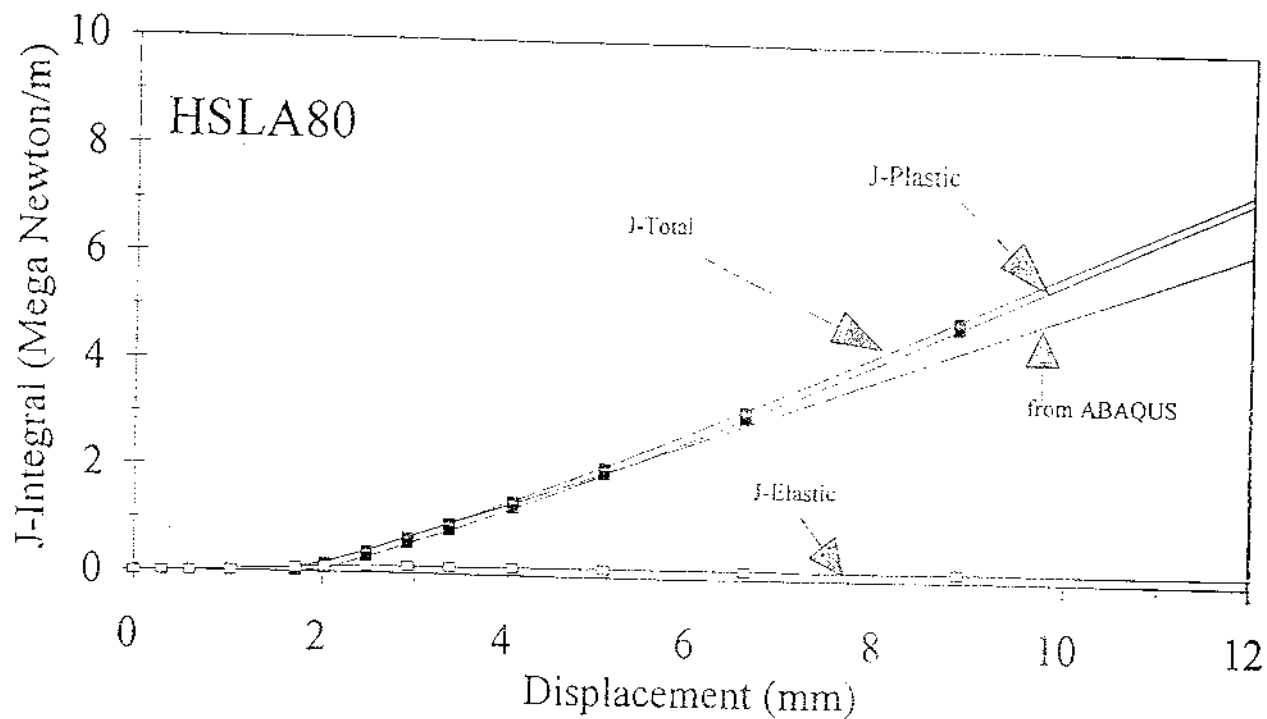
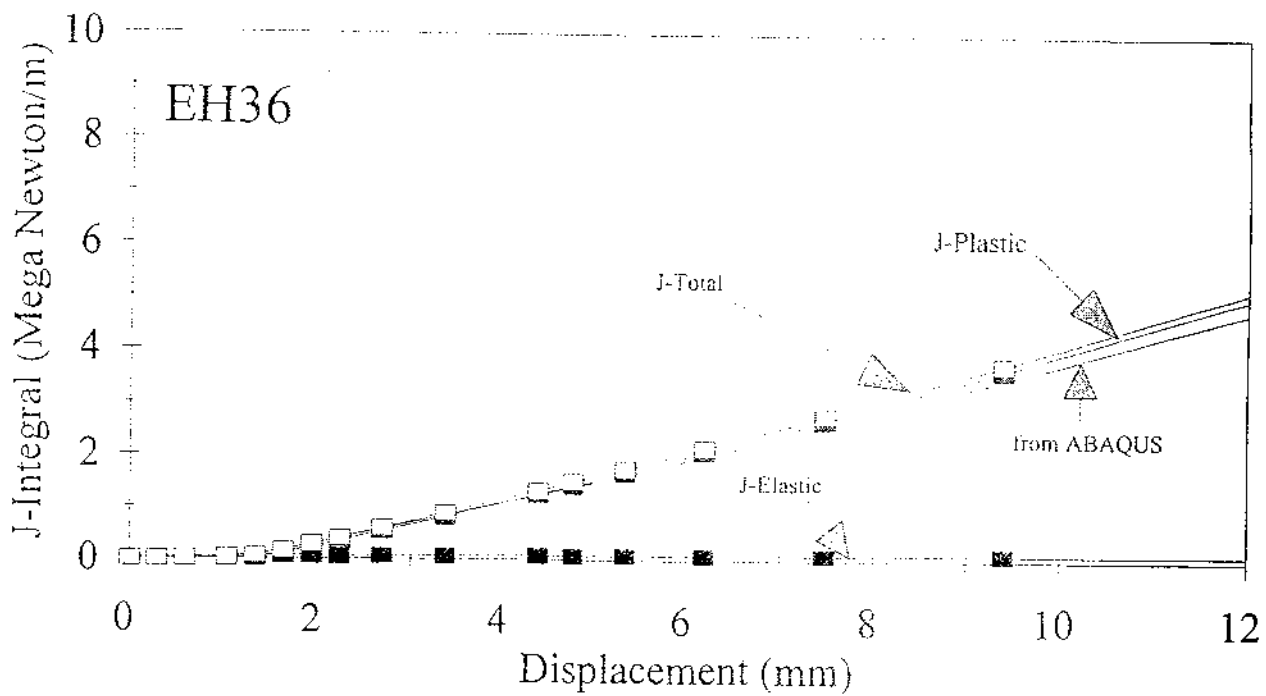


Figure 4.12 J vs. displacement curves computed using finite-element analysis and the contour integral as well as the solution of McCabe and Ernst for (a) HSLA-80 and (b) EH-36 CCT specimens with initial crack sizes of 76 mm

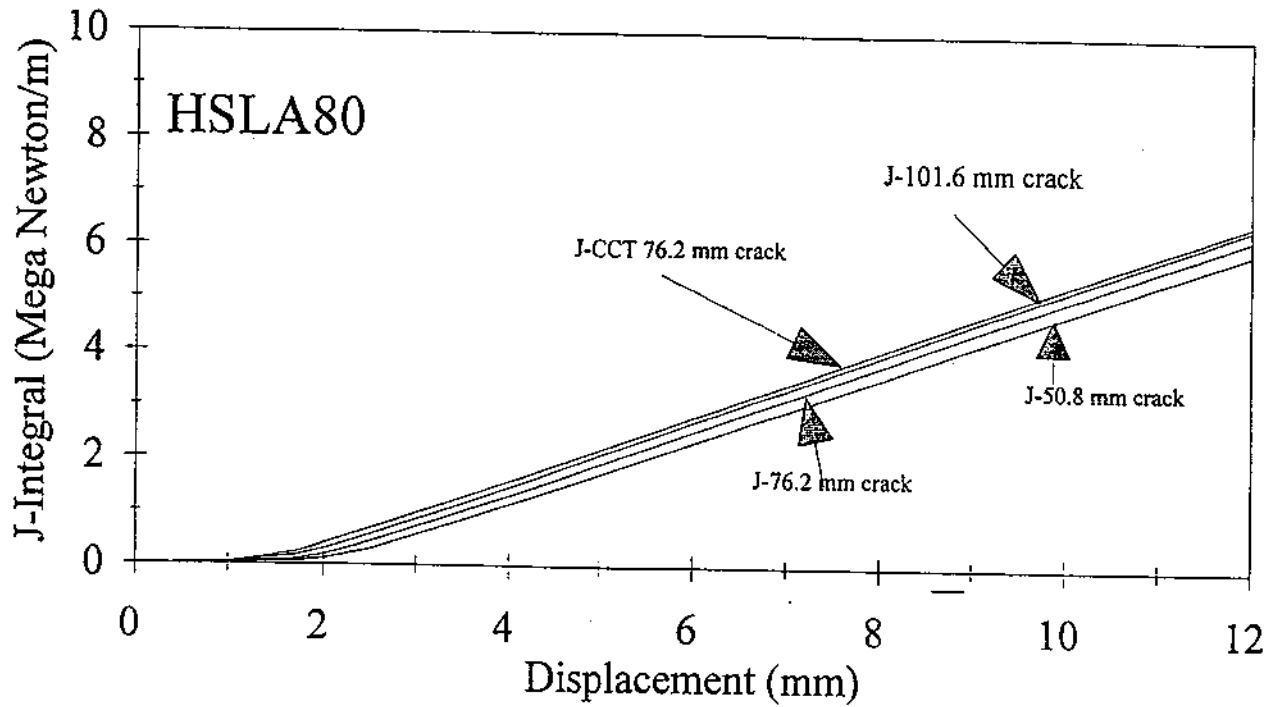


(a)

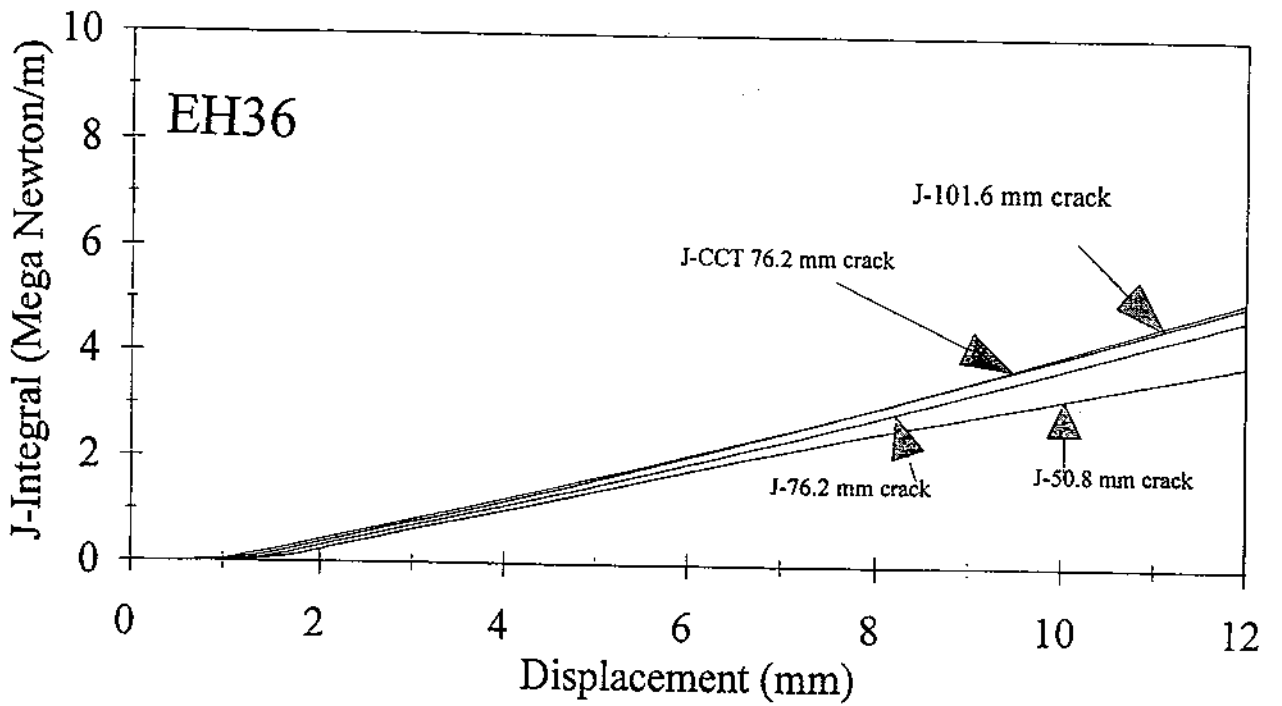


(b)

Figure 4.13 J vs. displacement curves computed using finite-element analysis and the contour integral as well as the solution of McCabe and Ernst for (a) HSLA-80 and (b) EH-36 cope-hole specimens with initial crack sizes of 76 mm obtained from finite-element analysis



(a)



(b)

Figure 4.14

J vs. displacement curves computed using finite-element analysis and the contour integral for several initial crack sizes for the (a) HSLA-80 and (b) EH-36 cope-hole and CCT specimens

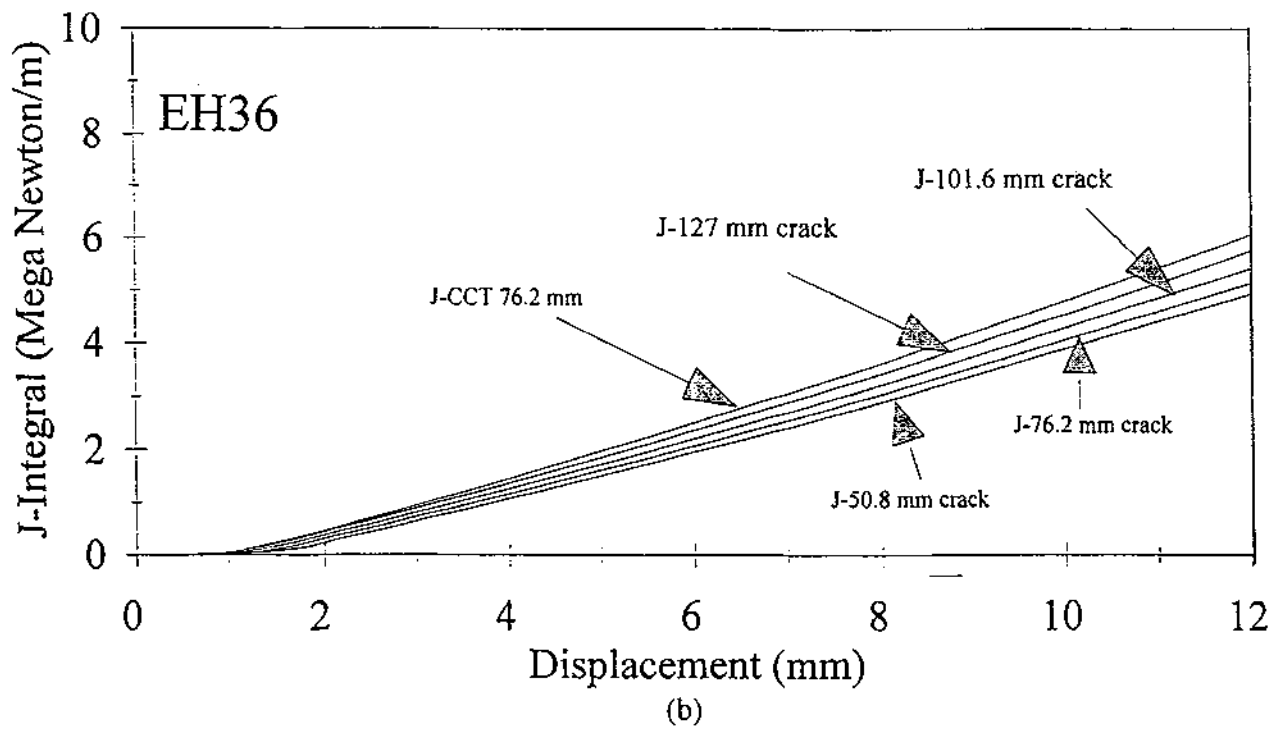
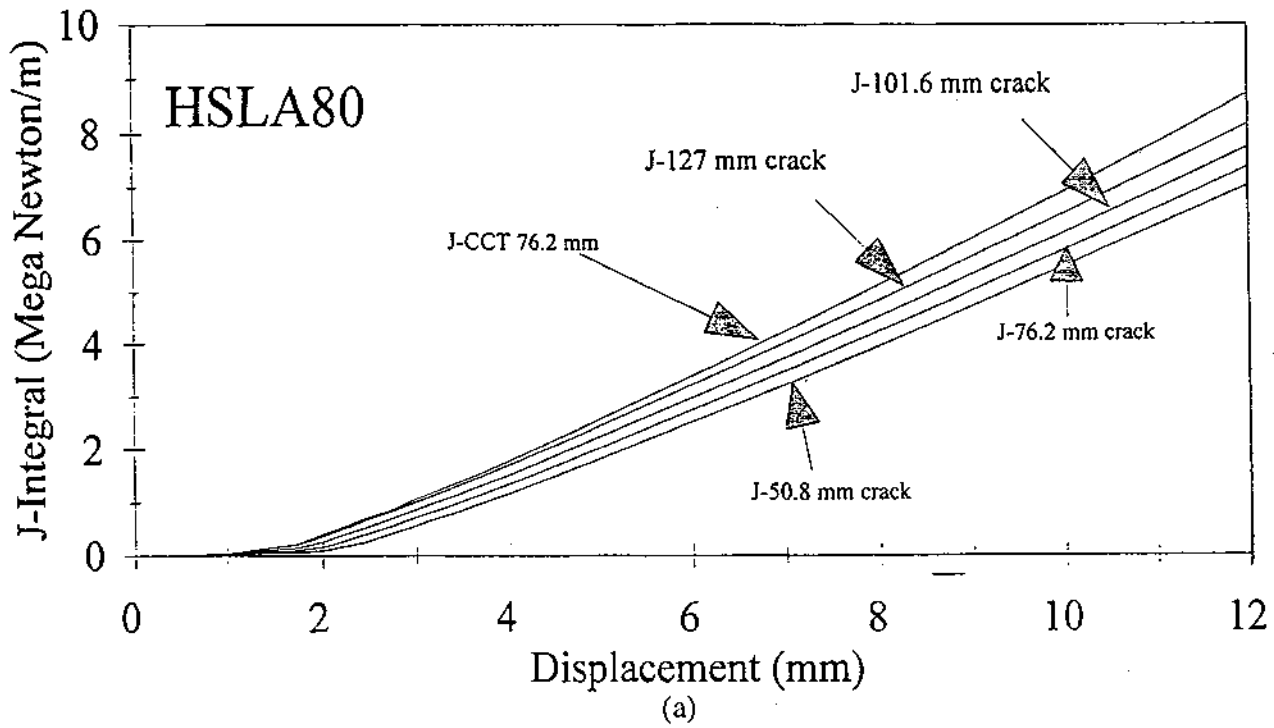


Figure 4.15 J vs. displacement curves for the (a) HSLA-80 and (b) EH-36 cope-hole and CCT specimens calculated using the McCabe and Ernst solution.

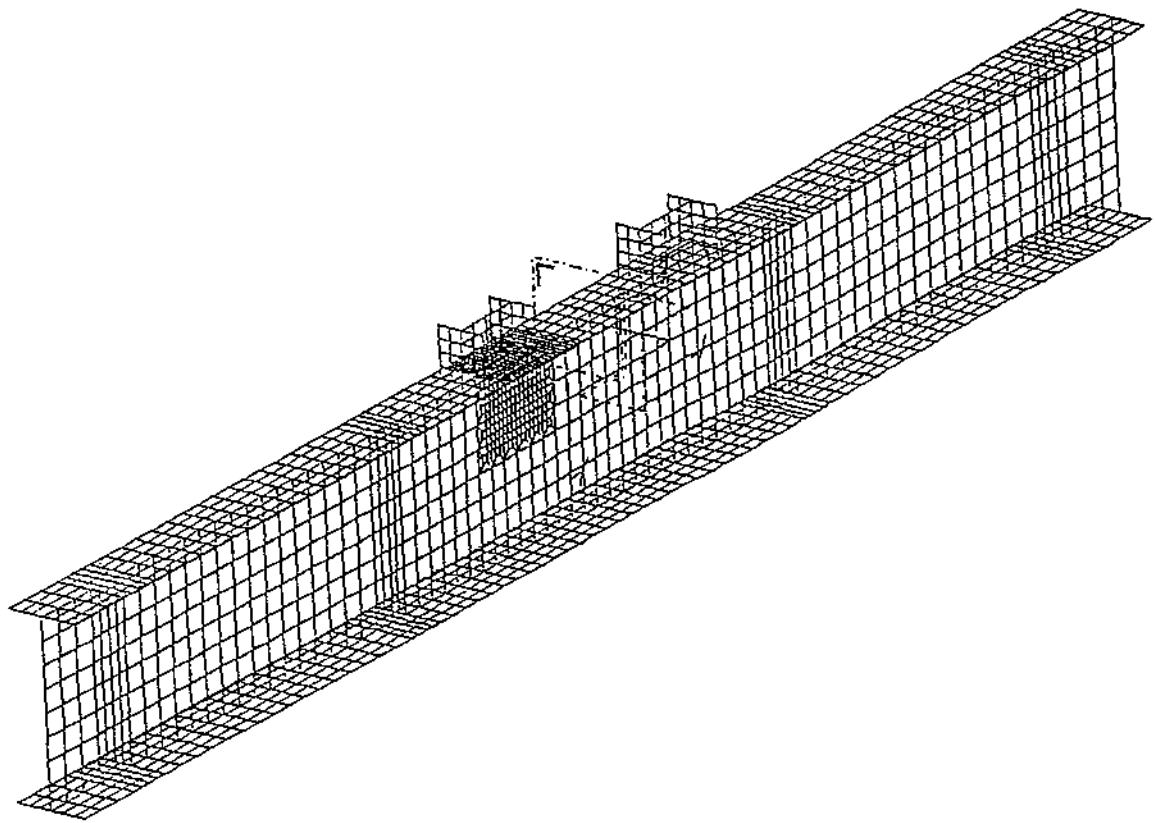


Figure 4.16 Refined finite-element model of I-beam specimen incorporating attachment details

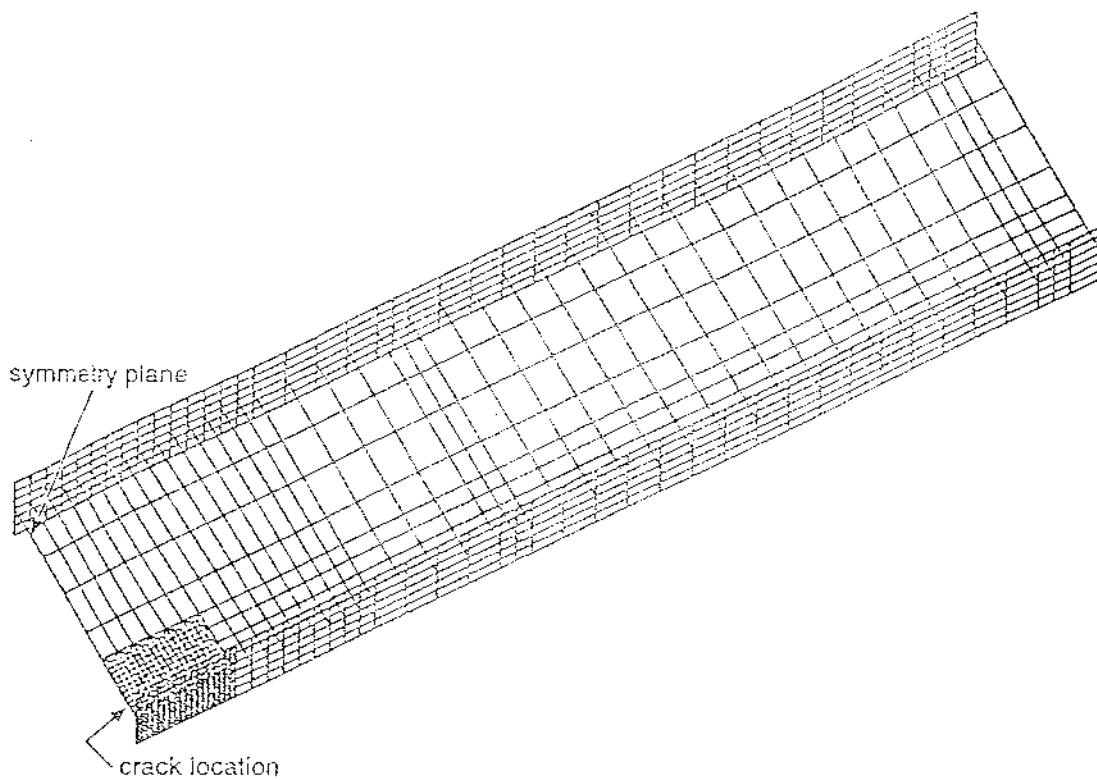


Figure 4.17 Simplified finite-element model of I-beam specimen

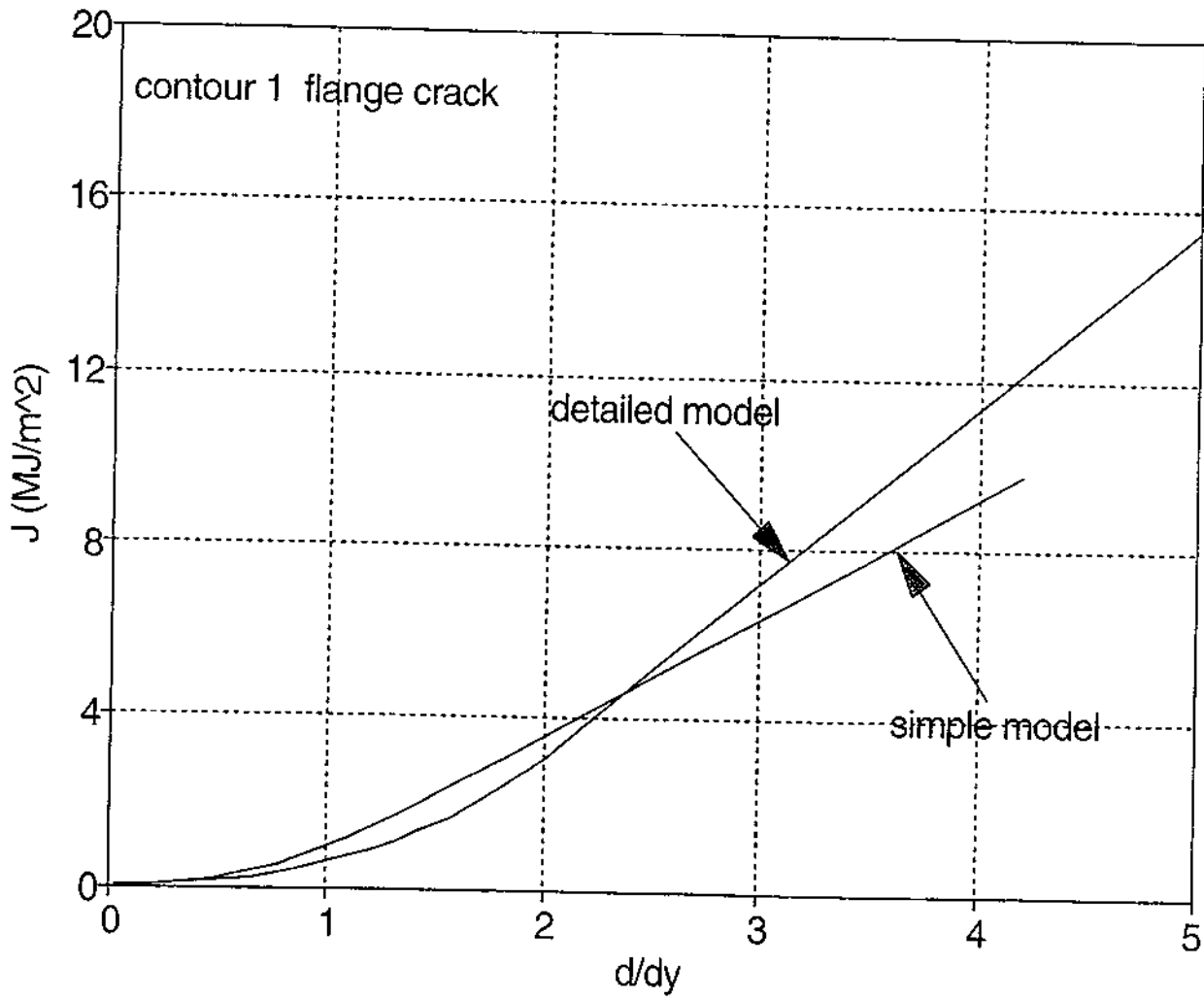


Figure 4.18 Computed J vs. displacement for the flange crack from the two finite element models of I-beam specimen A18 showing good agreement and therefore adequate refinement

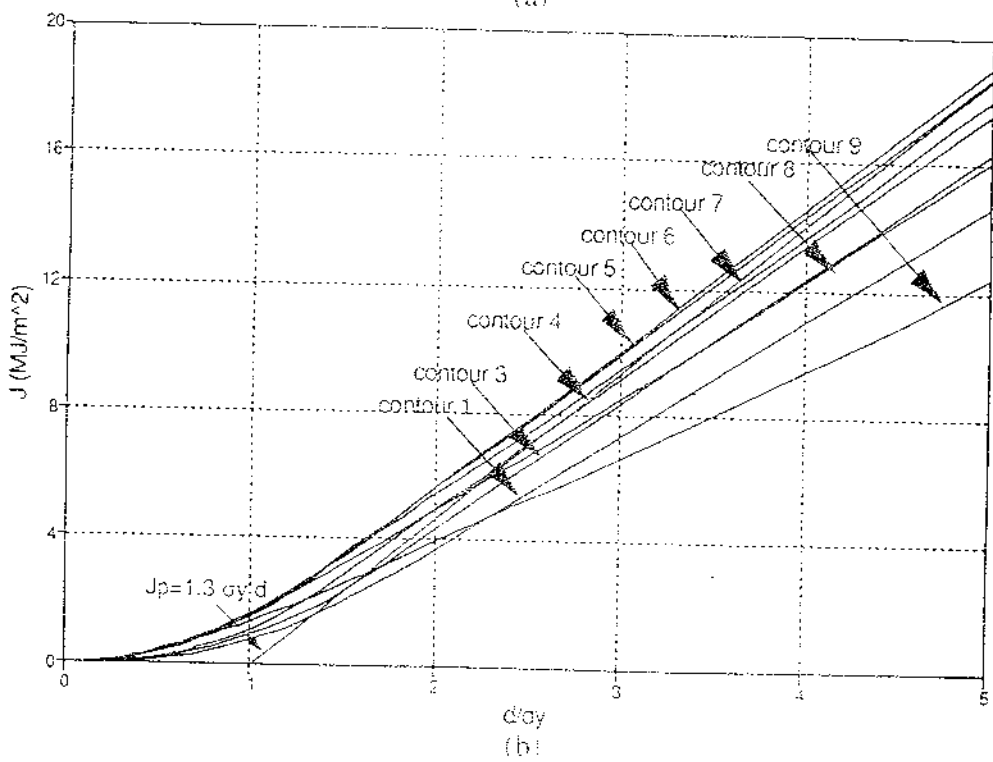
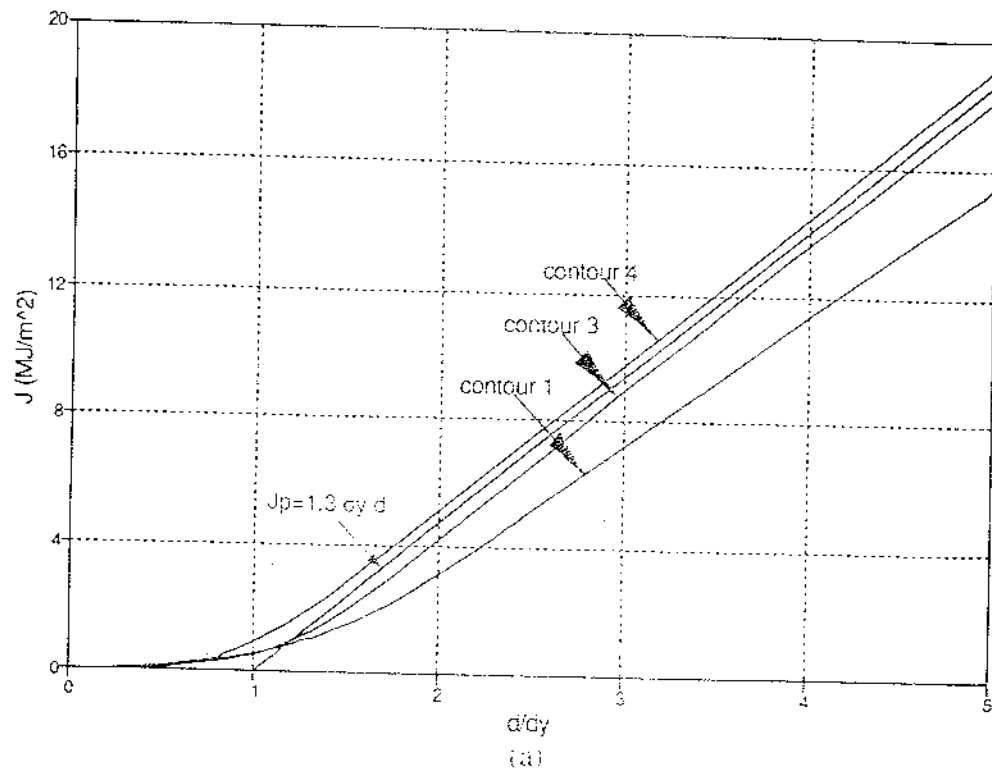


Figure 4.19 Computed J vs. displacement for the first four crack configurations for I-beam specimen A18 showing results calculated at the crack tips in the (a) flange and (b) web

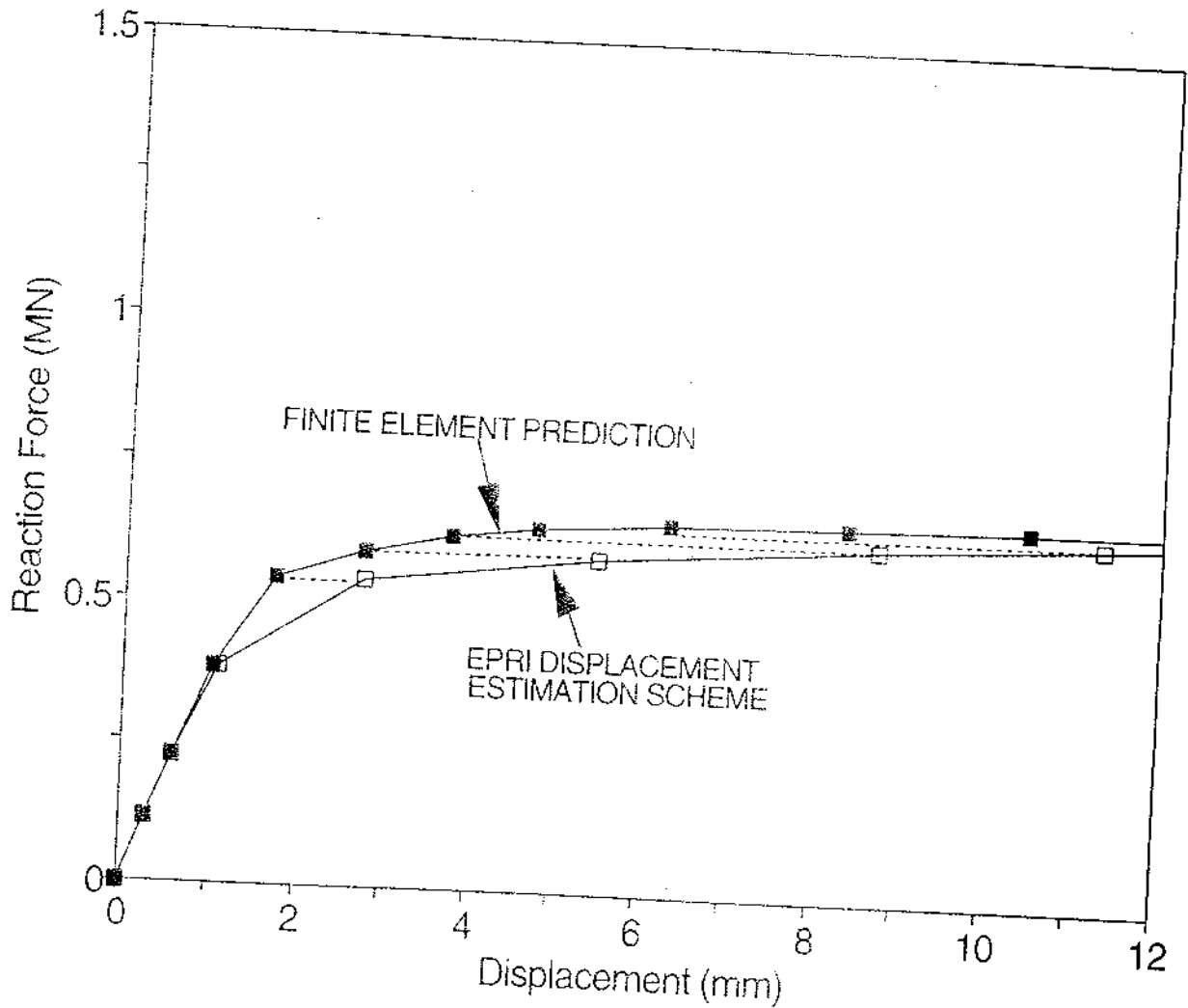


Figure 4.20

Comparison of load-displacement curves for the CCT specimen using the finite-element model and the EPRI estimation scheme for displacement (Equation 4-6). Dotted lines show corresponding load points from each curve

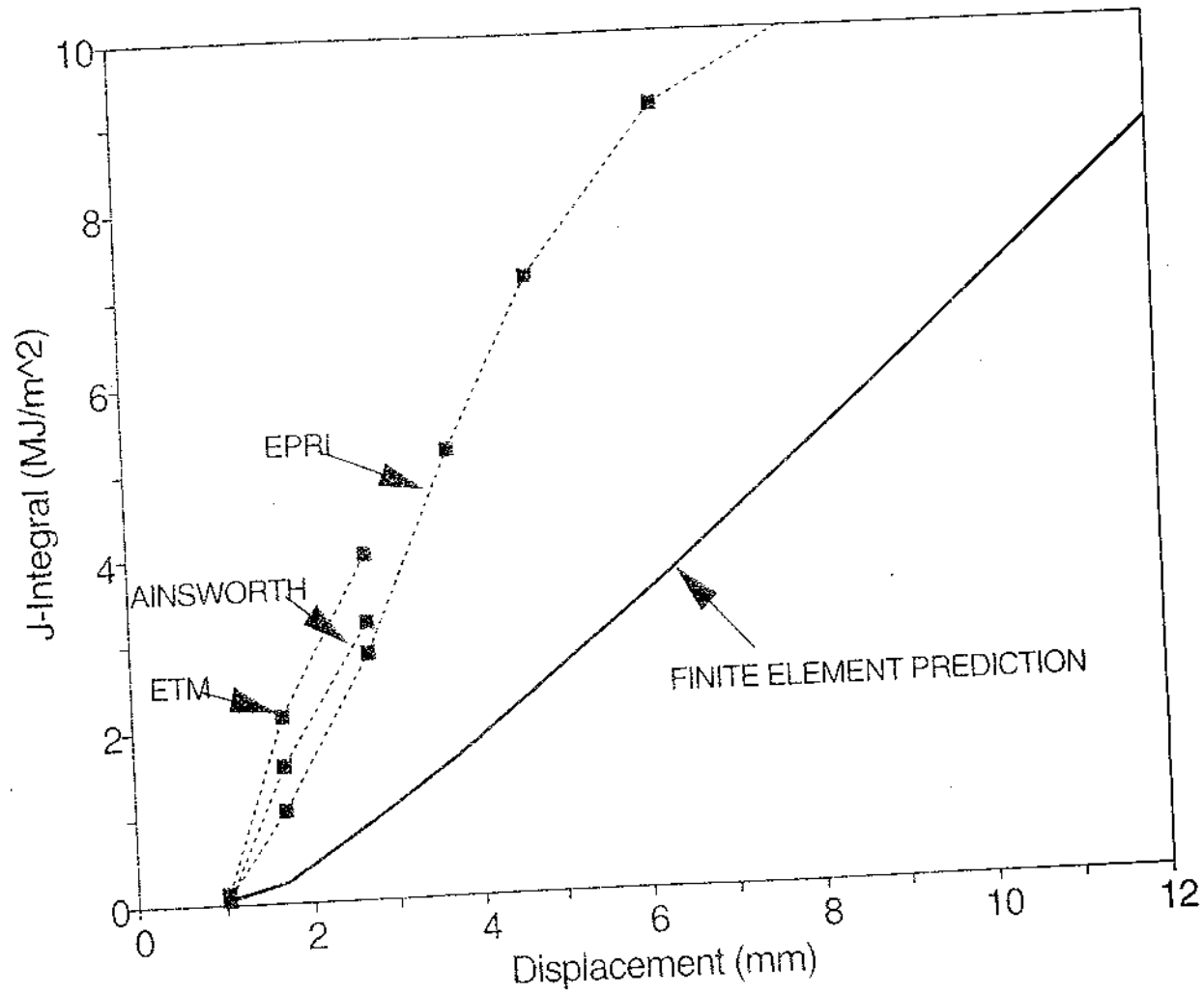


Figure 4.21 J vs. displacement curves for the CCT specimen calculated using the EPRI, ETM, and Ainsworth estimation schemes compared to the result obtained using finite-element analysis and the contour integral

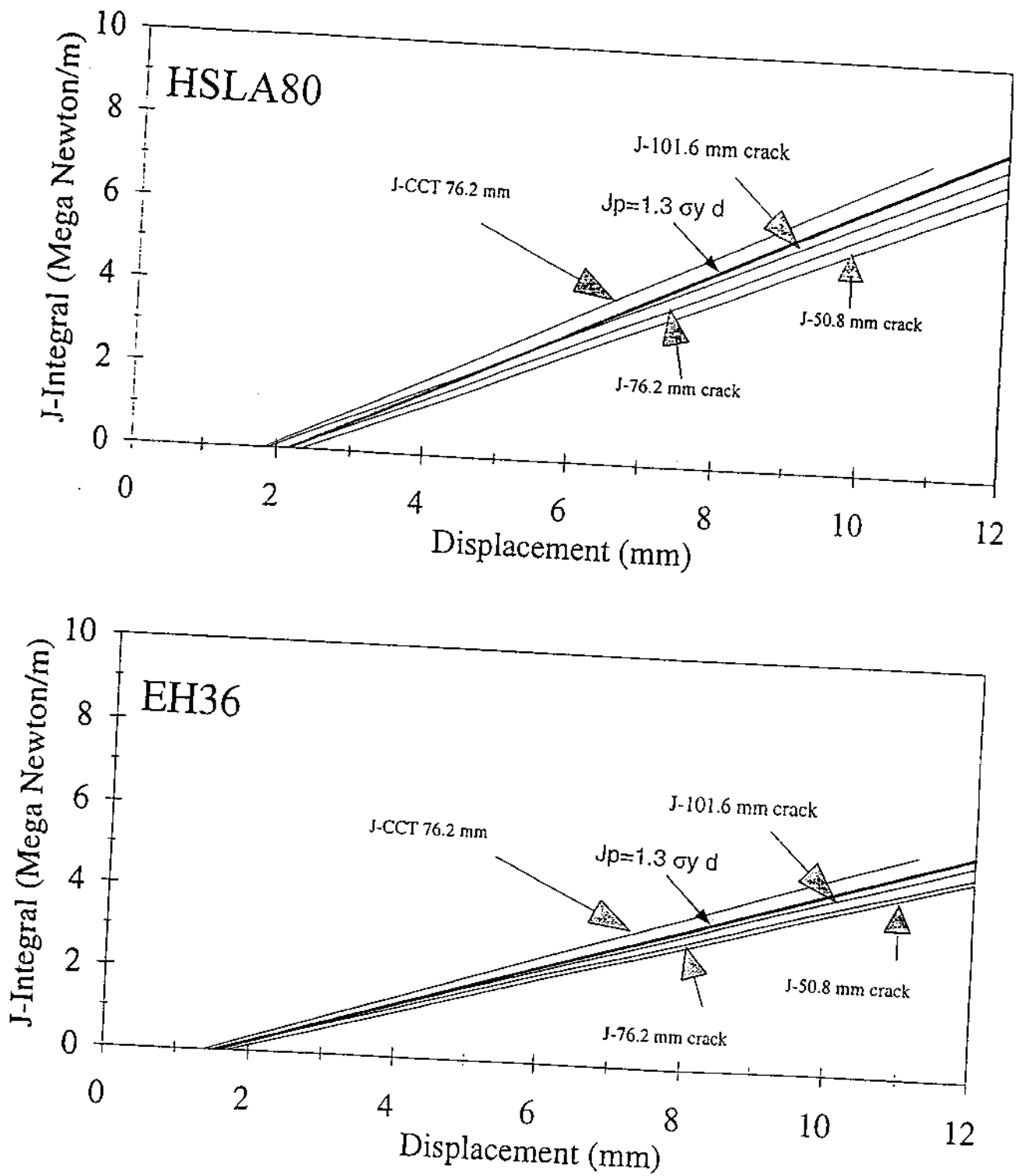


Figure 4.22 Linear fits to the J solution of McCabe and Ernst for various cope-hole and CCT configurations showing simple J estimation equation.

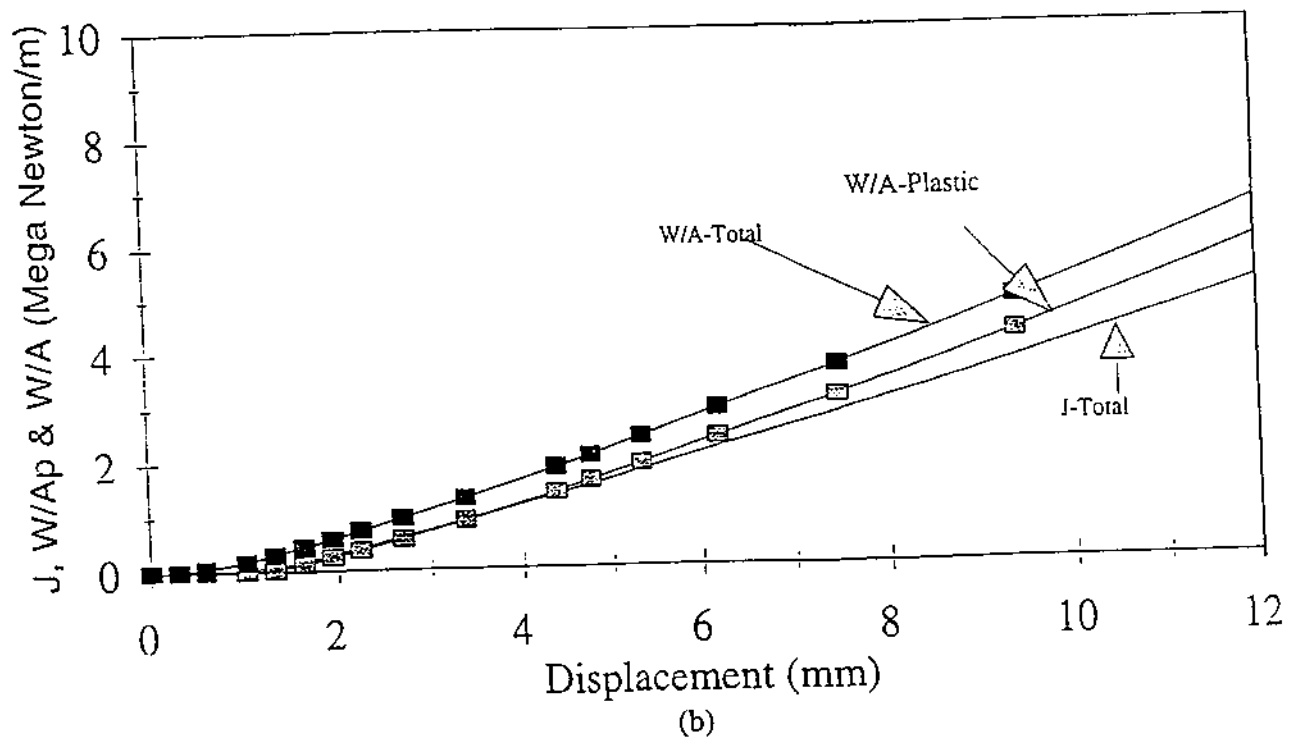
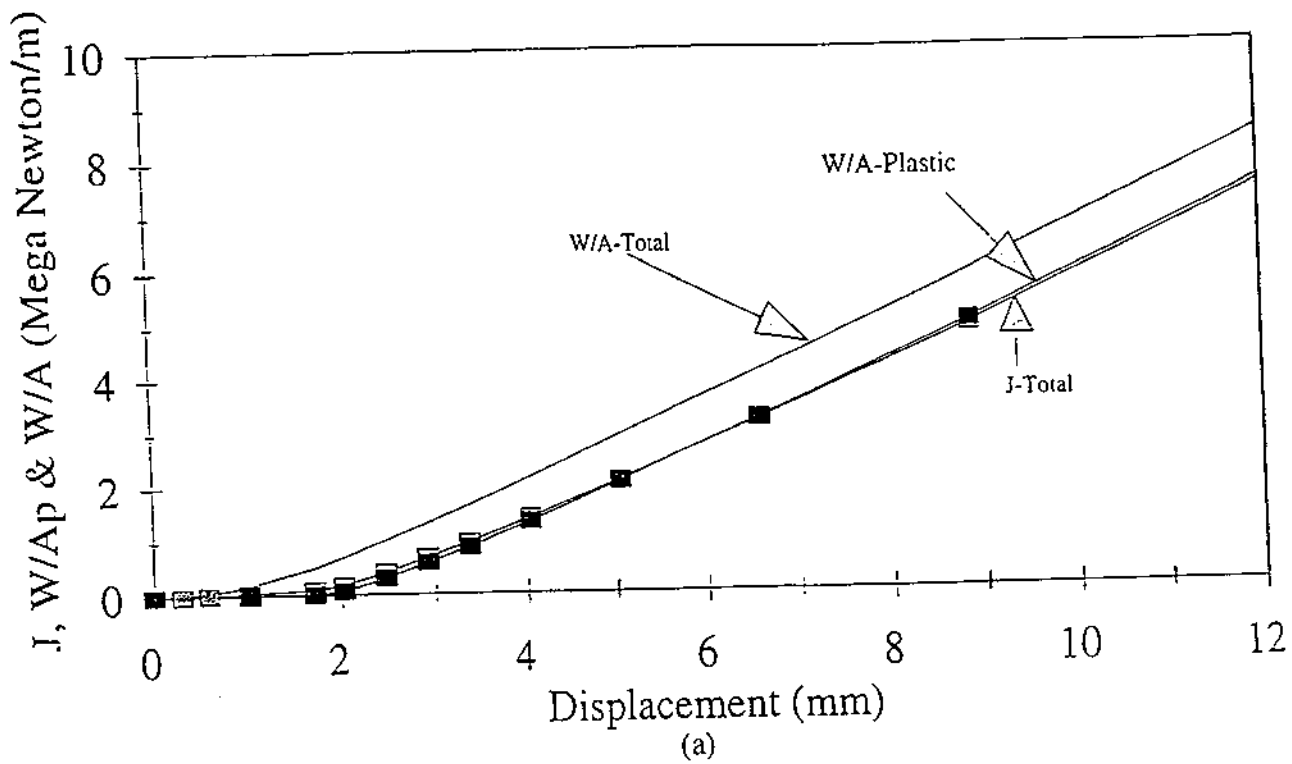


Figure 4.23 J , plastic work per unit area, and total work per unit area as a function of displacement for the (a) HSLA-80 and (b) EH-36 cope-hole specimens with initial crack sizes of 76 mm

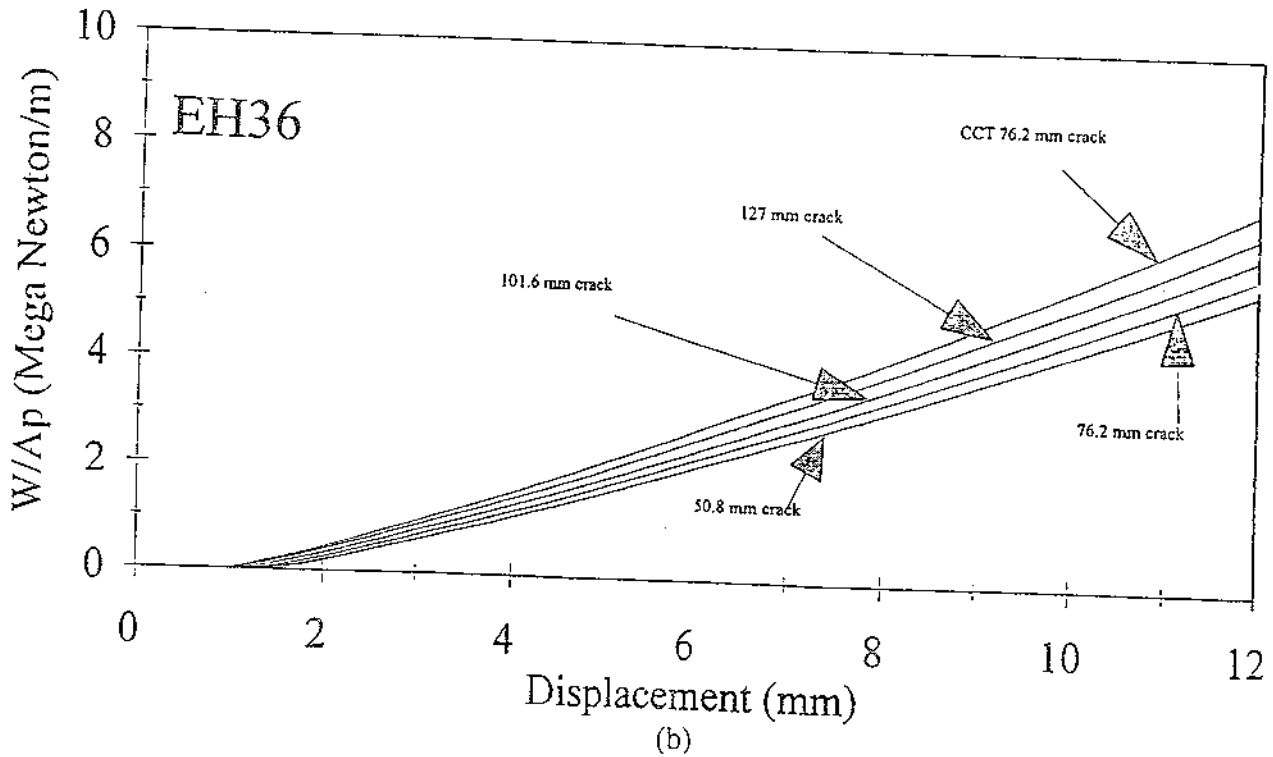
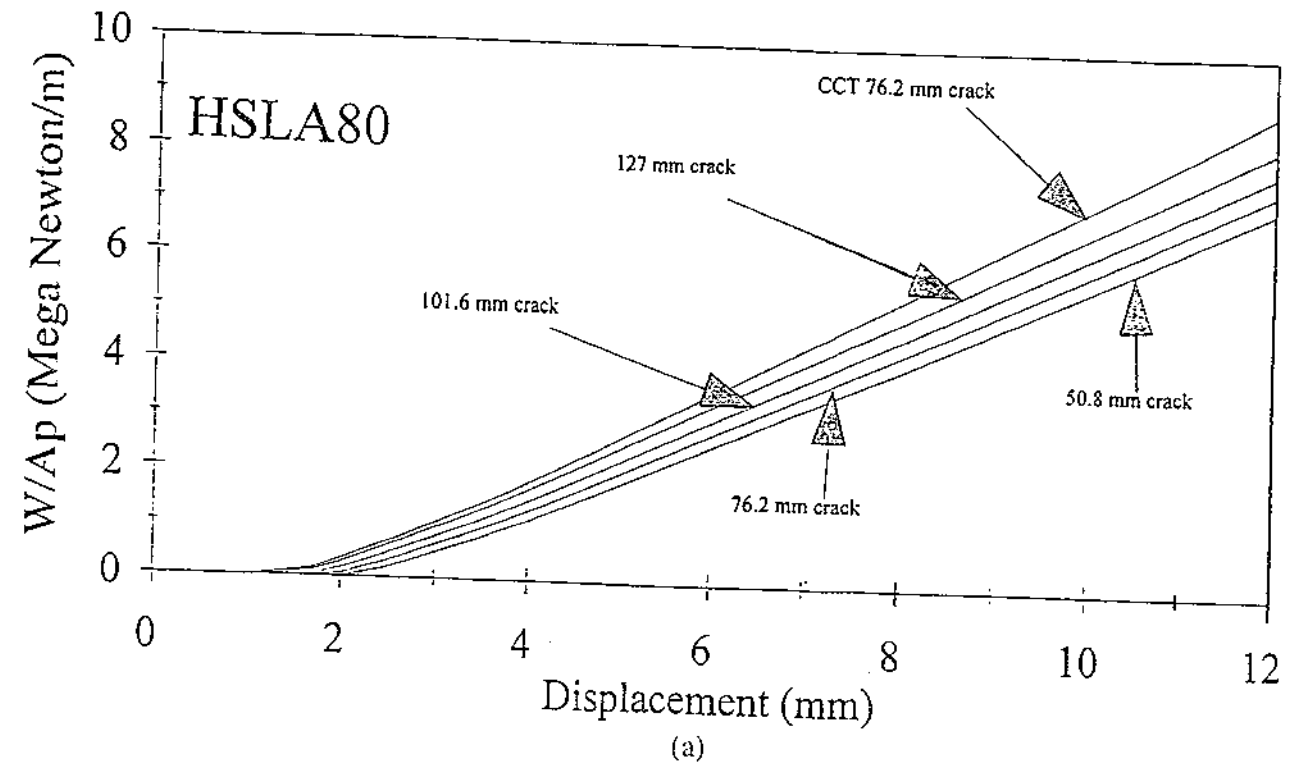


Figure 4.24 Work per unit area as a function of displacement for all crack sizes of the (a) HSLA-80 and (b) EH-36 cope-hole specimens. Also shown are the CCT specimens with 76 mm cracks

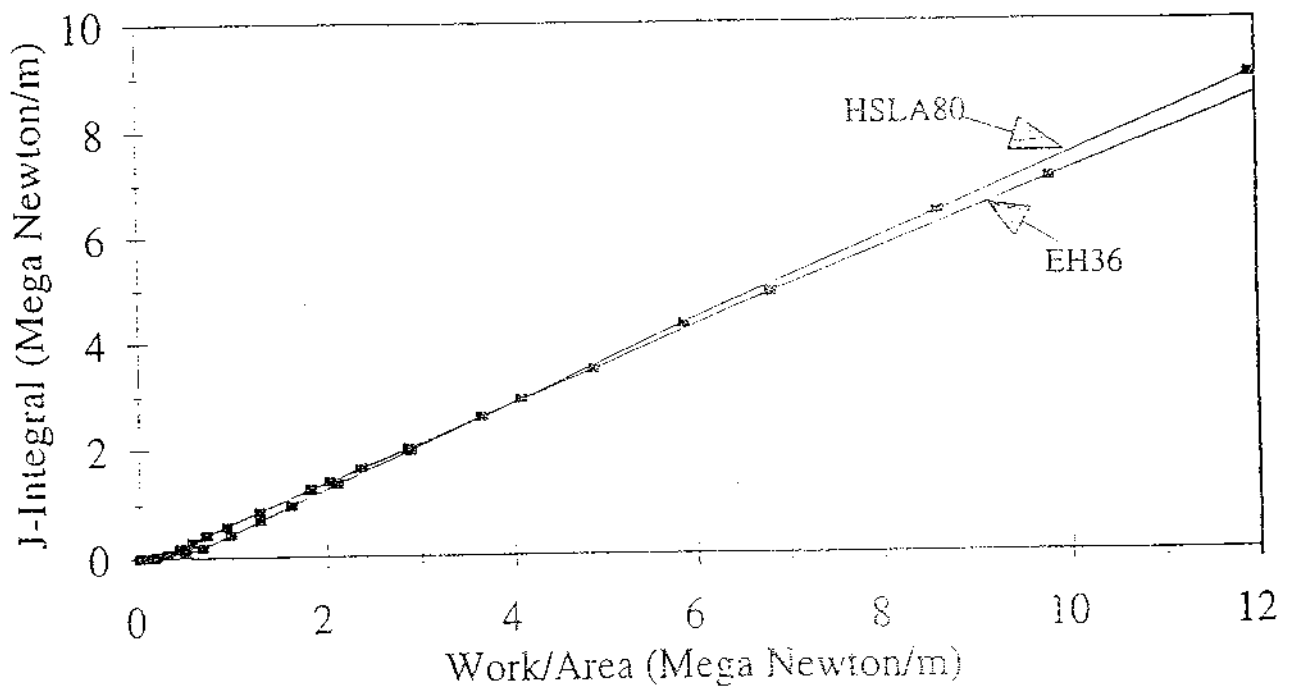


Figure 4.25 J as a function of work per unit area for the HSLA-80 and EH-36 cope-hole specimens with initial crack sizes of 76 mm

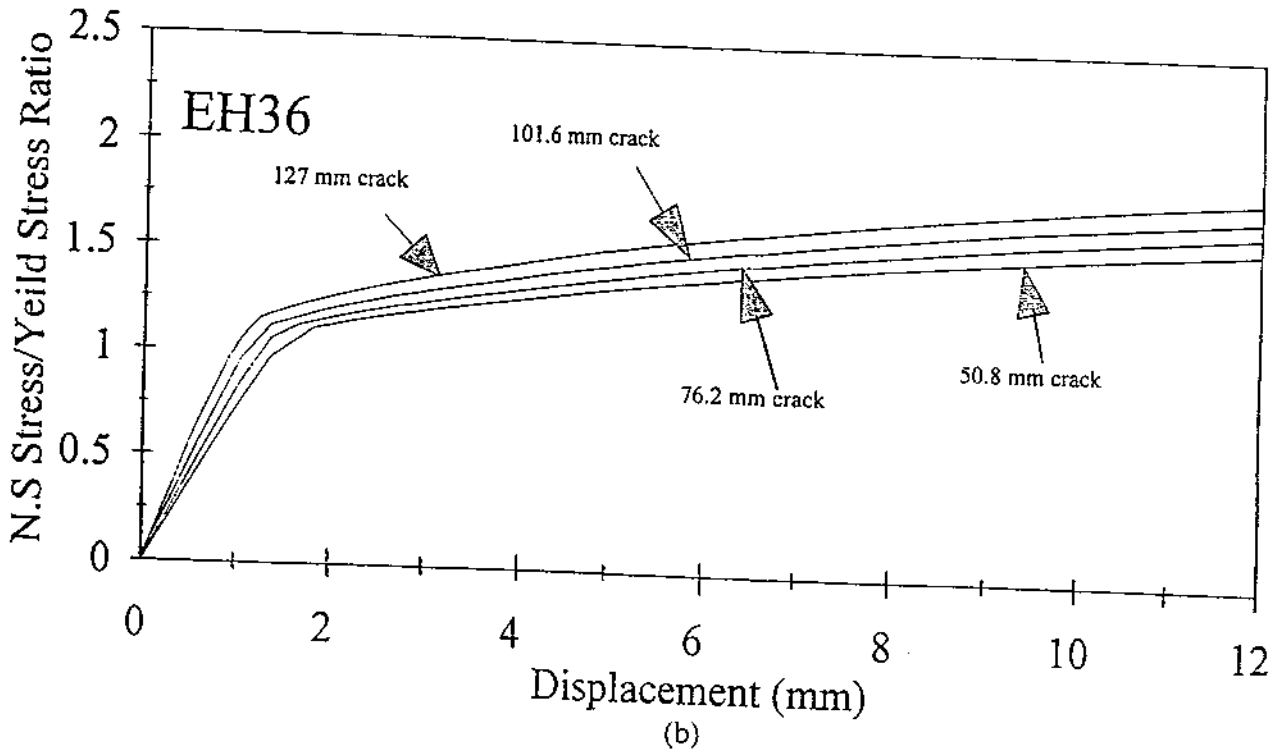
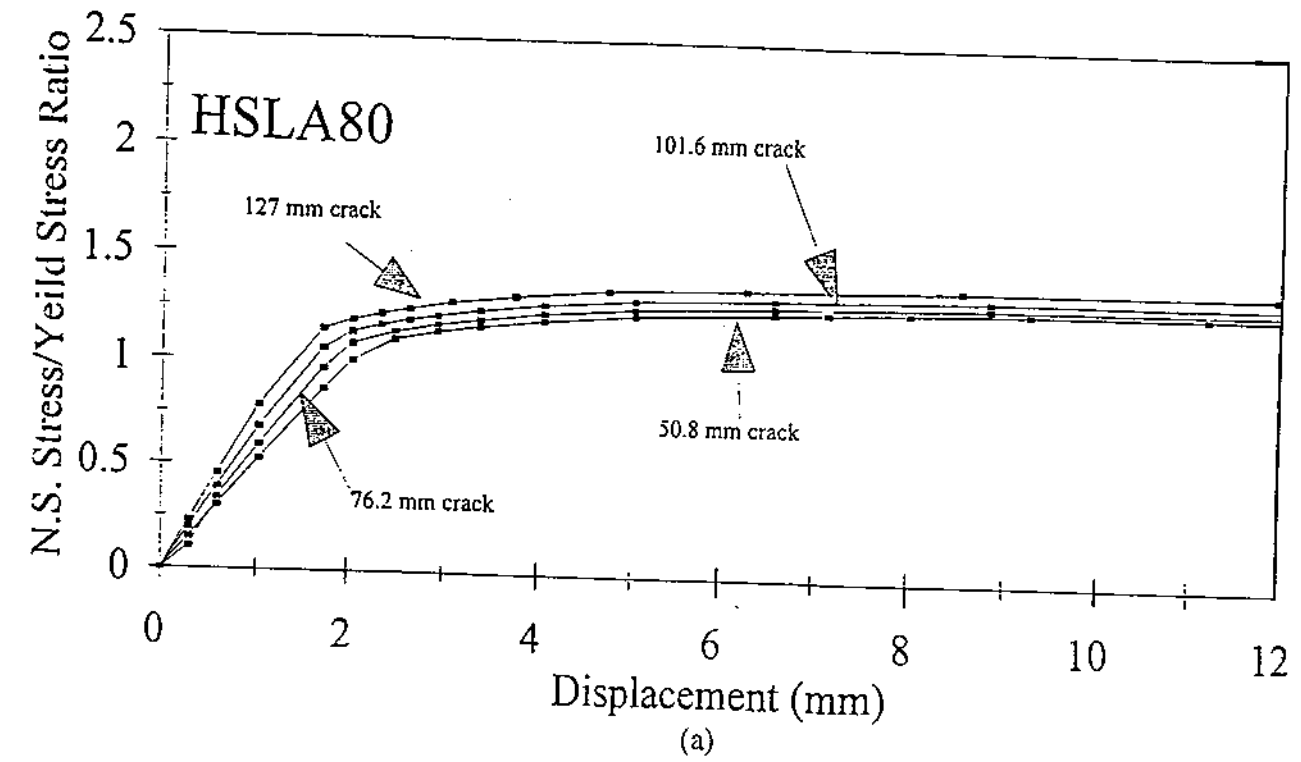
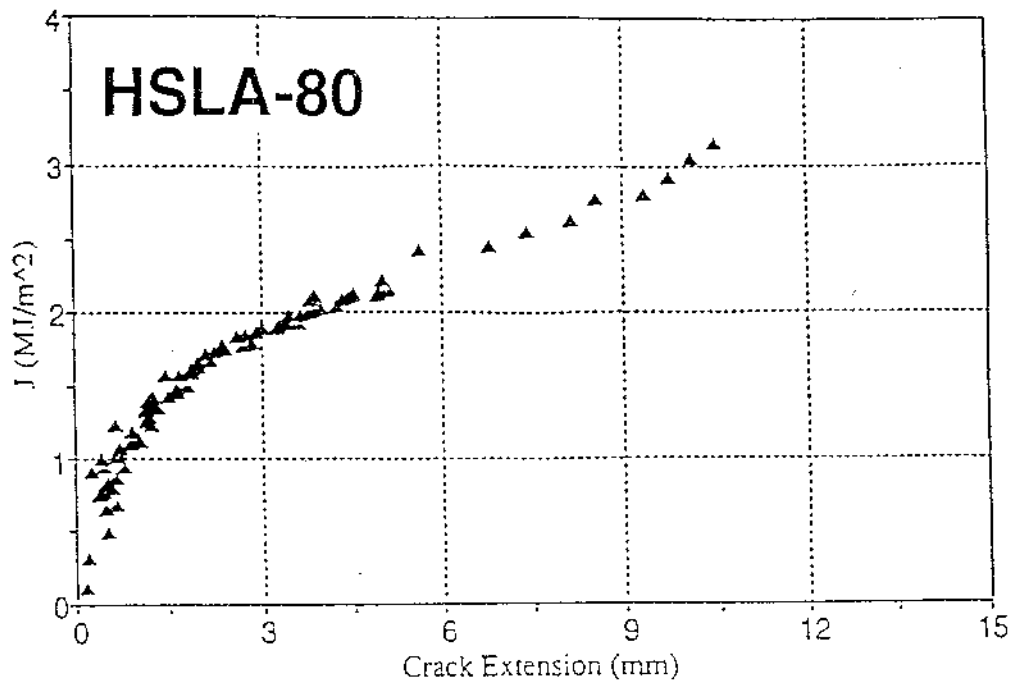
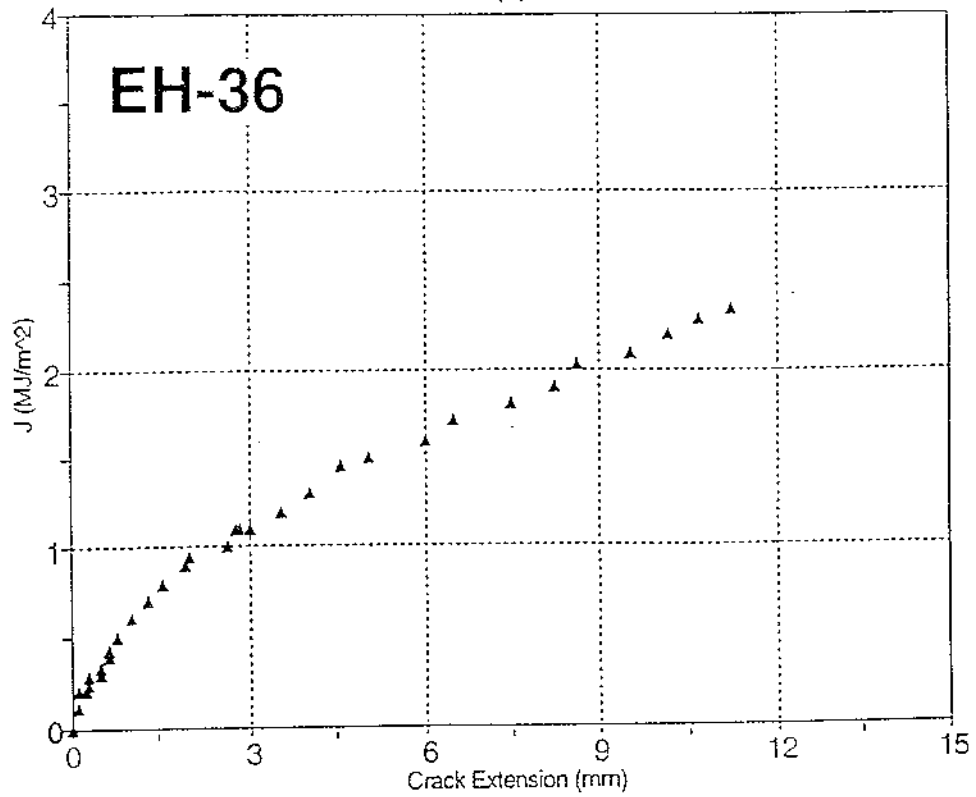


Figure 4.26 Average net-section stress as a function of displacement for the (a) HSLA-80 and (b) EH-36 cope-hole specimens

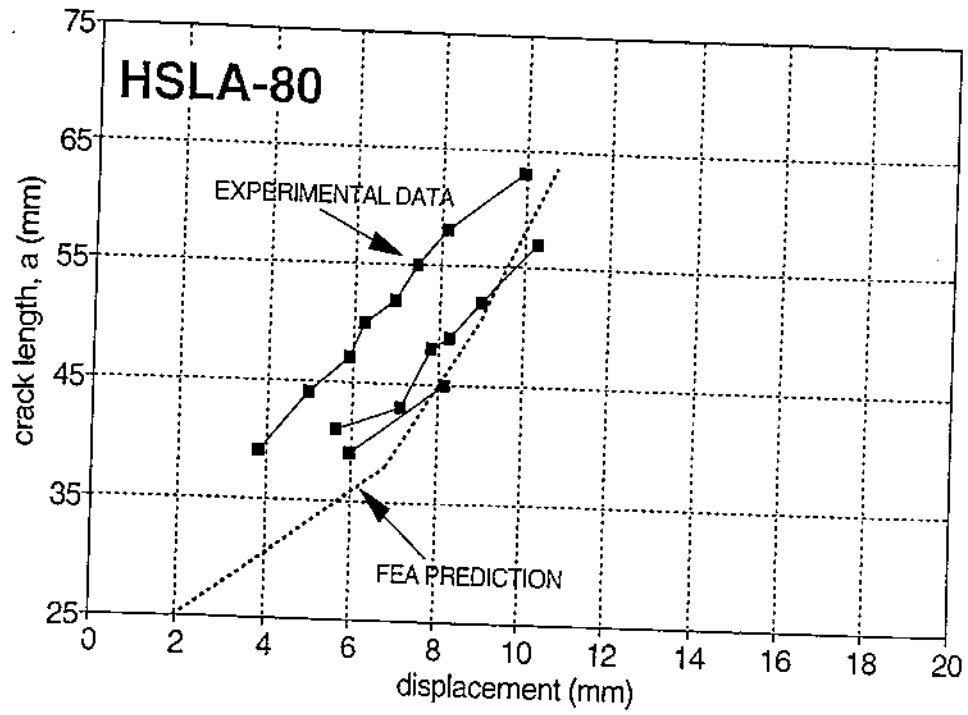


(a)

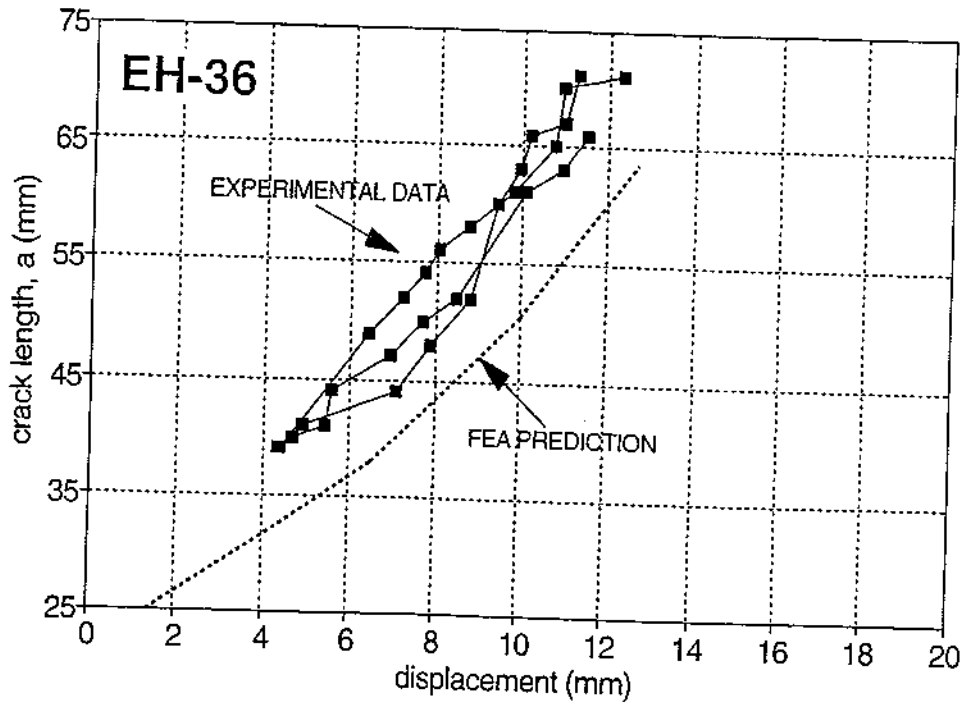


(b)

Figure 4.27 Extended J-R curves used to predict crack extension for the (a) HSLA-80 and (b) EH-36 materials



(a)



(b)

Figure 4.28 Predicted crack extension history as a function of displacement for the (a) HSLA-80 and (b) EH-36 cope -hole specimens compared to several replicate experimental results

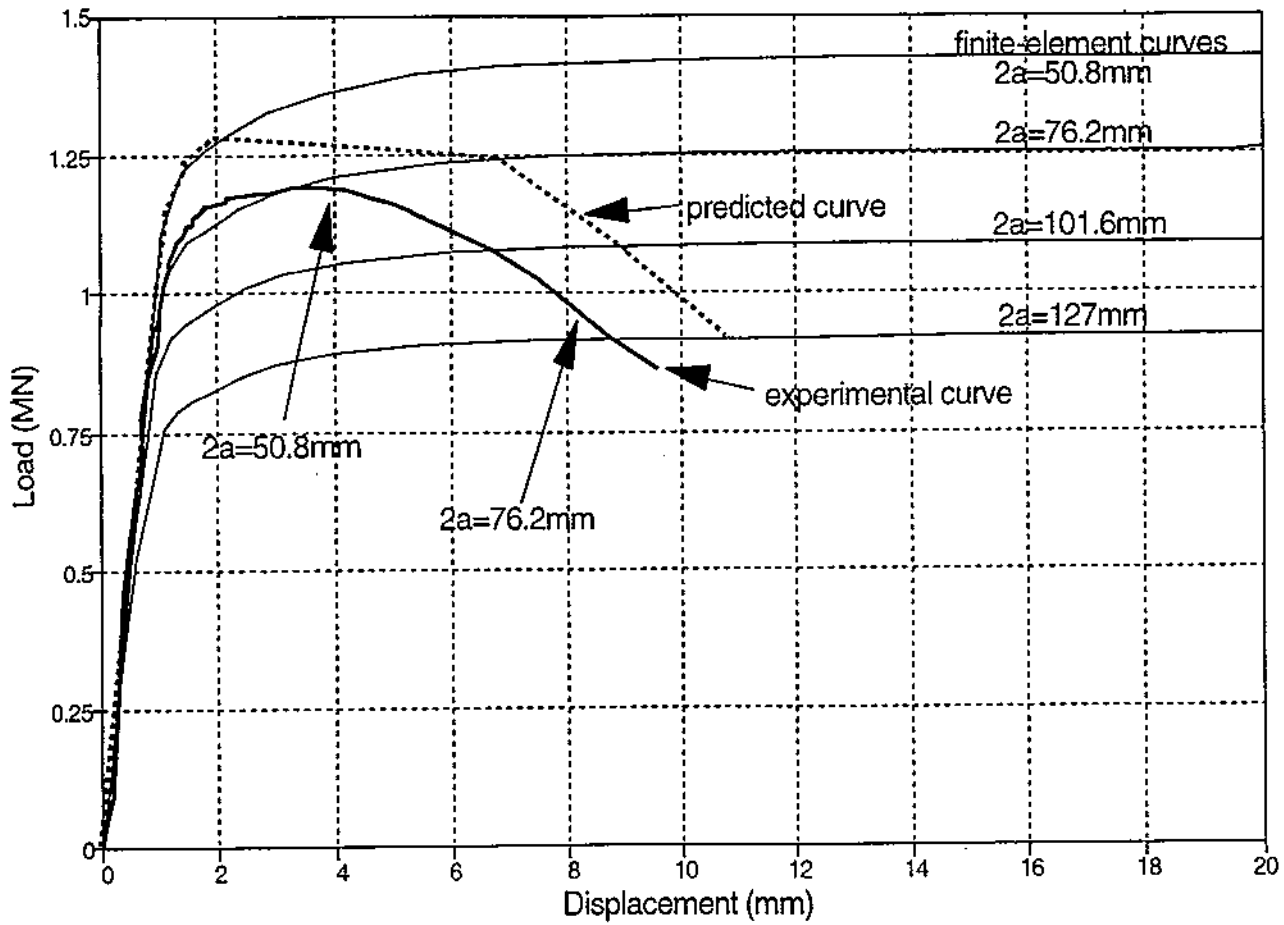


Figure 4.29

Load-displacement curve generated using finite-element analysis and the J-R curve analysis compared to experimental result for the HSLA-80 cope-hole specimen with an initial crack size of 50 mm. Also shown are the "stationary" crack load-displacement curves used to make the prediction.

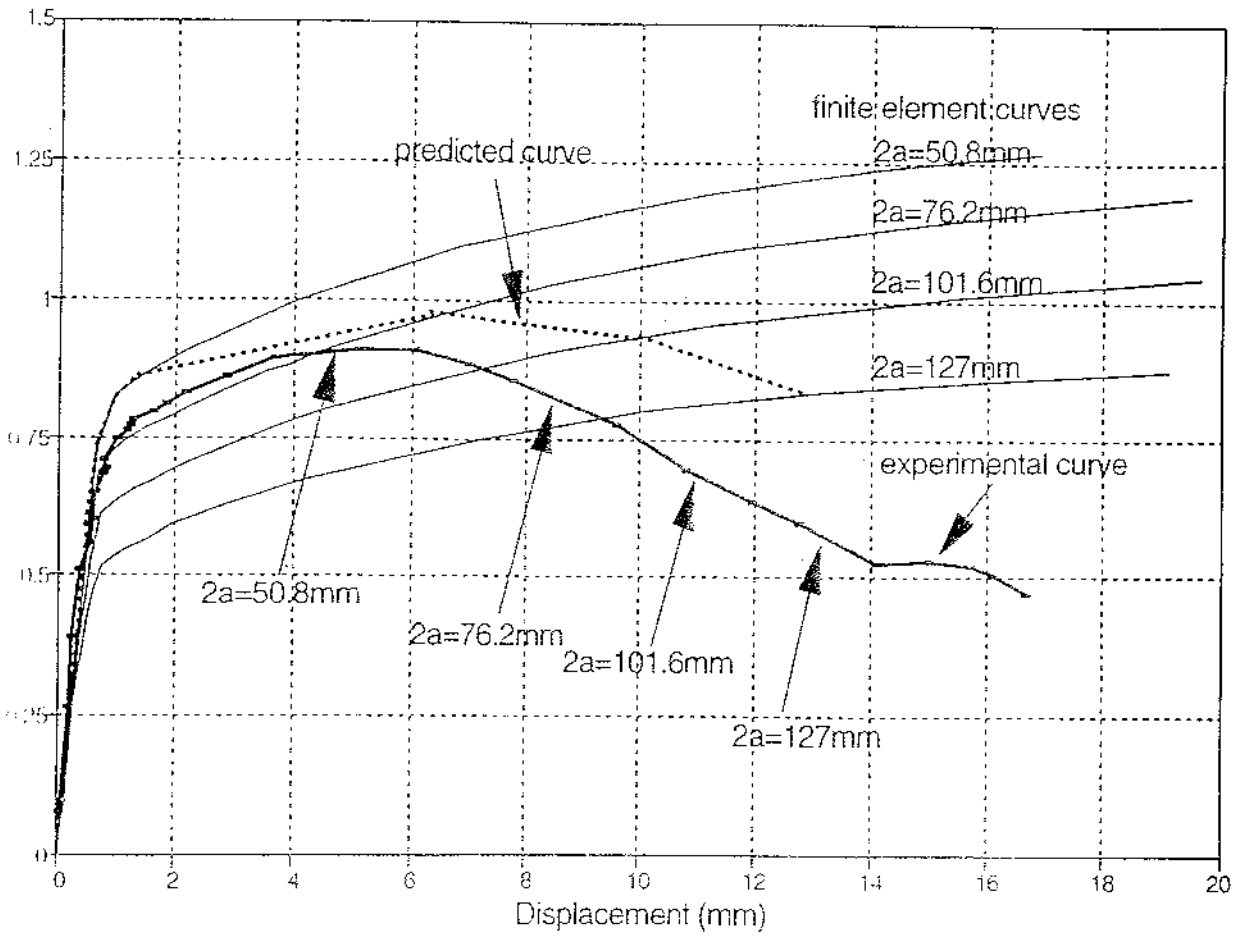


Figure 4.31 Load-displacement curve generated using finite-element analysis and the J-R curve analysis compared to experimental result for the EH-36 cope-hole specimen with an initial crack size of 50 mm. Also shown are the "stationary-crack" load-displacement curves used to make the prediction

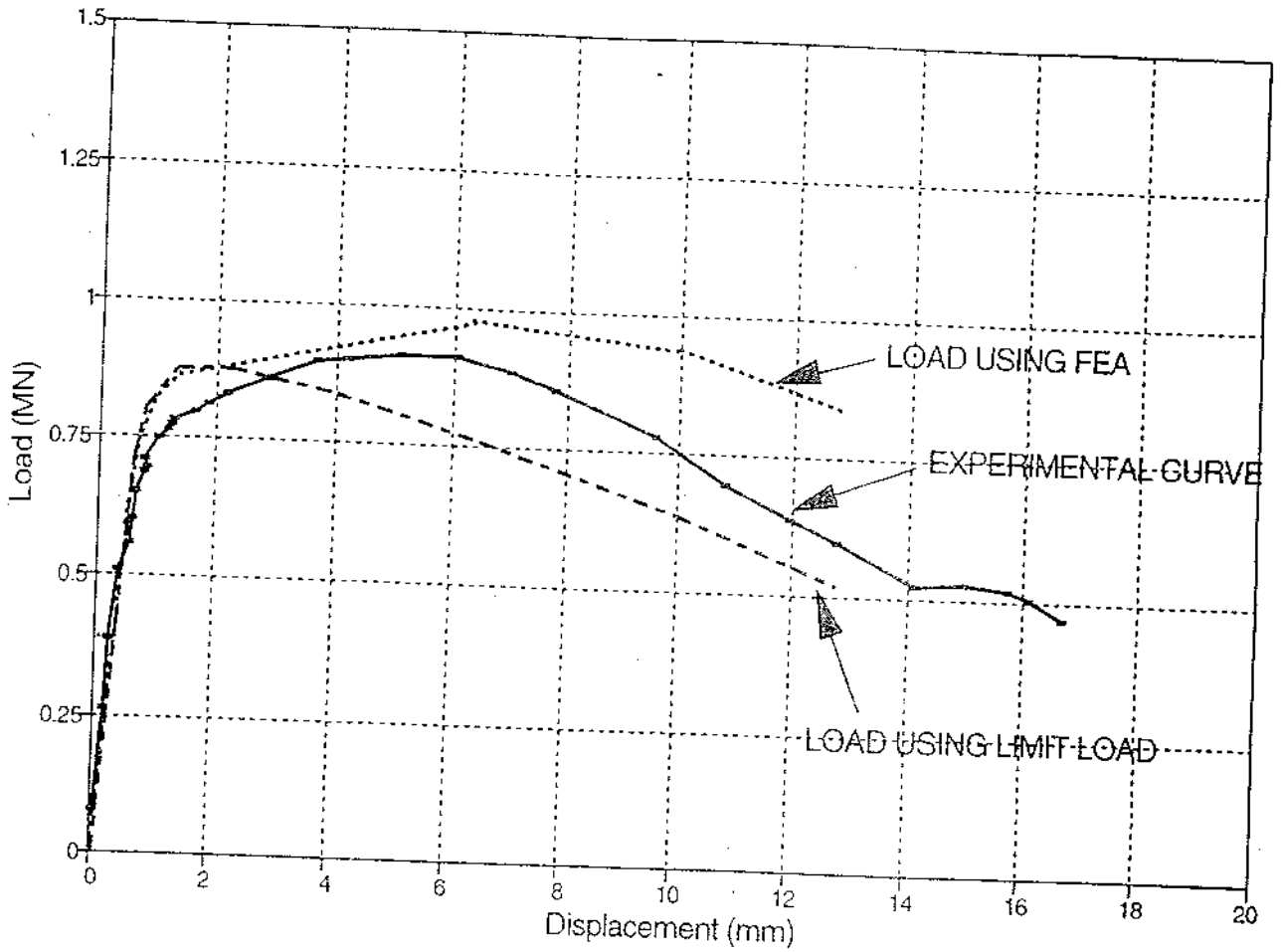


Figure 4.32

Load-displacement curve generated using the crack extension history from the finite-element model with a limit-load solution to calculate load for the EH-36 cope-hole specimen. Also shown are the experimental result and the finite-element prediction from Figure 4.31

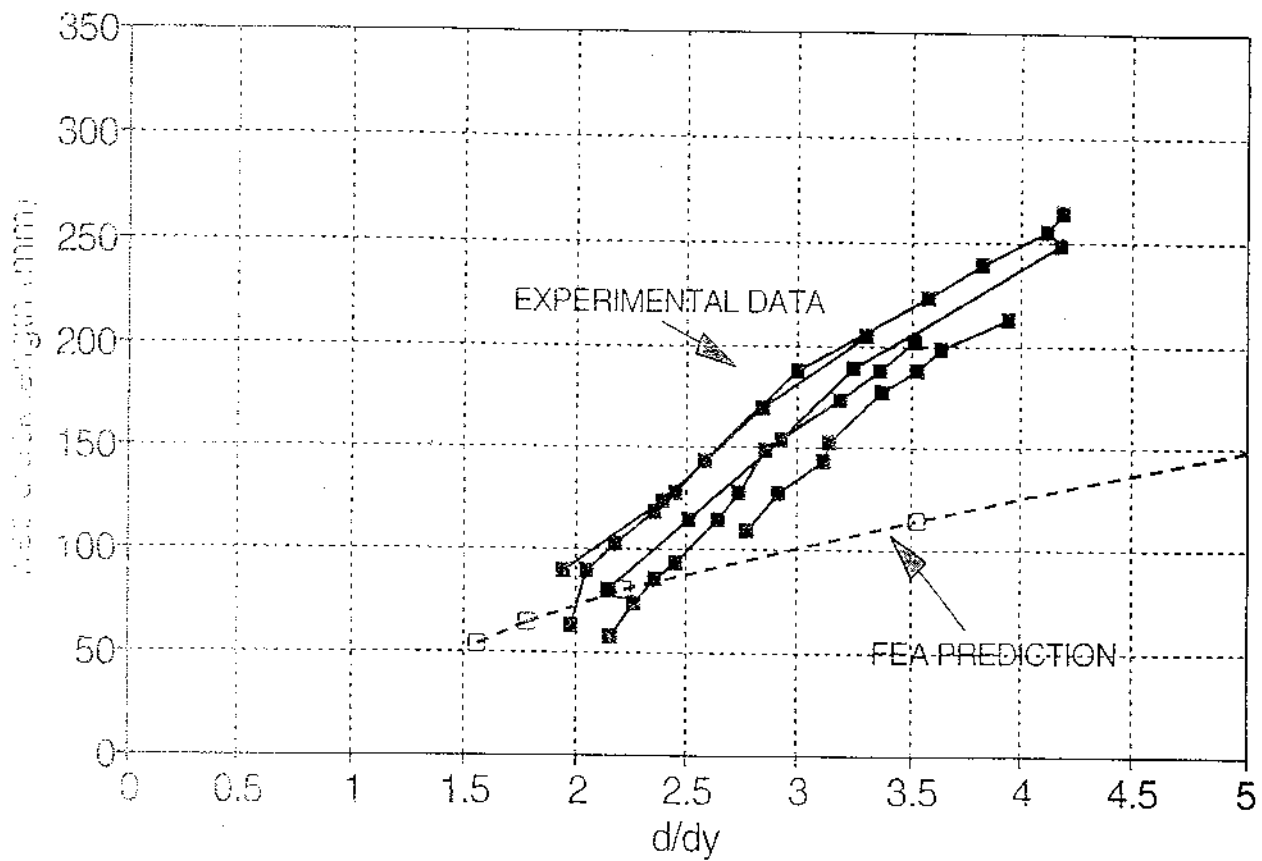


Figure 4.33 Finite-element prediction of web crack extension as a function of displacement for I-beam specimen A18. The result is unconservative with respect to crack extension data for the I-beam specimens

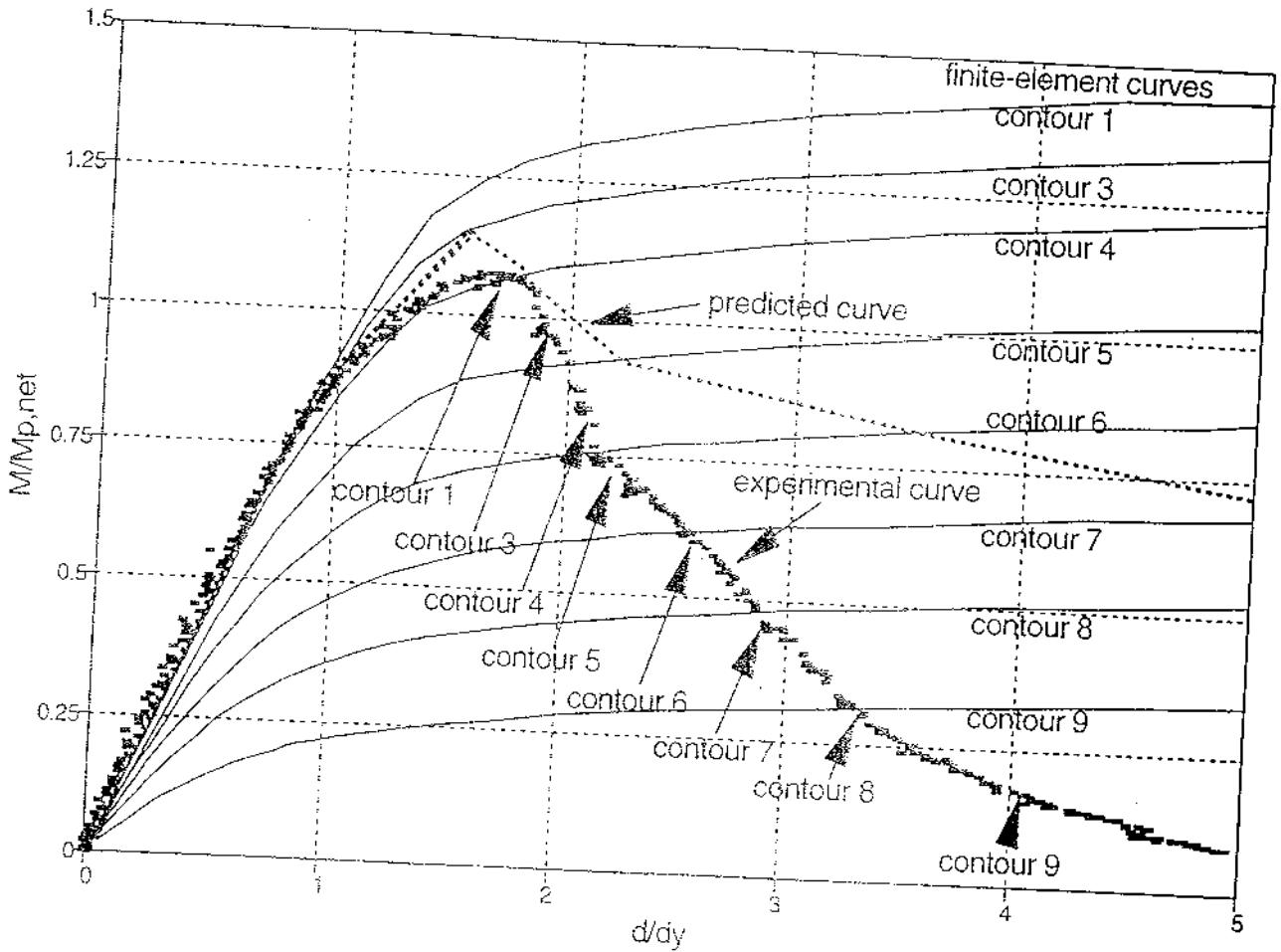


Figure 4.34 Finite-element predicted load-displacement curve compared to experimental result for I-beam specimen A18. Also shown are the "stationary-crack" load-displacement curves for various crack configurations (contours) that were used to make the prediction

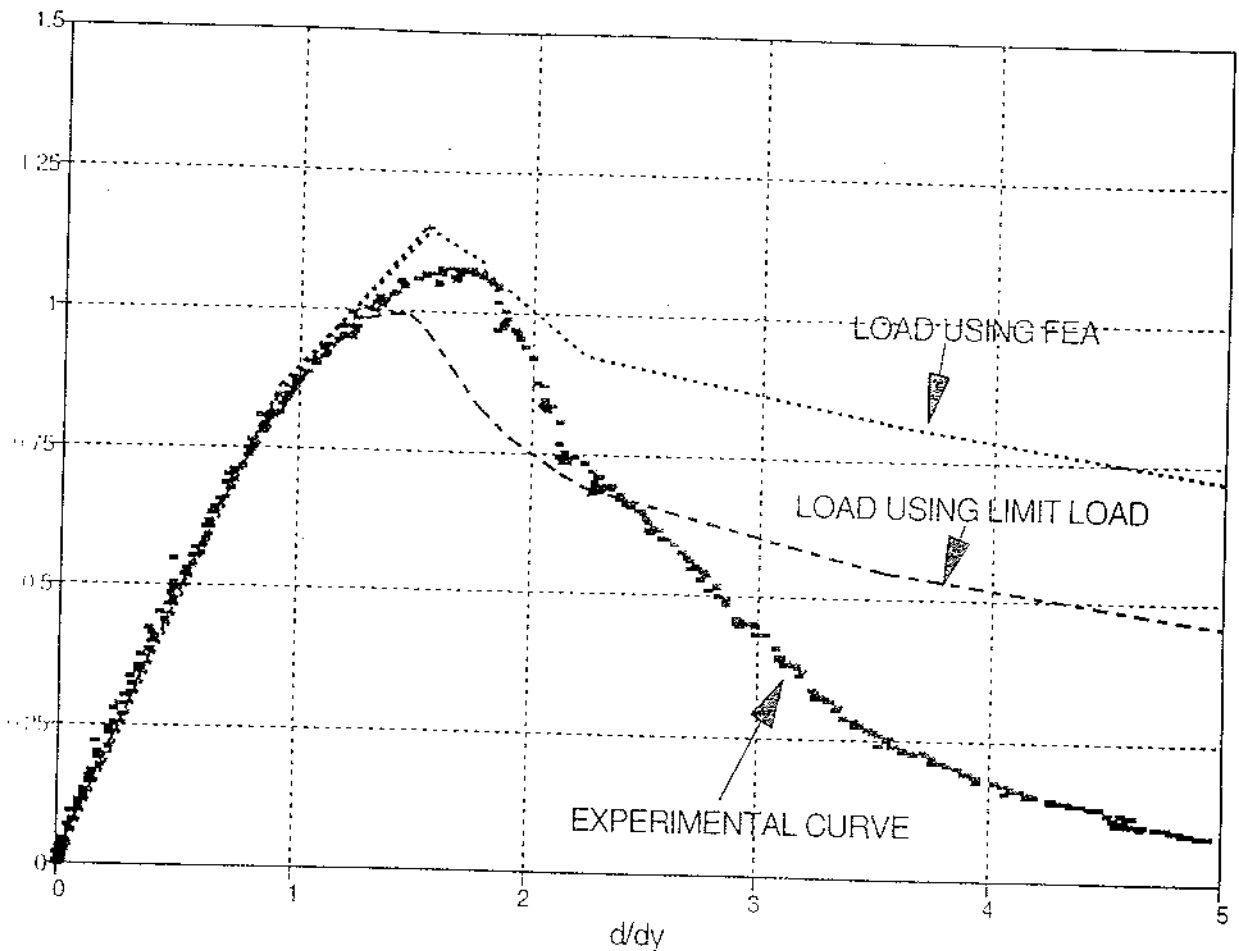
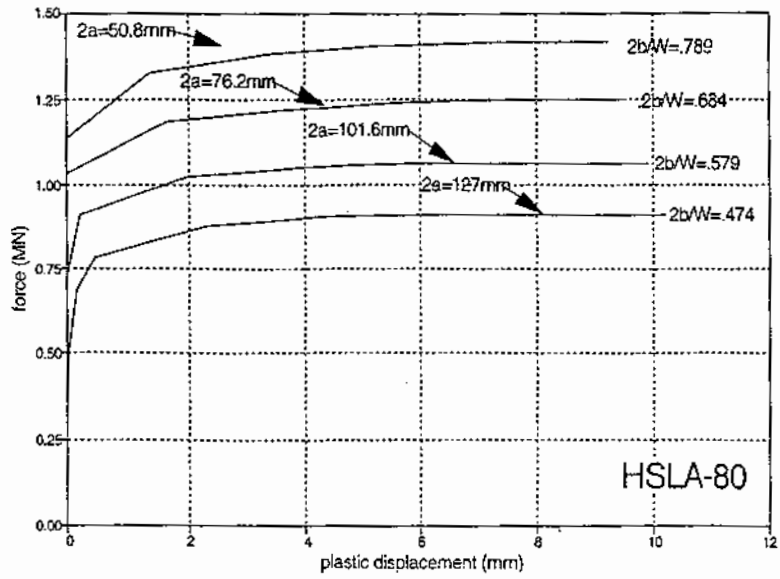
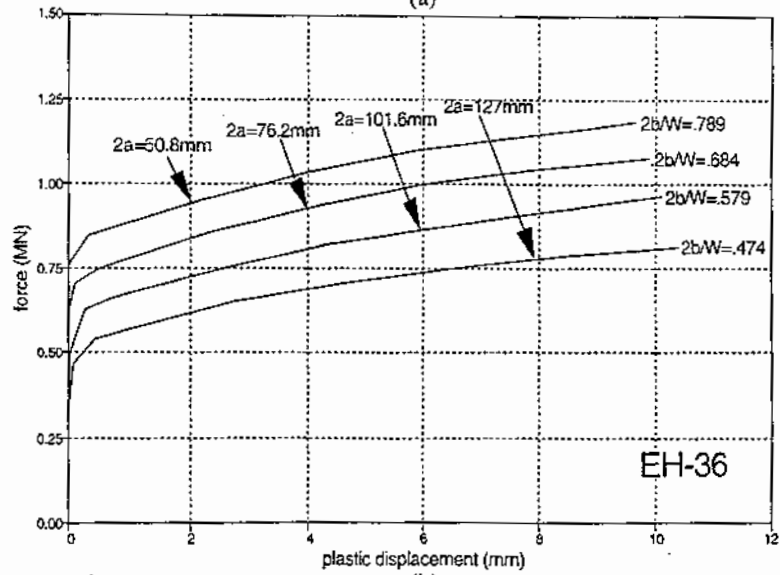


Figure 4.35 Load-displacement curve generated using the crack extension history from the finite-element model with a limit-load solution to calculate load for I-beam specimen A18. Also shown are the experimental result and the finite-element prediction from Figure 4.34



(a)



(b)

Figure 4.36

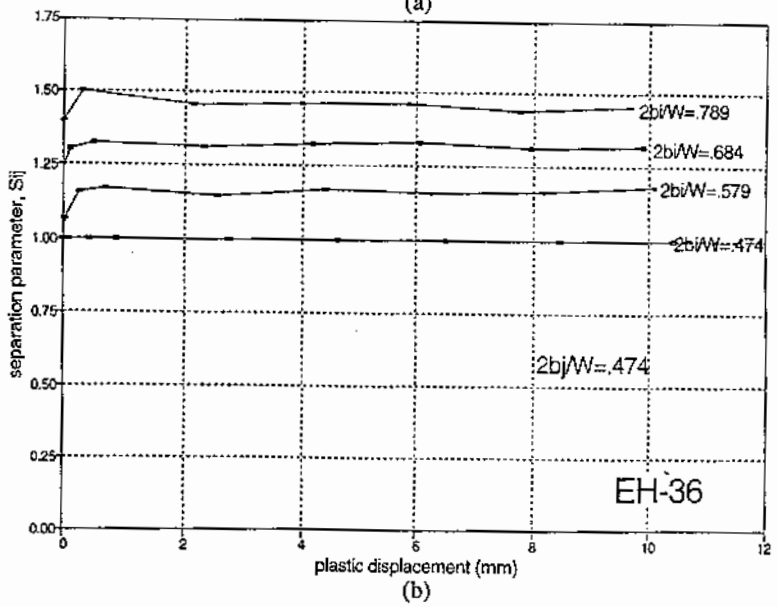
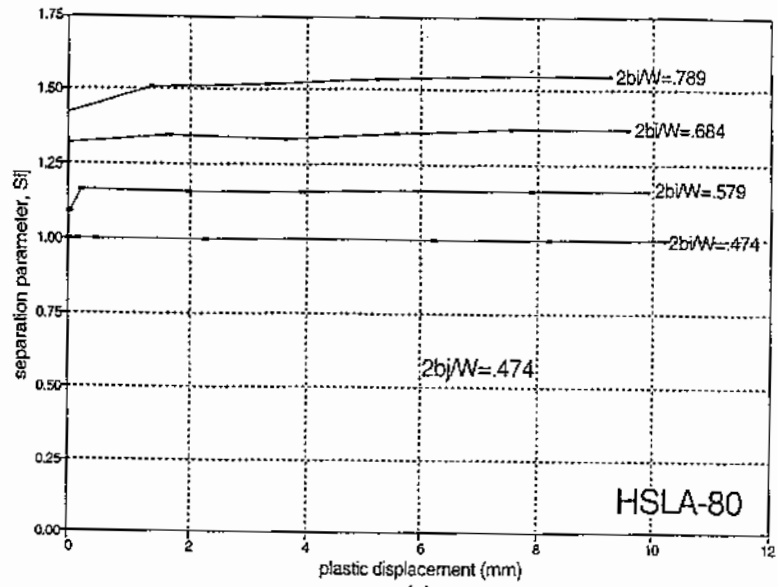
Load vs. plastic displacement for (a) HSLA-80 and (b) EH-36 cope-hole specimens from finite-element analysis showing each curve is approximately proportional to the others

$l=789$
 $l=684$
 $W=579$
 $2b/W=474$

 A-80
 12

$l=789$
 $W=684$
 $2b/W=579$
 $2b/W=474$

 EH-36
 12



and (b) EH-36 cope-
 wing each curve is

Figure 4.37 Separation parameter, S_{ij} , as function of plastic displacement for the (a) HSLA-80 and (b) EH-36 cope-hole specimens normalized by the curve for the largest crack length

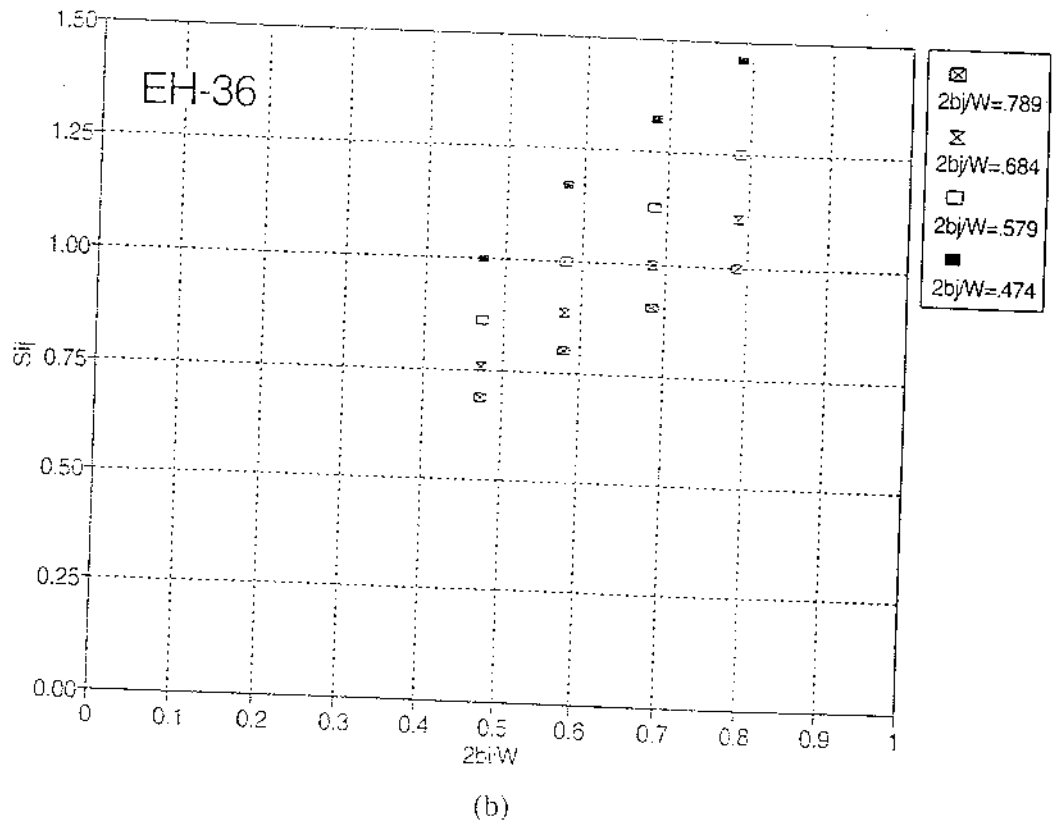
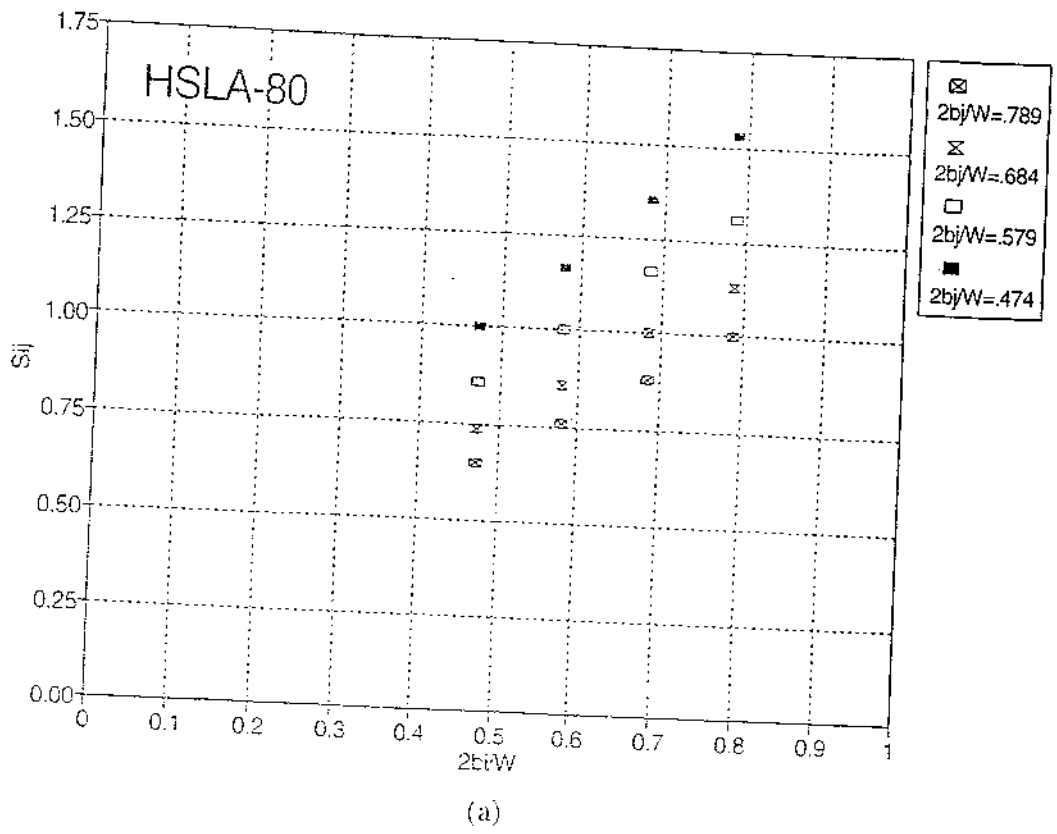
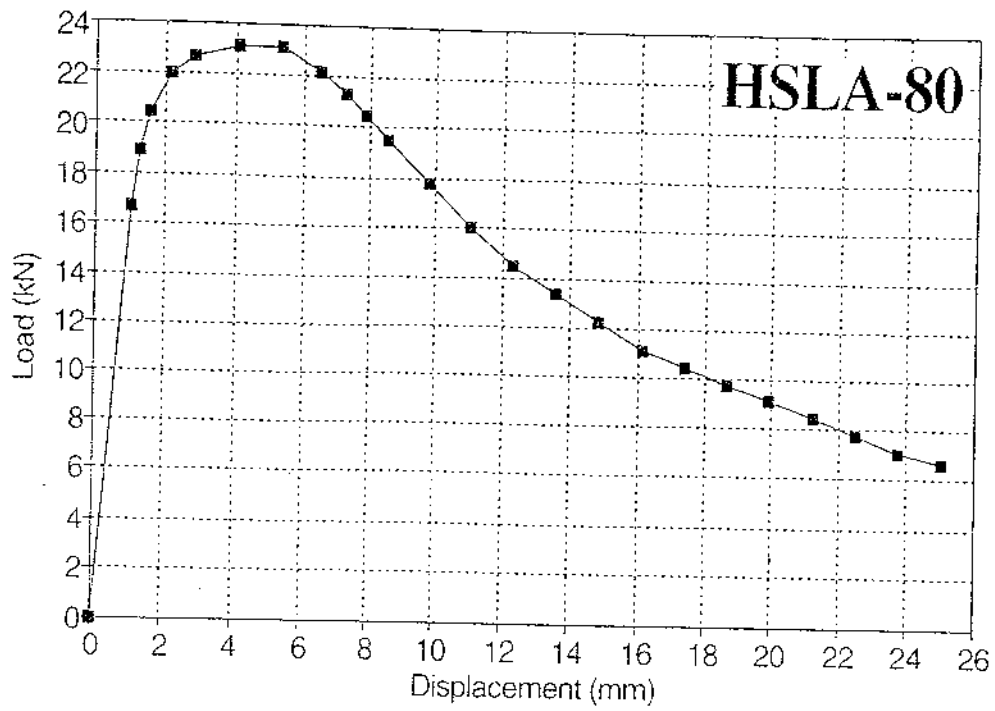
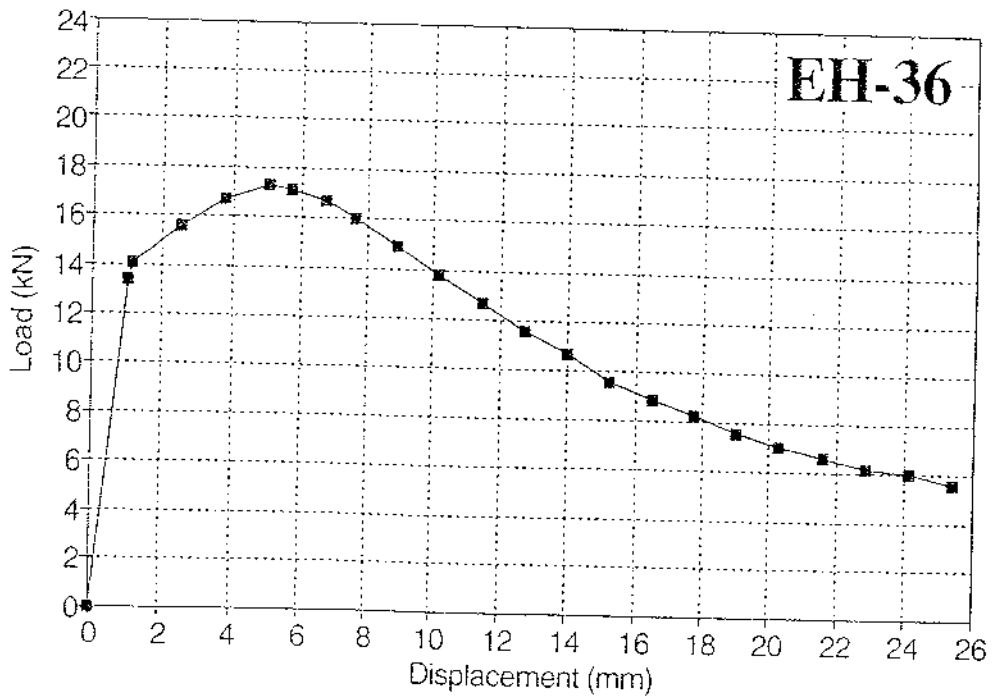


Figure 4.38 Separation parameter, S_{ij} , for the (a) HSLA-80 and (b) EH-36 cope-hole specimens showing an almost linear relationship to $2b_i/W$



(a)



(b)

Figure 4.39 Load-displacement curves for the (a) HSLA-80 and (b) EH-36 CT specimens associated with the extended J-R curves shown in Figure 4.27. (The periodic unloadings have been removed).

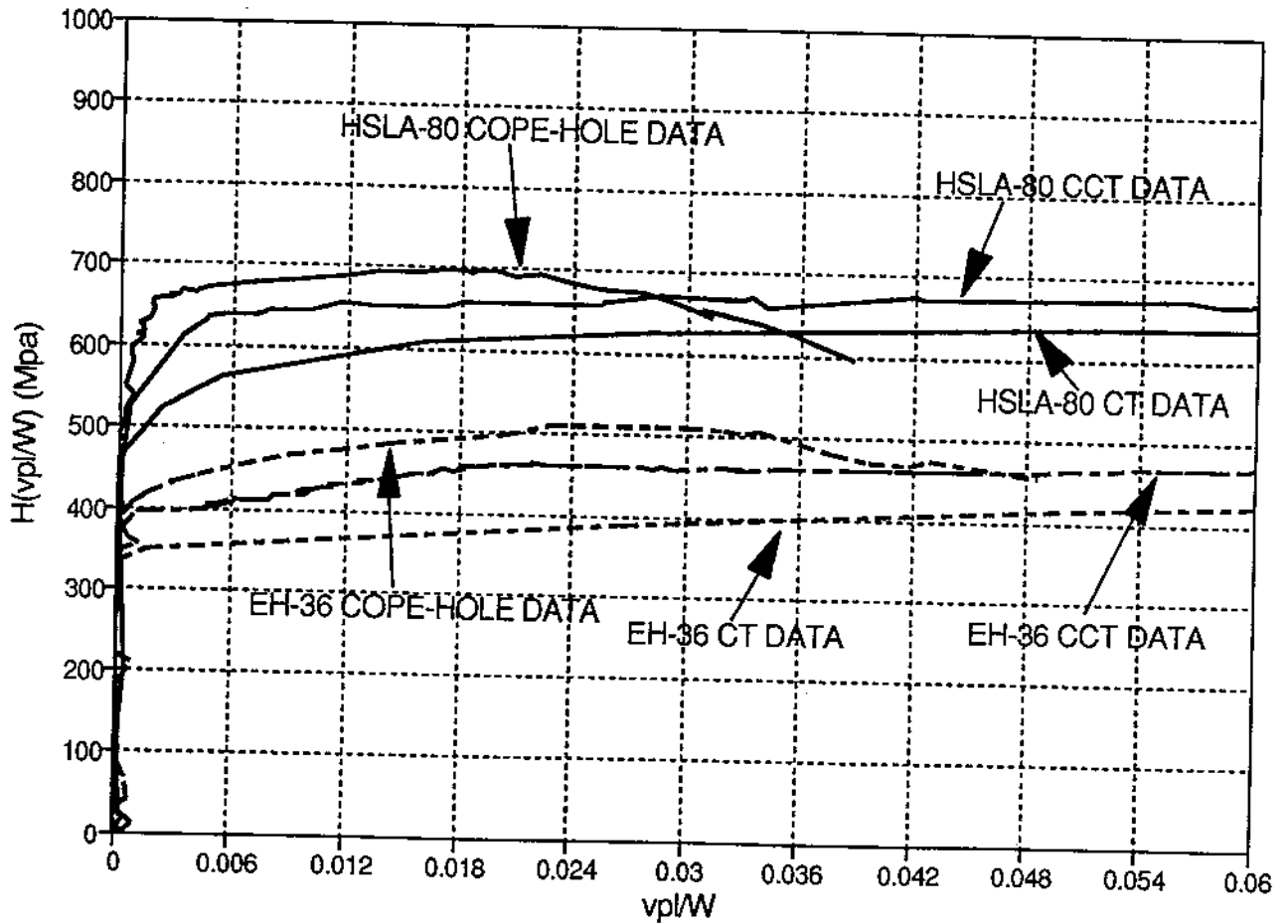


Figure 4.40

Comparison of $H(v_{pl}/W)$ functions for the HSLA-80 and EH-36 cope-hole, CCT, and CT specimens. The good agreement between these curves relative to the scatter among replicate tensile test results attests to the good accuracy of the Landes normalization method.

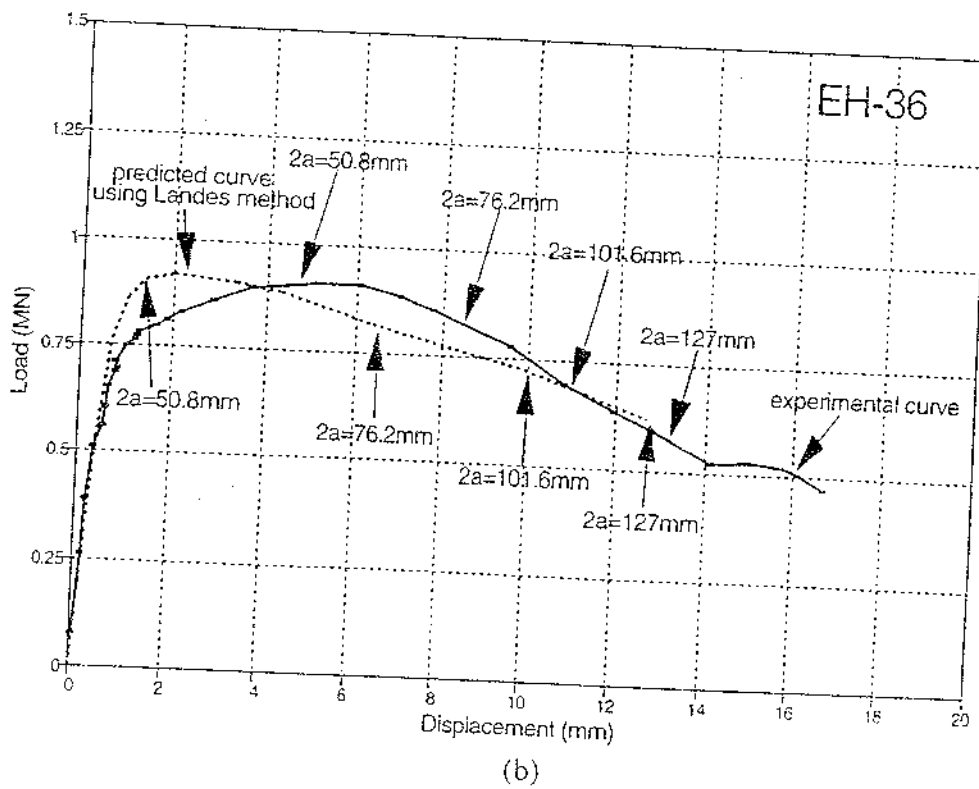
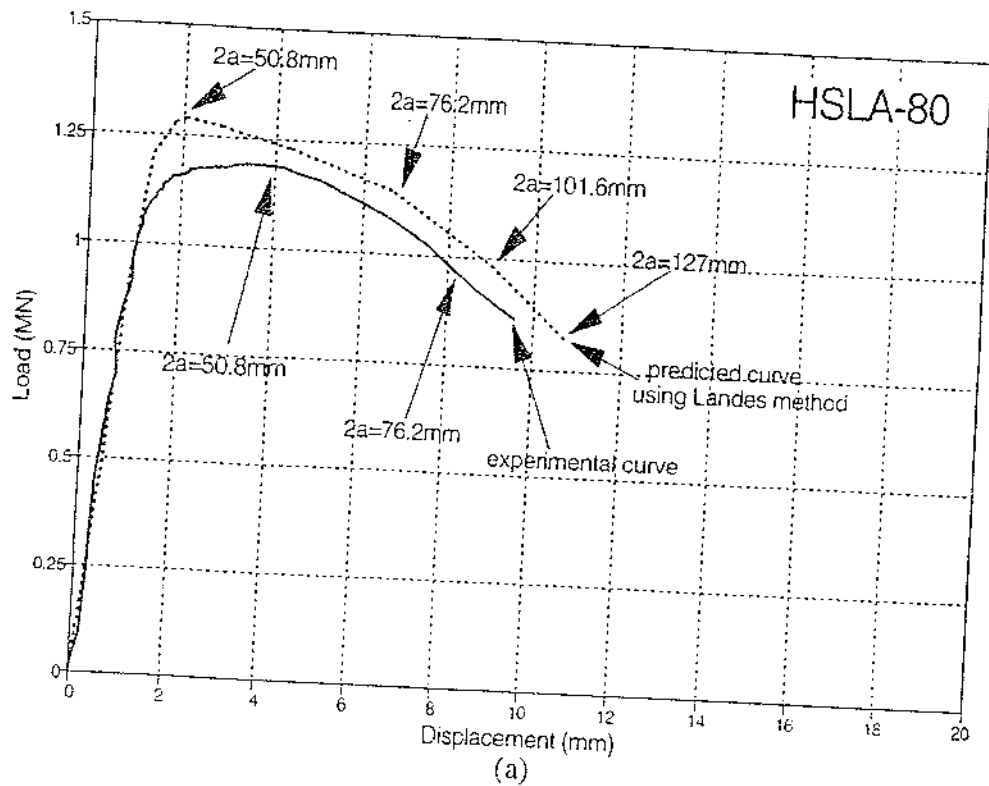


Figure 4.4] Load-displacement curves generated using the Landes method for the (a) HSLA-80 and (b) EH-36 cope-hole specimens with initial crack sizes of 50 mm showing very good agreement to the experimental data

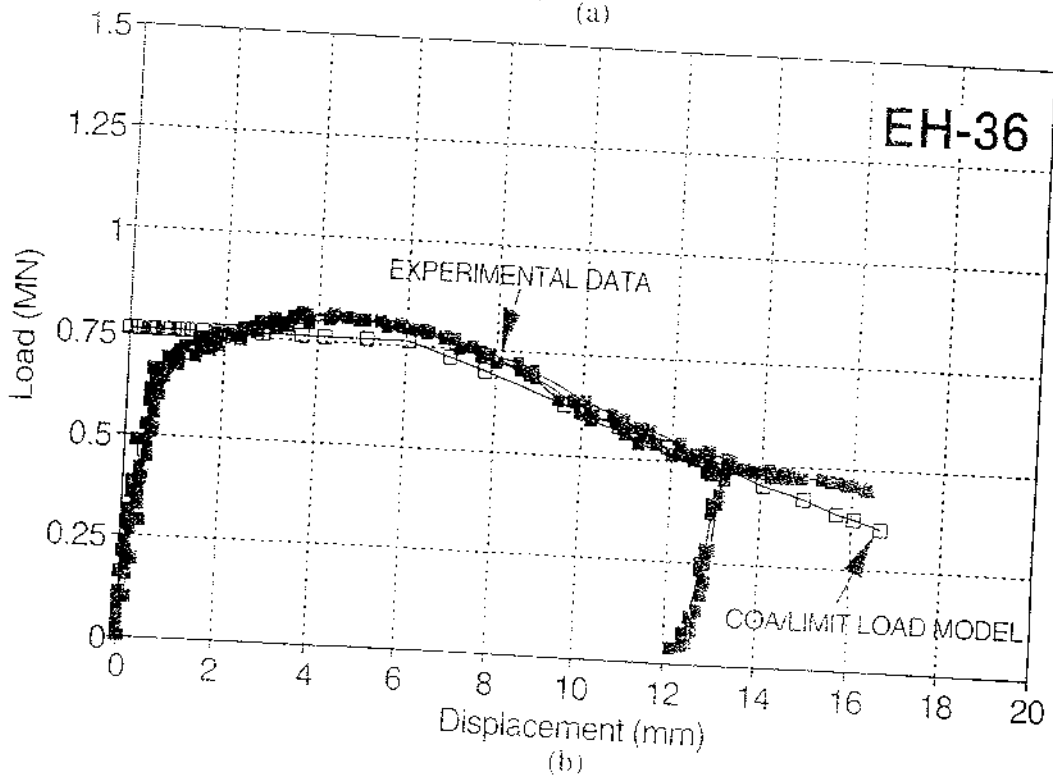
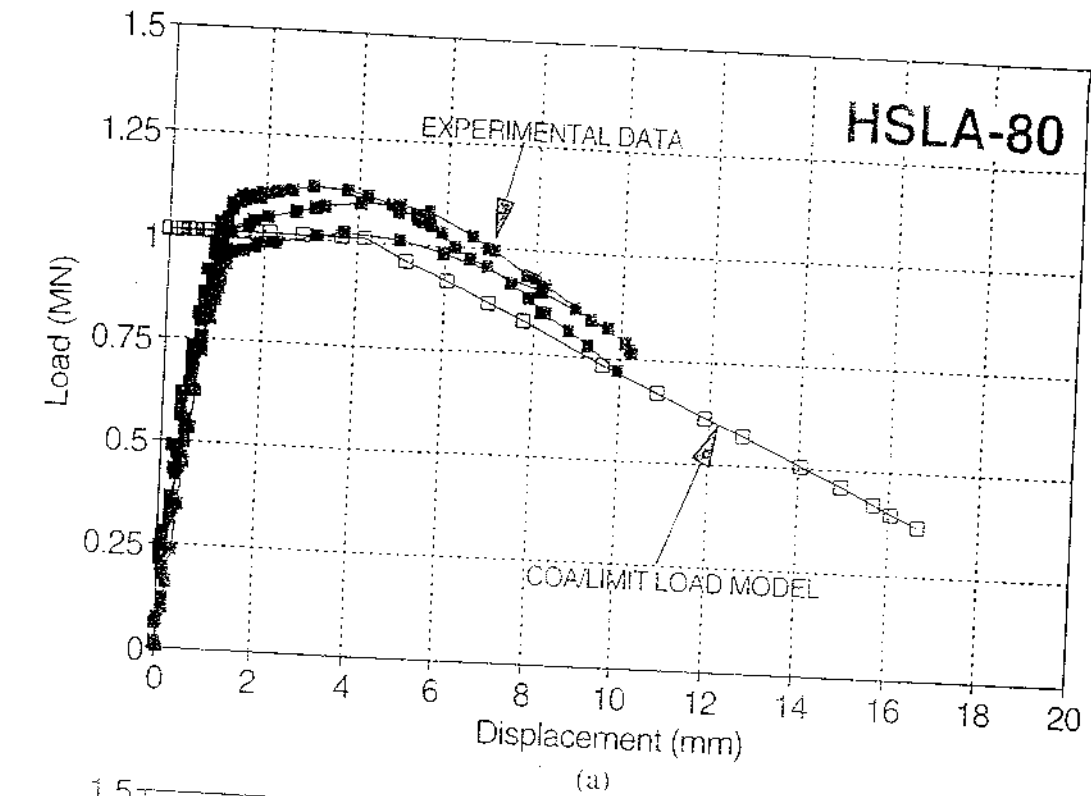


Figure 4.42 Load-displacement curves generated using the simple crack-opening-angle/limit-load model for the (a) HSLA-80 and (b) EH-36 cope-hole specimens showing very good agreement to the experimental data

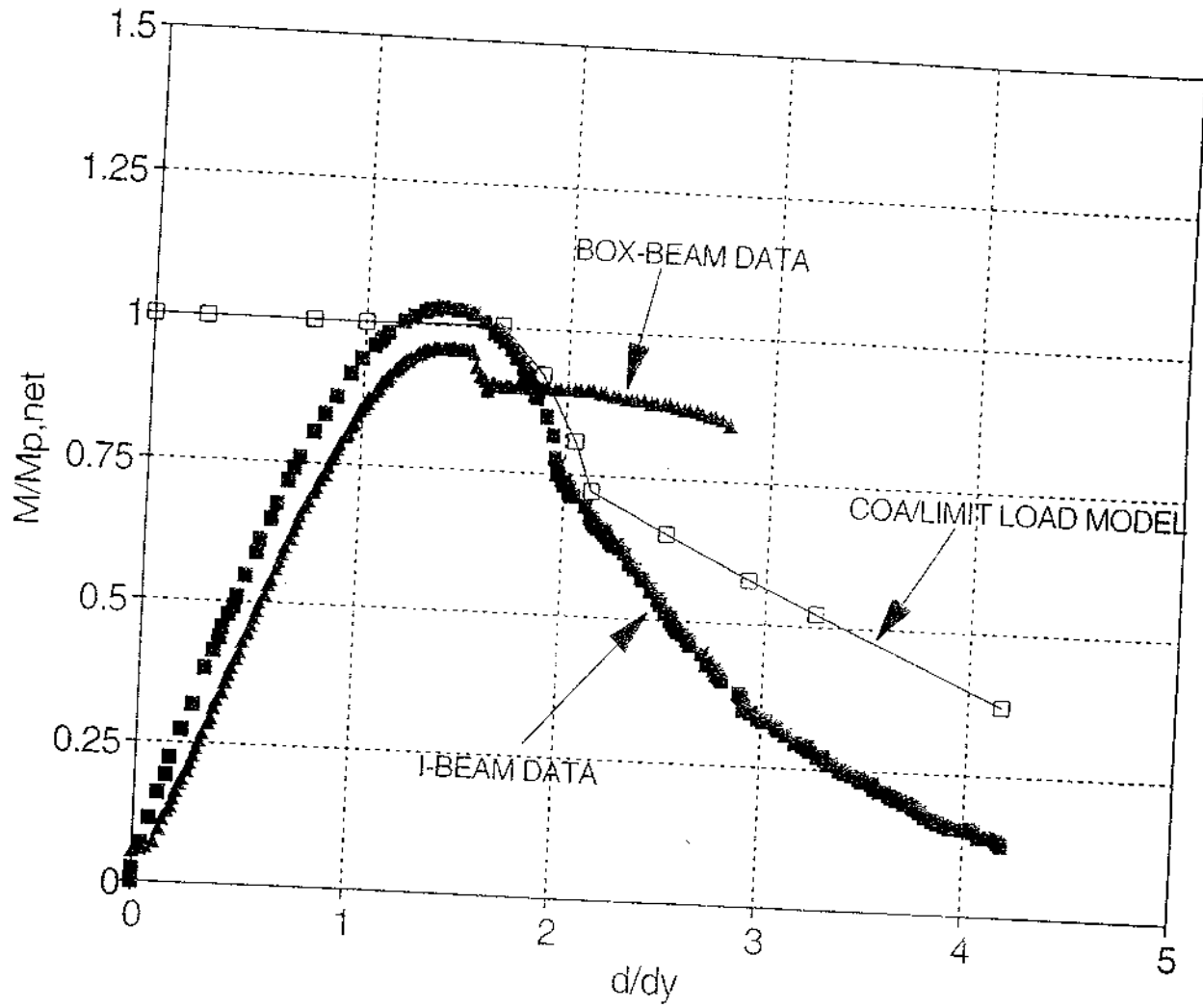


Figure 4.43

Normalized load-displacement curves generated using the simple crack-opening-angle/limit-load model for I-beam specimen A18 showing good agreement to the experimental data for specimen A18. The load is normalized by net section plastic moment, 349 kN-m, and the displacement is normalized by the yield displacement for the gross section, 11.9 mm. In this normalized form, the result is also in good agreement with the experimental data for the box sections.

5.0 GUIDELINES FOR APPLICATION OF DUCTILE FRACTURE MODELS TO SHIP STRUCTURES

The results of the experimental program, the finite-element analysis and fracture-mechanics calculations, and the survey of the relevant literature have been synthesized into a set of guidelines for the application of ductile fracture models in welded structures comprised of relatively thin (i.e. less than 51 mm thick) structural steel plates and shapes.

5.1 Specification of steel and filler metal

Ships fabricated from relatively thin plates will typically not exhibit brittle fracture, despite the presence of large fatigue cracks (greater than 200 mm long). This is because, in most cases, the steels and filler metals which are presently used in shipbuilding are specified with a Charpy test requirement (CVN). The CVN requirement should be sufficient to assure that the materials have good fracture toughness over the range of possible service temperatures, especially for plate thickness less than 26 mm [5.1]. Here "good" fracture toughness means toughness which would allow yielding to occur despite the existence of a large crack. A large crack will likely extend under a strain level of several times the yield strain, but this is accepted provided that the crack extension is limited and takes place in a stable manner. However, before assuming that the fracture mode will be ductile, the specifications for the steel and (if possible) the mill report, filler-metal certifications, and weld procedure should be examined to verify that the requirements were adequate and were achieved, especially the chemical and CVN requirements.

The chemistry and processing control the fracture toughness of steel and weld metal. Most alloy elements are added to steels to increase strength and consequently are detrimental to fracture toughness. Therefore, microalloyed steel compositions employ only small amounts of alloying elements. Of the usual alloy elements added to structural steels (C,Mn,Mo,V,Nb), carbon has the most deleterious influence on toughness. Nickel is unique as an alloy element in that it both increases strength and toughness and is frequently added to steel and weld metal (1.0-2.0 wt %) for this purpose. Unintentional or residual alloy elements in steel, such as sulfur, phosphorus, and nitrogen, also can have a deleterious effect on fracture toughness. However, improved steel making practices in use today have reduced these elements to where they have only small effects on toughness. Lamellar tearing, at one time a major problem in welded fabrication, caused primarily by poor through-thickness properties in plate steels with high sulfide inclusion content, has also been reduced by controlling sulfur levels to less than 0.01 wt. % in steel.

Grain refinement increases both fracture toughness and strength simultaneously. Cooling rates largely determine the grain size of steels as well as the type of microconstituents developed. Thicker sections will tend to have coarser grain size, coarser microconstituents, and lower toughness than thinner sections. Microalloyed steels contain elements added specifically to control ferrite grain size, e.g. niobium and vanadium.

The effect of composition and microstructure on weld metal toughness follows much the same trends. In general, weld metal toughness is usually as good or superior to plate or shape toughness largely due to the lower carbon and inherent fine grain structure and finer microconstituents which results from the high cooling rates associated with most welding processes. Only in slow-cooling high-heat-input weld processes does the resulting grain size have a detrimental effect on the weld fracture toughness.

More often, weld toughness is influenced by the incorporation of undesirable elements such as oxygen and nitrogen in the weld pool which reduce toughness. Controlling these elements is the role of the shielding gas and/or flux used in the weld process. Fluxes contain deoxidizers such as silicon and aluminum for this purpose. Welding procedures must be monitored to control toughness as well as to avoid defects. Qualification tests are often carried out on plates 25 mm thick. The procedure may then be applied to thinner plate, where cooling rates will decrease and the toughness may be lower than qualification tests indicate. Typically, higher heat input decreases cooling rate and toughness.

As was shown in Figure 2.7, steel exhibits a transition from brittle to ductile fracture behavior as the temperature increases. These results are typical for ordinary hot-rolled structural steel. The transition behavior of steel is exploited as a means to screen out brittle materials in ship fracture control plans. For example, the ship steel specifications (ASTM A131) requires a minimum CVN energy (called notch toughness) at a specified temperature for the base metal in two orientations, as shown in Table 1. As long as large defects do not exist, the notch toughness requirement assures that the fracture will not be brittle. Because the Charpy test is relatively easy to perform, it will likely continue to be the measure of toughness used in steel specifications. Often the abbreviation "CVN" is used to represent the impact energy. Often 34 J (25 ft-lbs), 27 J (20 ft-lbs), or 20 J (15 ft-lbs) are specified at a particular temperature. The intent of specifying any of these numbers is the same, i.e to make sure that the transition starts below this temperature.

The ship steel CVN requirements can be compared to the requirements for steel and weld metal for bridges, which are shown in Table 2. These tables are simplified and do not include all the requirements. The bridge steel specifications require a CVN at a temperature which is 38°C *greater* than the minimum service temperature. This "temperature shift" accounts for the effect of strain rates, which are lower in the service loading of bridges (on the order of 10^{-3}) than in the Charpy test (greater than 10^1). It is possible to measure the toughness using a Charpy specimen loaded at a strain rate characteristic of ships and bridges, called an intermediate strain rate, although the test is more difficult and the results are more variable. When the CVN energies from an intermediate strain rate are plotted as a function of temperature, the transition occurs at a temperature at least 38°C lower for materials with yield strength up to 450 MPa.

It is important to assure that there is a CVN requirement for the weld metal. For example, several types of self-shielded flux-cored arc weld (FCAW-SS) filler metals without

a CVN requirement are known to produce weld metal with very low fracture toughness, which have resulted in numerous brittle fractures [5.2]. Usually weld metal has low carbon and toughness greater than the steel plate. As shown in Table 2, the AWS D1.5 Bridge Welding Code specifications for weld metal toughness are more demanding than the specifications for base metal. This is reasonable because the weld metal is always the location of discontinuities and high tensile residual stresses. Because of variability in the cooling rate and resultant microstructure and grain size, weld metal toughness can vary widely from manufacturers certification, to weld procedure qualification test, to the fabrication of the structure [5.3].

Decades of experience with the present ship steel specifications have proved that they are successful in significantly reducing the number of brittle fractures. Specifications should also emphasize fabrication controls and inspection requirements in addition to the CVN requirements. Good detailing and control of the stress range will improve structural reliability by reducing the occurrence of fatigue cracking.

5.2 Fracture Mechanics Test Methods

Fracture tests can be divided according to the objective or use of the data. Screening tests, like the CVN test, can rank materials and give a relative indication of toughness but the result cannot be directly used in a quantitative analysis. On the other hand, fracture mechanics tests are intended to get a quantitative value of fracture toughness that can be used directly to predict fracture in structural members. As explained in Section 2.3, it is sometimes possible to indirectly infer a quantitative value of K_c from a correlation to a screening tests result like CVN.

One of the first fracture-mechanics tests was ASTM E399, "Standard Test Method for Plane-Strain Fracture Toughness of Metallic Materials". The K_c value determined from this test is given the special subscript "I" for plane strain, K_{Ic} . K_{Ic} is commonly measured on the Compact-Tension (CT) specimen, although single edge-notched bend (SENB) bars may also be used. In all fracture-mechanics tests, the specimen must be fatigue precracked. The load and crack mouth displacement are monitored in the test, and K is computed from the load either at the point of instability or at some small offset from the elastic slope. In order for the test to be considered valid, the specimens must have large planar dimensions and be very thick, approximating plane strain. Specifically, the remaining ligament (b) and the thickness (B) must be:

$$(5-1)$$

This requirement is intended to assure that the specimen size dimensions are on the order of 50 times bigger than the plastic zone at the crack tip.

Consider the very low toughness materials with K_{Ic} of $45 \text{ MPa}\cdot\text{m}^{1/2}$ and a yield strength of 450 MPa. Even for these brittle materials, a specimen thickness greater than 25 mm would be required. If the plate or flange thickness were less thick, valid K_{Ic} could not be obtained. For materials with adequate toughness, greater than $100 \text{ MPa}\cdot\text{m}^{1/2}$ for example, require specimens thicker than 120 mm. Clearly, it can be seen that this is a test which is impractical for all but the most brittle materials. For brittle materials for which a valid K_{Ic} can be obtained, invalid K_c values obtained with specimens that are too small will be larger than the valid K_{Ic} . However, if the test specimen and the structural member have the same thickness, invalid data are often used with caution. For ductile fracture, the relation between the apparent toughness from small specimens and large specimens is different than for brittle fracture. For ductile fracture, invalid K_c from a small-specimen J or CTOD test is usually less than the apparent K_c in larger specimens.

The J-integral tests were developed for elastic-plastic fracture where the fracture mode was ductile tearing rather than cleavage. The most simple of these is ASTM E813, "Standard Test Method for J_{Ic} , A Measure of Fracture Toughness" gives a value of J at the initiation of ductile tearing. This test is typically performed on CT specimens, although SENB specimens may also be used. In these J tests, the load and crack mouth displacement are monitored and J is computed from the work done on the specimen, i.e. from the area under the load displacement curve. In order to identify the initiation of ductile tearing, changes in compliance are monitored by performing periodic partial unloading of the specimen. The crack extension is determined from these compliance measurements.

The specimen size requirements for ASTM E813 are much less stringent than E399, i.e:

(5-2)

For a given value of fracture toughness the specimen may be about 50 times thinner than for ASTM E399 (K_{Ic}). For moderate toughness of about $100 \text{ MPa}\cdot\text{m}^{1/2}$ ($J = 48 \text{ kJ/m}^2$), the specimen ligament and thickness are required to be greater than 3 mm, which can be easily met.

ASTM E1290, "Standard Test Method for Crack-Tip Opening Displacement (CTOD) Fracture Toughness Measurement" gives a slightly different test which is easier to perform but gives results which are more variable. This test is typically performed on SENB specimens, although the CT specimen can also be used. The specimens are the full thickness of the plate or shape and there are no validity requirements. The load and crack-mouth displacement are monitored during the test, and the CTOD is inferred from the crack-mouth displacement. A variety of outcomes are possible including short propagation or pop-in of the crack without instability. The critical CTOD is either at the point of "pop-in" or at the maximum load for more ductile behavior.

Recognizing that all of these tests are performed on similar specimens and that all of the various fracture toughness measures can be related, BSI has recently developed a unified testing procedure BS 7448, "Fracture Mechanics Toughness Tests". Using this method, a test is performed and then, based on the results, it is decided how the test should be interpreted. ASTM is currently working on a similar unified test method.

5.3 Recommended ductile fracture models

Ductile fracture models were studied in order to evaluate their usefulness and degree of conservatism with regard to experiments on full scale structural members. The following fracture assessment procedures are recommended on the basis of this research. The authors have intended to strike a balance between the level of refinement required for the purposes of evaluating cracks in ships in service and the complexity in the analysis, considering that assessments may have to be made by non-experts on hundreds of cracks in a single ship. Chapter 4 explains the fracture prediction methods in detail and the results of the analyses.

5.3.1 British Standards Institute PD 6493

The procedures contained in PD 6493 can be used to make accurate and conservative predictions of the maximum load for cracked structural members. While it does predict maximum load, PD 6493 cannot predict ductility which may also be needed for an evaluation of structural integrity in the presence of large fatigue cracks.

British Standards Institute document PD 6493 provides a rationale for assessing the peak load for fracture in the form of failure assessment diagrams. These diagrams are interaction curves that form an envelope to account for both the fracture and plastic collapse modes of failure. There are three levels of assessment. The first level uses a simplified stress distribution and a failure envelope based on the CTOD design curve. This level is intended to be a "screening" level and is very conservative. The second level uses a more accurate stress distribution and utilizes a failure envelope based on a strip yield model assuming an elastic-perfectly plastic material. As discussed in Section 4.1, this second level is very accurate and relatively easy to use. The third level may be more suitable for high-strain-hardening steels, but for ordinary ship steel, level 3 analysis offers no significant advantages to justify the significant additional effort relative to level 2.

To define S_r in the level 2 analysis, the applied bending moment was normalized by the fully plastic bending moment based on the net cross-section of the cracked section of the beam. The yield stress was used rather than the flow stress, since this is the typical way the plastic moment is calculated in structural engineering. The limit-load calculations are explained further in Appendix 6.

Analytic solutions for the stress-intensity factor, K , for the complex cracked ship structural details do not currently appear in the literature. Therefore, it is recommended that the stress intensity factor at each crack tip in the specimen be approximated by treating the beam section as a monolithic block and using an equivalent elliptical crack geometry. This approximation was discussed in Section 4 (see Figures 4.3 through 4.5 for example). Appendix 5 explains the calculations in detail and shows an example of the spreadsheet a set of K calculations.

Although cracks can be loaded by shear, experience shows that only the tensile stress normal to the crack is important in causing fatigue or fracture in steel structures. This tensile loading is referred to as "Mode I". When the plane of the crack is not normal to the maximum principal stress, a crack which propagates subcritically or in stable manner will generally turn as it extends such that it becomes normal to the principal tensile stress. Therefore, it is typically recommended that a welding defect or crack-like notch which is not oriented normal to the primary stresses can be idealized as an equivalent crack with a size equal to the projection of the actual crack area on a plane which is normal to the primary stresses (see PD6493 for example).

To use the failure assessment diagrams to predict maximum load, K_r and S_r are plotted as a function of increasing load (applied moment). The load that produced a critical combination of S_r and K_r should be taken as the maximum load prediction. If the crack has more than one crack tip, an interaction path of K_r vs. S_r was plotted for each crack tip as a function of applied moment. The intersection of the path and the failure assessment envelope that provided the lowest allowable applied moment is taken as the maximum load prediction. If the crack tip is adjacent to an attachment or other stress raiser, a stress concentration factor is applied to the stresses in the calculation of K but not in the limit load calculation. Residual stresses should be ignored in the calculation of the stress intensity factors as well as the collapse load. The exclusion of residual stress can be rationalized because the magnitude of residual stress decreases with depth through the thickness of the plate. Also, the crack tends to alleviate the residual stresses by reducing the constraint on the weld.

The predicted maximum load values are expected to be conservative and accurate within 20 percent for relatively simple members. In more complex structure such as the box-section experiments, the error on the conservative side may be up to 39 percent. The conservatism of these predictions, even with the exclusion of residual stresses, provides evidence that PD 6493 is a reasonable way to conservatively estimate peak loads before fracture.

5.3.2 Predicting crack extension using a constant crack-opening angle

Predicting the crack extension as a function of displacement is the critical issue in predicting load-deformation behavior. Two different but related methods were investigated for predicting crack extension as a function of increasing displacement: 1) a constant crack-opening angle; and, 2) a J-R curve analysis. For the latter approach, finite-element analysis was used to calculate the J integral, as well as a variety of estimation schemes. Using a J-R curve approach for extended crack propagation in complex ship structural details requires finite-element analysis and is very difficult and time consuming. In the end this approach is not even very accurate.

As shown in Section 3, the I-beams, box-beams, and cope-hole specimens of both materials exhibited the same constant rate of crack-opening displacement with respect to crack extension. This rate is called the crack-opening angle (COA), and in all of these experiments it was about 24 percent radian (13 degrees), e.g. see Figure 3.27. Many other researchers have shown similar results in tearing of thin steel and aluminum plates. Based on this constant COA concept, a simple kinematic model was developed based on the experimental observations.

The model is based on d_0 , the minimum observed displacement at peak load, just prior to significant crack extension and the descending branch of the load-displacement curve. For the tensile specimens (CCT and cope-hole specimens) it was noted that d_0 was 4 mm for the HSLA-80 steel and 6 mm for the EH-36 steel. For the tensile tests (CCT and cope-hole tests), the displacement, d , on the overall gage length is essentially the same as the CTOD₅. Therefore the displacement is concentrated on the crack plane. This displacement is equal to:

$$d = d_0 + COA (\Delta a) \quad (5-3)$$

where Δa is the crack extension and the other terms were defined above.

For the bending tests, the displacements were measured at various locations, but it was noted that all displacements increased approximately in proportion to one another. The beams formed a plastic hinge on the crack plane and all displacements resulted primarily from rotation, Θ , of this hinge. At the point where the yield stress is reached on the outer fibers of the gross section, Θ_y is equal to 3.2 percent radian. Taking the depth of the beam as 190 mm and assuming a linear displacement gradient, the "effective average" displacement at the outer fibers, d_y , is about 6 mm. The displacement at peak load, d_0 , is equal to 1.5 d_y or about 9 mm.

5.3.3 Limit Load Analysis

Given the crack extension vs. displacement history, the load-displacement curve can be computed using either a simple limit-load analysis or a finite-element analysis. In Section 4 limit load solutions were shown to be more accurate than finite-element analysis for prediction of the load-displacement curve. The simple limit-load calculation is based on the net section area assuming elastic-perfectly plastic behavior in pure bending. More detail on the limit load calculations are provided in Appendix 6. The limit load approach provides a simple and accurate method of predicting the specimen's remaining load capacity with respect to crack extension. These calculations are simple enough to be performed with a spreadsheet, and are the type of calculations that can be practically implemented with regard to common ship structural details. Of course, in order to predict the load-deformation curve, it is necessary to predict the crack extension history correctly.

5.4 References

- 5.1 Pense, A.W., "Evaluation of Fracture Criteria for Ship Steels and Weldments", Report SSC-307, Ship Structure Committee, Washington, D.C., 1981.
- 5.2 Kaufmann, E.J., Xue, M., Lu, L.-W., and Fisher, J.W., "Achieving Ductile Behavior of Moment Connections", *Modern Steel Construction*, Vol. 36, No. 1, pp. 30-39, January, 1996.
- 5.3 Easterling, K., Introduction to the Physical Metallurgy of Welding, Butterworths Monographs in Materials, London, 1983.

Table 5.1: Minimum Charpy test requirements for ship steel from ASTM A131

Material:	Orientation:	Charpy V-Notch Energy	
		L-T	T-L
		Joules@°C	Joules@°C
Grade A		none	none
Grade B (none if 25 mm or under)		27@0	19@0
Grade D		27@-10	19@-10
Grade E		27@-40	19@-40
Grade AH32, AH36		34@0	23@0
Grade DH32, DH36		34@-20	23@-20
Grade EH32, EH36		34@-40	23@-40

*These requirements are for steel up to 51 mm thick.

Table 5.2: Minimum Charpy test requirements for bridge steel and weld metal

Material: (L-T orientation)	minimum service temperature		
	-18°C	-34°C	-51°C
	Joules@°C	Joules@°C	Joules@°C
Steel: non-fracture critical members*, **	20@21	20@4	20@-12
Steel: fracture critical members*, **	34@21	34@4	34@-12
Weld metal for non-fracture critical*	27@-18	27@-18	27@-29
Weld metal for fracture critical*, **	34@-29°C for all service temperatures		

*These requirements are for welded steel with minimum specified yield strength up to 350 MPa up to 38 mm thick. Fracture critical members are defined as those which if fractured would result in collapse of the bridge.

**The requirements pertain only to members subjected to tension or tension due to bending.

6.0 CONCLUSIONS AND RECOMMENDATIONS FOR FURTHER RESEARCH

Ductile fracture models were evaluated with respect to their usefulness and degree of conservatism with regard to experiments on full-scale ship structural members. The following conclusions were drawn.

1. Welded steel structural members and their connections are expected to have a ductility greater than 3 times the yield strain so that the overall structure performs as expected when subjected to extreme or accidental loading. The effect of the presence of fatigue cracks on this ductility has not been previously considered. Full-scale fracture experiments with HSLA-80 and EH-36 steel consistently show the development of the plastic limit load on the net section and ductility greater than 3, despite large fatigue cracks.
2. The procedures contained in PD 6493 can be used to make conservative and relatively accurate predictions of the maximum load for cracked structural members. While it does predict maximum load, PD 6493 cannot predict ductility which may also be needed for an evaluation of structural integrity in the presence of large fatigue cracks.
3. Predicting crack extension using a J-R curve measured on small compact-tension (CT) specimens produced reasonable results on full-scale specimens loaded in tension, but gave unconservative results when applied to full-scale specimens loaded in bending. Estimation schemes gave conservative but very inaccurate results for J at large displacements. Therefore, the J-R curve approach requires difficult and time-consuming finite-element analysis for non-standard geometries.
4. Predicting crack extension using a constant crack-opening angle of 24 percent radian is a very simple and accurate approach, which seems to be generally applicable to tension and bending and was found to be the same angle for the two steels investigated.
5. If the crack length history with respect to deflection is known for a structural component constructed of high-toughness steel, a simple limit-load analysis accurately predicts the load as a function of displacement.

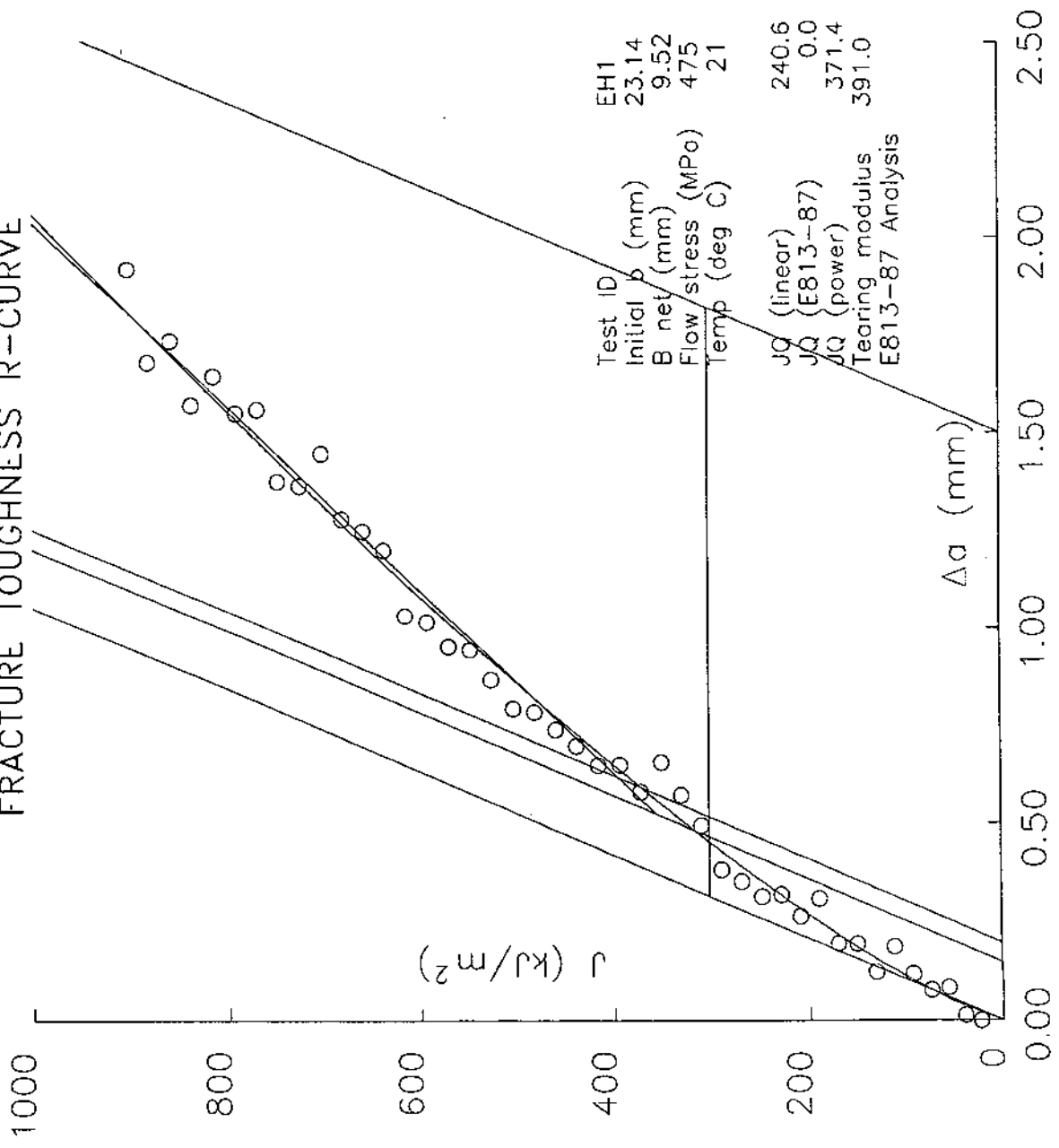
The crack-opening angle seems to be an aspect of crack extension which is relatively general, i.e. it does not appear to be a material property like fracture toughness. More experiments should be done to verify the constant crack-opening angle approach for various steels and detail types and to determine if 24 percent radian is a reasonable lower bound for various ship steels.

The box beam specimens exhibited a plateau where there was extensive ductility at a large fraction of the peak load. The plateau occurred when the crack encountered a

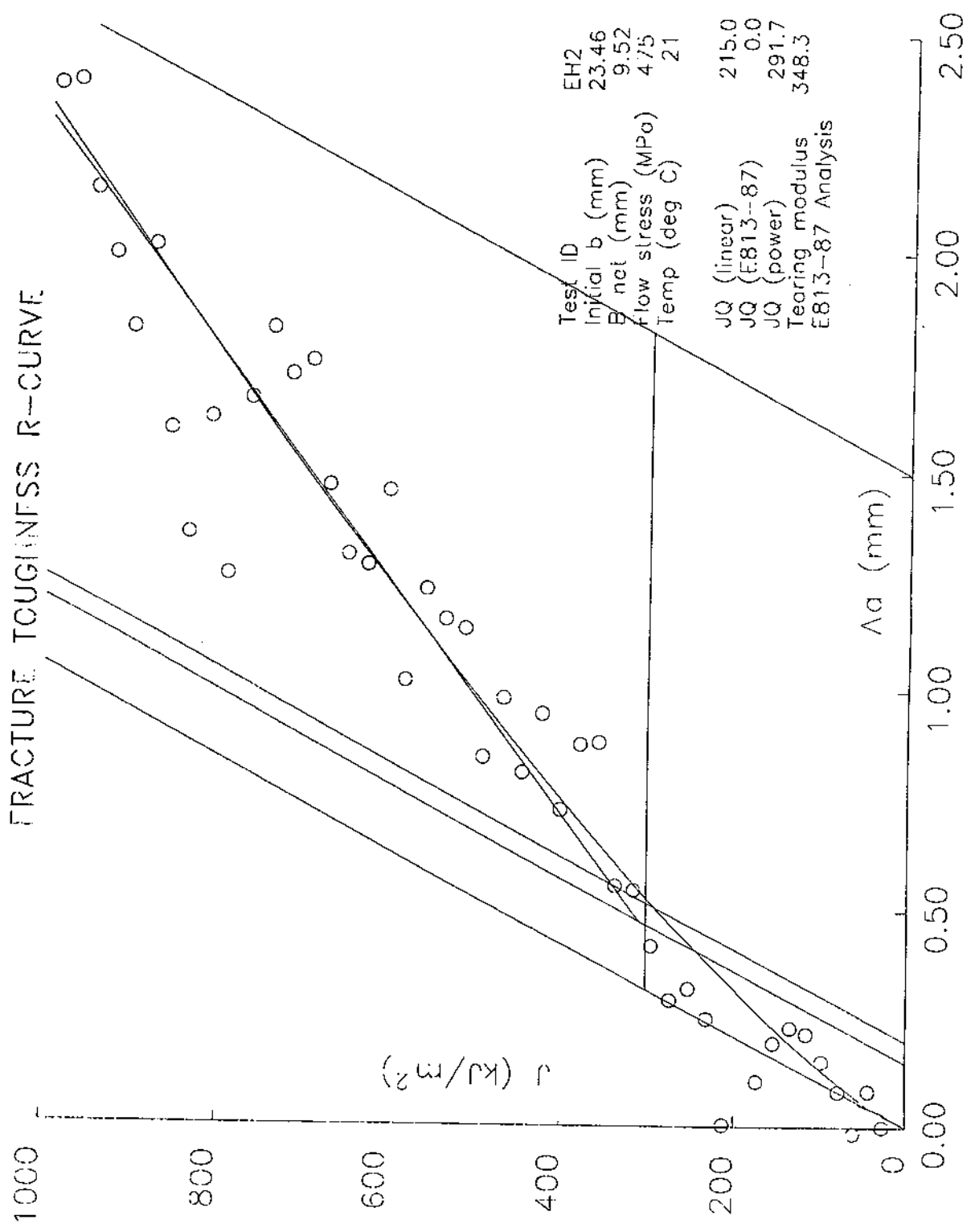
transverse plate (the second flange). The crack did not easily penetrate the second flange because the web is intercostal (not continuous) through the flange. Thus, the second flange is an effective but temporary crack arrestor. After sufficient deformation, the crack bursts through the second flange in a catastrophic manner. More experiments should be done to characterize the amount of deformation it would take to penetrate various types of crack arresters.

Appendix 1
Selected J-R Curves for the HSLA-80 and EH-36 Materials

FRACTURE TOUGHNESS R-CURVE

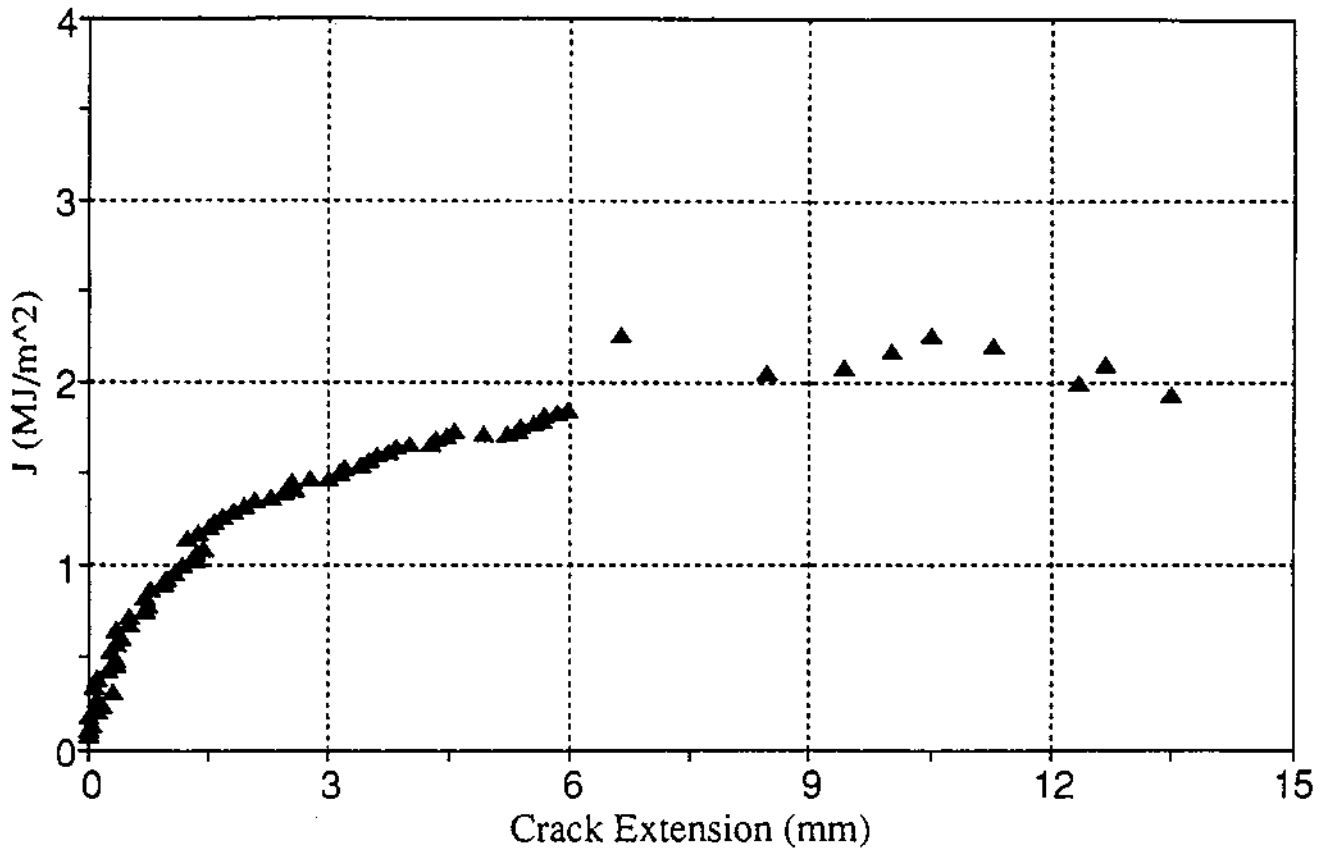


FRACTURE TOUGHNESS R-CURVE



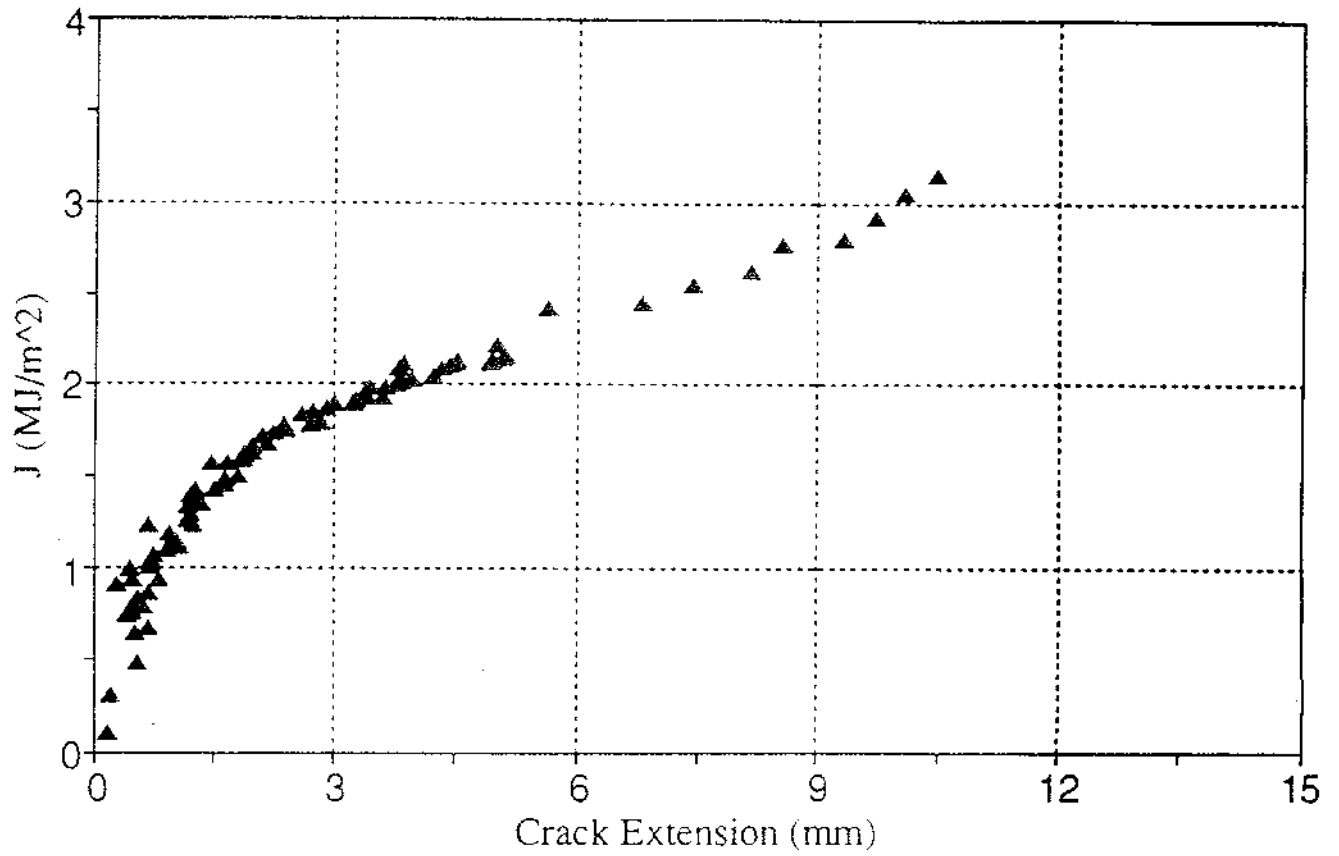
J - Resistance Curve

9.5mm - LT



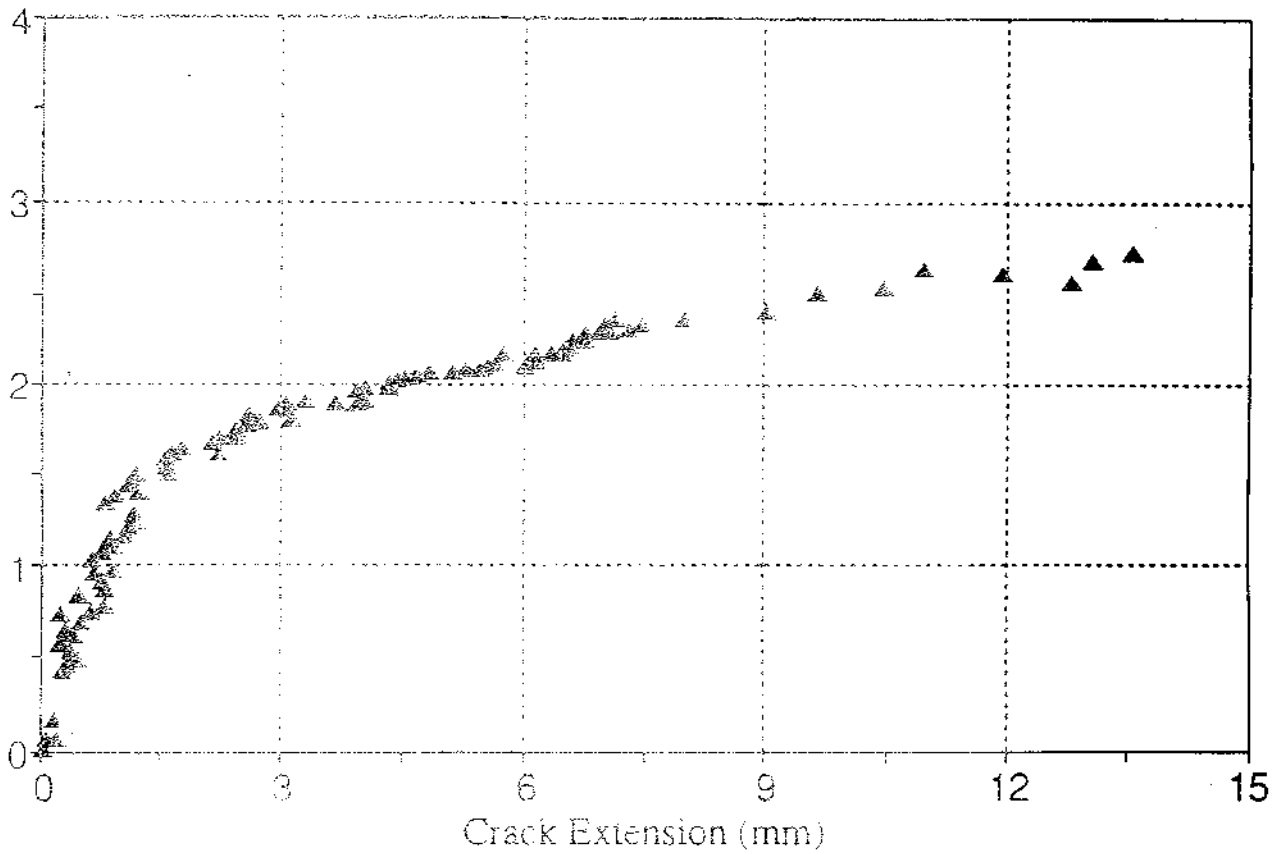
J - Resistance Curve

12.7mm - LT



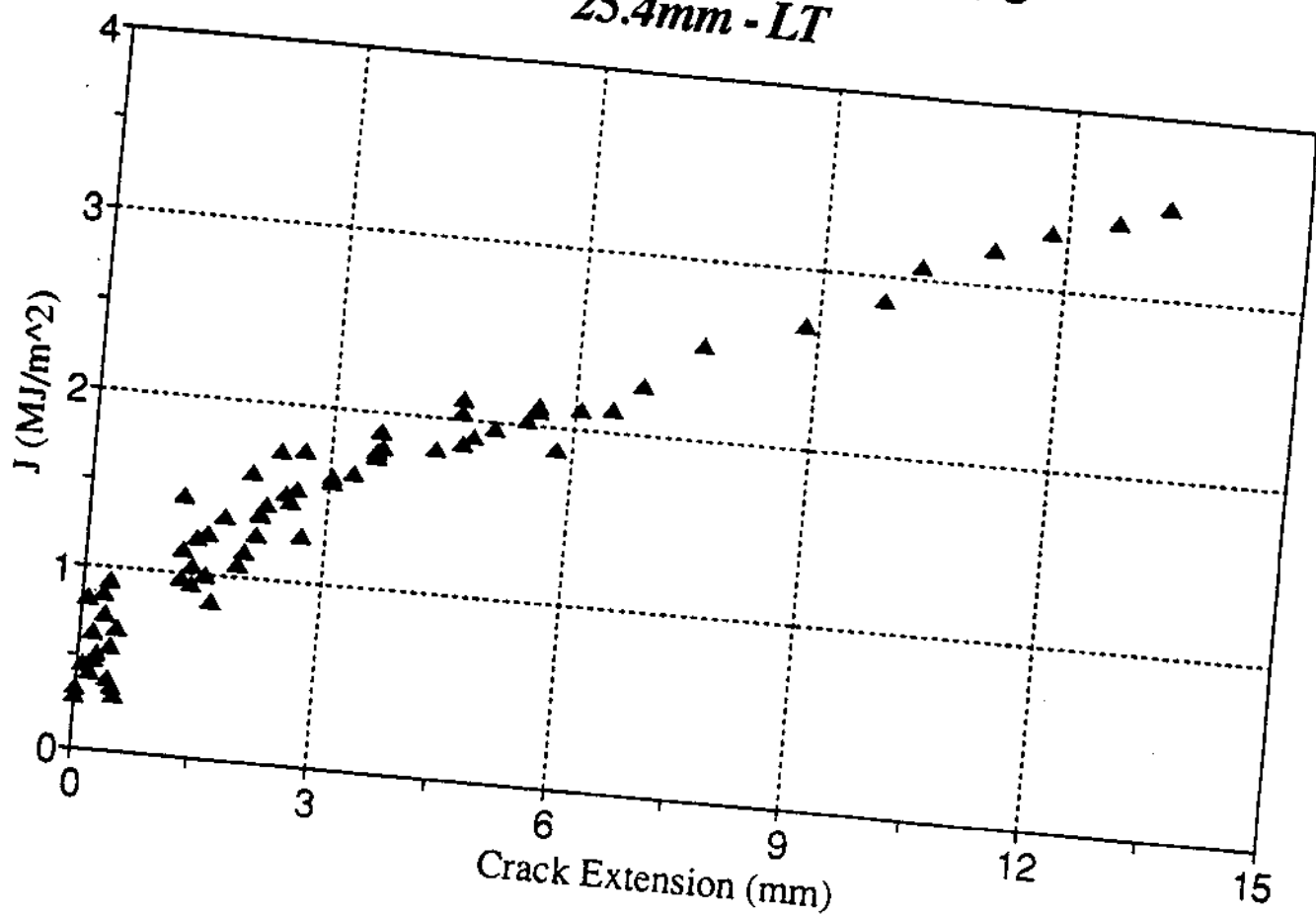
J - Resistance Curve

12.7mm - TL

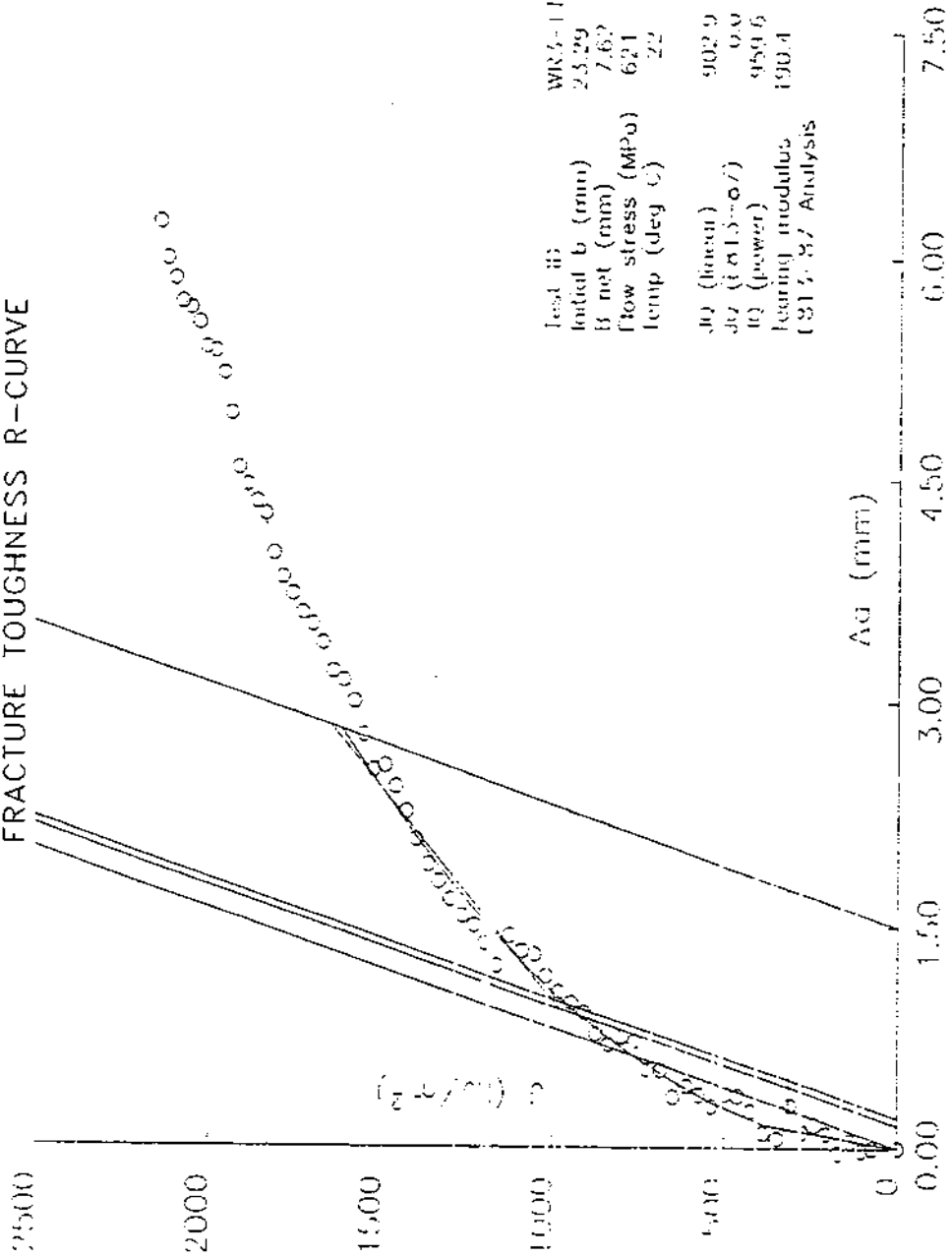


J - Resistance Curve

25.4mm - LT

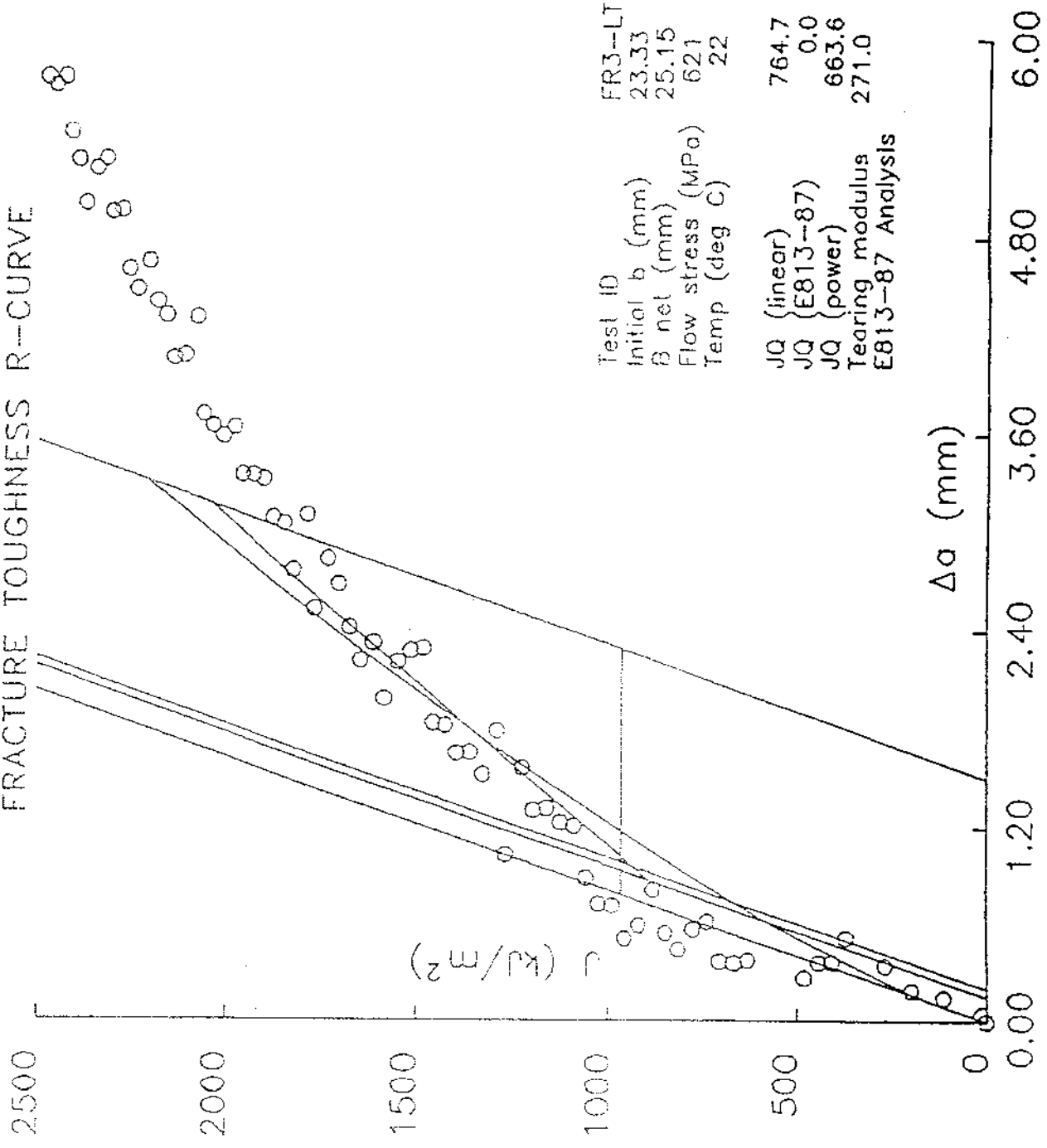


FRACTURE TOUGHNESS R-CURVE



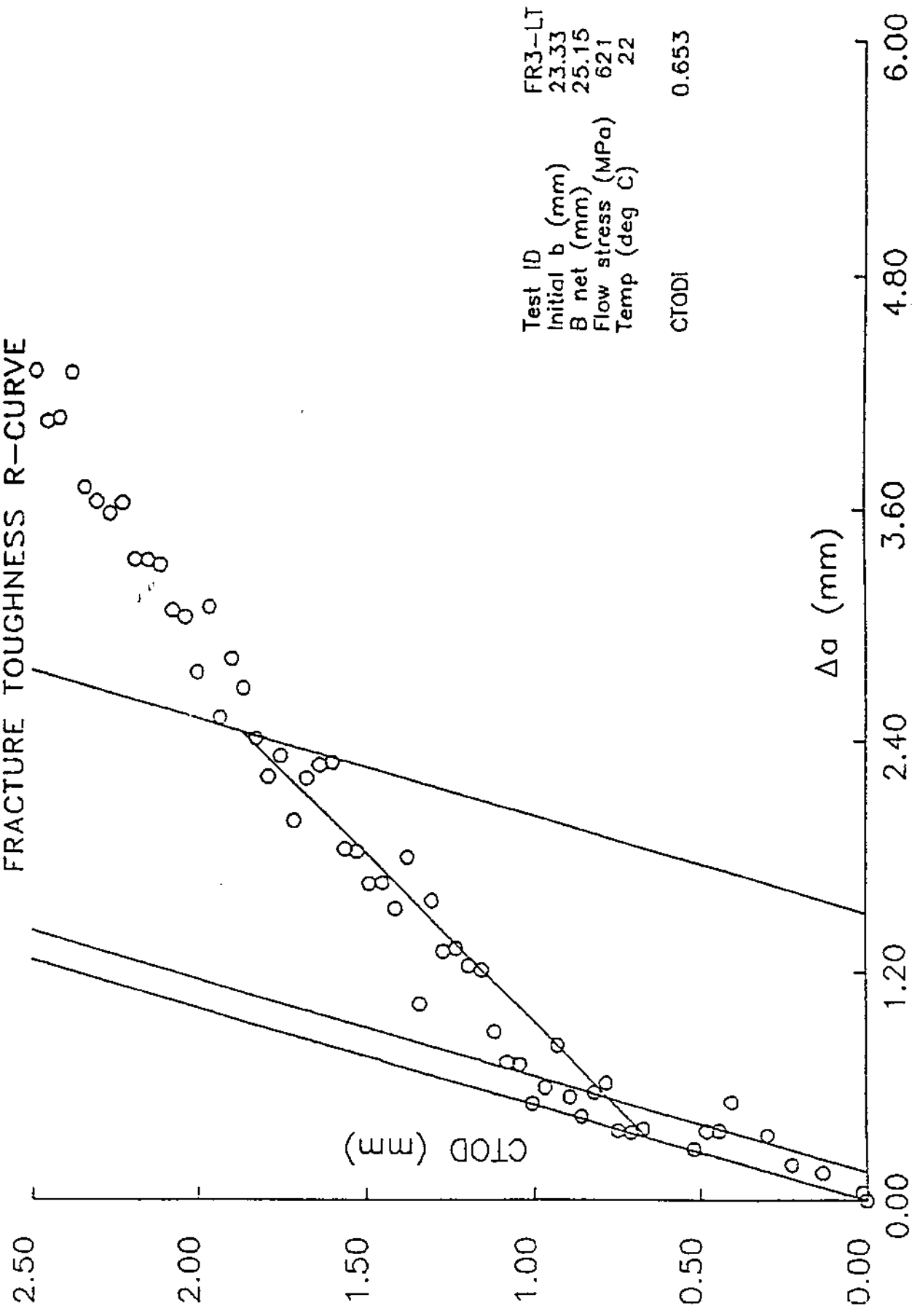
Test ID: WRS-11
 Initial b (mm): 23.29
 B net (mm): 7.62
 Flow stress (MPa): 621
 Temp (deg C): 22
 J0 (linear): 902.9
 J0 (81.5-a/): 0.0
 W (power): 459.6
 tearing modulus: 190.4
 (81.5-a/ Analysis)

FRACTURE TOUGHNESS R-CURVE



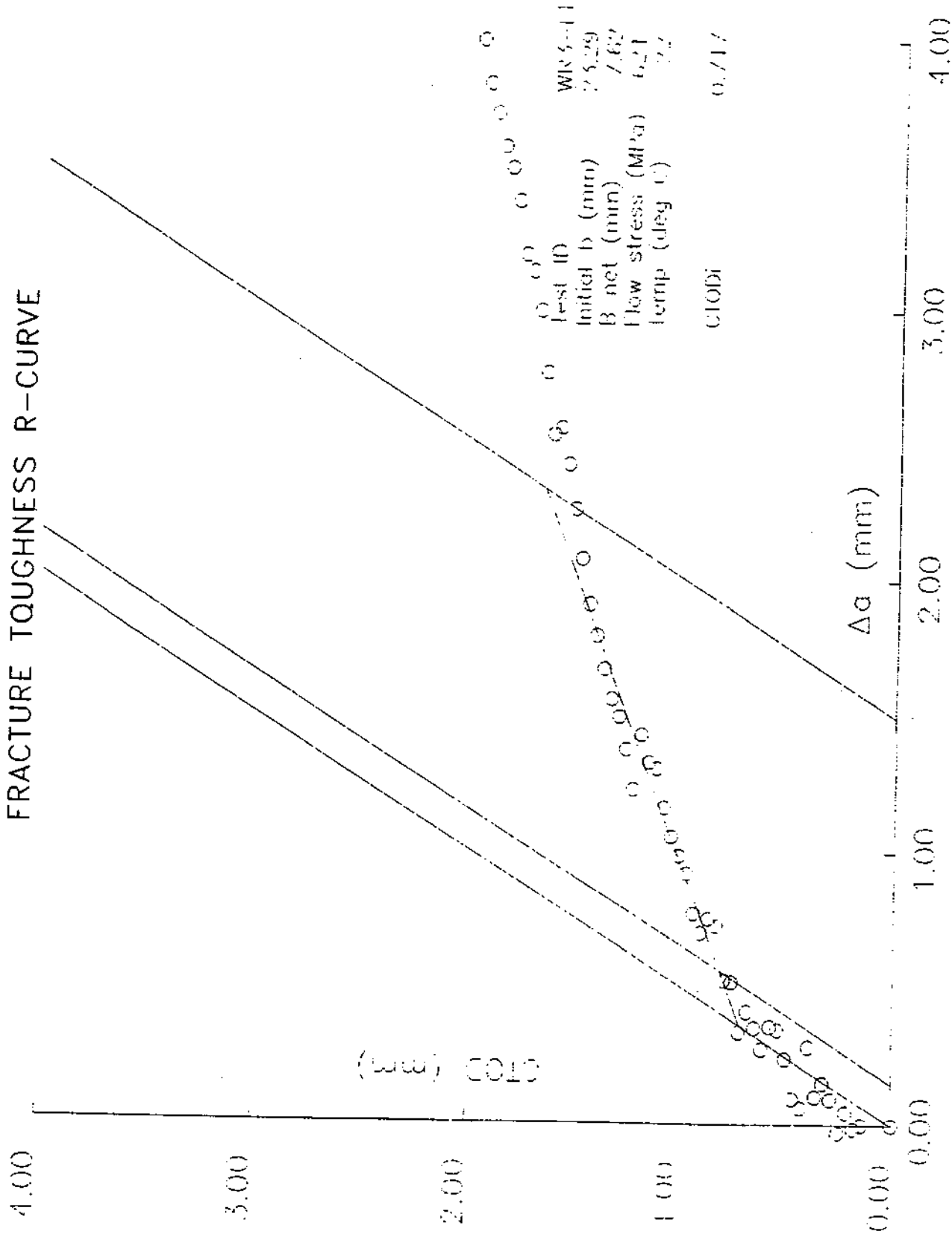
Test ID	FR3-LT
Initial b (mm)	23.33
B net (mm)	25.15
Flow stress (MPa)	621
Temp (deg C)	22
JQ (linear)	764.7
JQ (E813-87)	0.0
JQ (power)	663.6
Tearing modulus E813-87 Analysis	271.0

FRACTURE TOUGHNESS R-CURVE

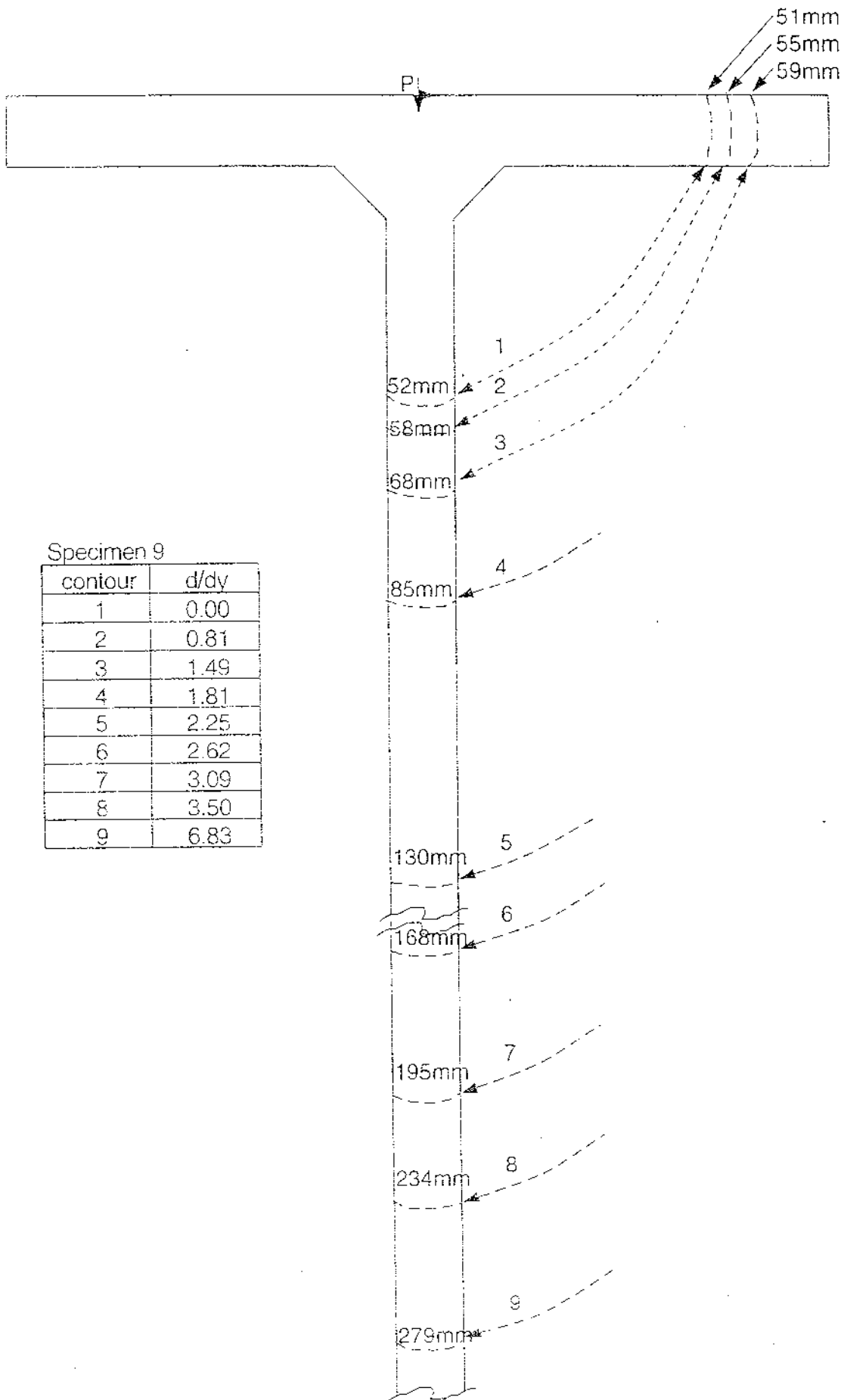


Test ID FR3-LT
 Initial b (mm) 23.33
 B net (mm) 25.15
 Flow stress (MPa) 621
 Temp (deg C) 22
 CTODI 0.653

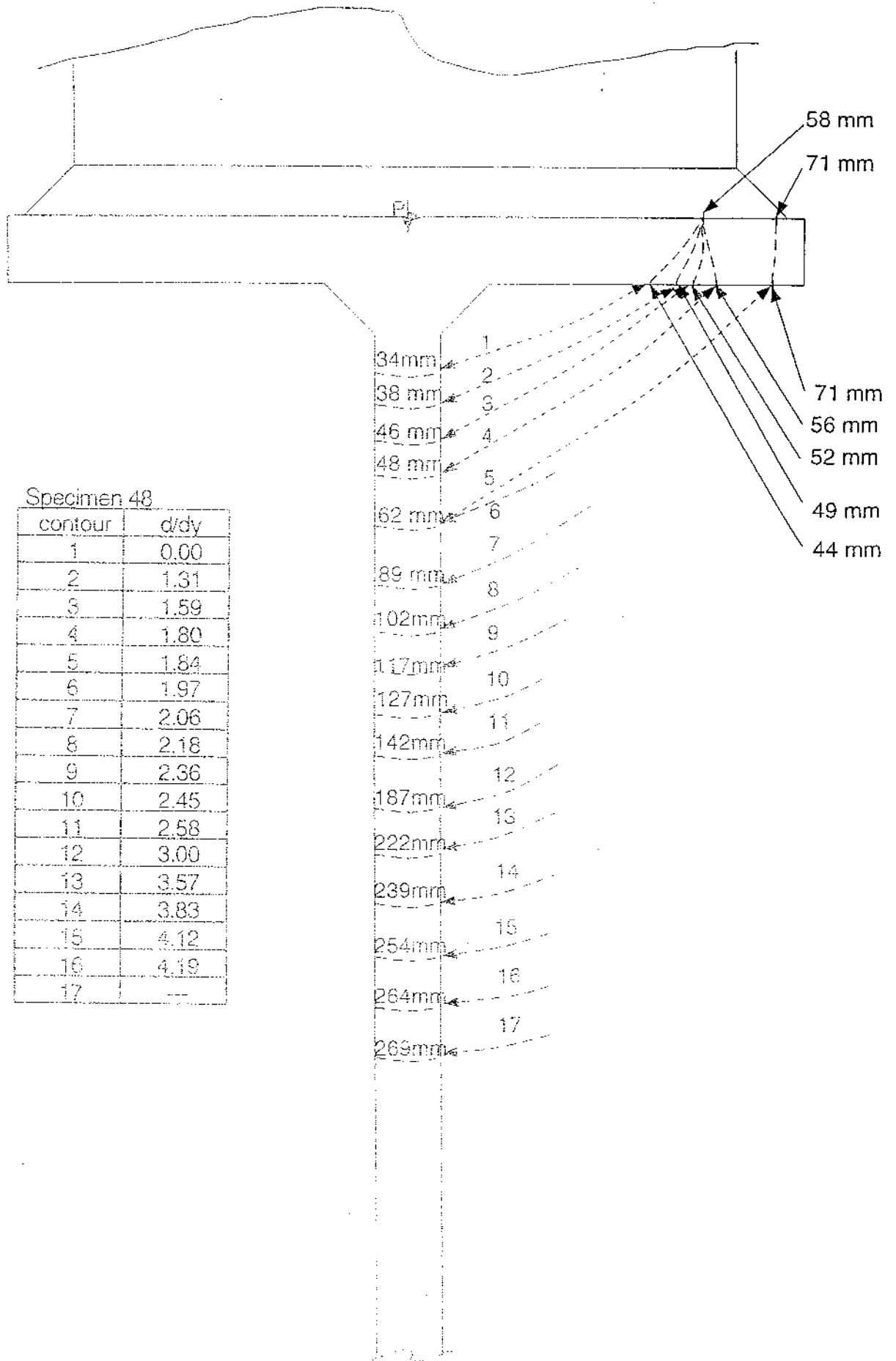
FRACTURE TOUGHNESS R-CURVE



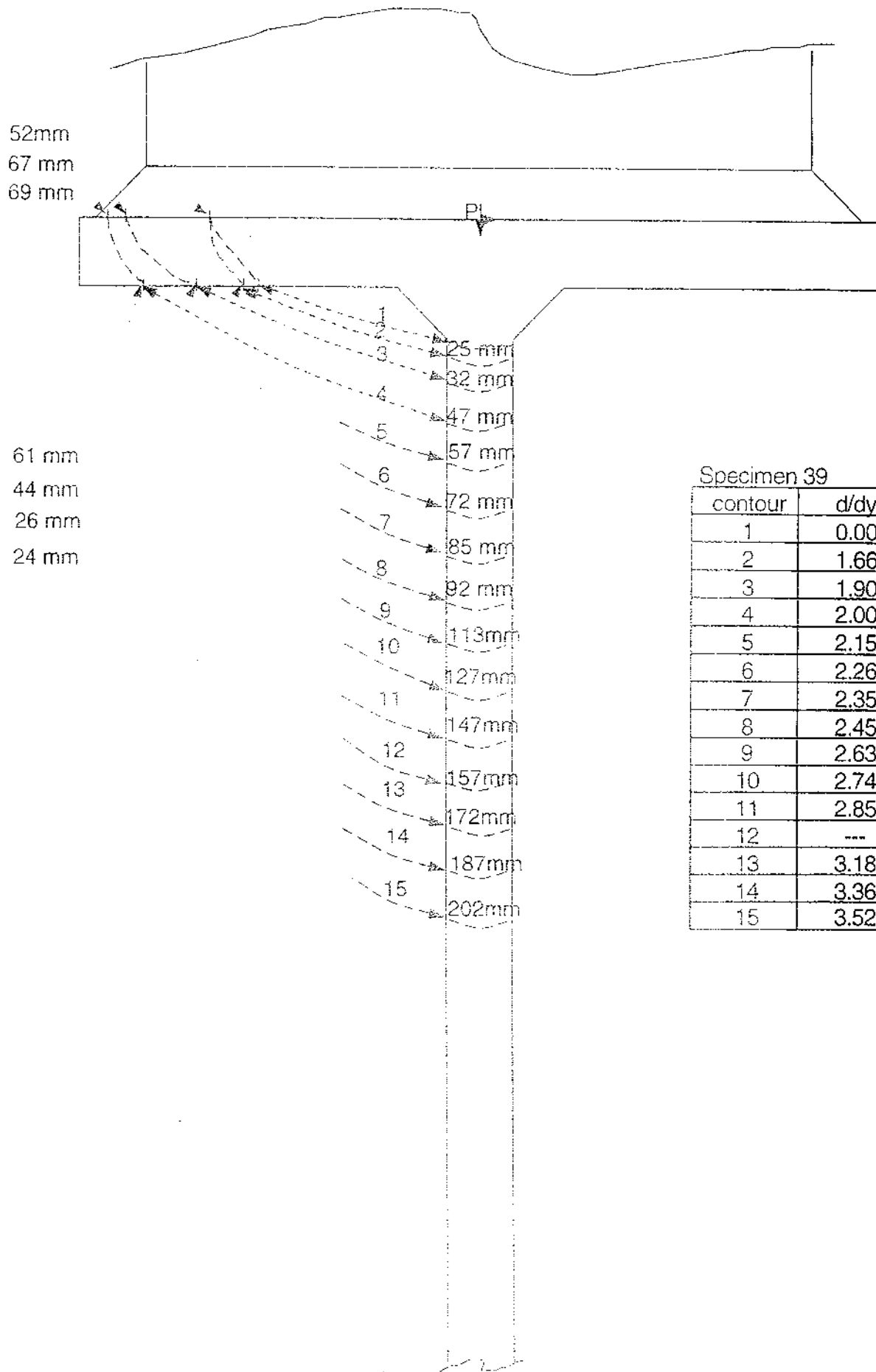
Appendix 2
Experimental Data from I-Beam Experiments



distances are measured from point P

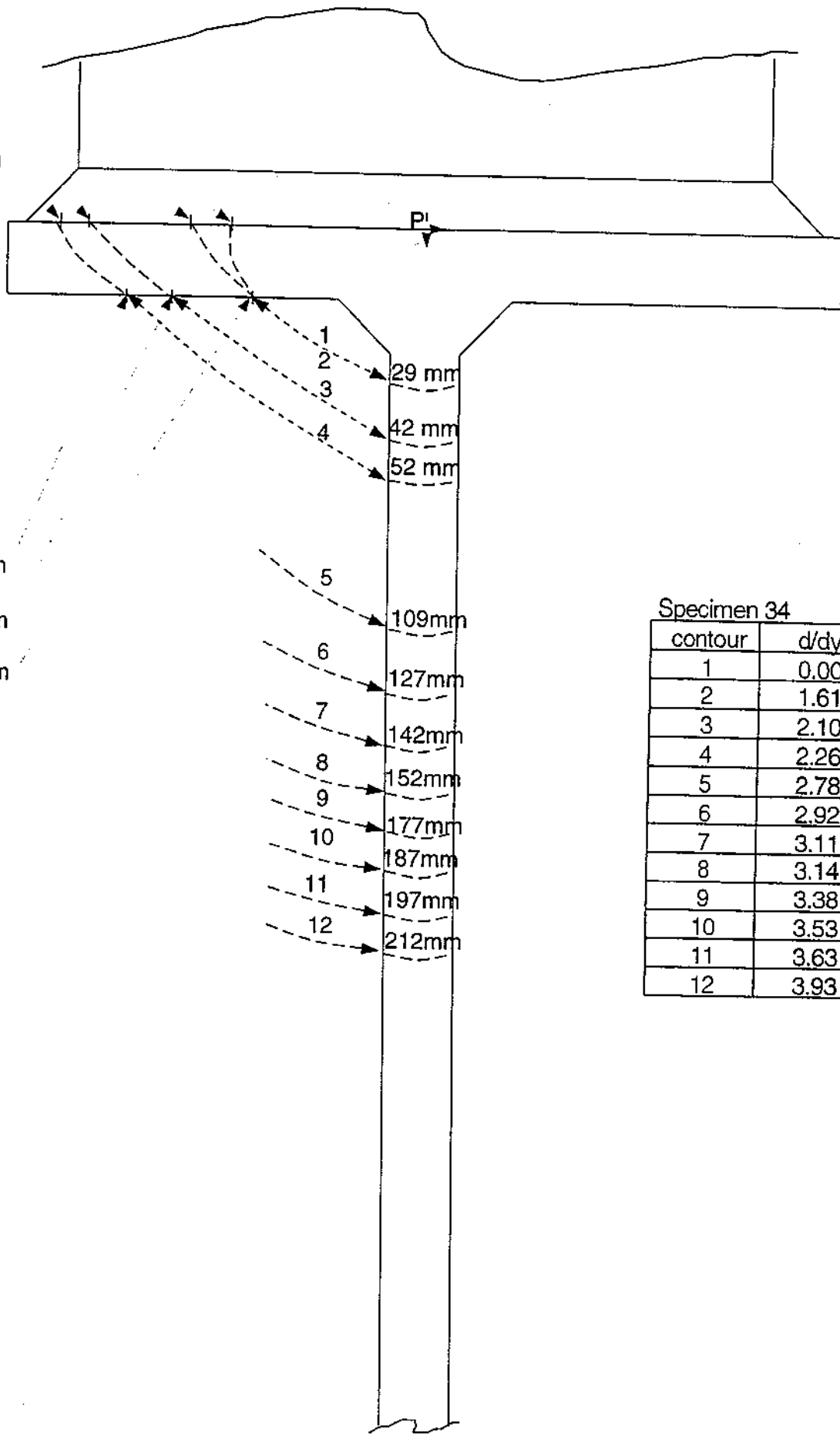


distances are measured from point P



distances are measured from point P

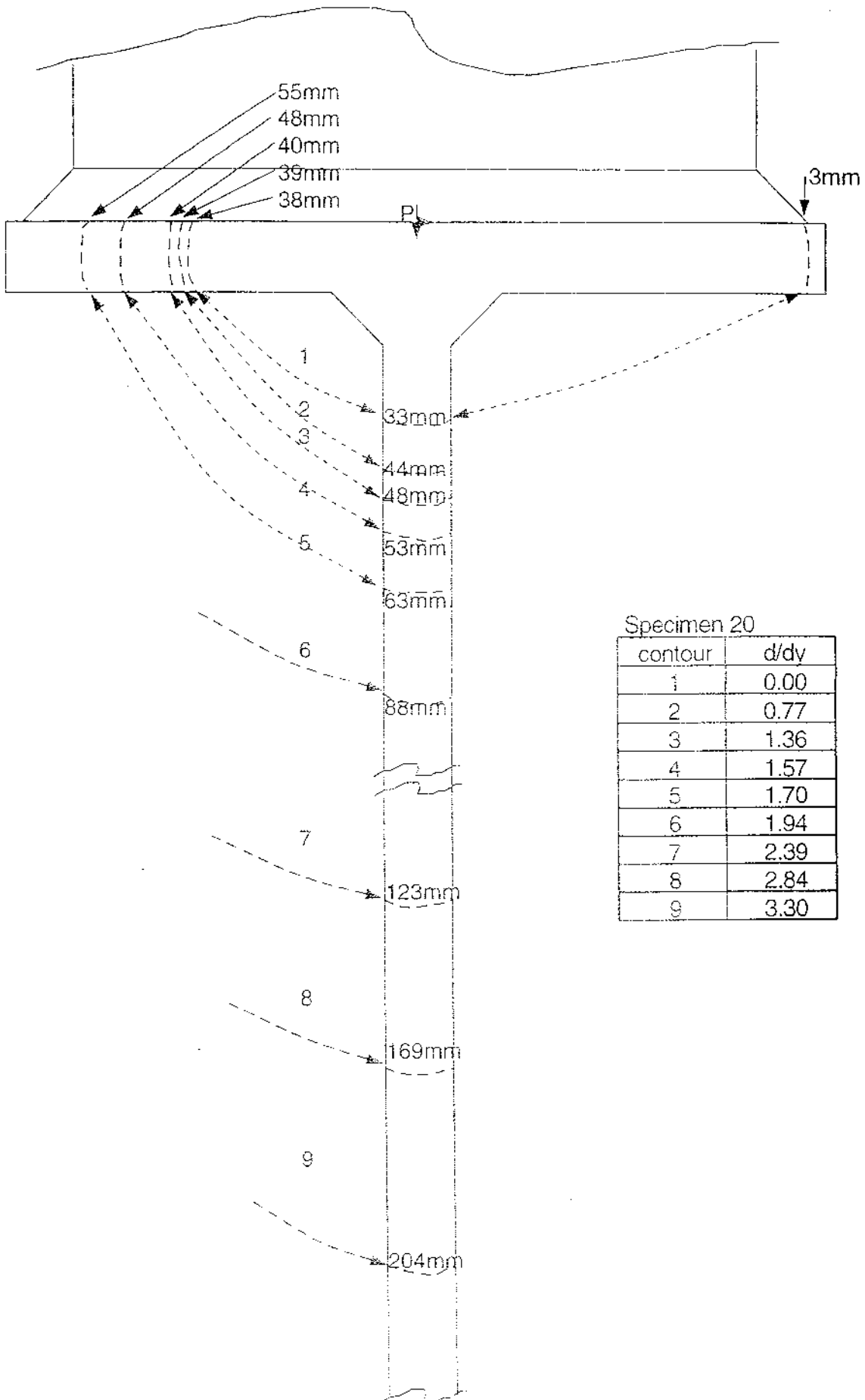
24 mm
27 mm
59 mm
64 mm



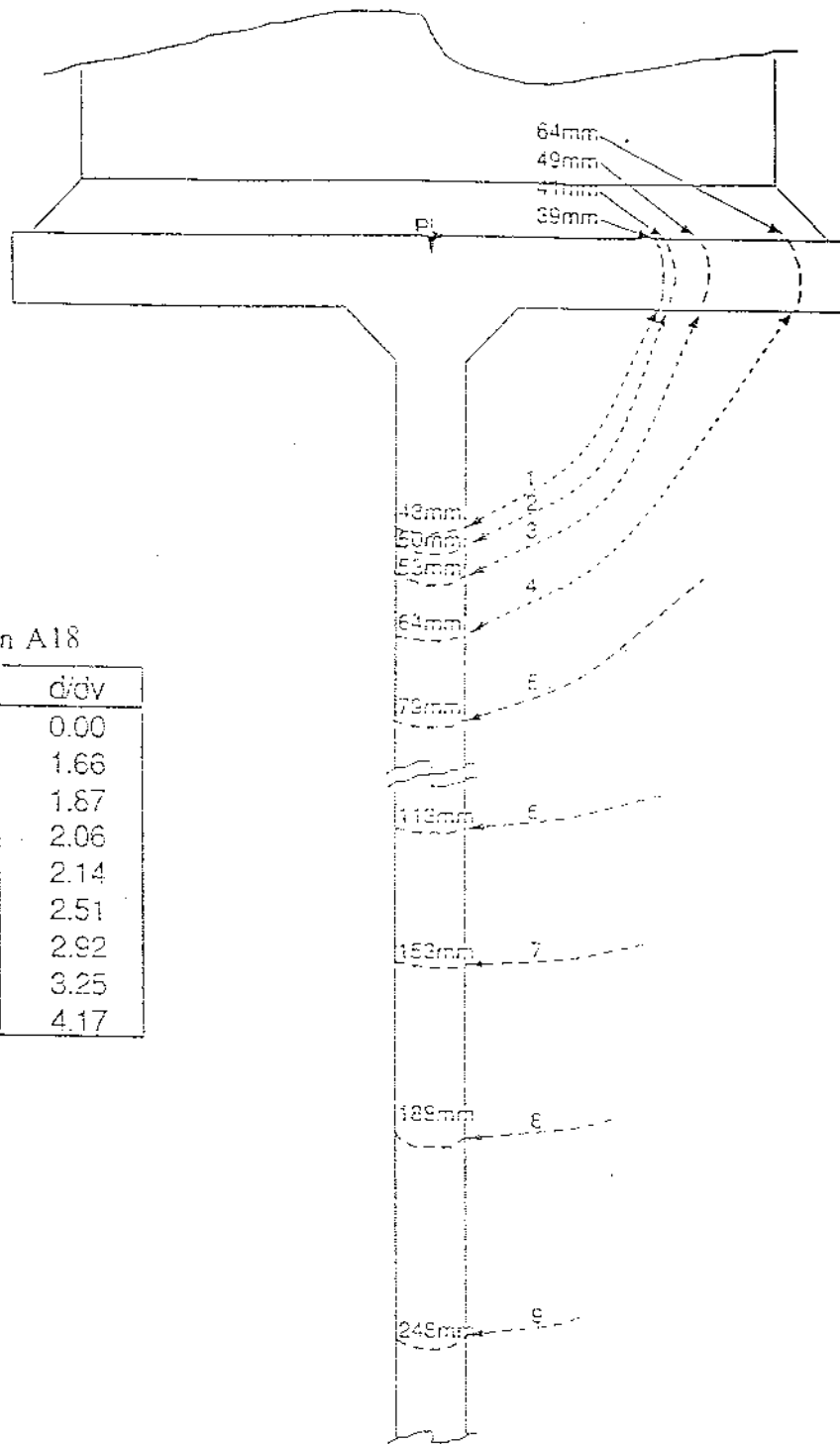
Specimen 34

contour	d/dy
1	0.00
2	1.61
3	2.10
4	2.26
5	2.78
6	2.92
7	3.11
8	3.14
9	3.38
10	3.53
11	3.63
12	3.93

distances are measured from point P

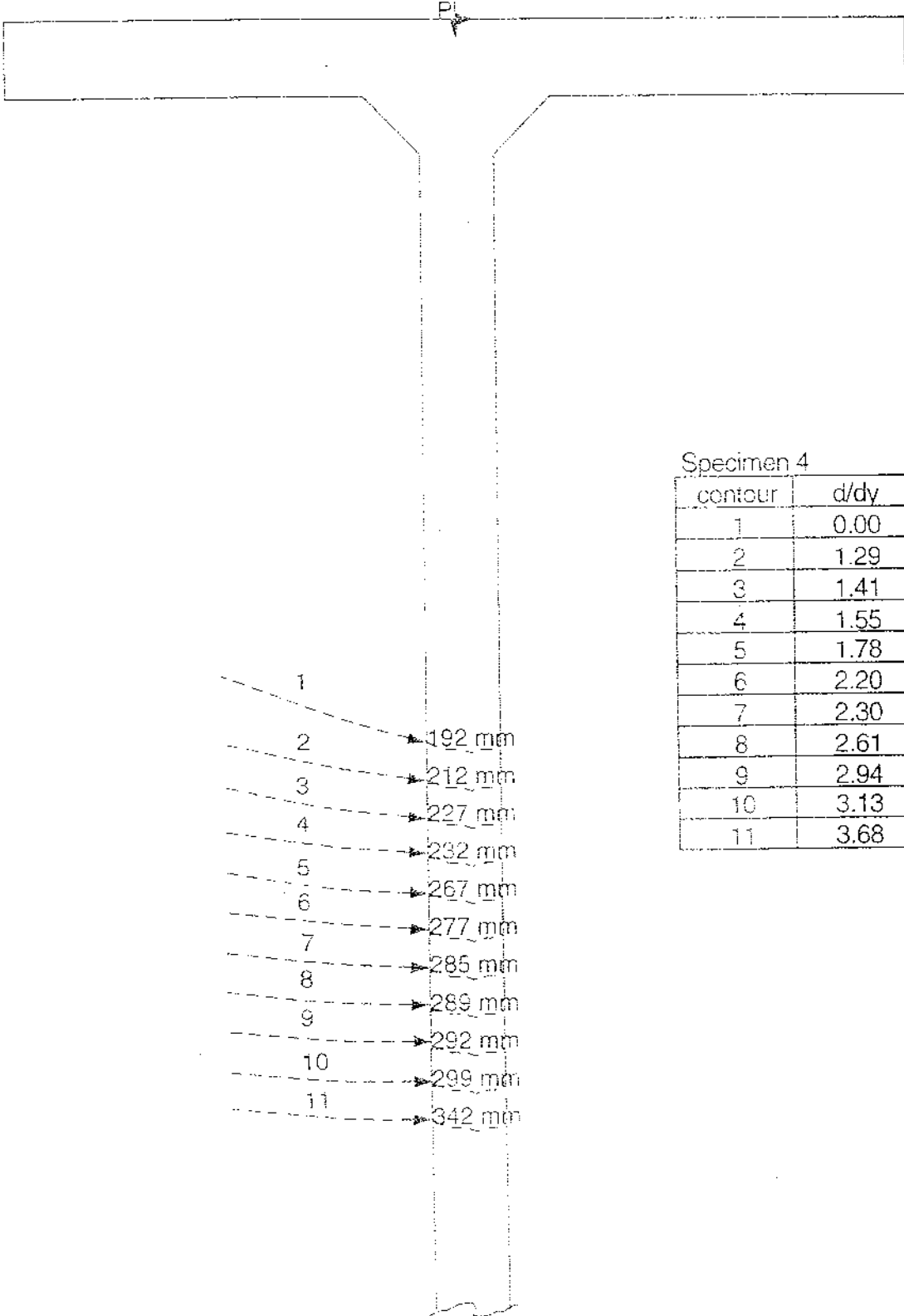


distances are measured from point P



specimen A18

CONTOUR	d'ov
1	0.00
2	1.66
3	1.87
4	2.06
5	2.14
6	2.51
7	2.92
8	3.25
9	4.17



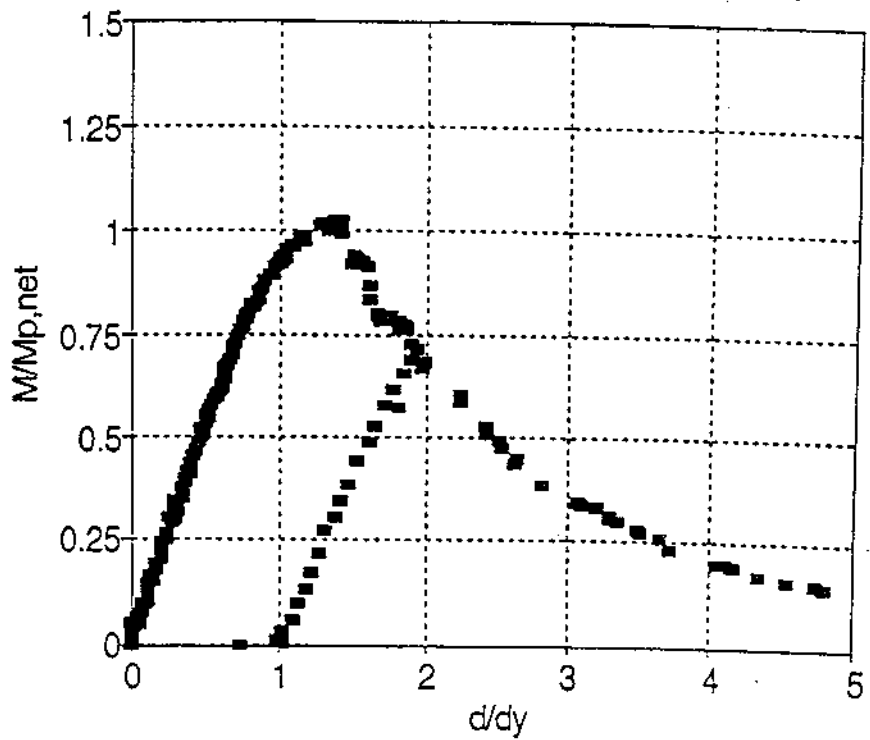
Specimen 4

contour	d/dy
1	0.00
2	1.29
3	1.41
4	1.55
5	1.78
6	2.20
7	2.30
8	2.61
9	2.94
10	3.13
11	3.68

distances are measured from point P

SPECIMEN 9

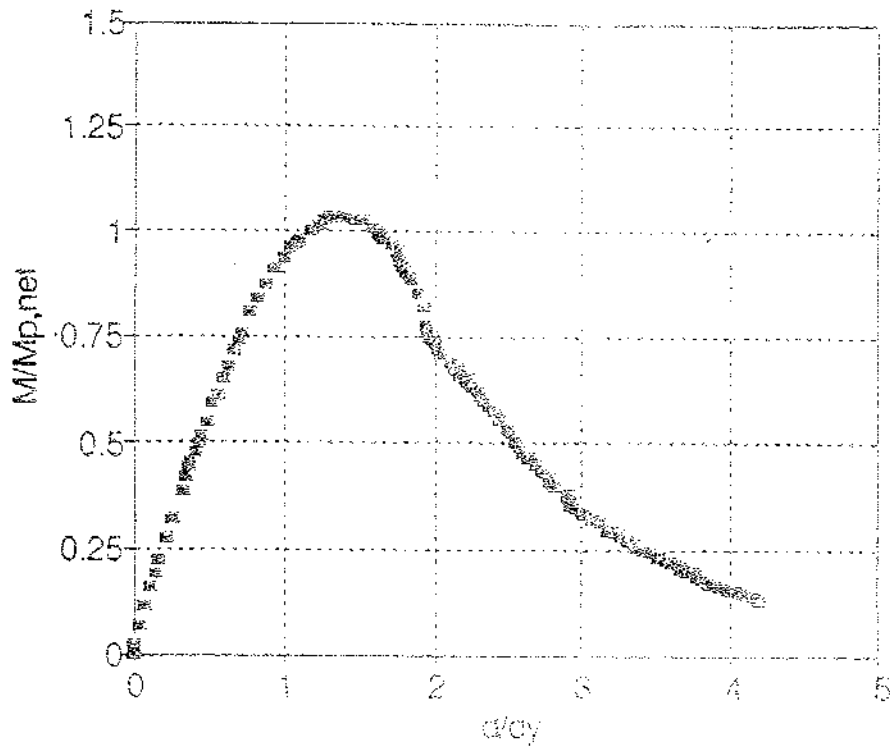
normalized load history



$M_y = 592 \text{ KN.m}$
 $d_y = 9.8 \text{ mm}$
 $M_{p.net} = 388$

SPECIMEN 48

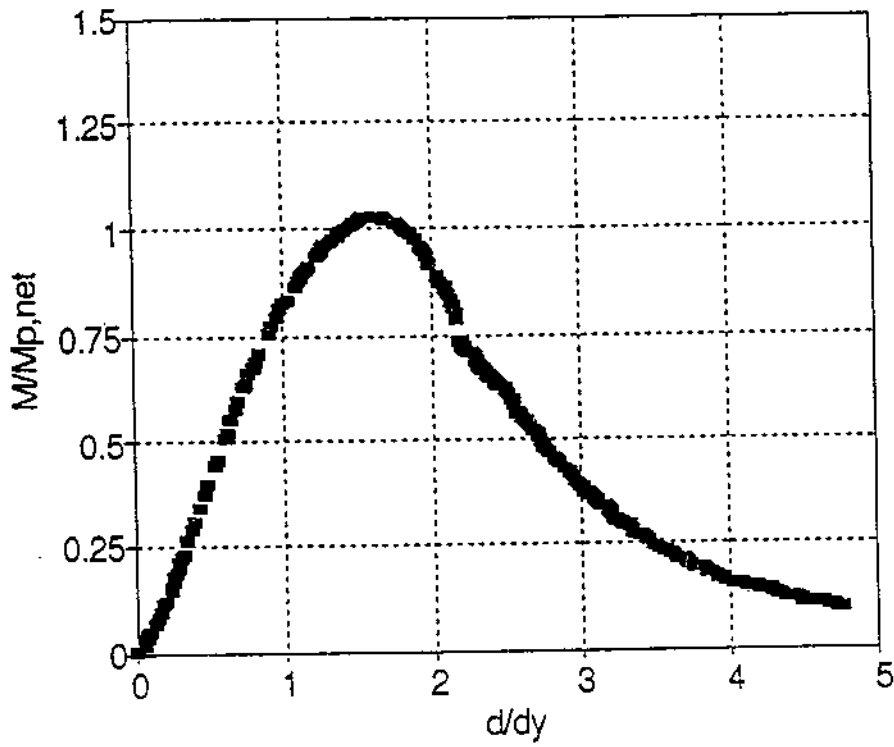
normalized load history



$I_y = 532 \text{ KN.m}$
 $d_y = 11.9 \text{ mm}$
 $M_{p,net} = 360$

SPECIMEN 39

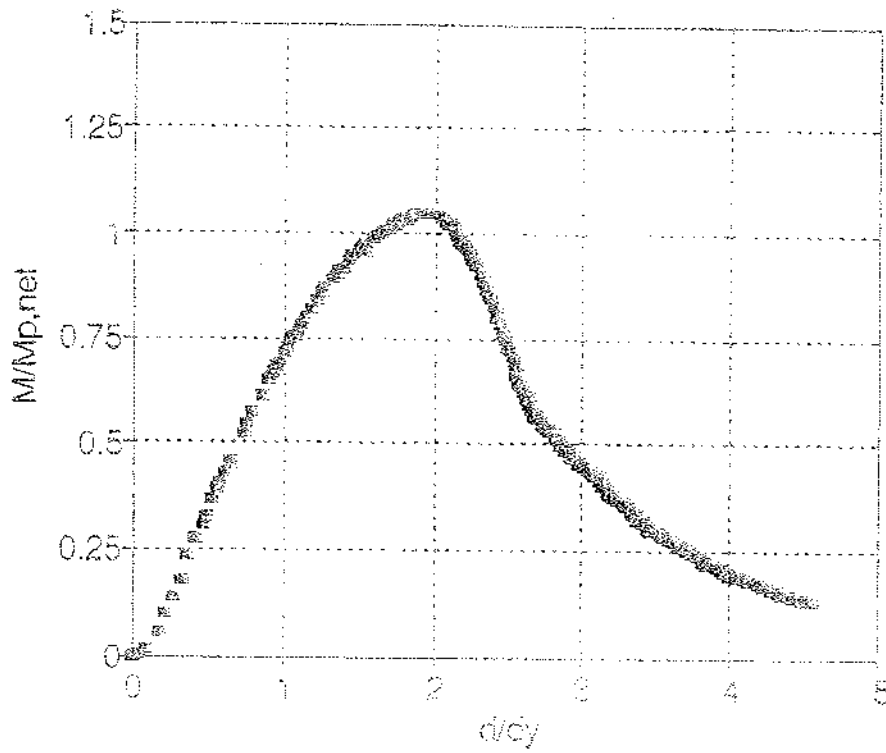
normalized load history



$M_y = 532 \text{ KN.m}$
 $d_y = 11.9 \text{ mm}$
 $M_{p,net} = 403$

SPECIMEN 34

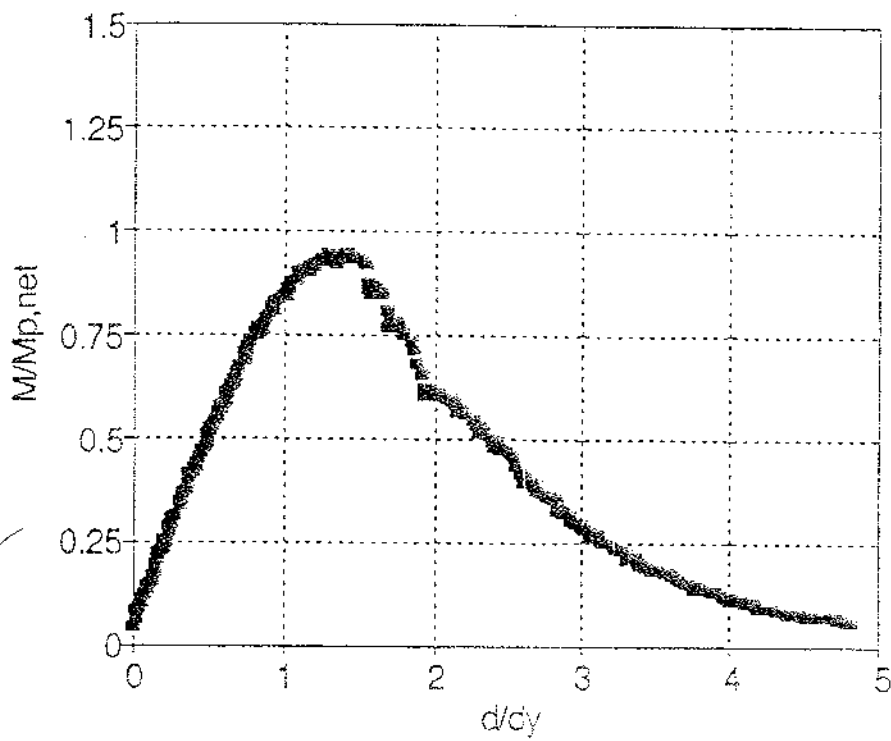
normalized load history



$M_y = 532 \text{ KN.m}$
 $d_y = 11.9 \text{ mm}$
 $M_{p,net} = 425$

SPECIMEN 20

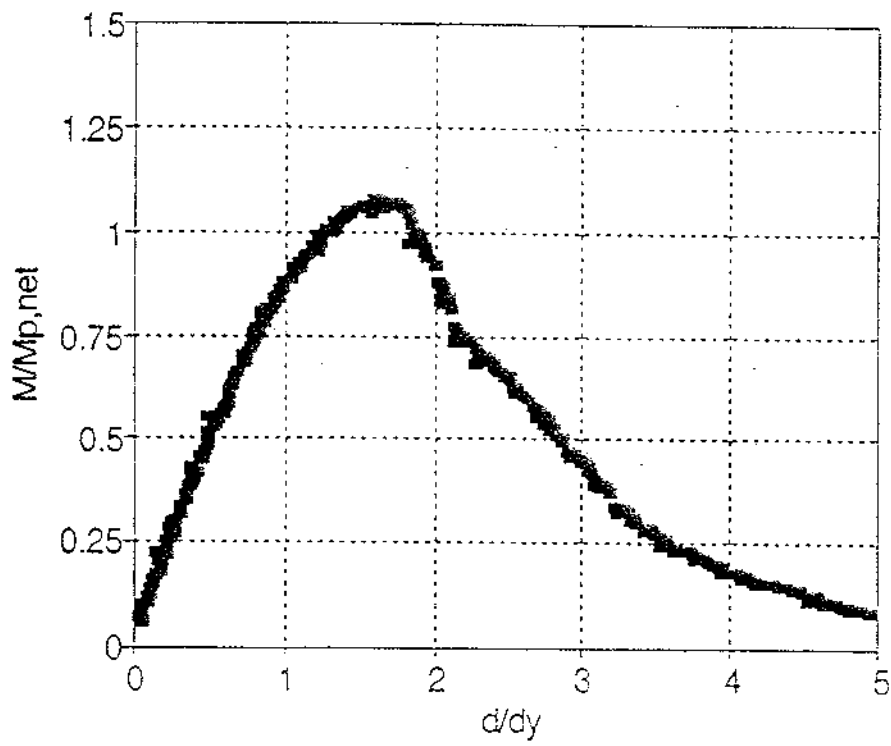
normalized load history



$M_y = 532 \text{ KN.m}$
 $d_y = 11.9 \text{ mm}$
 $M_{p,net} = 399$

SPECIMEN 18

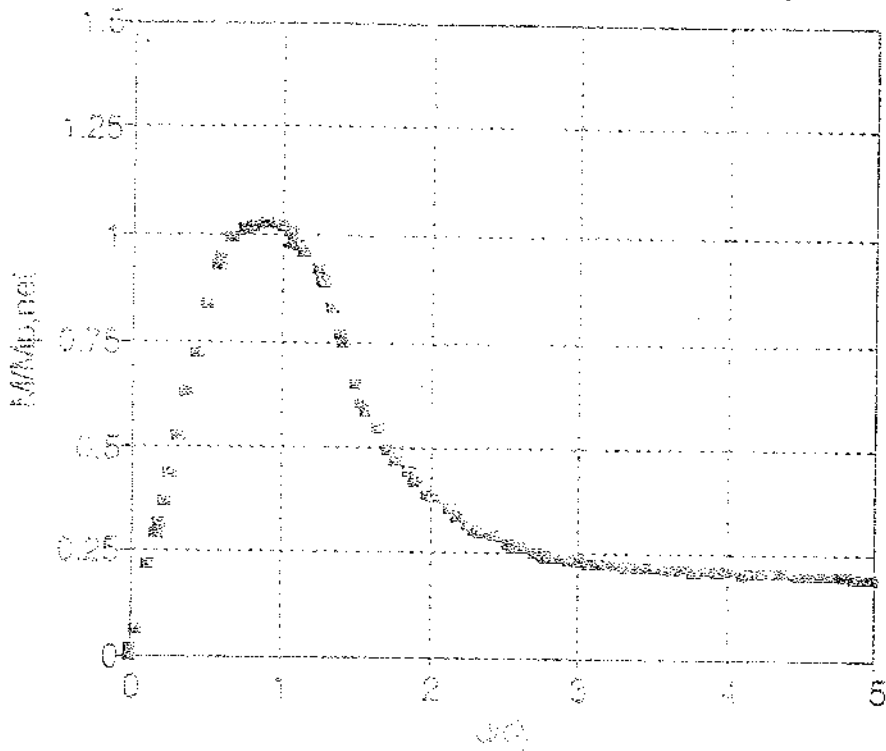
normalized load history



$M_y = 532 \text{ KN.m}$
 $d_y = 11.9 \text{ mm}$
 $M_{p,net} = 349$

SPECIMEN 4

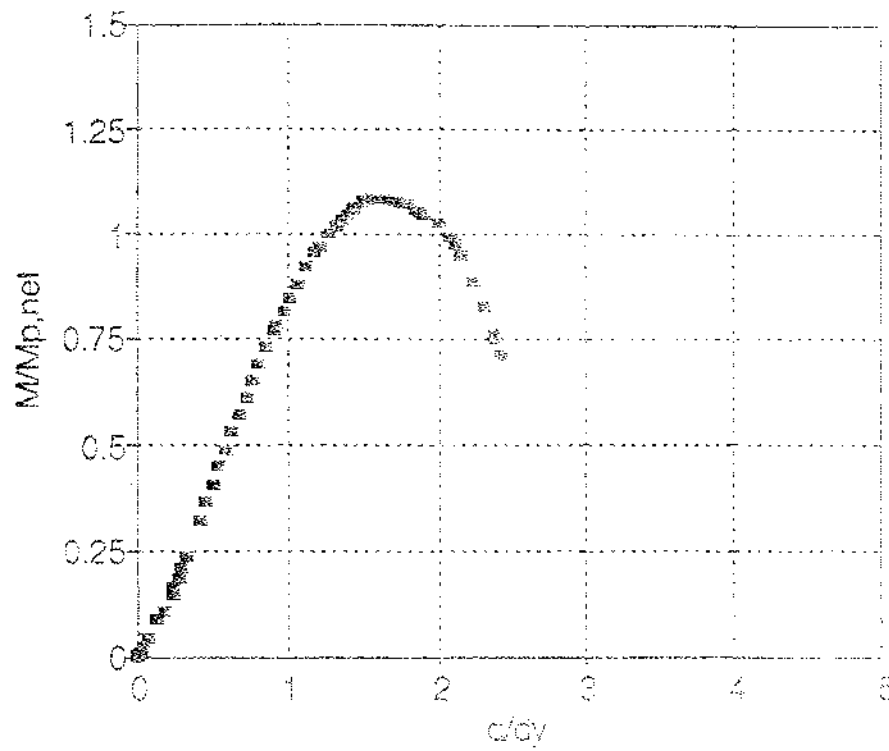
normalized load history



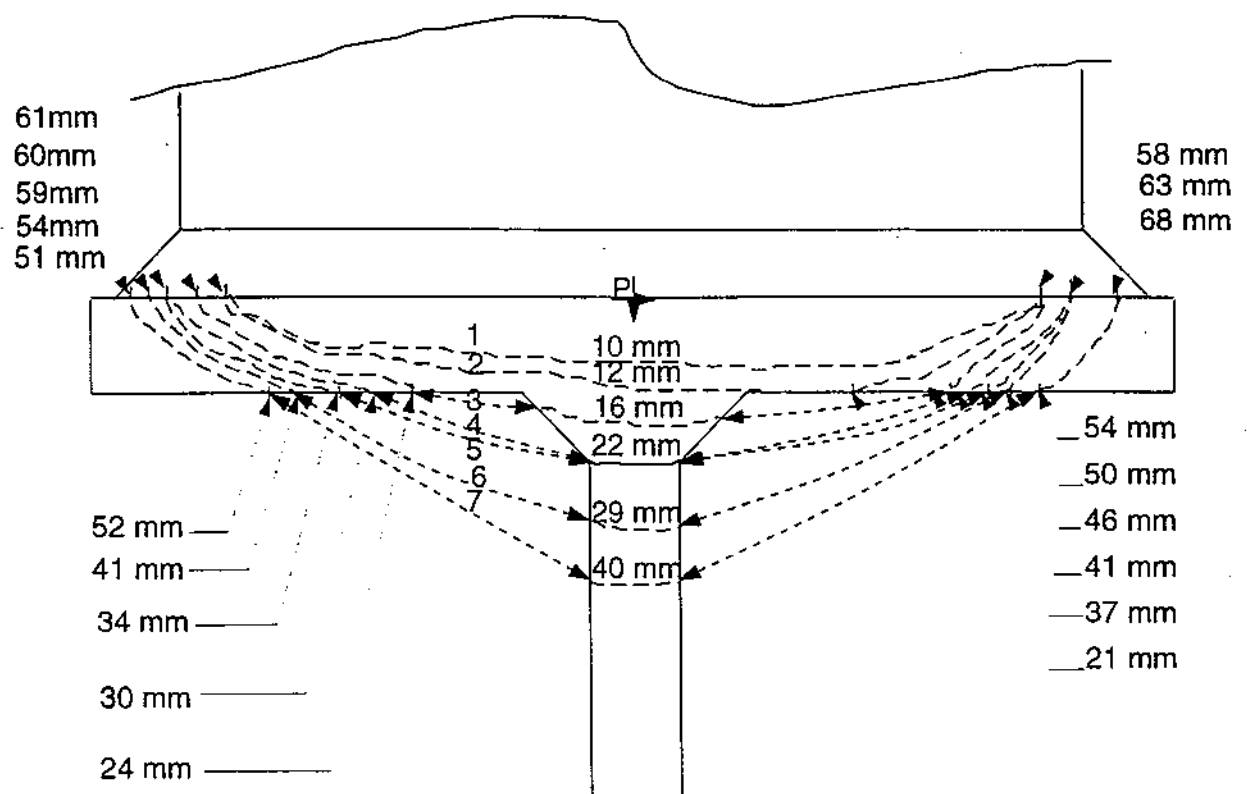
$M_y = 592 \text{ KN.m}$
 $d_y = 9.8 \text{ mm}$
 $M_{p.net} = 114$

SPECIMEN 42

normalized load history



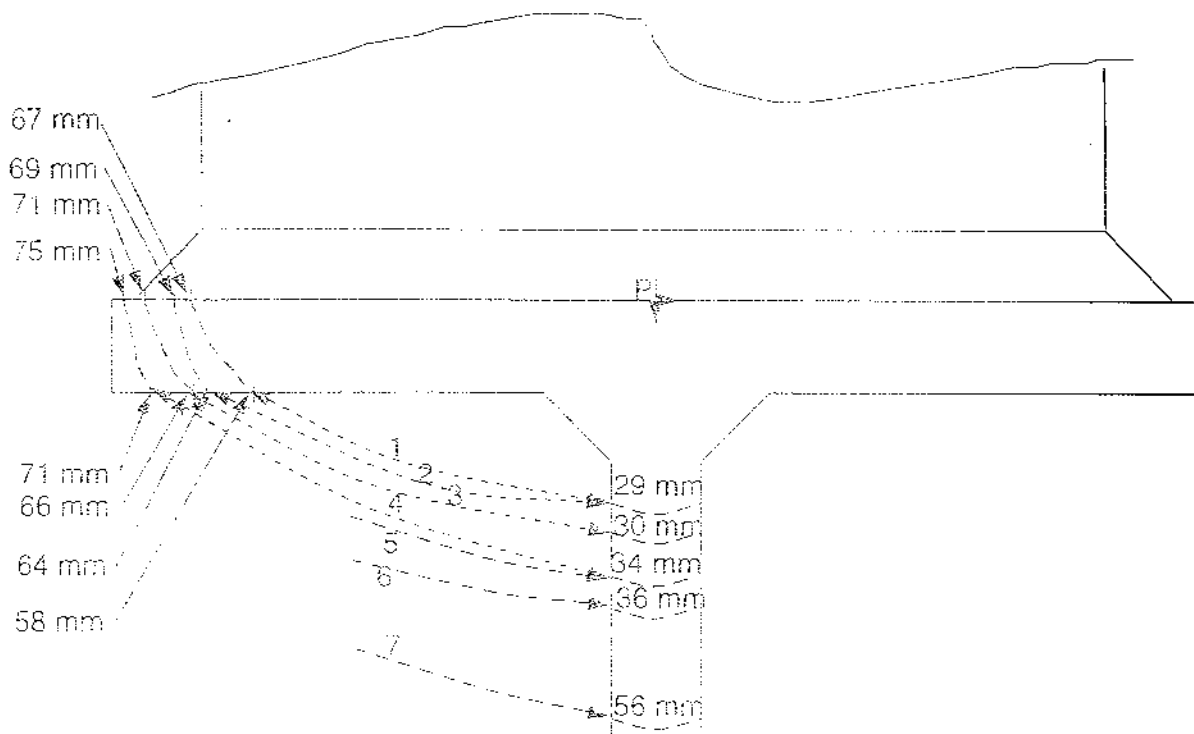
$M_y = 532 \text{ KN.m}$
 $d_y = 11.9 \text{ mm}$
 $M_{p,net} = 462$



Specimen 42

contour	d/dy
1	0.00
2	1.41
3	1.67
4	1.80
5	2.00
6	2.11
7	2.25

distances are measured from point P



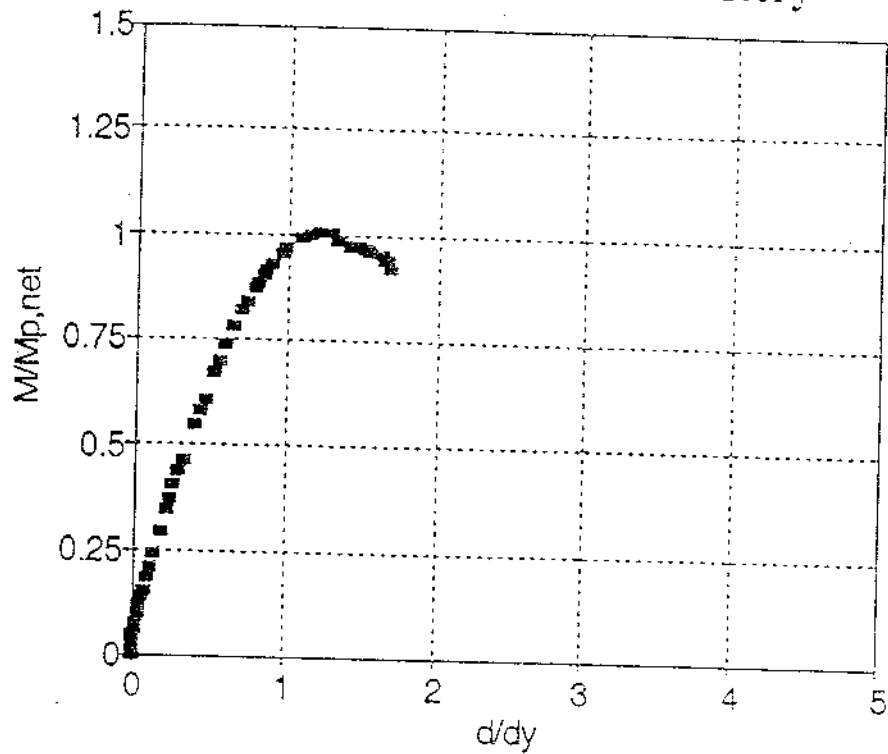
Specimen 33

contour	d/dy
1	0.00
2	0.81
3	0.96
4	1.09
5	1.33
6	1.47
7	1.70

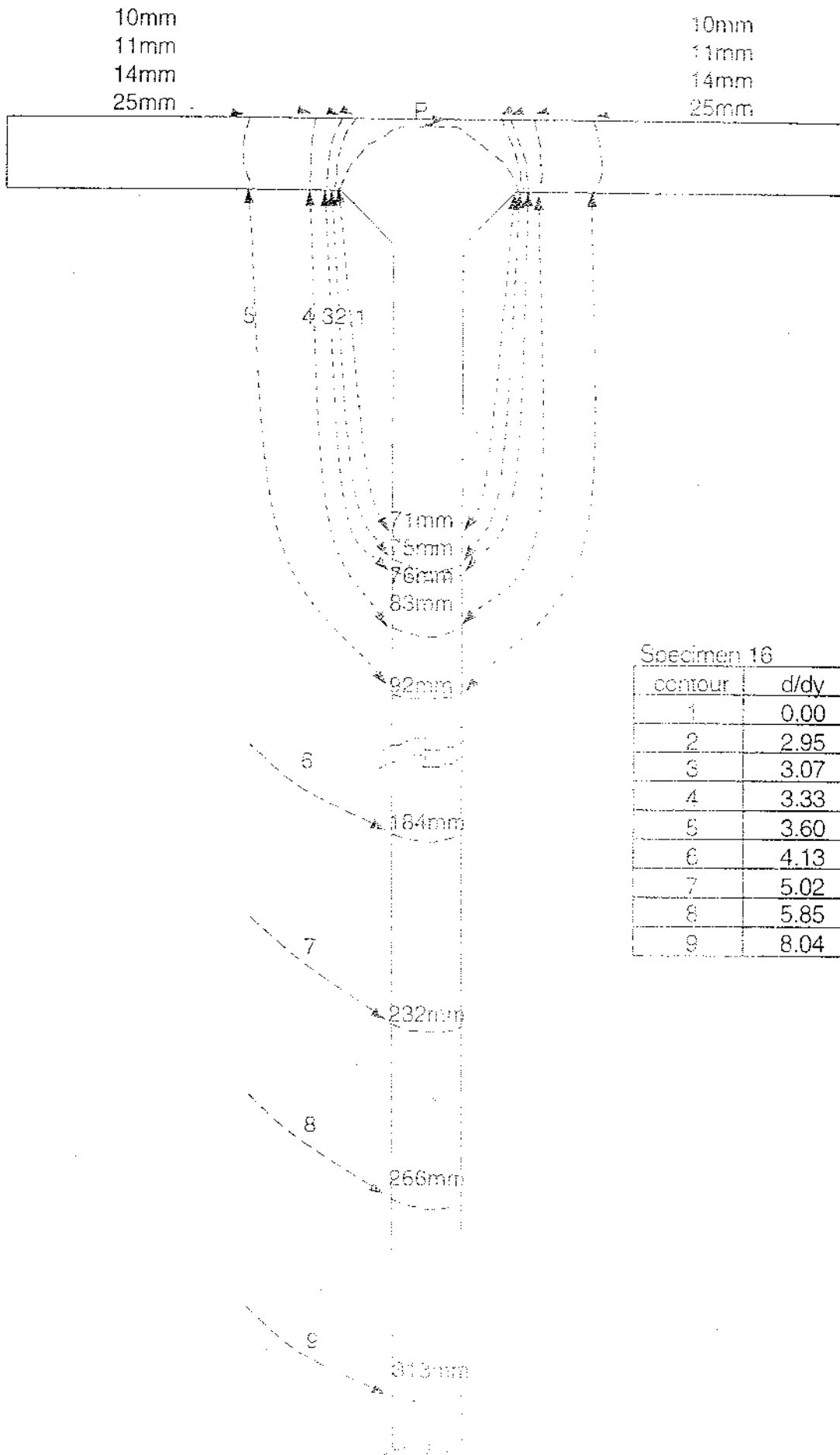
distances are measured from point P

SPECIMEN 33

normalized load history



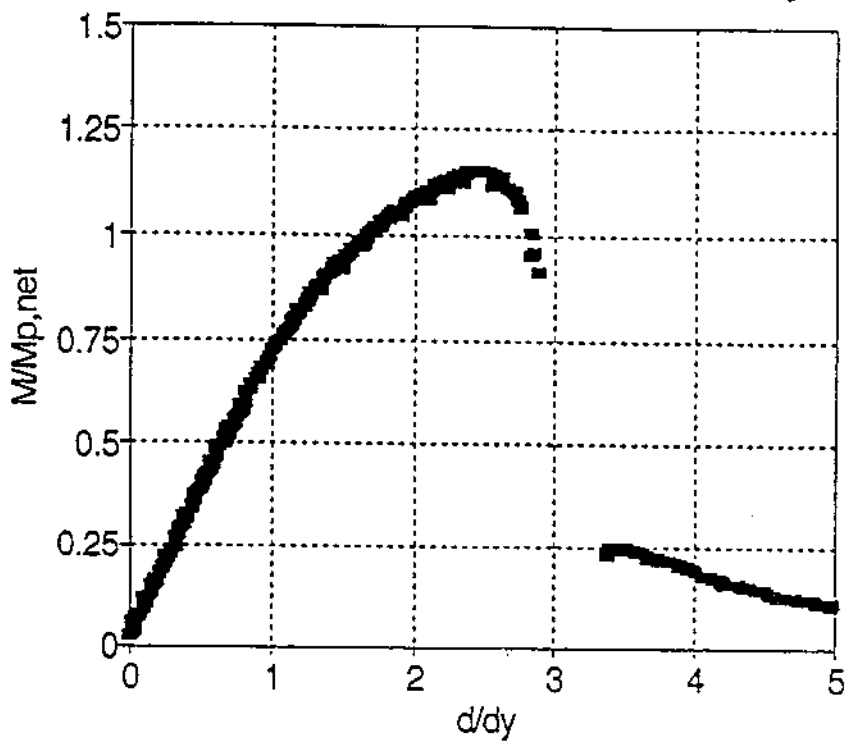
$M_y = 532 \text{ KN.m}$
 $d_y = 11.9 \text{ mm}$
 $M_{p,net} = 334$



distances are measured from point P

SPECIMEN 16

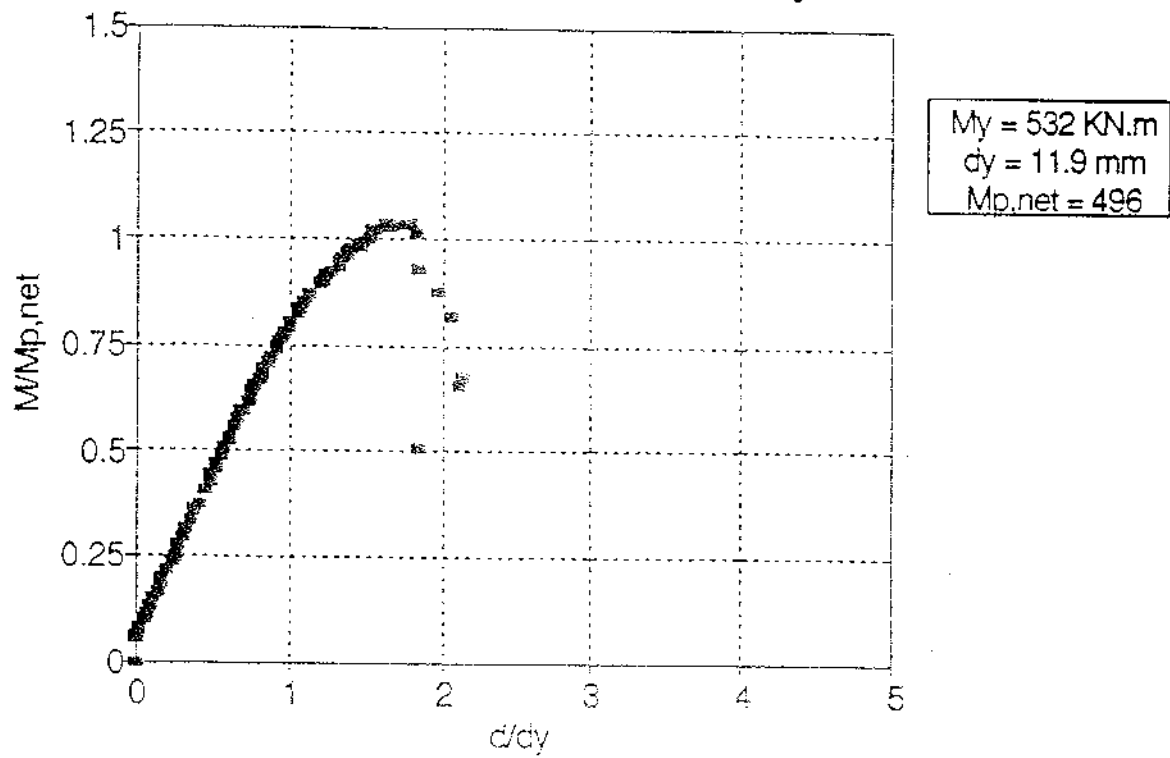
normalized load history



$M_y = 592 \text{ KN.m}$
 $d_y = 9.8 \text{ mm}$
 $M_{p,net} = 649$

SPECIMEN 1

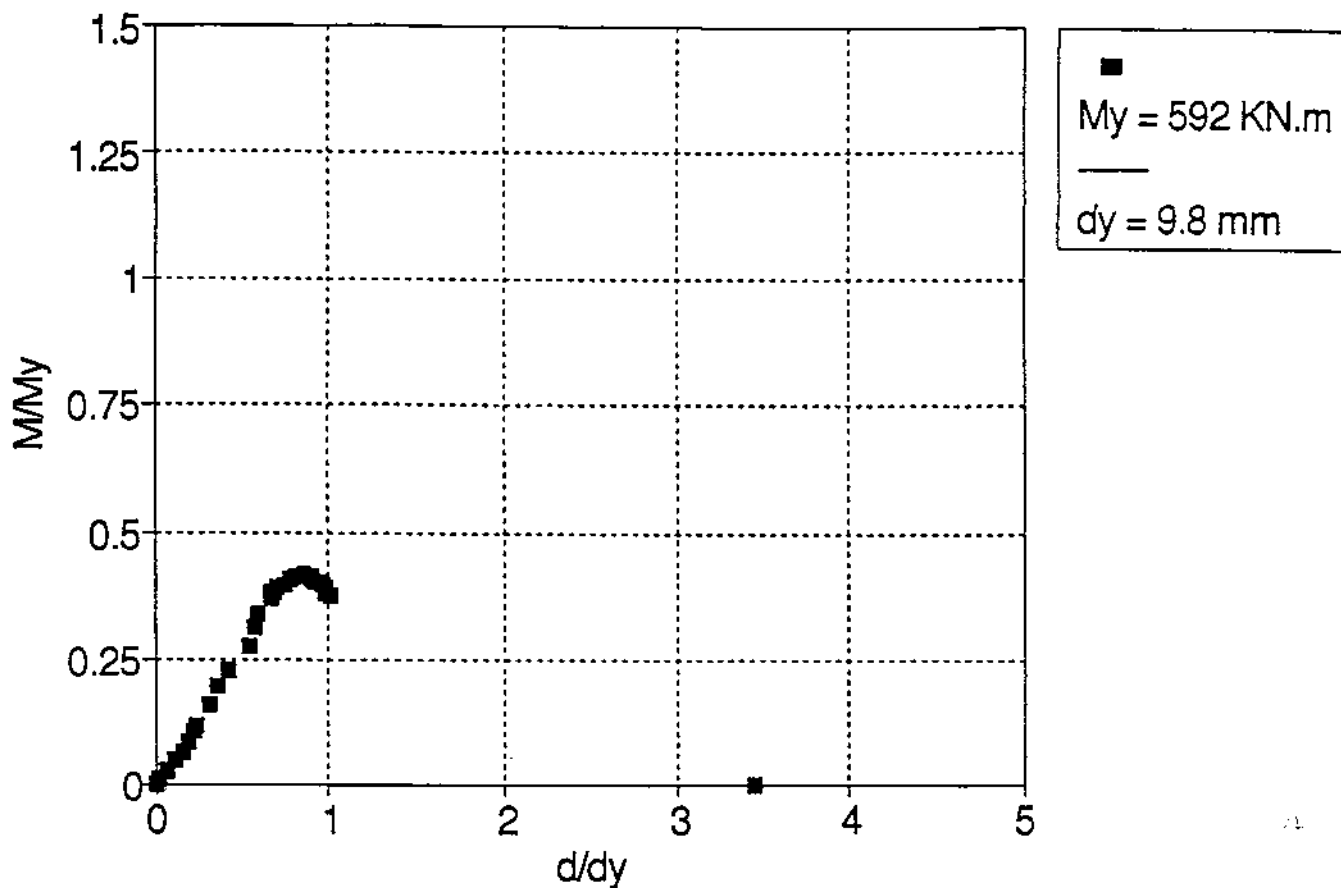
normalized load history



Note: Test was completed before significant crack extension. For this reason, a crack extension diagram is not available.

SPECIMEN 26

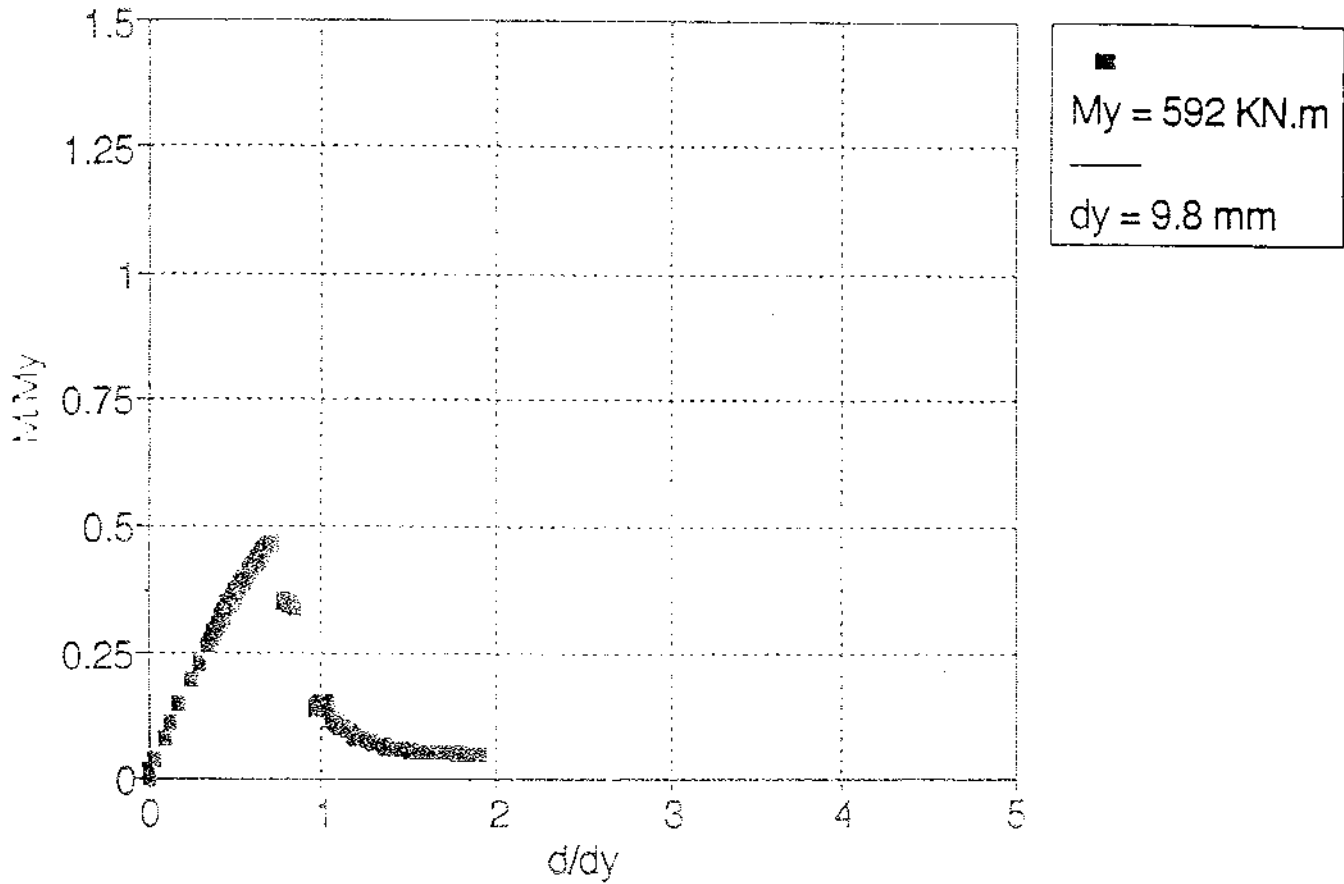
nondimensionalized load history



Note: Crack extension occurred under brittle conditions (fast fracture). For this reason, a crack extension diagram is not available.

SPECIMEN 27

nondimensionalized load history

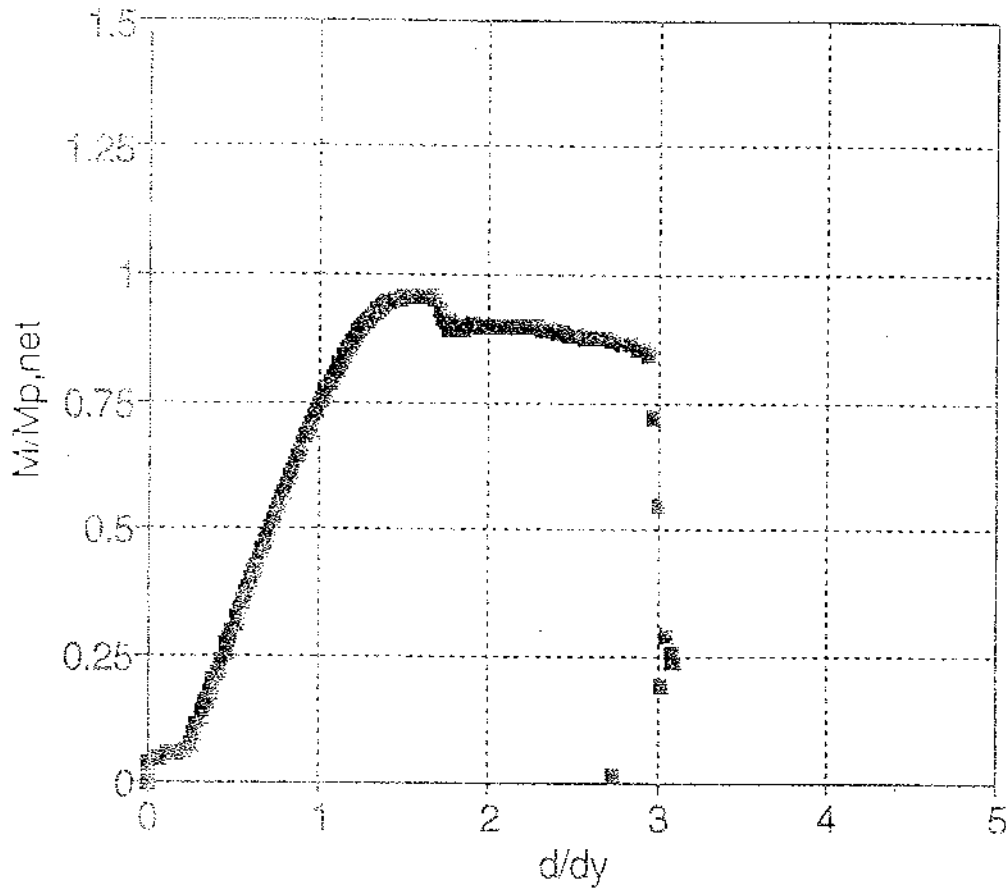


Note: Crack extension occurred under brittle conditions (unstable fracture). For this reason, a crack extension diagram is not available.

Appendix 3
Experimental Data from Box-Beam Experiments

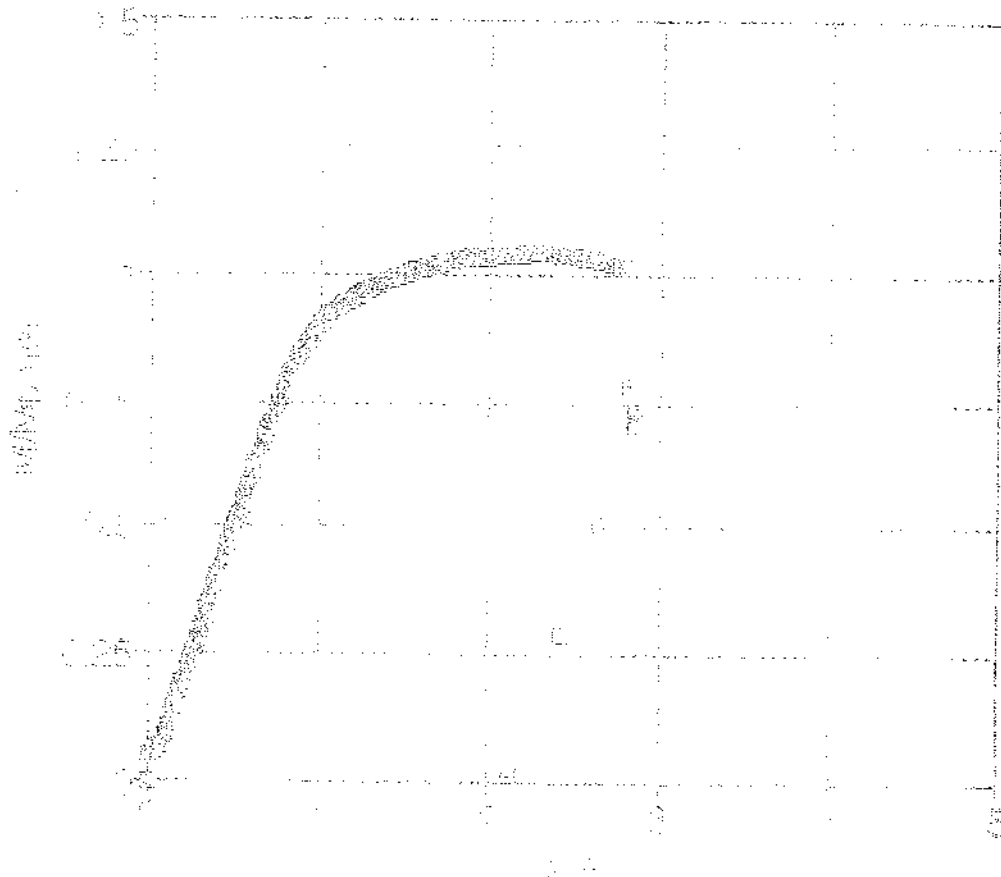
BOX 3

normalized load history



BOX 8

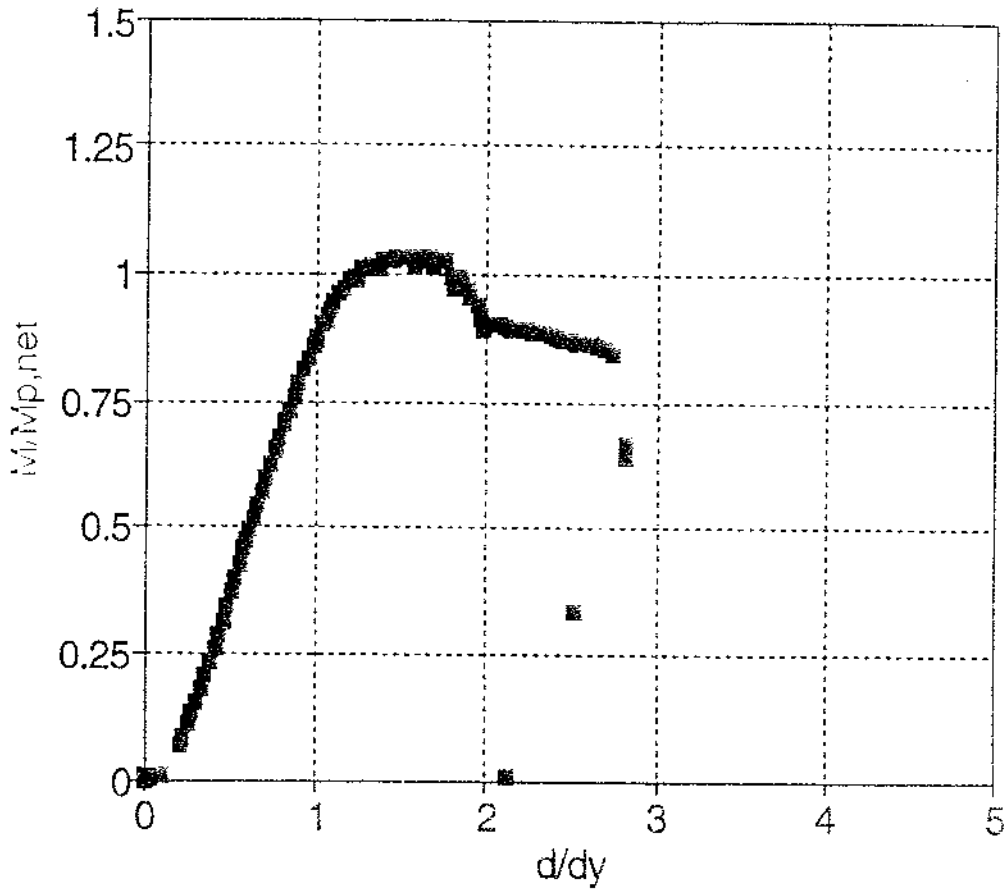
normalized load history



$M_{p,net} = 5928 \text{ KN.m}$
 $\delta_y = 38.3 \text{ mm}$

BOX 9

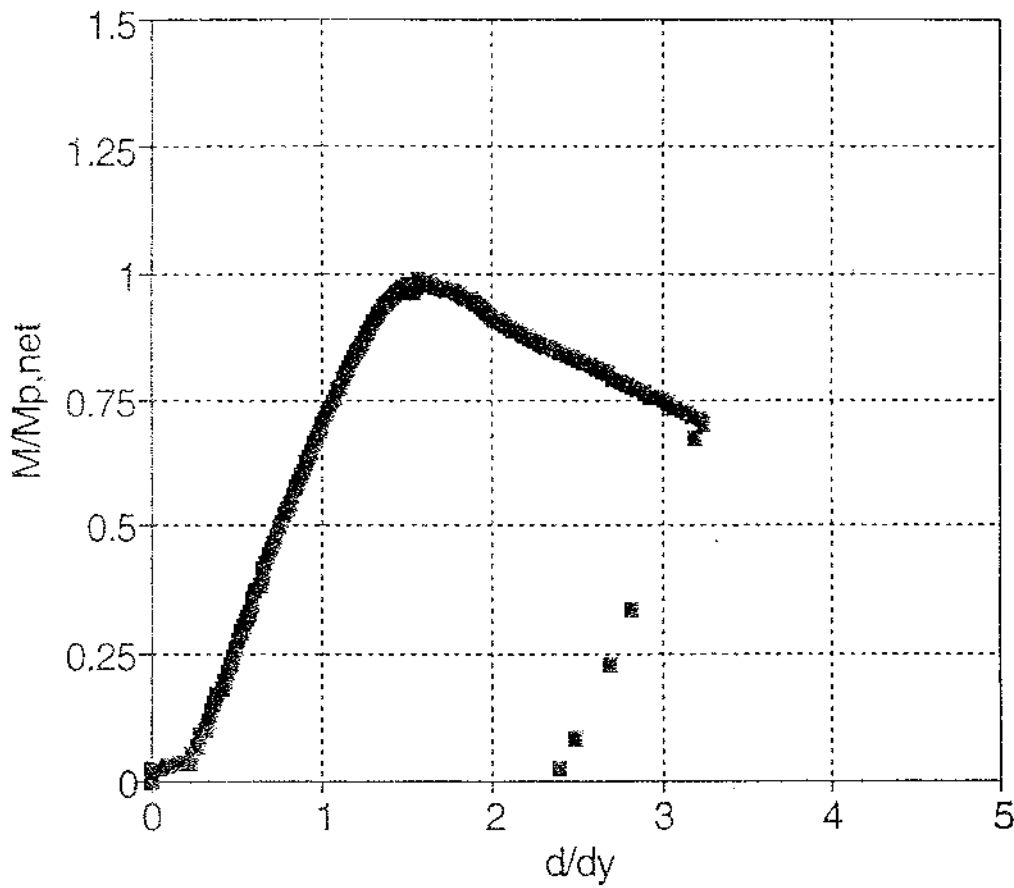
normalized load history



$M_{p,net} = 7177 \text{ KN.m}$
 $d_y = 38.3 \text{ mm}$

BOX 10

normalized load history



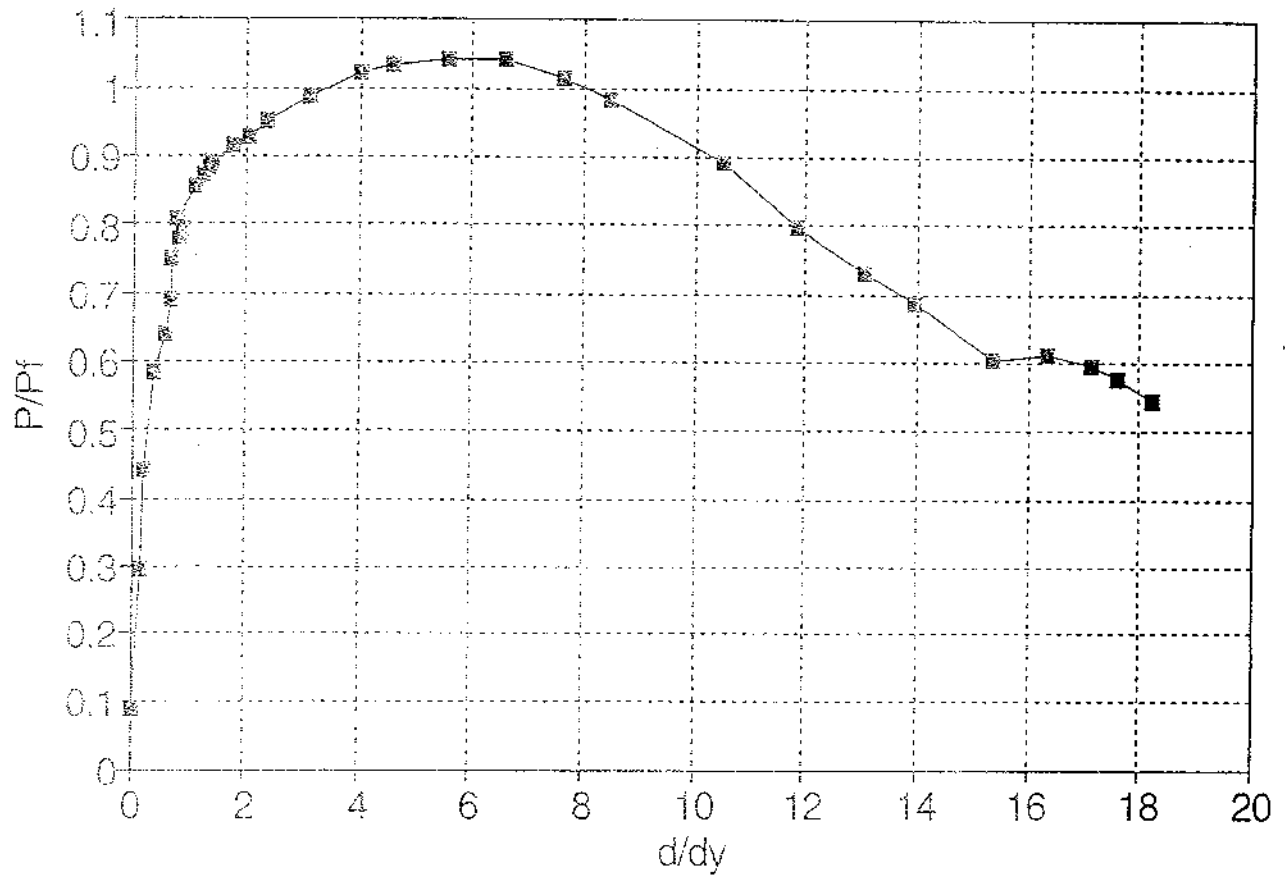
$M_{p,net} = 9608 \text{ KN.m}$

$d_y = 38.3 \text{ mm}$

Appendix 4
Experimental Data from Cope-Hole Experiments

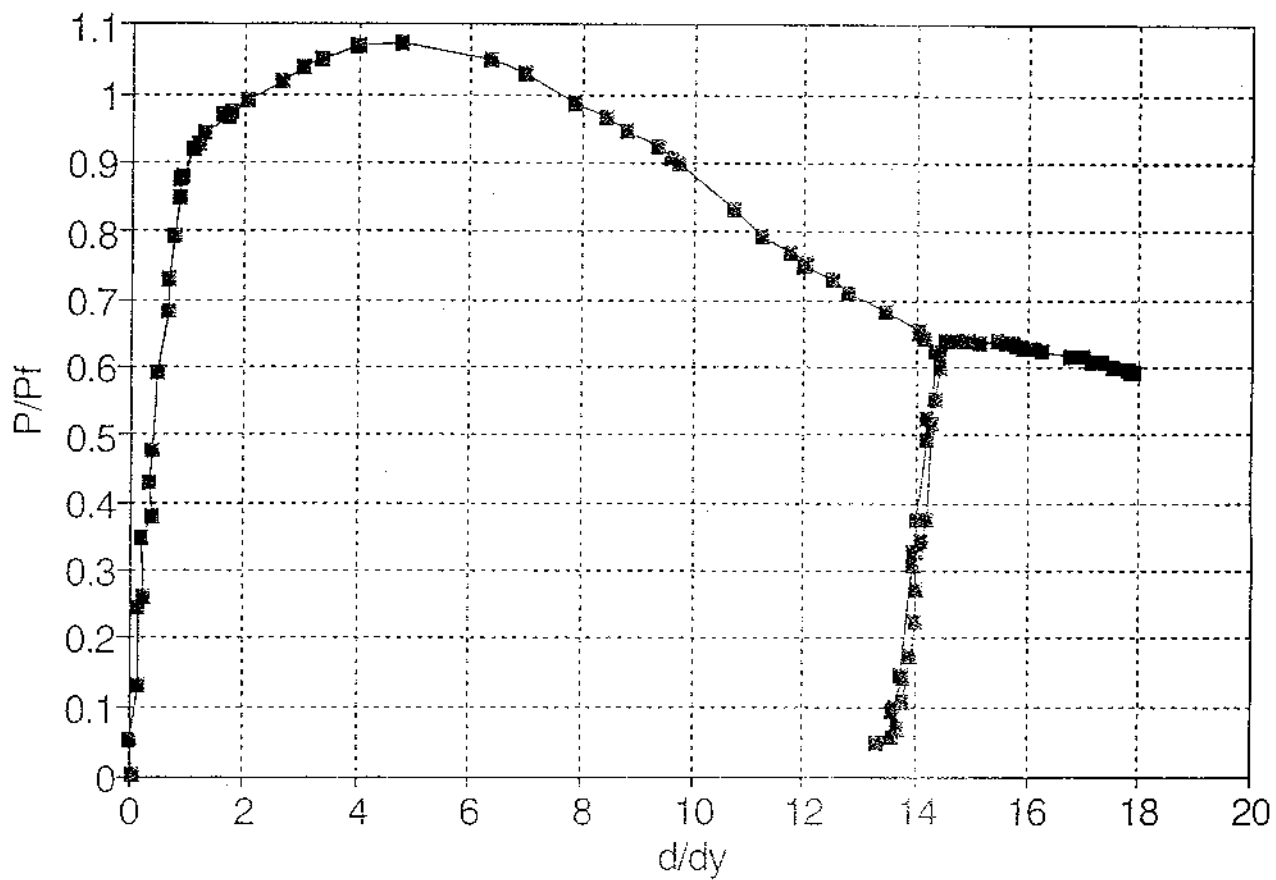
SPECIMEN EH-36 #3

normalized load-displacement curve



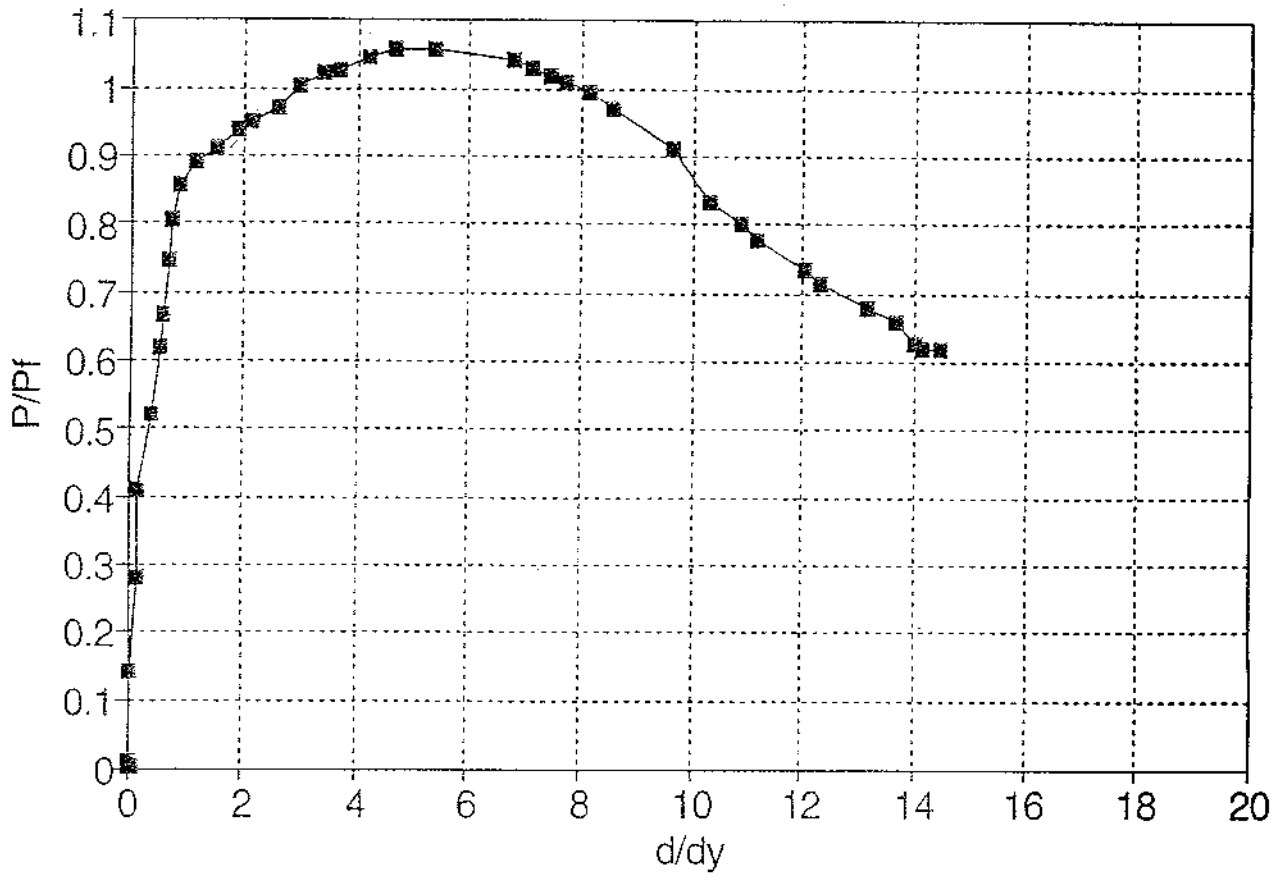
SPECIMEN EH-36 #4

normalized load-displacement curve



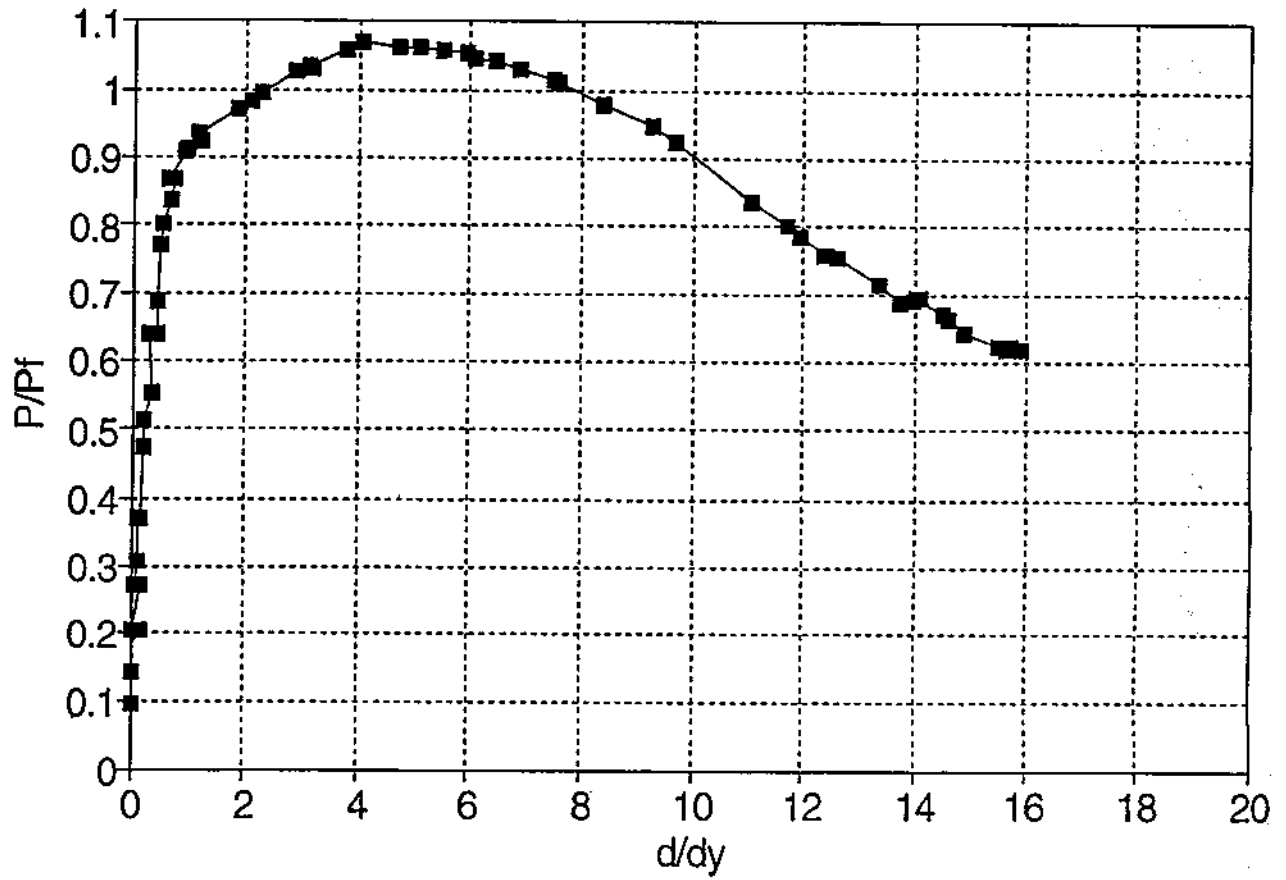
SPECIMEN EH-36 #5

normalized load-displacement curve



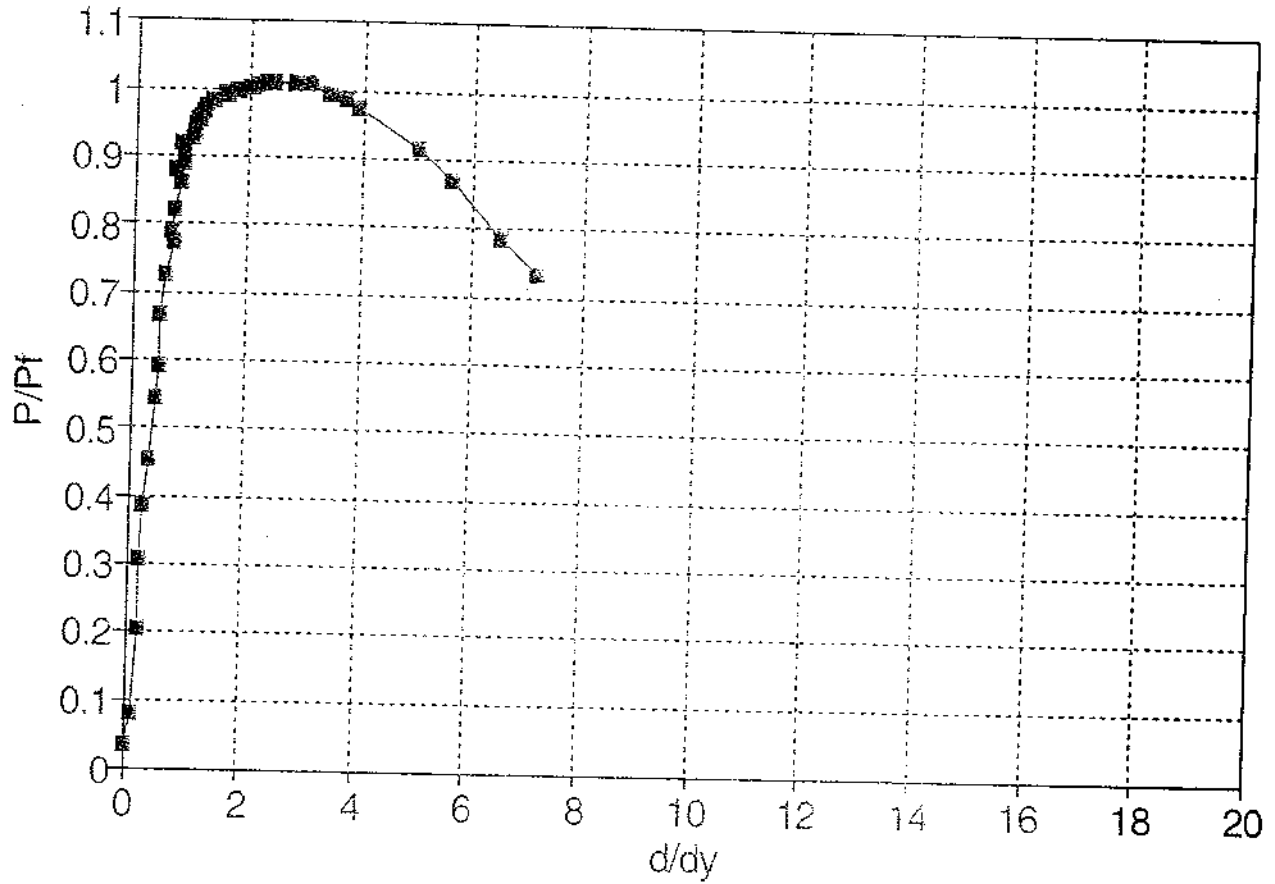
SPECIMEN EH-36 #6

normalized load-displacement curve



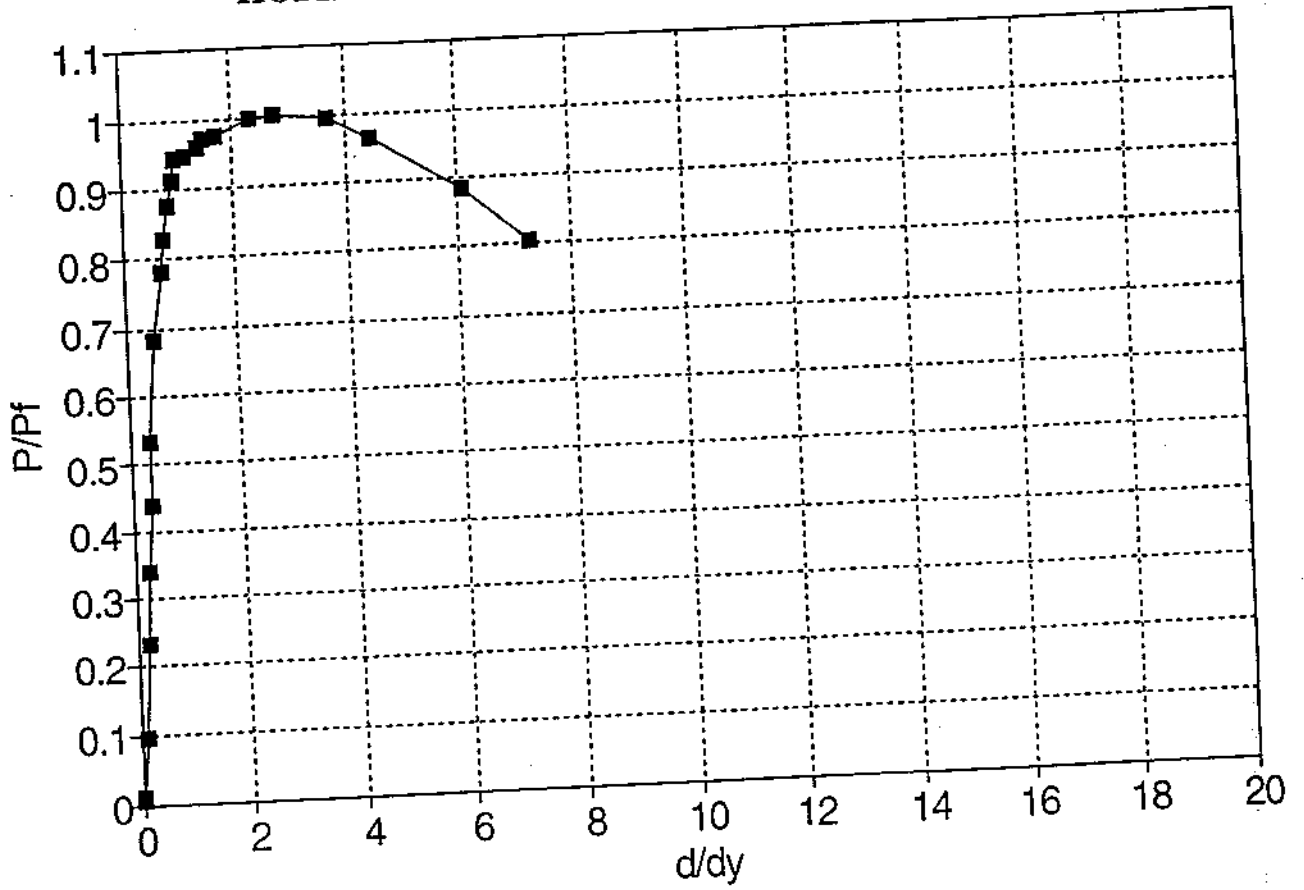
SPECIMEN HSLA-80 #3

normalized load-displacement curve



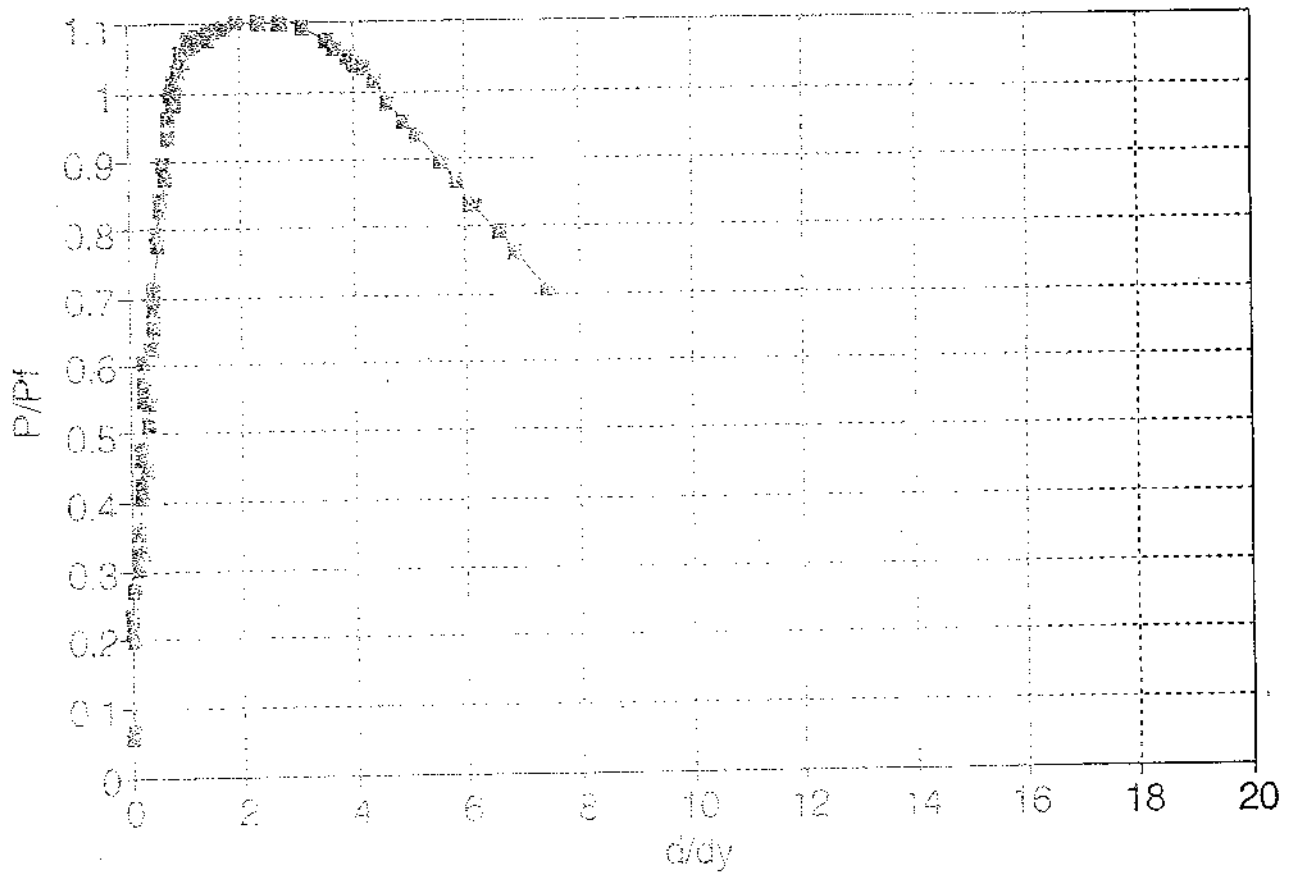
SPECIMEN HSLA-80 #4

normalized load-displacement curve



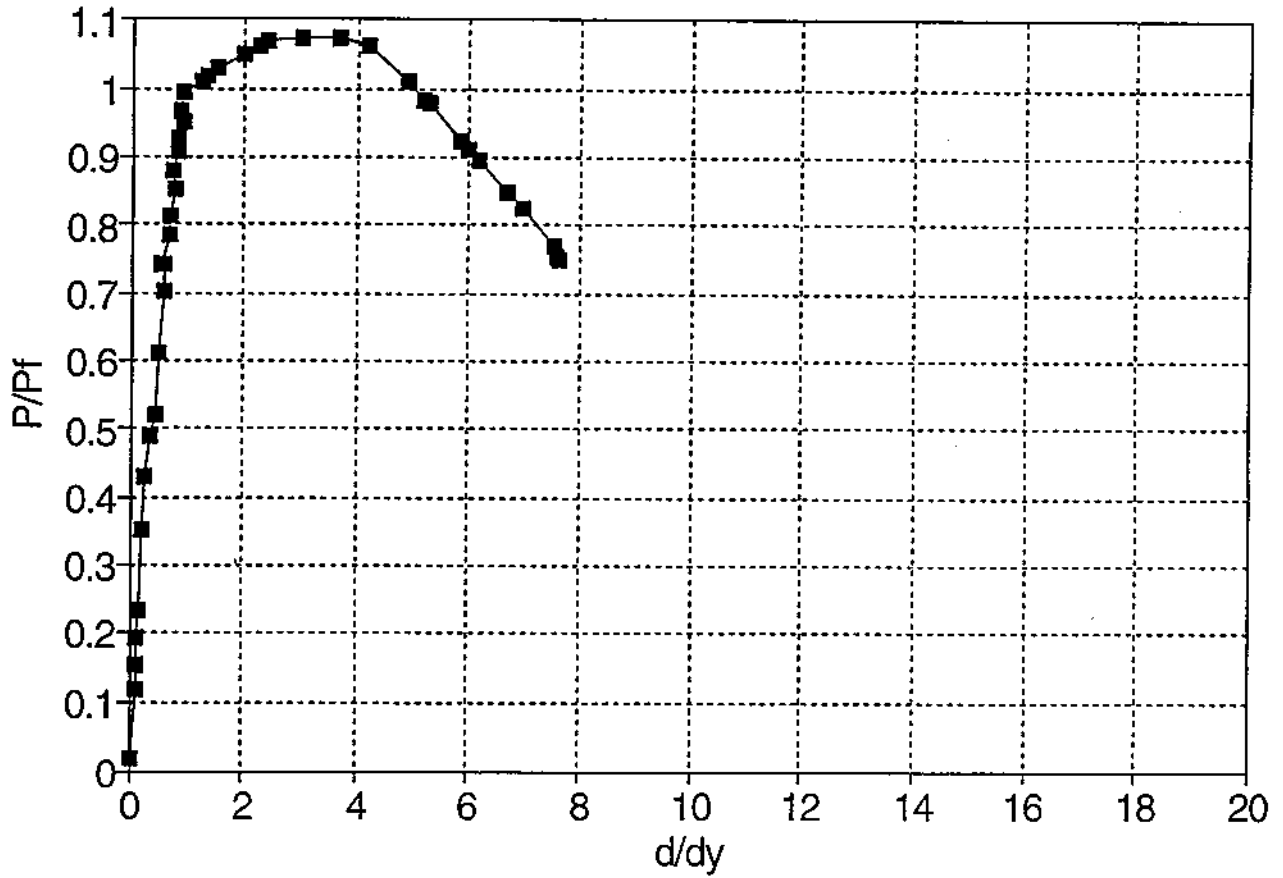
SPECIMEN HSLA-80 #5

normalized load-displacement curve



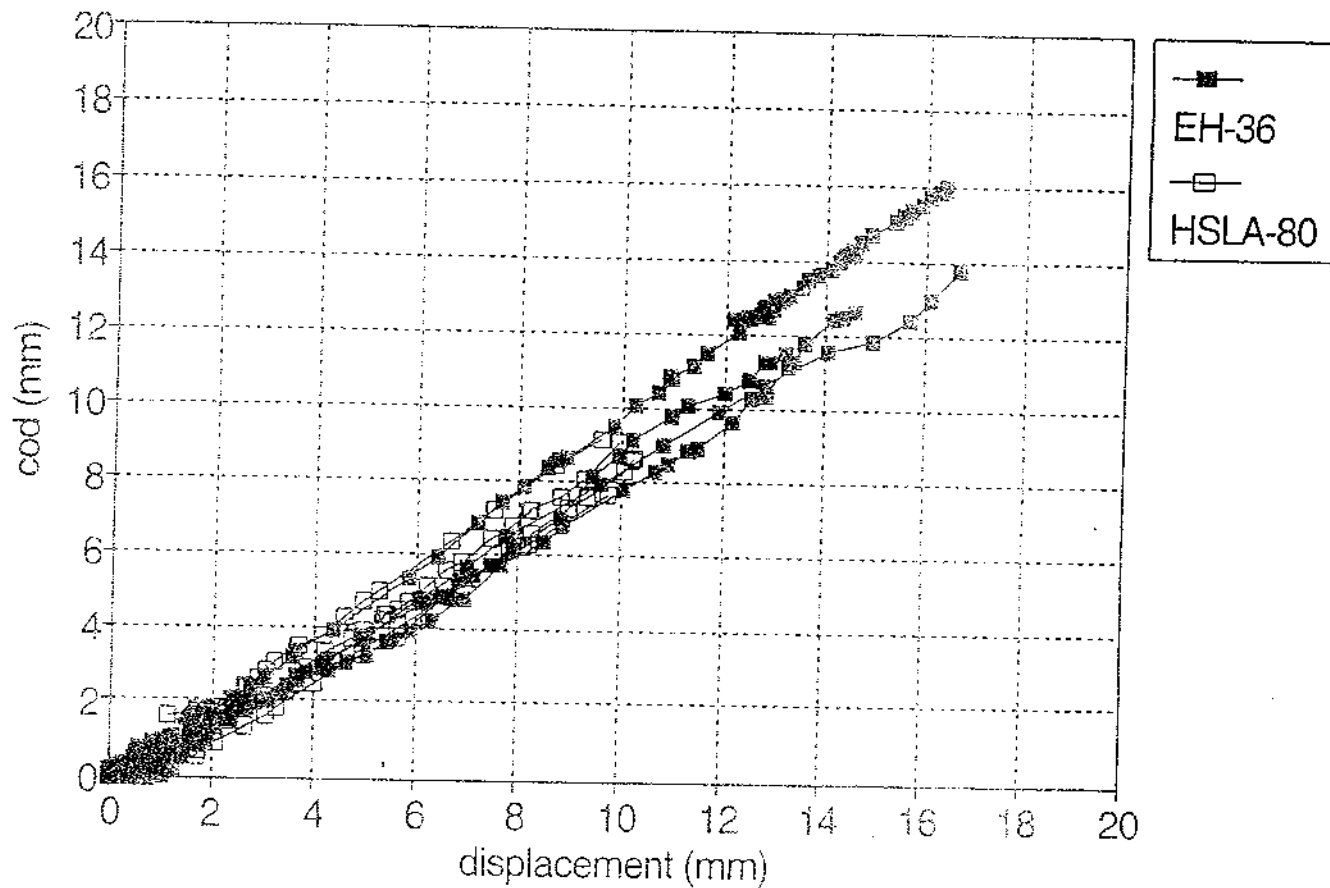
SPECIMEN HSLA-80 #6

normalized load-displacement curve



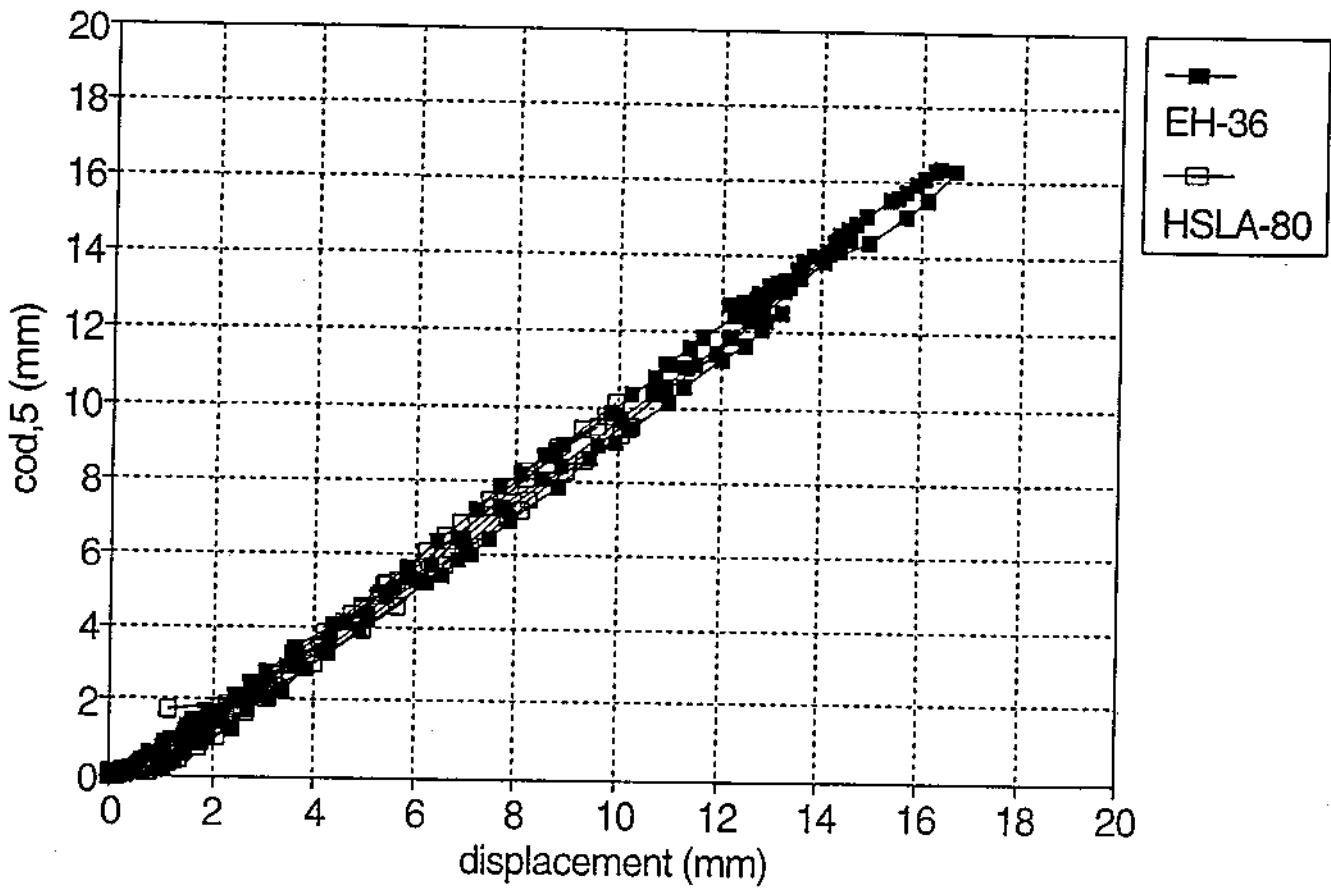
ALL COPE HOLE SPECIMENS

cod-displacement curves

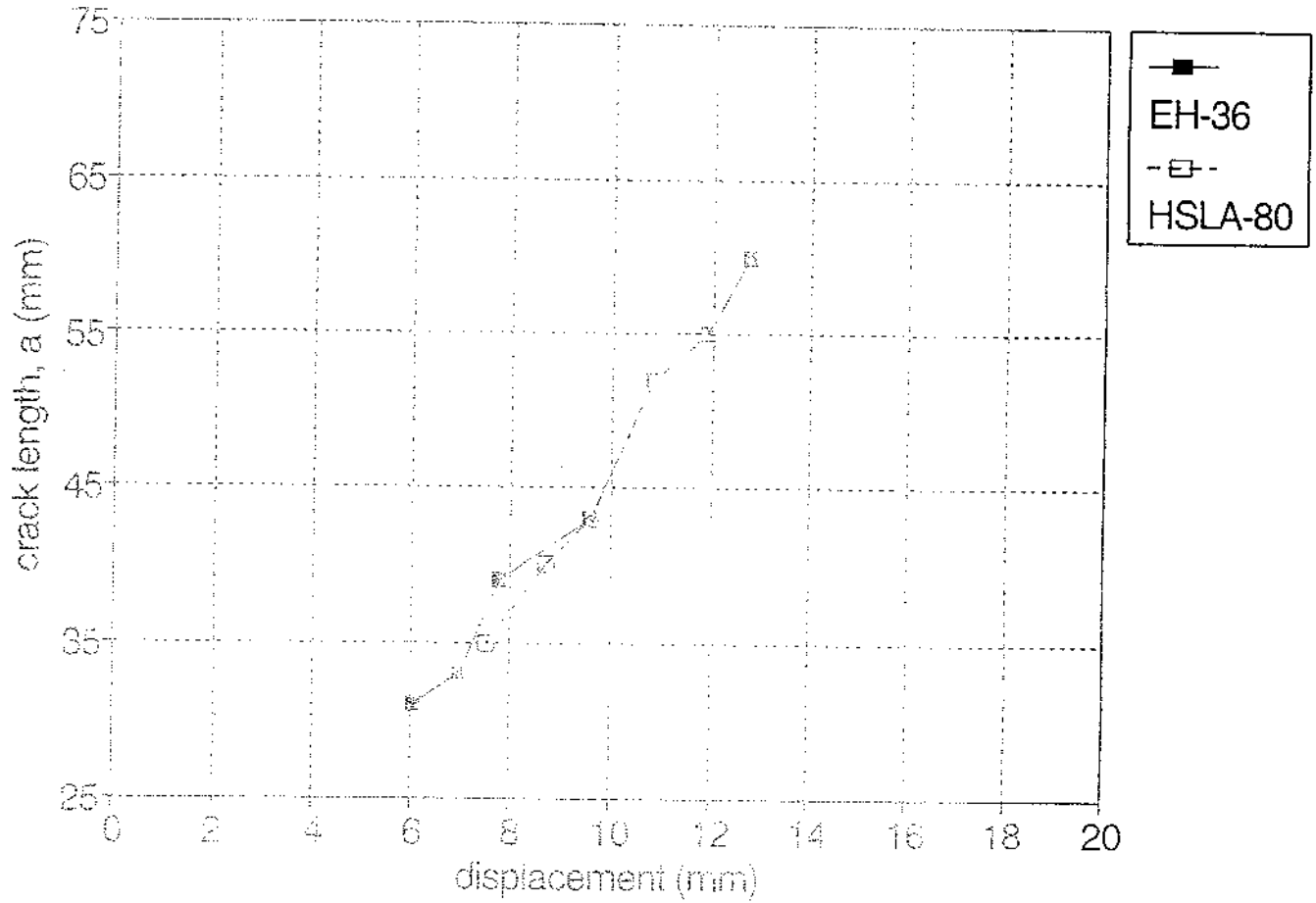


ALL COPE HOLE SPECIMENS

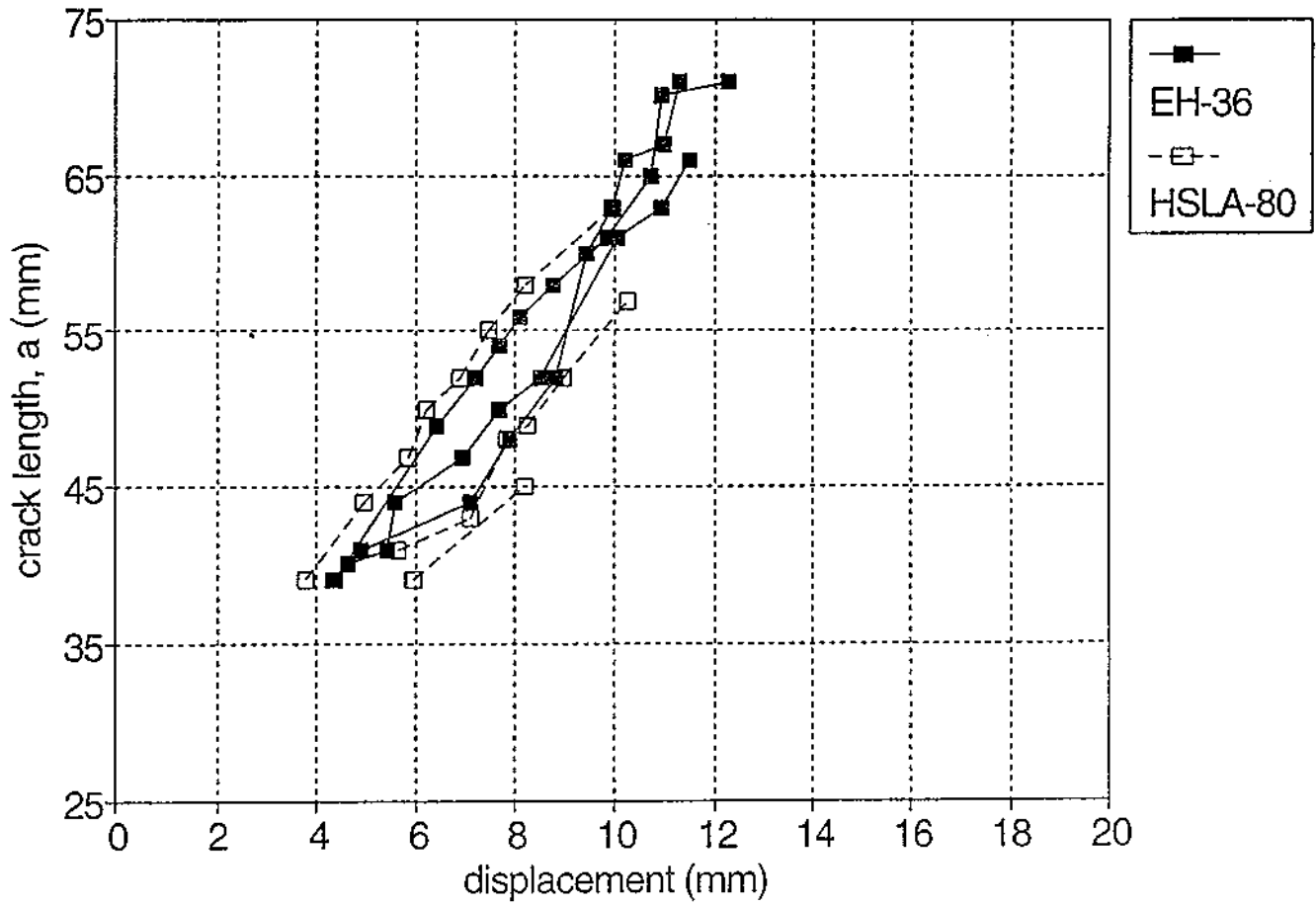
cod,5-displacement curves



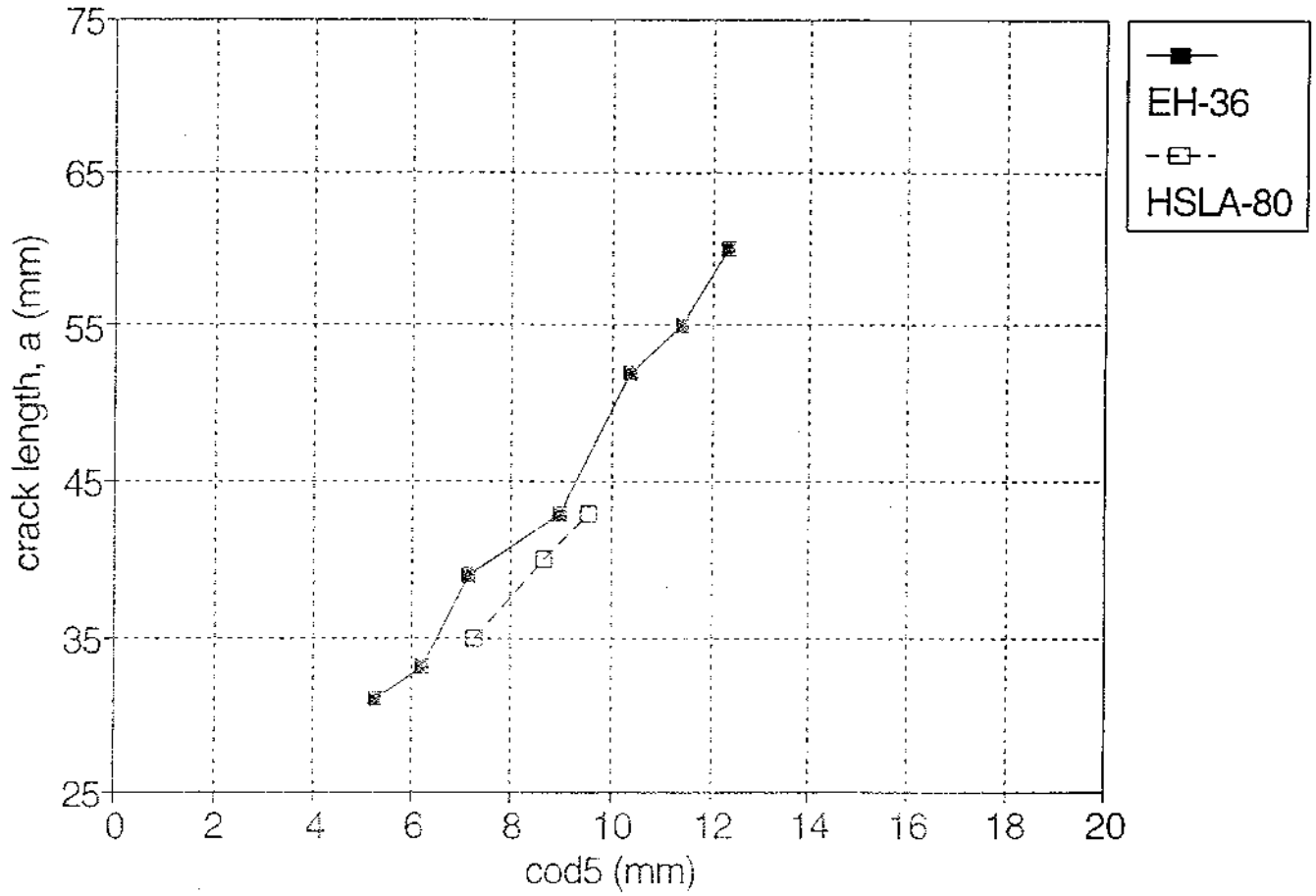
COPE HOLE SPECIMENS, $2a = 50$ mm crack length-displacement curves



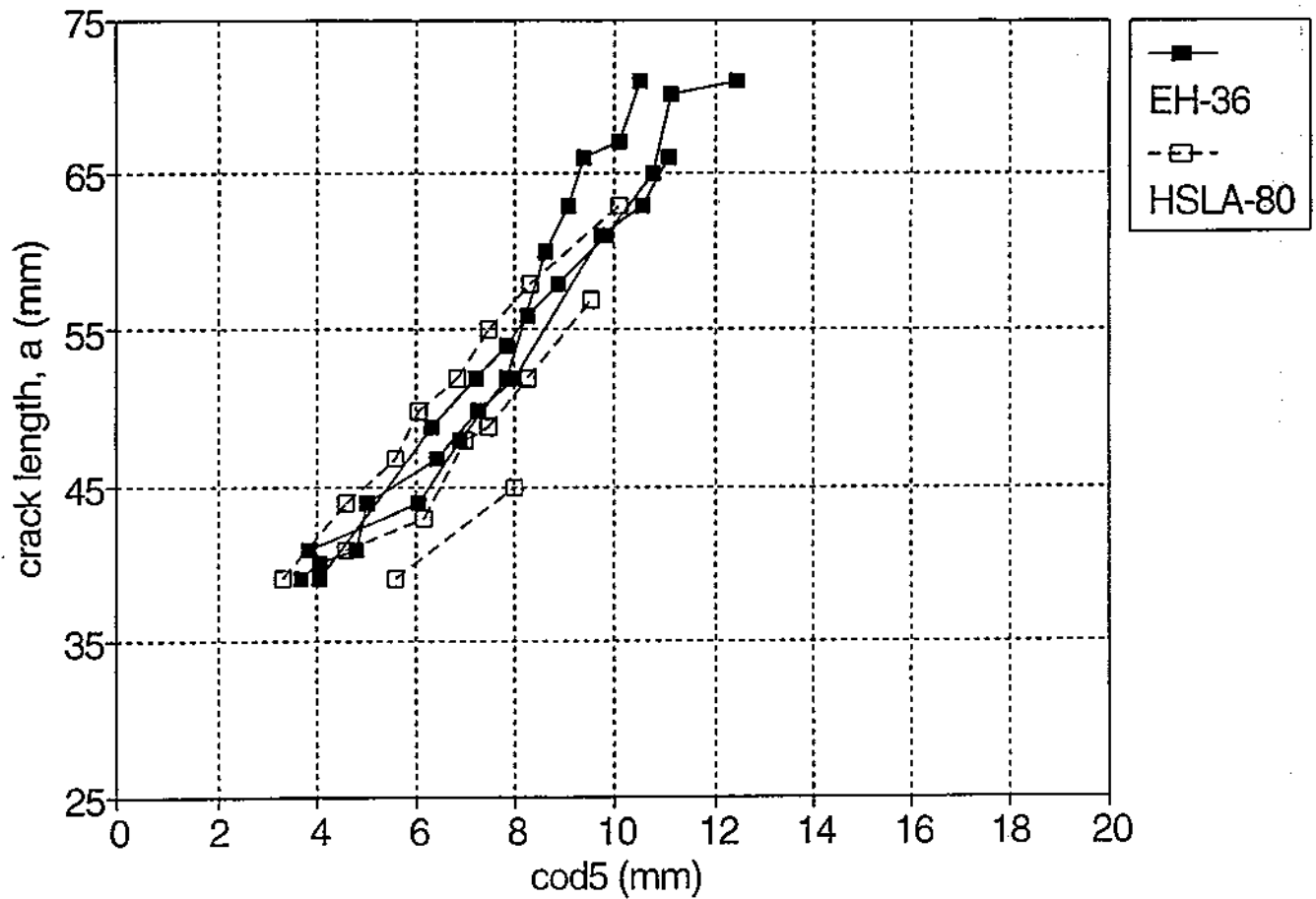
COPE HOLE SPECIMENS, $2a = 76$ mm crack length-displacement curves



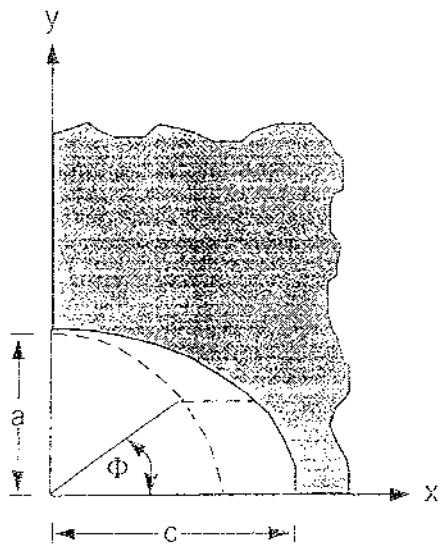
COPE HOLE SPECIMENS, $2a = 50$ mm crack length-displacement curves



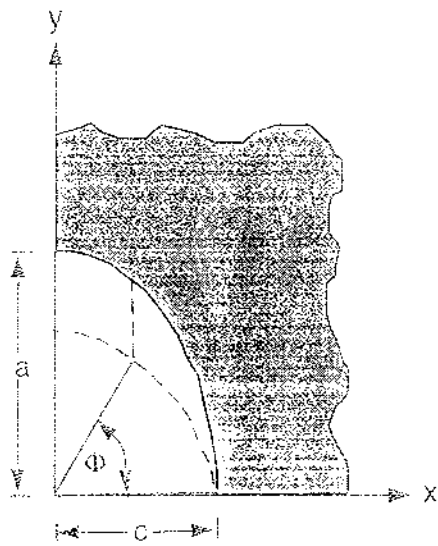
COPE HOLE SPECIMENS, $2a = 76$ mm crack length-displacement curves



Appendix 5
Sample Stress Intensity Factor Calculation



$$\frac{a}{c} \leq 1$$



$$\frac{a}{c} > 1$$

FIGURE A.1.1

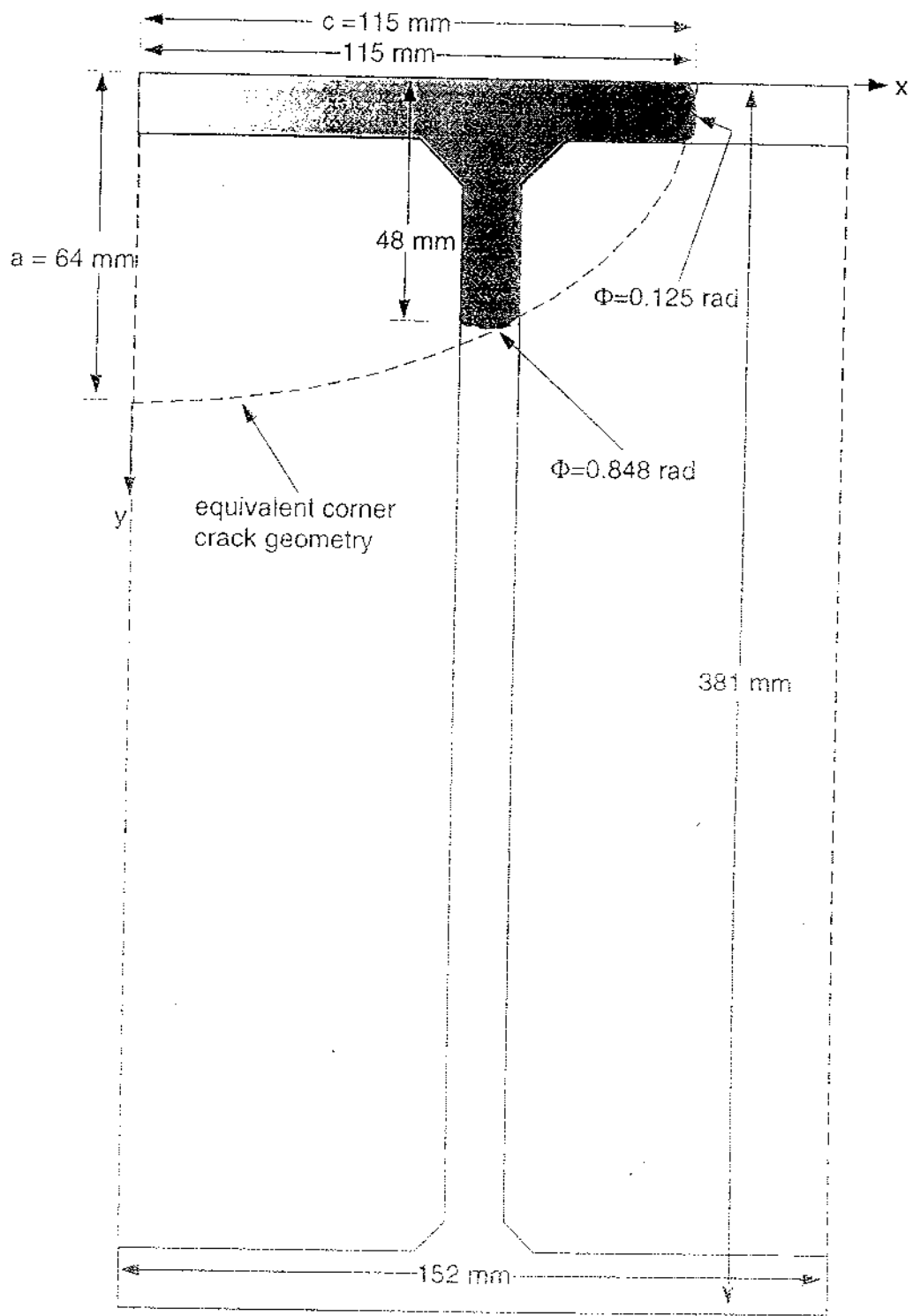
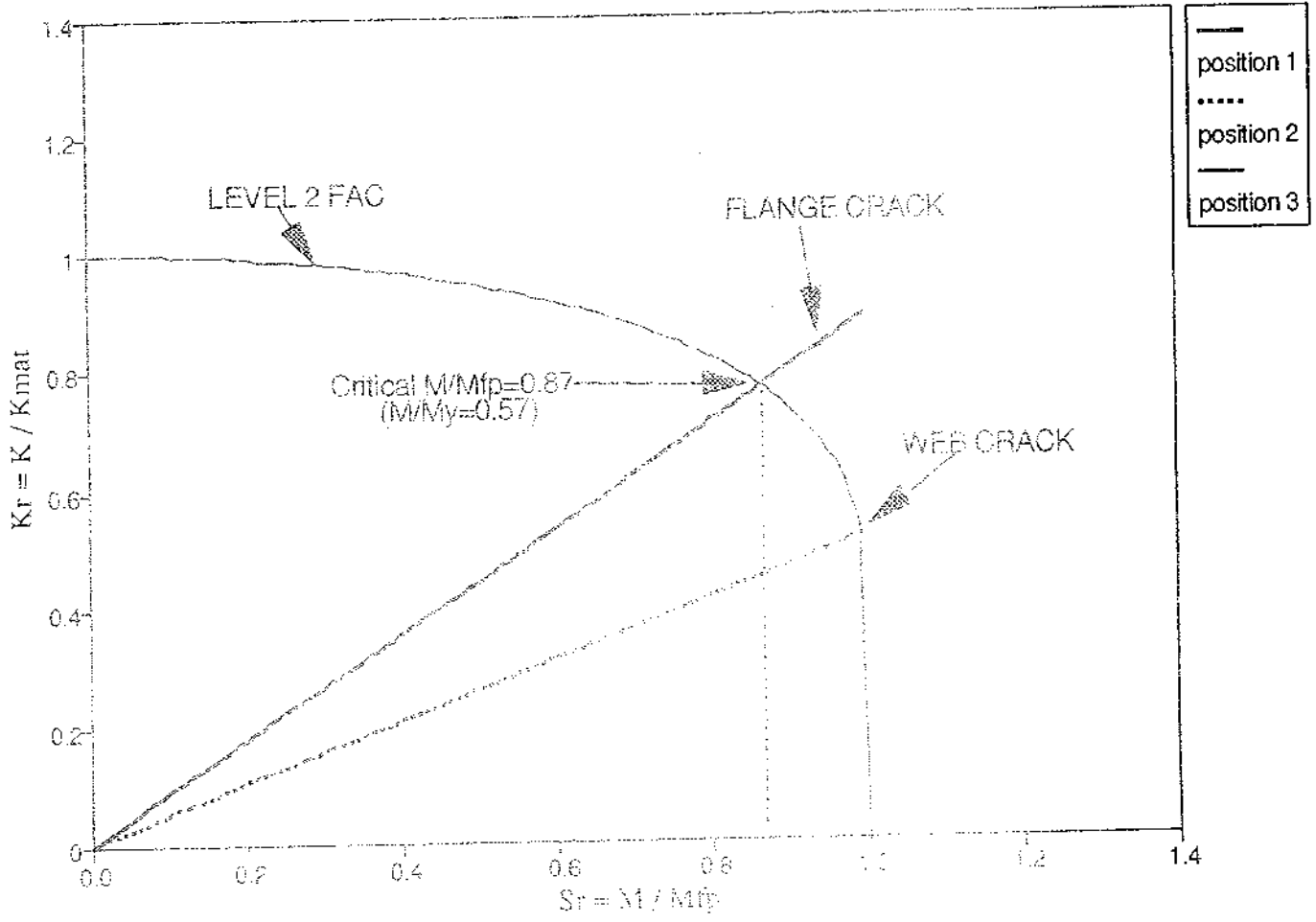


FIGURE A5.2

SPECIMEN 18
Level 2



Appendix A5: Sample Calculation for I-beam Specimen A18

Stress Intensity Factor Calculation To Determine Failure Analysis Points

The following example describes the procedures used to calculate stress intensity factors and plot failure analysis points on the PD6493 failure assessment diagram. This particular example corresponds to the level 2 analysis of I-beam specimen A18. The steps outlined here were taken to make the PD6493 predictions at all levels for the I-beam, box-beam, and cope-hole specimens.

In order to determine the failure analysis points (FAP) for use in the failure assessment diagram (FAD), it is necessary to determine the stress intensity factor, K , as a function of applied moment for each crack tip in the I-beam specimen. As discussed in chapter 4, this is accomplished using an equivalent elliptical crack stress intensity solution on a monolithic block representation of the cracked I-beam cross-section. The crack stress intensity solution for this geometry as derived by Newman and Raju [A5.1] is given by the following equations:

$$K = (S_t + H_j S_b) (\pi a/Q)^{1/2} F_j$$

Where S_t and S_b are the remote uniform tensile stress and remote bending stress on the outer fiber of the beam, a is crack length, Q is the elliptical shape factor, and H_j and F_j are geometric parameters given by:

$$F_j = [M_1 + M_2 (a/t)^2 + M_3 (a/t)^4] g f_\phi f_w$$

$$H_j = H_1 + (H_2 - H_1) \sin^p \phi$$

$$Q = 1 - 1.464 (a/c)^{1.65} \quad \text{for } a/c \leq 1$$

$$Q = 1 + 1.464 (c/a)^{1.65} \quad \text{for } a/c > 1$$

A detailed discussion of the equations derived above can be found in [A5.1]. The variables a , c , and ϕ are shown in Figure A5.1.

In order to determine the variables a and c for the crack geometry of I-beam specimen A18, the crack shape was fit with an ellipse that intersected the crack tips in the web and flange. This is shown in Figure A5.2. Since the ratio a/c is less than one, the circumferential position along the crack front will be defined by the angle ϕ as shown in the left side of Figure A5.1. This elliptic representation of the crack will yield stress intensity solutions for the crack tip in the flange at $\phi=0.125$ rad and the crack tip in the web at $\phi=.848$ rad as noted in Figure A5.2.

Using the values of a and c determined above for a monolithic block of 152 mm width and 381 mm height, the stress intensity equations above were solved as a function of ϕ using a spreadsheet. This spreadsheet is shown in Figure A5.3. Calculations for K at the crack tips in the flange ($\phi=0.125$ rad) and web ($\phi=.848$ rad) are marked with boxes. These values of ϕ correspond to the midplane of the flange and web.

The calculations shown in Figure A5.3 are carried out for a unit bending stress ($S_b=1$) so that failure analysis points may be easily calculated as a function of applied moment, M , i.e.:

$$K_{\text{applied}} = K_u \sigma_{\text{outer fiber}}$$

where K_{applied} is the stress intensity factor at the crack tip, $\sigma_{\text{outer fiber}}$ is the bending stress (Mc/I) at the outer fiber of the beam, and K_u is the stress intensity factor for 1 unit of bending stress as determined by the spreadsheet calculation. This method allows stress intensity values to be calculated as a function of applied moment in an efficient manner as opposed to repeating the spreadsheet calculation for successive values of S_b .

The total stress intensity factor at a given crack tip is equal to the sum of the stress intensity factors from the applied and residual stresses:

$$K = SCF K_{\text{applied}} + K_{\text{residual stress}}$$

where SCF is the stress concentration factor (if any) that exists at the crack location. This can be written in terms of K_u and $\sigma_{\text{outer fiber}} = Mc/I$ as follows:

$$K = SCF \frac{Mc}{I} K_u + K_u \sigma_{\text{residual stress}}$$

assuming residual stresses are negligible and substituting the definitions of K_r and S_r from PD6493, i.e., $K=K_{\text{mat}}K_r$ and $M=M_{fp} S_r$, the equation above can be written as:

$$K_r = SCF \frac{c}{I} \frac{K_u}{K_{\text{mat}}} M_{fp} S_r$$

The above equation was used to generate a ray of failure assessment points for each crack tip in the I-beam specimen. Note that at $\phi=0.125$ where the attachment was present on the flange, the SCF=1.6, and at $\phi=0.848$ there is no concentration effect so the SCF=1. This relationship is plotted in Figure A5.4 along with the level 2 failure assessment curve. The ray that intersects the FAC at the lowest value of S_r was used to determine the critical value of applied moment, M . For this specimen, the level 2 prediction yield a critical value of $M/M_{fp}=0.87$.

References

- A5.1 Newman, J. C., Raju, I. S., "Stress Intensity Factor Equations for Cracks in Three-Dimensional Finite Bodies Subjected to Tension and Bending Loads", Computational Methods in the Mechanics of Fracture, Vol 2, Satyan Alturi, ed., Elsevier Science Publishers B.V., 1986

CORNER CRACK STRESS INTENSITY FACTOR SPREADSHEET

REFERENCE: COMPUTATIONAL METHODS IN FRACTURE MECHANICS
 4, TURI, 1988
 NEWMAN AND RAJU, CHAPTER 6 PG 612

SPECIMEN 18

CRACK GEOMETRY

a	c	b	l
0.064	0.115	0.1524	0.381
a/c	a/b	a/l	c
0.558622	0.167975	0.754593	1.556558

GEOMETRY (INPUT)

APPLIED STRESS

σ_1	σ_2
0	1

UNIT STRESS (INPUT)

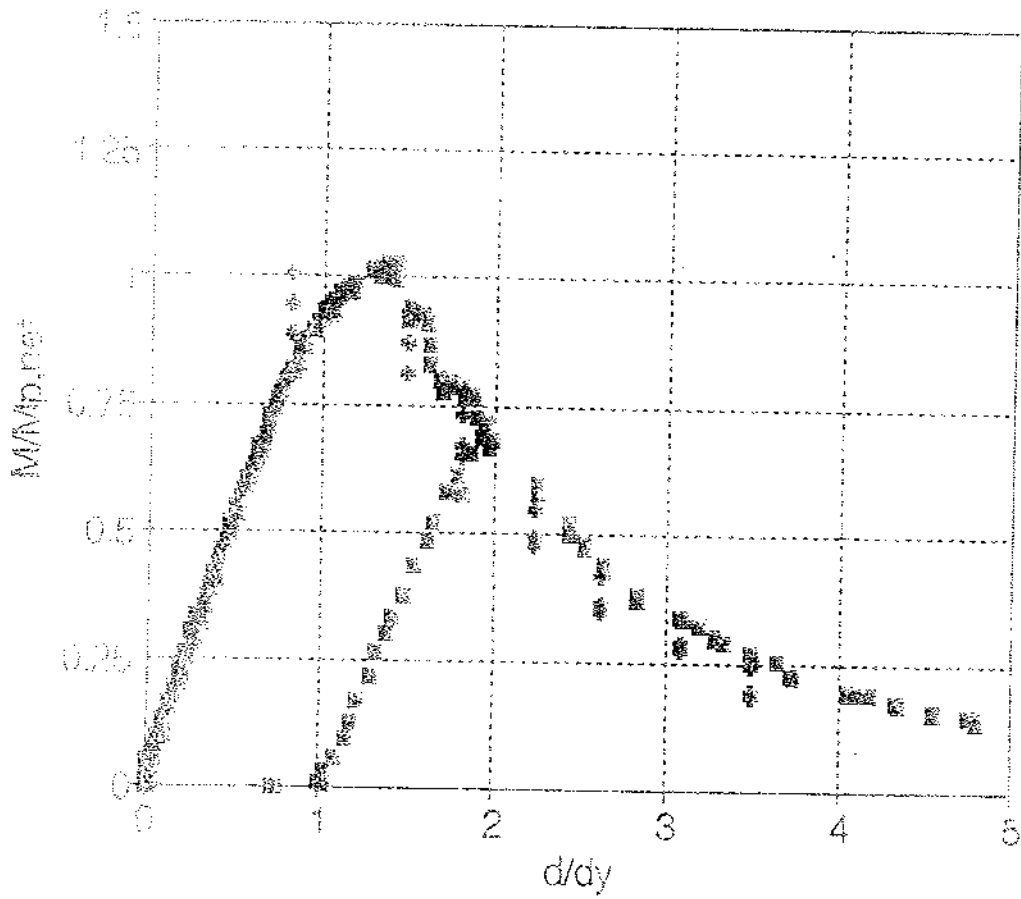
K_{IC} (OUTPUT)

Prk	M1	M2	M3	G1	G2	FPH	ALPHA	FW	Q1	Q2	H1	H2	H3	PC	K	Z ² PHX	FC/HC	K(SB/PA/C)S	G11	G12	
0.017453	1.063304	0.797563	-0.36079	1.051287	1.064253	0.746904	0.399972	1.511258	0.657039	-1.28678	0.158677	0.932834	0.755322	0.932834	1.446072	0.458561	0	1.350478	1.350478	-0.77672	0.878624
0.034907	1.063304	0.797563	-0.36079	1.051287	1.064253	0.746904	0.399972	1.511258	0.657039	-1.28678	0.158677	0.932834	0.755322	0.932834	1.446072	0.458561	0.011111	1.333074	1.333074	-0.77672	0.878624
0.052361	1.063304	0.797563	-0.36079	1.051287	1.064253	0.746904	0.399972	1.511258	0.657039	-1.28678	0.158677	0.932834	0.755322	0.932834	1.446072	0.458561	0.022222	1.317857	1.317857	-0.77672	0.878624
0.069815	1.063304	0.797563	-0.36079	1.051287	1.064253	0.746904	0.399972	1.511258	0.657039	-1.28678	0.158677	0.932834	0.755322	0.932834	1.446072	0.458561	0.033333	1.303945	1.303945	-0.77672	0.878624
0.087269	1.063304	0.797563	-0.36079	1.051287	1.064253	0.746904	0.399972	1.511258	0.657039	-1.28678	0.158677	0.932834	0.755322	0.932834	1.446072	0.458561	0.044444	1.291154	1.291154	-0.77672	0.878624
0.104723	1.063304	0.797563	-0.36079	1.051287	1.064253	0.746904	0.399972	1.511258	0.657039	-1.28678	0.158677	0.932834	0.755322	0.932834	1.446072	0.458561	0.055556	1.279384	1.279384	-0.77672	0.878624
0.122177	1.063304	0.797563	-0.36079	1.051287	1.064253	0.746904	0.399972	1.511258	0.657039	-1.28678	0.158677	0.932834	0.755322	0.932834	1.446072	0.458561	0.066667	1.268564	1.268564	-0.77672	0.878624
0.139631	1.063304	0.797563	-0.36079	1.051287	1.064253	0.746904	0.399972	1.511258	0.657039	-1.28678	0.158677	0.932834	0.755322	0.932834	1.446072	0.458561	0.077778	1.258693	1.258693	-0.77672	0.878624
0.157085	1.063304	0.797563	-0.36079	1.051287	1.064253	0.746904	0.399972	1.511258	0.657039	-1.28678	0.158677	0.932834	0.755322	0.932834	1.446072	0.458561	0.088889	1.249655	1.249655	-0.77672	0.878624
0.174539	1.063304	0.797563	-0.36079	1.051287	1.064253	0.746904	0.399972	1.511258	0.657039	-1.28678	0.158677	0.932834	0.755322	0.932834	1.446072	0.458561	0.1	1.241273	1.241273	-0.77672	0.878624
0.191993	1.063304	0.797563	-0.36079	1.051287	1.064253	0.746904	0.399972	1.511258	0.657039	-1.28678	0.158677	0.932834	0.755322	0.932834	1.446072	0.458561	0.111111	1.233748	1.233748	-0.77672	0.878624
0.209447	1.063304	0.797563	-0.36079	1.051287	1.064253	0.746904	0.399972	1.511258	0.657039	-1.28678	0.158677	0.932834	0.755322	0.932834	1.446072	0.458561	0.122222	1.226942	1.226942	-0.77672	0.878624
0.226901	1.063304	0.797563	-0.36079	1.051287	1.064253	0.746904	0.399972	1.511258	0.657039	-1.28678	0.158677	0.932834	0.755322	0.932834	1.446072	0.458561	0.133333	1.220817	1.220817	-0.77672	0.878624
0.244355	1.063304	0.797563	-0.36079	1.051287	1.064253	0.746904	0.399972	1.511258	0.657039	-1.28678	0.158677	0.932834	0.755322	0.932834	1.446072	0.458561	0.144444	1.215337	1.215337	-0.77672	0.878624
0.261809	1.063304	0.797563	-0.36079	1.051287	1.064253	0.746904	0.399972	1.511258	0.657039	-1.28678	0.158677	0.932834	0.755322	0.932834	1.446072	0.458561	0.155556	1.210468	1.210468	-0.77672	0.878624
0.279263	1.063304	0.797563	-0.36079	1.051287	1.064253	0.746904	0.399972	1.511258	0.657039	-1.28678	0.158677	0.932834	0.755322	0.932834	1.446072	0.458561	0.166667	1.206177	1.206177	-0.77672	0.878624
0.296717	1.063304	0.797563	-0.36079	1.051287	1.064253	0.746904	0.399972	1.511258	0.657039	-1.28678	0.158677	0.932834	0.755322	0.932834	1.446072	0.458561	0.177778	1.202431	1.202431	-0.77672	0.878624
0.314171	1.063304	0.797563	-0.36079	1.051287	1.064253	0.746904	0.399972	1.511258	0.657039	-1.28678	0.158677	0.932834	0.755322	0.932834	1.446072	0.458561	0.188889	1.199198	1.199198	-0.77672	0.878624
0.331625	1.063304	0.797563	-0.36079	1.051287	1.064253	0.746904	0.399972	1.511258	0.657039	-1.28678	0.158677	0.932834	0.755322	0.932834	1.446072	0.458561	0.2	1.196452	1.196452	-0.77672	0.878624
0.349079	1.063304	0.797563	-0.36079	1.051287	1.064253	0.746904	0.399972	1.511258	0.657039	-1.28678	0.158677	0.932834	0.755322	0.932834	1.446072	0.458561	0.211111	1.194161	1.194161	-0.77672	0.878624
0.366533	1.063304	0.797563	-0.36079	1.051287	1.064253	0.746904	0.399972	1.511258	0.657039	-1.28678	0.158677	0.932834	0.755322	0.932834	1.446072	0.458561	0.222222	1.192297	1.192297	-0.77672	0.878624
0.383987	1.063304	0.797563	-0.36079	1.051287	1.064253	0.746904	0.399972	1.511258	0.657039	-1.28678	0.158677	0.932834	0.755322	0.932834	1.446072	0.458561	0.233333	1.190835	1.190835	-0.77672	0.878624
0.401441	1.063304	0.797563	-0.36079	1.051287	1.064253	0.746904	0.399972	1.511258	0.657039	-1.28678	0.158677	0.932834	0.755322	0.932834	1.446072	0.458561	0.244444	1.189749	1.189749	-0.77672	0.878624
0.418895	1.063304	0.797563	-0.36079	1.051287	1.064253	0.746904	0.399972	1.511258	0.657039	-1.28678	0.158677	0.932834	0.755322	0.932834	1.446072	0.458561	0.255556	1.189104	1.189104	-0.77672	0.878624
0.436349	1.063304	0.797563	-0.36079	1.051287	1.064253	0.746904	0.399972	1.511258	0.657039	-1.28678	0.158677	0.932834	0.755322	0.932834	1.446072	0.458561	0.266667	1.188906	1.188906	-0.77672	0.878624
0.453803	1.063304	0.797563	-0.36079	1.051287	1.064253	0.746904	0.399972	1.511258	0.657039	-1.28678	0.158677	0.932834	0.755322	0.932834	1.446072	0.458561	0.277778	1.188504	1.188504	-0.77672	0.878624
0.471257	1.063304	0.797563	-0.36079	1.051287	1.064253	0.746904	0.399972	1.511258	0.657039	-1.28678	0.158677	0.932834	0.755322	0.932834	1.446072	0.458561	0.288889	1.188565	1.188565	-0.77672	0.878624
0.488711	1.063304	0.797563	-0.36079	1.051287	1.064253	0.746904	0.399972	1.511258	0.657039	-1.28678	0.158677	0.932834	0.755322	0.932834	1.446072	0.458561	0.3	1.18913	1.18913	-0.77672	0.878624
0.506165	1.063304	0.797563	-0.36079	1.051287	1.064253	0.746904	0.399972	1.511258	0.657039	-1.28678	0.158677	0.932834	0.755322	0.932834	1.446072	0.458561	0.311111	1.18918	1.18918	-0.77672	0.878624
0.523619	1.063304	0.797563	-0.36079	1.051287	1.064253	0.746904	0.399972	1.511258	0.657039	-1.28678	0.158677	0.932834	0.755322	0.932834	1.446072	0.458561	0.322222	1.19073	1.19073	-0.77672	0.878624
0.541073	1.063304	0.797563	-0.36079	1.051287	1.064253	0.746904	0.399972	1.511258	0.657039	-1.28678	0.158677	0.932834	0.755322	0.932834	1.446072	0.458561	0.333333	1.191845	1.191845	-0.77672	0.878624
0.558527	1.063304	0.797563	-0.36079	1.051287	1.064253	0.746904	0.399972	1.511258	0.657039	-1.28678	0.158677	0.932834	0.755322	0.932834	1.446072	0.458561	0.344444	1.191517	1.191517	-0.77672	0.878624
0.575981	1.063304	0.797563	-0.36079	1.051287	1.064253	0.746904	0.399972	1.511258	0.657039	-1.28678	0.158677	0.932834	0.755322	0.932834	1.446072	0.458561	0.355556	1.191638	1.191638	-0.77672	0.878624
0.593435	1.063304	0.797563	-0.36079	1.051287	1.064253	0.746904	0.399972	1.511258	0.657039	-1.28678	0.158677	0.932834	0.755322	0.932834	1.446072	0.458561	0.366667	1.192277	1.192277	-0.77672	0.878624
0.610889	1.063304	0.797563	-0.36079	1.051287	1.064253	0.746904	0.399972	1.511258	0.657039	-1.28678	0.158677	0.932834	0.755322	0.932834	1.446072	0.458561	0.377778	1.192659	1.192659	-0.77672	0.878624
0.628343	1.063304	0.797563	-0.36079	1.051287	1.064253	0.746904	0.399972	1.511258	0.657039	-1.28678	0.158677	0.932834	0.755322	0.932834	1.446072	0.458561	0.388889	1.193669	1.193669	-0.77672	0.878624
0.645797	1.063304	0.797563	-0.36079	1.051287	1.064253	0.746904	0.399972	1.511258	0.657039	-1.28678	0.158677	0.932834	0.755322	0.932834	1.446072	0.458561	0.4	1.201995			

Appendix 6
Results of Limit Load Predictions for I-Beam and Box-Beam Specimens

SPECIMEN 9

normalized load history

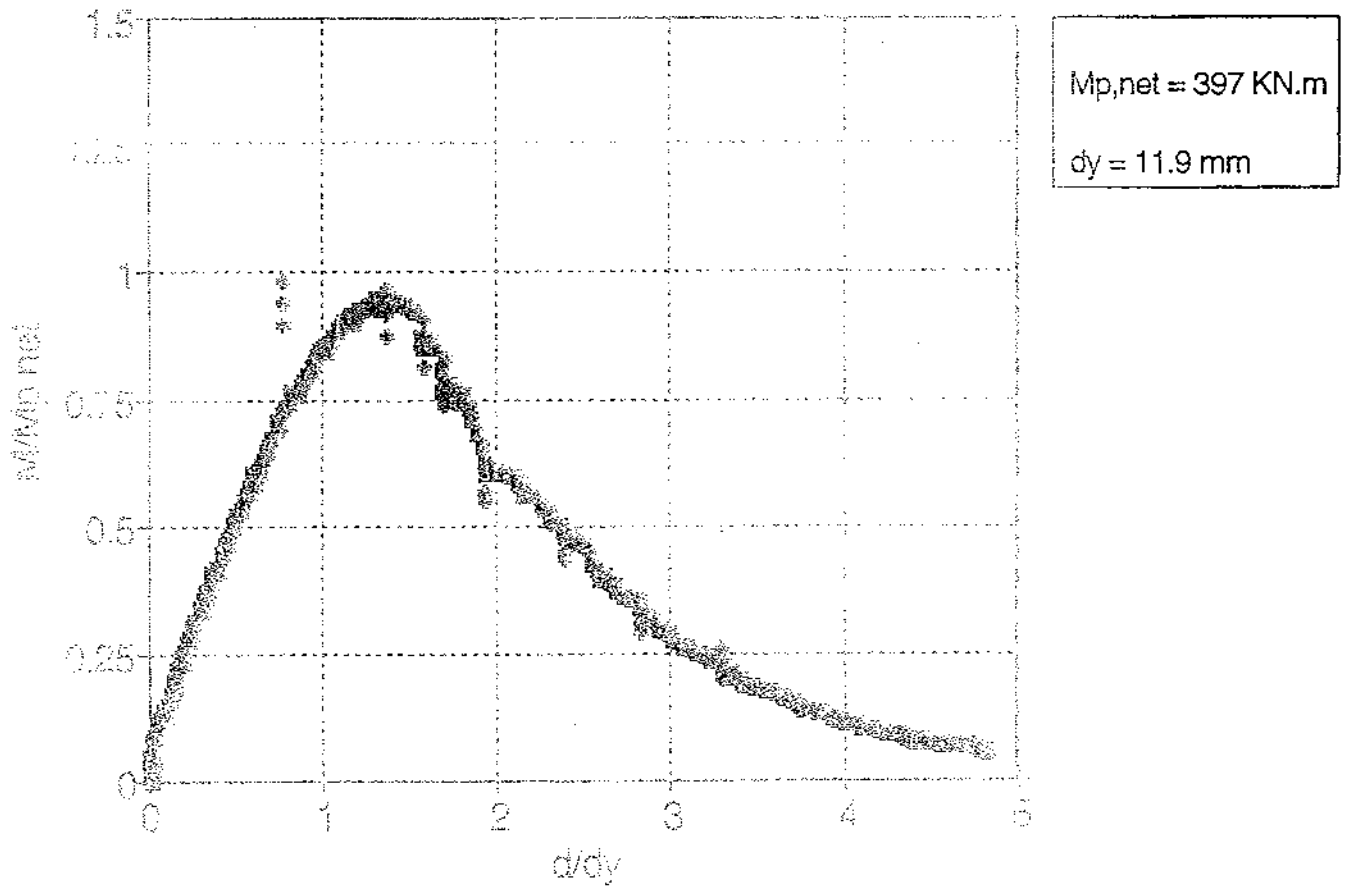


$M_{p,net} = 388 \text{ KN.m}$

$d_y = 9.8 \text{ mm}$

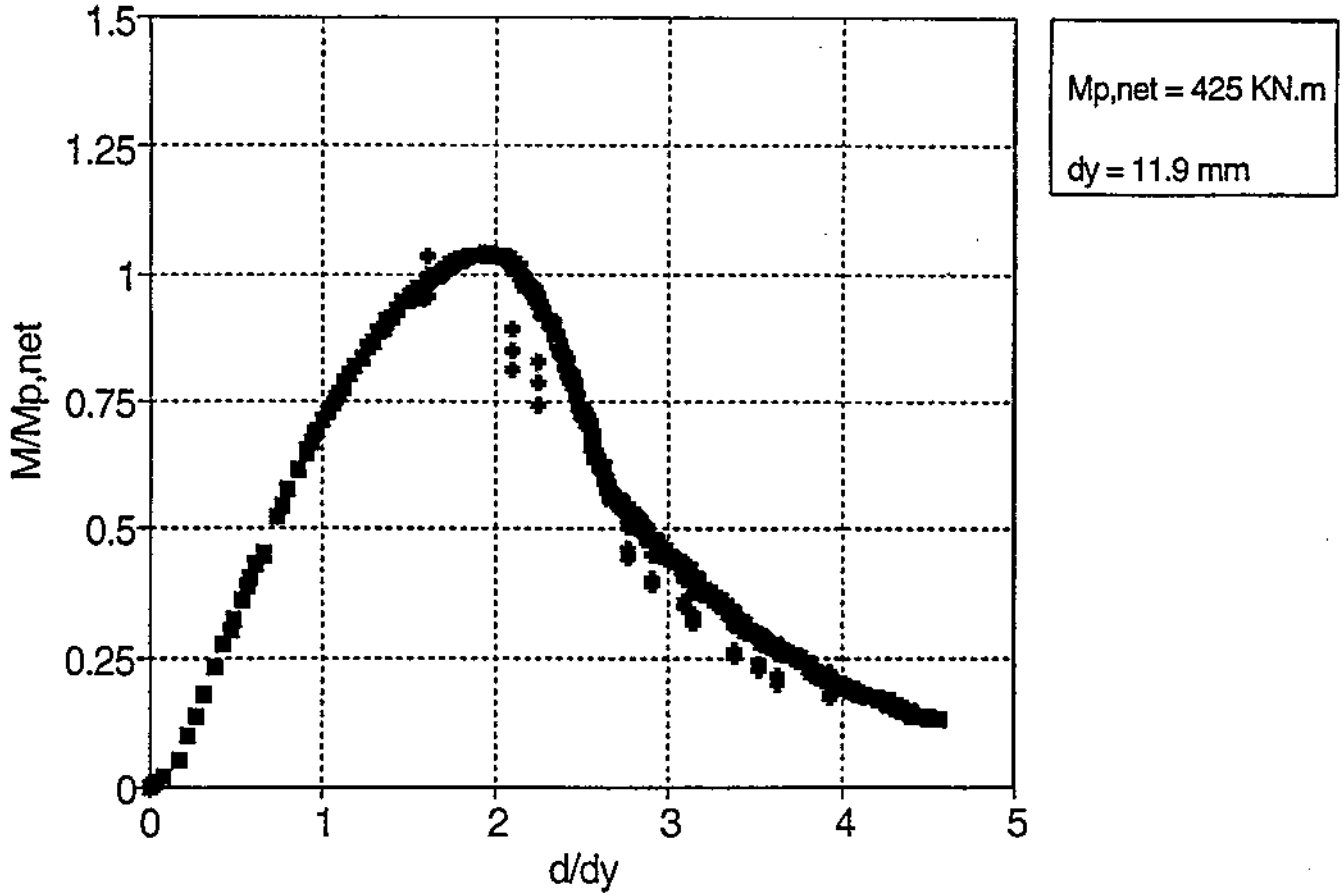
SPECIMEN 20

normalized load history



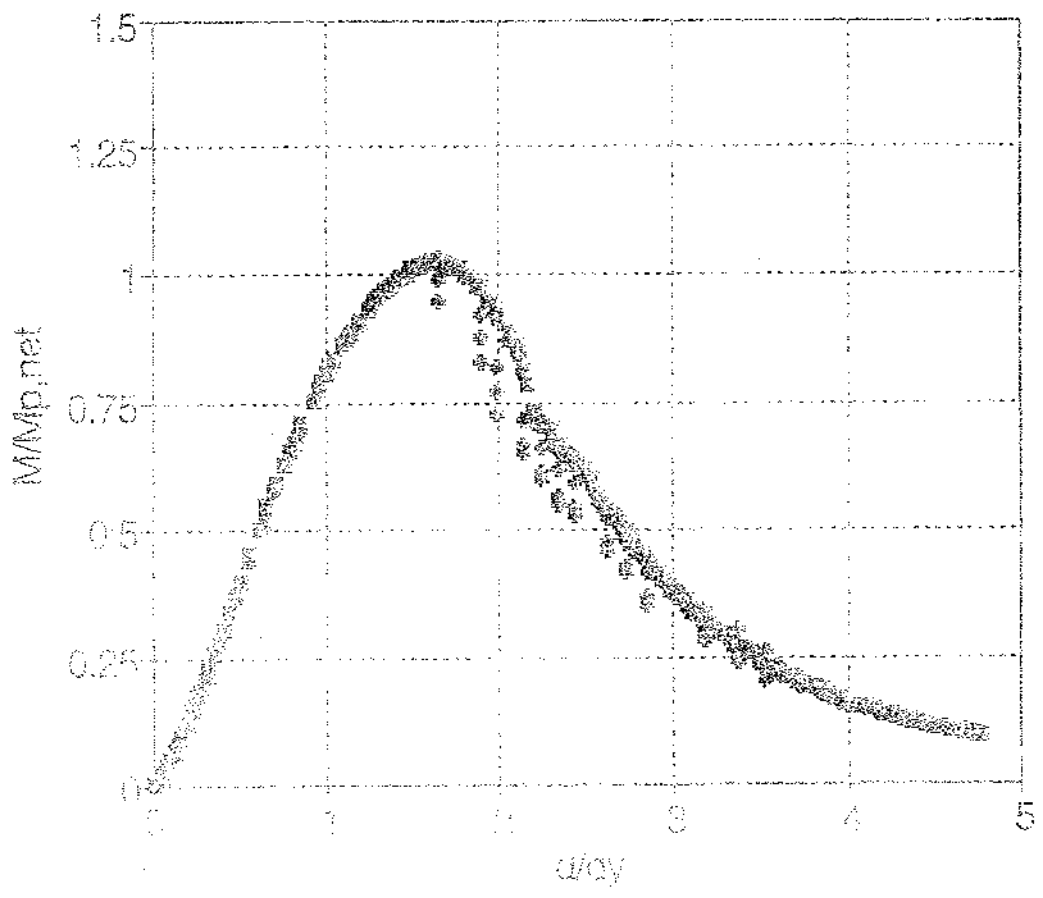
SPECIMEN 34

normalized load history



SPECIMEN 39

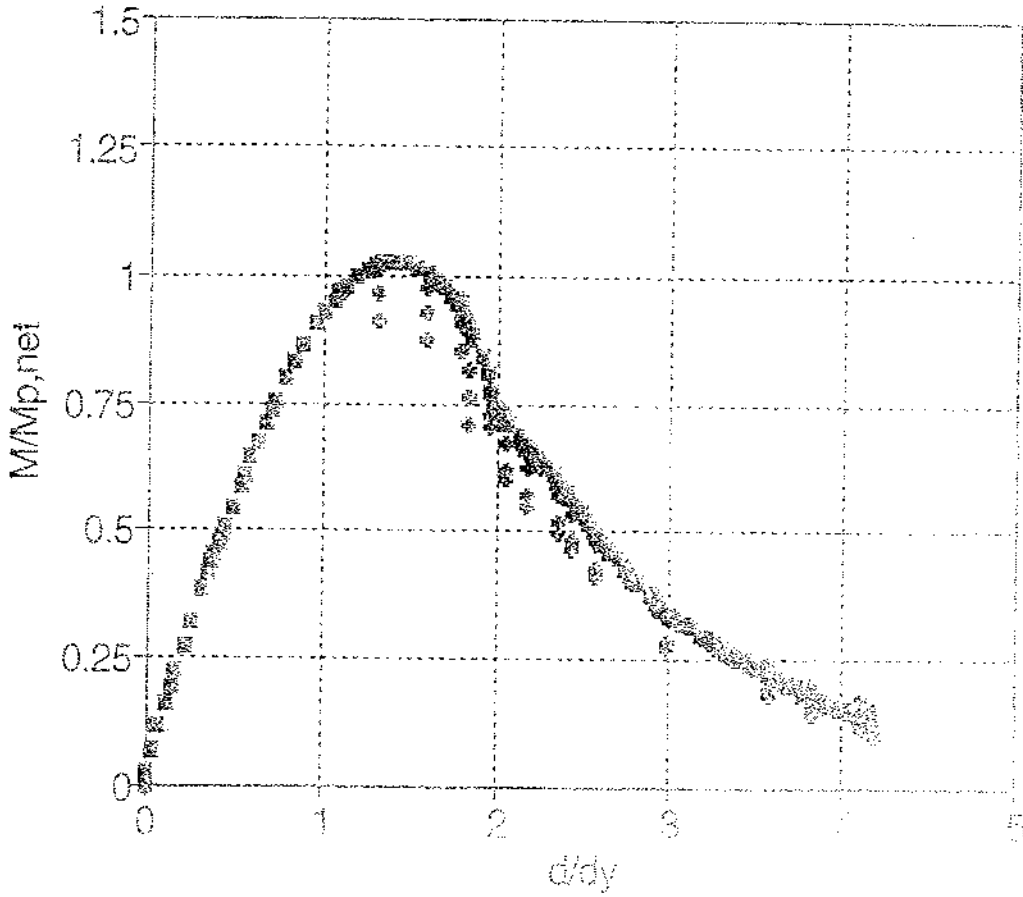
normalized load history



$M_{p,net} = 403 \text{ KN.m}$
 $d_y = 11.9 \text{ mm}$

SPECIMEN 48

normalized load history

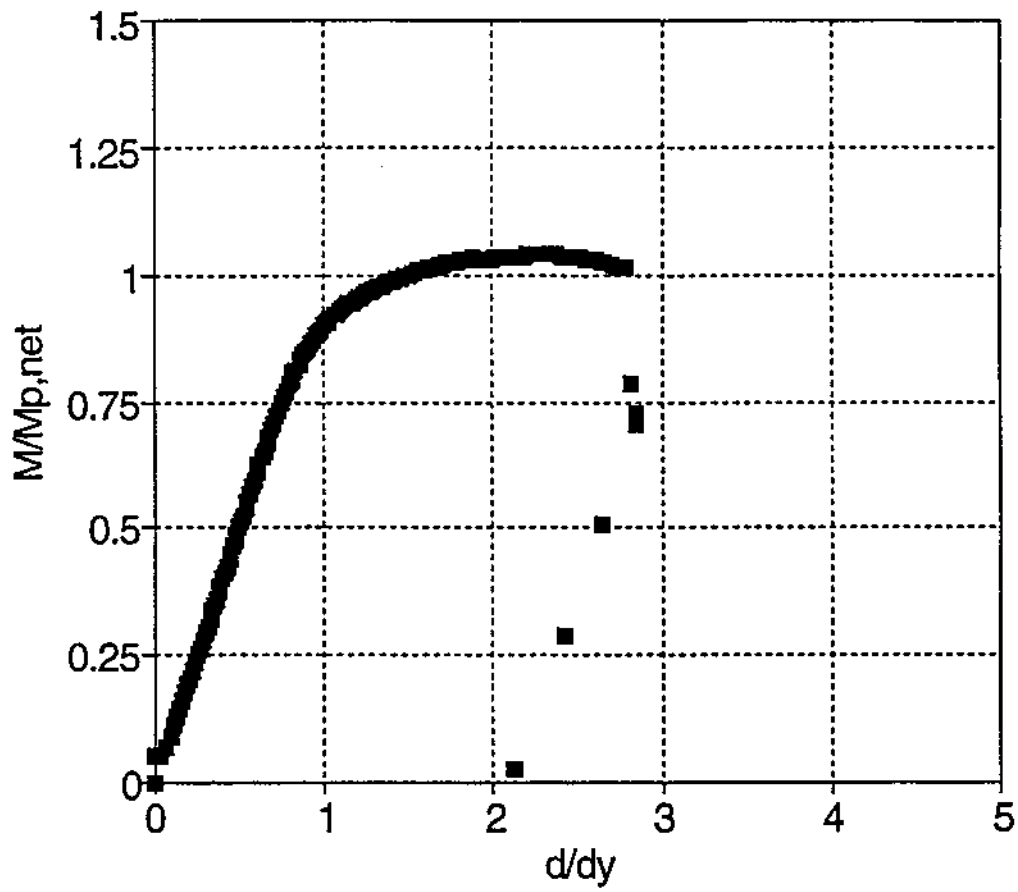


$M_{p,net} = 360 \text{ KN.m}$

$d_y = 11.9 \text{ mm}$

BOX 8

normalized load history

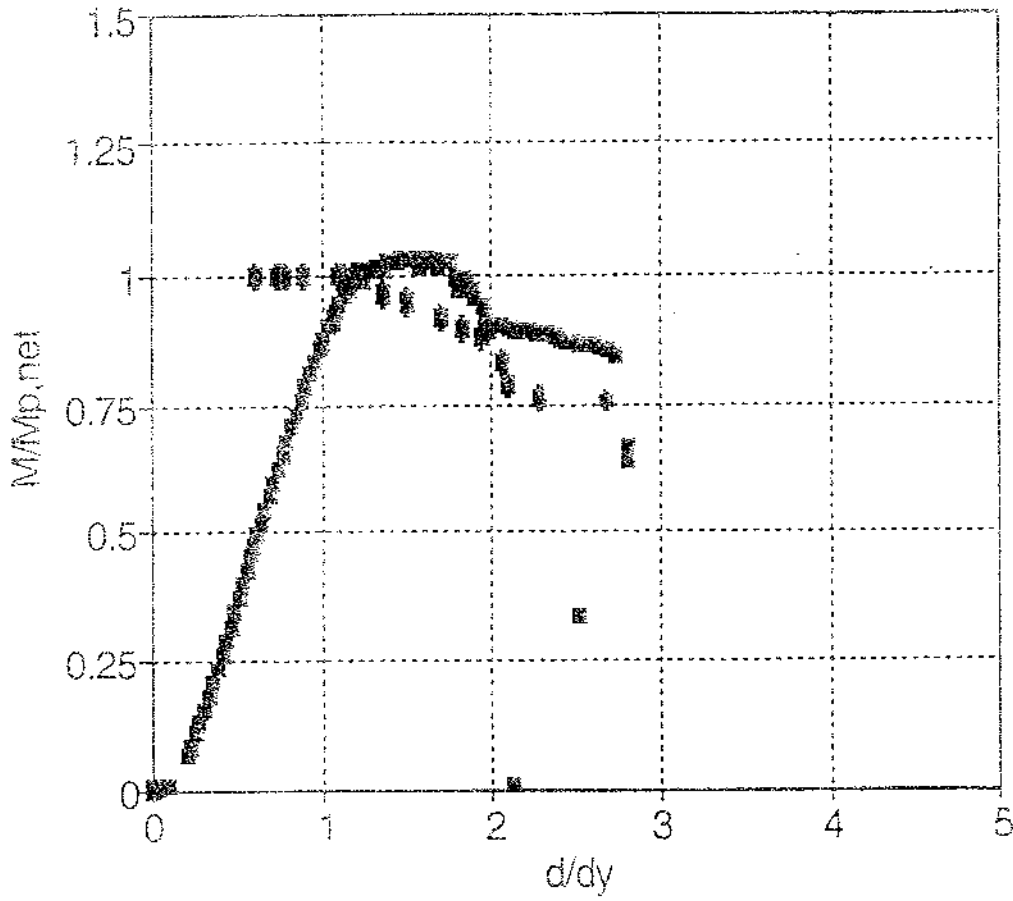


$Mp,net = 5928 \text{ KN.m}$

$dy = 38.3 \text{ mm}$

BOX 9

normalized load history



$M_{p,net} = 7177 \text{ KN.m}$

$d_y = 38.3 \text{ mm}$

Sample Calculation of Limit Load for I-beam Specimen A18

This example shows how to calculate the fully plastic moment for I-beam Specimen A18. This same procedure can be used to make calculations for any of the I-beam specimens for a given amount of crack extension provided that the crack tips propagate in the base metal.

Step 1: Determine location of plastic neutral axis, Pna.

Refer to the figure on the following page. The remaining ligament area is idealized as rectangular blocks. The area above the plastic neutral axis must equal the area below it, therefore:

$$A1 + A2 = A3 + A4$$

$$(12.7)(152) + (Pna-12.7)(9.5) = (333-Pna)(9.5) + 39(12.7)$$

solving for Pna, it is found that

$$Pna = 97.32 \text{ mm} = 0.097 \text{ m}$$

Step 2: Sum moments about Pna assuming flow stress is attained across entire ligament.

The fully plastic moment is given by:

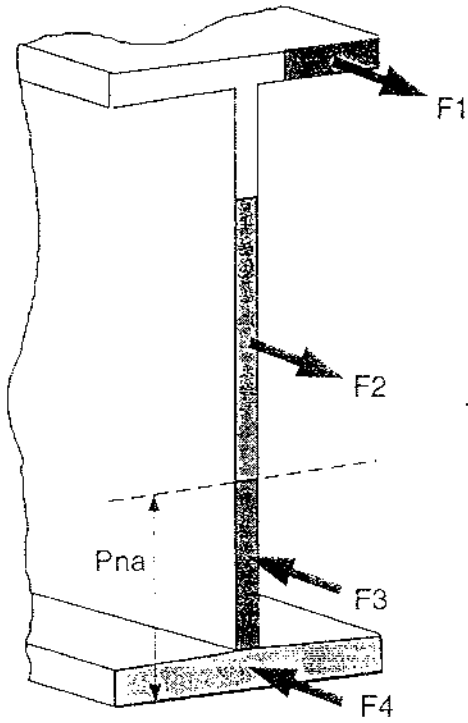
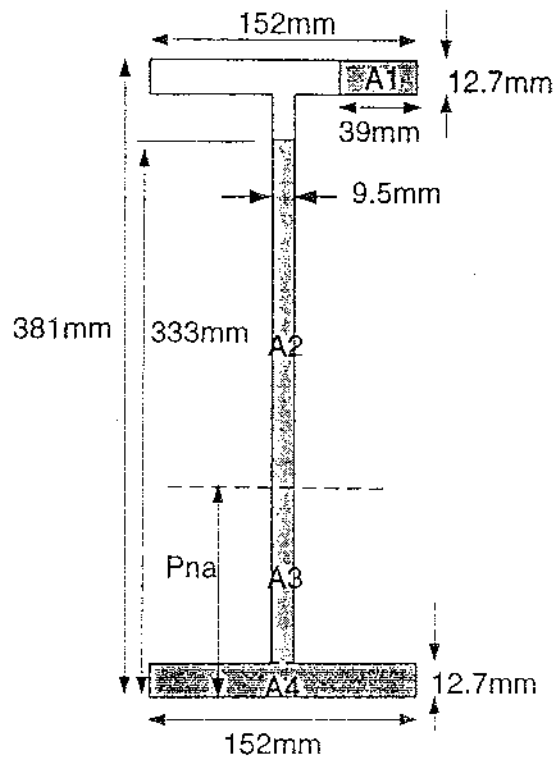
$$M_{fp} = F1 d1 + F2 d2 + F3 d3 + F4 d4$$

where d1, d2, d3, and d4 are the distances from F1, F2, F3, and F4 to Pna, respectively. F1, F2, F3, and F4 act at the centroid of their corresponding areas. Assuming that the flow stress, σ_f , acts across the entire remaining ligament.

$$M_{fp} = \sigma_f [A1 d1 + A2 d2 + A3 d3 + A4 d4]$$

For the HSLA-80 material, the flow stress is approximately equal to the ultimate stress (690 MPa). Using the dimensions shown on the figure,

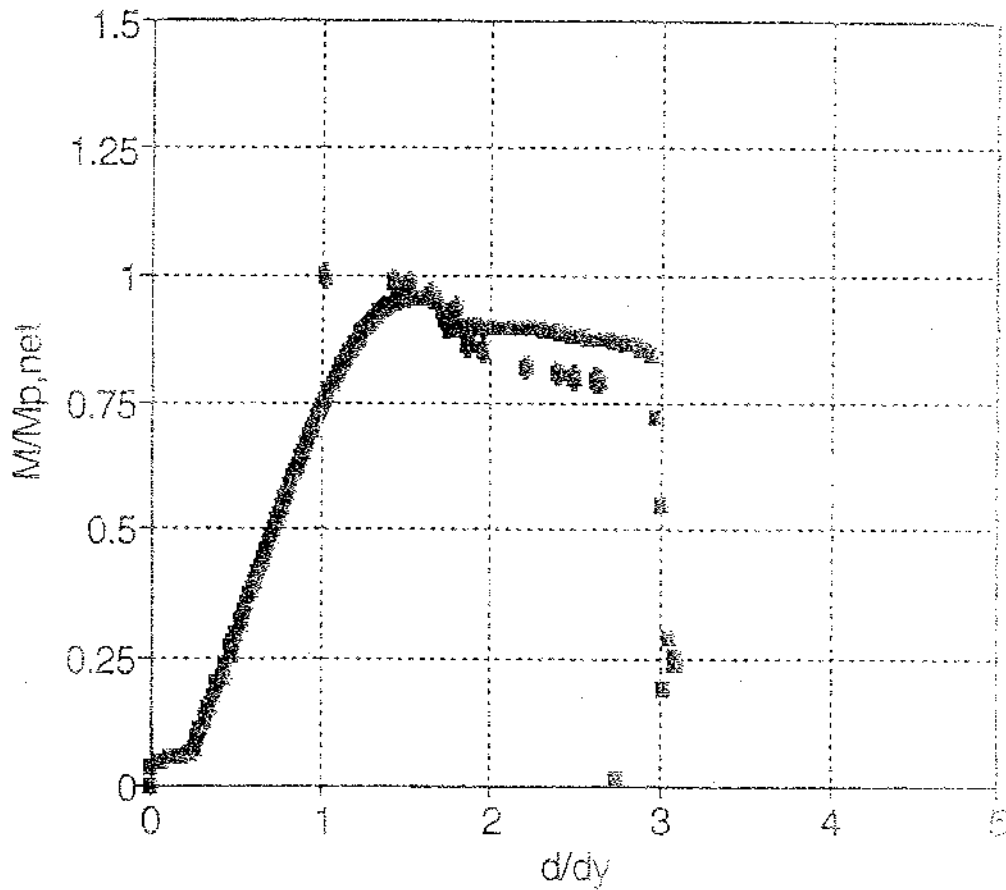
$$M_{fp} = 349 \text{ kN-m}$$



Calculation of plastic limit load for I-beam specimen A18

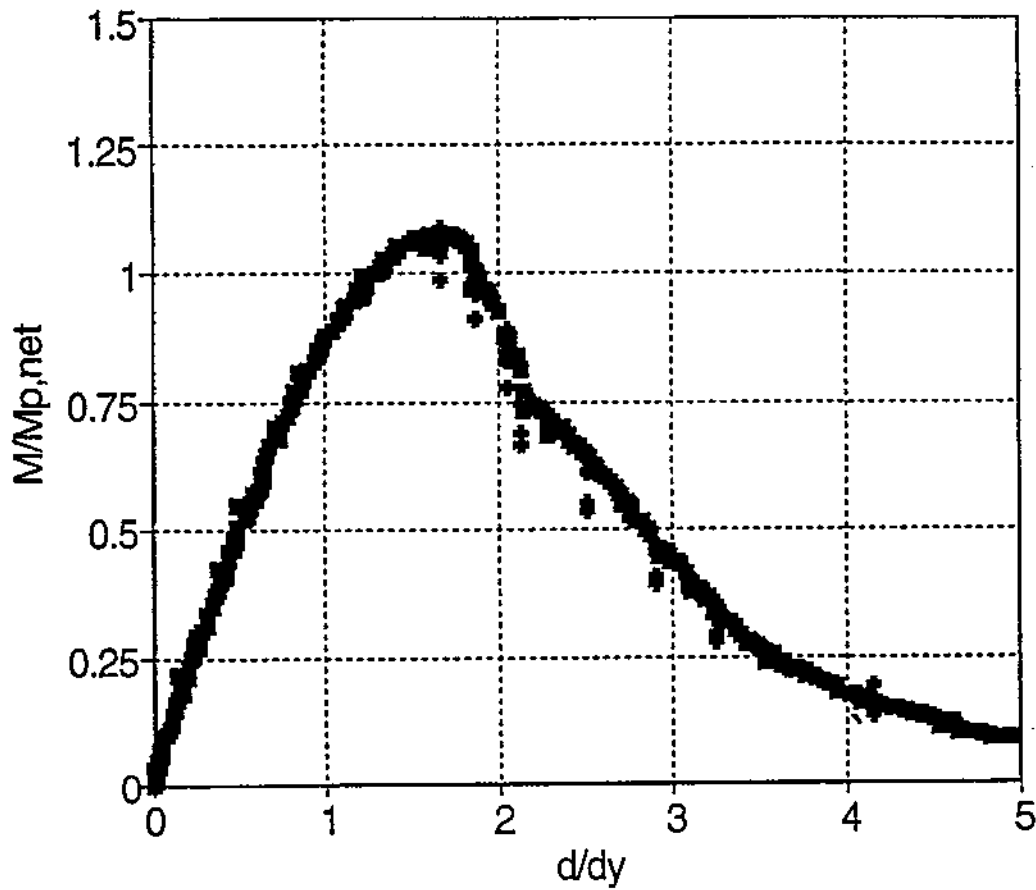
BOX 3

normalized load history



SPECIMEN 18

normalized load history



$M_{p,net} = 349 \text{ KN.m}$
 $d_y = 11.9 \text{ mm}$

PROJECT TECHNICAL COMMITTEE MEMBERS

The following persons were members of the committee that represented the Ship Structure Committee to the Contractor as resident subject matter experts. As such they performed technical review of the initial proposals to select the contractor, advised the contractor in cognizant matters pertaining to the contract of which the agencies were aware, and performed technical review of the work in progress and edited the final report.

Chairman

Dr. Walter Reuter Idaho National Engineering Laboratory

Members

Mr. William Hanzalek American Bureau of Shipping

Mr. David Ku American Bureau of Shipping

Dr. John Landes University of Tennessee

Dr. Harold Reemsnyder Bethlehem Steel

Mr. William Siekierka Naval Sea Systems Command,
Contracting Officer's Technical Representative

Dr. Robert Sielski National Academy of Science,
Marine Board Liaison

CDR Steve Sharpe U.S. Coast Guard, Executive Director
Ship Structure Committee

COMMITTEE ON MARINE STRUCTURES

Commission on Engineering and Technical Systems

National Academy of Sciences - National Research Council

The COMMITTEE ON MARINE STRUCTURES has technical cognizance over the interagency Ship Structure Committee's research program.

Dr. John Landes, *Chairman*, University of Tennessee, Knoxville, TN

Mr. Howard M. Bunch, University of Michigan, Ann Arbor, MI

Dr. Dale G. Karr, University of Michigan, Ann Arbor, MI

Mr. Andrew Kendrick, NKF Services, Montreal, Quebec

Dr. John Niedzwecki, Texas A & M University, College Station, TX

Dr. Alan Pense, NAE, Lehigh University, Bethlehem, PA

Dr. Barbara A. Shaw, Pennsylvania State University, University Park, PA

Dr. Robert Sielski, National Research Council, Washington, DC

CDR Stephen E. Sharpe, Ship Structure Committee, Washington, DC

DESIGN WORK GROUP

Dr. John Niedzwecki, *Chairman*, Texas A&M University, College Station, TX

Dr. Bilal Ayyub, University of Maryland, College Park, MD

Mr. Ovide J. Davis, Pascagoula, MS

Mr. Andy Davidson, NASSCO, San Diego, CA

Dr. Maria Celia Ximenes, Chevron Shipping Co., San Francisco, CA

Mr. Jeffrey Geiger, Bath Iron Works, Bath, ME

Mr. Hugh Rynn, Sea-Land Services, Elizabeth, NJ

MATERIALS WORK GROUP

Dr. Barbara A. Shaw, *Chairman*, Pennsylvania State University, University Park, PA

Dr. David P. Edmonds, Edison Welding Institute, Columbus, OH

Dr. John F. McIntyre, Advanced Polymer Sciences, Avon, OH

Dr. Harold S. Reemsnyder, Bethlehem Steel Corp., Bethlehem, PA

Dr. Bruce R. Somers, Lehigh University, Bethlehem, PA

RECENT SHIP STRUCTURE COMMITTEE PUBLICATIONS

Ship Structure Committee Publications - A Special Bibliography This bibliography of SSC reports may be downloaded from the internet at: <http://www.dot.gov/dotinfo/uscg/hq/g-m/gmhome.htm>

- SSC-392 Probability Based Ship Design: Implementation of Design Guidelines A.
Mansour, P. Wirsching, G. White, B. Ayyub 1996
- SSC-391 Evaluation of Marine Structures Education in North America R. Yagle
1996
- SSC-390 Corrosion Control of Inter-hull Structures M. Kikuta, M. Shimko, D
Ciscom 1996
- SSC-389 Inspection of Marine Structures L. Demsetz, R. Cario, R. Schulte-
Strathaus, B. Bea 1996
- SSC-388 Ship Structural Integrity Information System-Phase II M. Dry, R.
Schulte-Strathaus, B. Bea 1996
- SSC-387 Guideline for Evaluation of Finite Elements and Results R. I. Basu, K. J.
Kirkhope, J. Srinivasan 1996
- SSC-386 Ship's Maintenance Project R. Bea, E. Cramer, R. Schulte-Strauthaus, R.
Mayoss, K. Gallion, K. Ma, R. Holzman, L. Demsetz 1995
- SSC-385 Hydrodynamic Impact on Displacement Ship Hulls - An Assessment of
the State of the Art J. Daidola, V. Mishkevich 1995
- SSC-384 Post-Yield Strength of Icebreaking Ship Structural Members C.
DesRochers, J. Crocker, R. Kumar, D. Brennan, B. Dick, S. Lantos 1995
- SSC-383 Optimum Weld-Metal Strength for High Strength Steel Structures R.
Dexter and M. Ferrell 1995
- SSC-382 Reexamination of Design Criteria for Stiffened Plate Panels by D. Ghose
and N. Nappi 1995
- SSC-381 Residual Strength of Damaged Marine Structures by C. Wiernicki, D.
Ghose, N. Nappi 1995